Fall 2016

New polyanion-based cathode materials for alkali-ion batteries

Hooman Yaghoobnejad Asl

Department: Chemistry

NEW POLYANION-BASED CATHODE MATERIALS FOR ALKALI-ION BATTERIES

by

HOOMAN YAGHOOBNEJAD ASL

A DISSERTATION

Presented to the Faculty of the Graduate School of the

MISSOURI UNIVERSITY OF SCIENCE AND TECHNOLOGY

In Partial Fulfillment of the Requirements for the Degree

DOCTOR OF PHILOSOPHY

in

CHEMISTRY

2016

Approved by:

Amitava Choudhury, Advisor

Manashi Nath

Nicholas Leventis

Pericles Stavropoulos

Xinhua Liang

PUBLICATION DISSERTATION OPTION

The dissertation has been formatted according to the following five journal specifications: Paper I (pages 21—46) has been published in the journal, *RSC Advances*; Paper II (pages 47—72) has been published in the journal, *Journal of Materials Chemistry A*; Paper III (pages 73—91) has been published in the journal, *Inorganic Chemistry*; Paper IV (pages 92—125) has been published in the journal, *Chemistry of Materials*; Paper V (Pages 126—150) has been accepted for publication in the journal, *Chemistry of Materials*.

The associated supporting information (SI) for each publication is provided in the appendices in the following order:

Appendix 1 contains the SI for the paper I.

Appendix 2 contains the SI for the paper II.

Appendix 3 contains the SI for the paper III.

Appendix 4 contains the SI for the paper IV.

Appendix 5 contains the SI for the paper V.

ABSTRACT

A number of new materials have been discovered through exploratory synthesis with the aim to be studied as the positive electrode (cathode) in Li-ion and Na-ion batteries. The focus has been set on the ease of synthesis, cost and availability of active ingredients in the battery, and decent cycle-life performance through a combination of iron and several polyanionic ligands. An emphasis has been placed also on phosphite (HPO_3^{2-}) as a polyanionic ligand. The concept of mixed polyanions, for example, boro-phosphate and phosphate-nitrates were also explored. In each case the material was first made and purified via different synthetic strategies, and the crystal structure, which dominantly controls the performance of the materials, has been extensively studied through Single-Crystal X-ray Diffraction (SCXRD) or synchrotron-based Powder X-ray Diffraction (PXRD). This investigation yielded four new compositions, namely $Li_3Fe_2(HPO_3)_3Cl$, $LiFe(HPO_3)_2$, $Li_{0.8}Fe(H_2O)_2B[P_2O_8]\bullet H_2O$ and $AFePO_4NO_3$ (A = NH_4/Li, K). Furthermore, for each material the electrochemical performance for insertion of Li^+ ion has been studied by means of various electrochemical techniques to reveal the nature of alkali ion insertion. In addition Na-ion intercalation has been studied for boro-phosphate and $AFePO_4NO_3$. Additionally a novel synthesis procedure has been reported for tavorite $LiFePO_4F_{1-x}(OH)_x$, where $0 \leq x \leq 1$, an important class of cathode materials. The results obtained clearly demonstrate the importance of crystal structure on the cathode performance through structural and compositional effects. Moreover these findings may contribute to the energy storage community by providing insight into the solid-state science of electrode material synthesis and proposing new alternative compositions based on sustainable materials.

ACKNOWLEDGMENTS

I would like to express my sincere thanks to my advisor for his continued support and commitment for teaching, which made it possible for me to learn the basics of solid-state chemistry and crystallography.

I also thank the Office of Graduate Studies for their financial support through Dissertation Completion Fellowship which allowed me to devote more time and effort on research.

Especial thanks goes to Dr. Stavropoulos, Dr. Leventis and Dr. Nath for allowing me to use their argon glove box, potentiostat and AC-impedance spectrometer, respectively.

I sincerely thank Dr. Wisener for helping me to obtain the graduate student support from Central States Microscopy and Microanalysis Society.

Appreciations goes to my committee members, who dedicated time and effort in evaluating my graduate performance, and reading this dissertation and providing me with their invaluable suggestions.

Finally I would like to thank my family, friends, lab-mates, chemistry department staffs and everyone who helped me to complete my dissertation.

TABLE OF CONTENTS

APPENDICES

LIST OF ILLUSTRATIONS

LIST OF TABLES

1. INTRODUCTION

1.1. PERSPECTIVE AND BROADER IMPACT

Our technology has been built based on the fossil fuel, which can lead to a number of problems: 1) Dependence of countries on the imported fossil fuels which are not distributed evenly on a global scale and gives rise to geopolitical tensions; 2) Limited supplies of fossil fuels cannot sustain the ever increasing energy demands of the world in the next few decades; 3) Enormous CO_2 emission which affects the environment through global warming and climate change which certainly will affect the quality of our lives.

Nuclear energy may be envisaged as an alternative energy resource to the fossil fuels; however, the extensive use of Uranium and other actinide elements forces these elements to extinction in the next century. Added to this is the difficulty in locating, mining, extracting and processing of nuclear fuel as well as occurrence of catastrophic accidents in Chernobyl and Fukushima nuclear reactors, which places these energy resources marginal and non-dependable.

The only viable solution for replacing the fossil fuels is sustainable and regenerative energy resources, from which solar, wind, tidal, geothermal, biomass, etc. can be mentioned. For example, the amount of the solar energy received by earth during one hour can supply current world energy needs during a year. However, the intermittent nature of sustainable energy resources impeded their wide spread use as an alternative to fossil fuels. There is no doubt that mechanism for energy storage must be available to make sustainable energy as a reliable alternative to fossil fuels.

Currently only about 1% of the generated world energy is stored and 98% of that is through pumped-storage hydroelectricity; while wide-spread in use, this method can store only 3 Wh for every 1 metric ton water lifted by 1 m.[1]

The primary interest of a modern society running on sustainable energy can be divided in two parts: (1) design of mobile batteries for electric vehicles with high specific energy and power densities which can compete with internal combustion engines for transportation application; (2) design of durable batteries

based on low cost, abundant chemistries suitable for stationary electrochemical energy storage which can compete with the chemical energy stored in the fossil fuel.

Batteries are electrochemical energy storage devices which are by far more efficient than pumped-storage hydroelectricity in terms of energy storage (Fig. 1-1). The batteries are classified on a general basis as primary and secondary. Primary batteries are normally cheap energy storage devices which have been designed for a single use followed by disposal. On contrary secondary batteries can be recharged many times, as an example lead storage batteries can be mentioned.

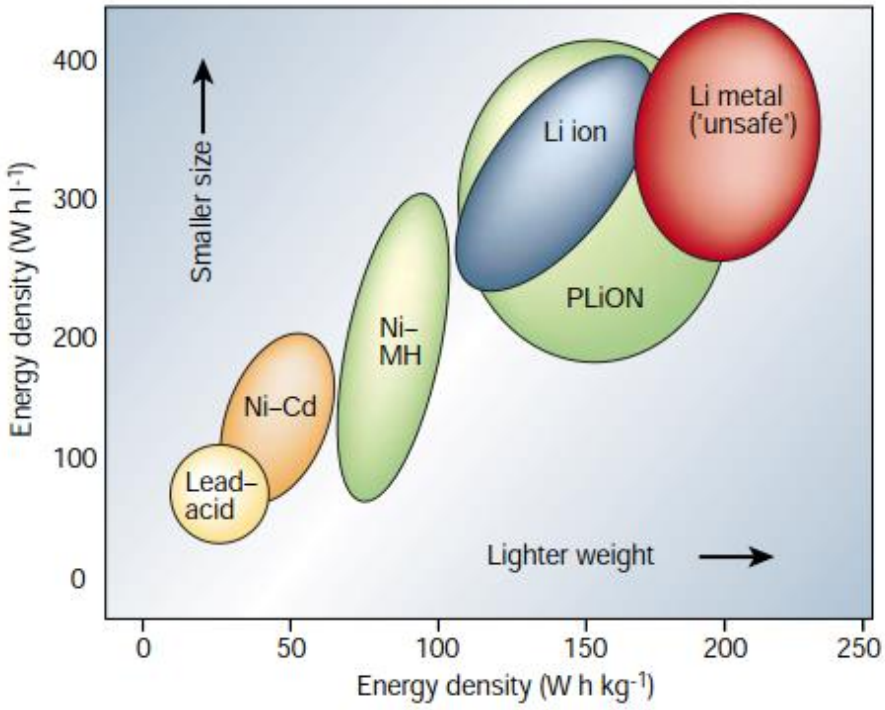

Figure 1-1. Comparison of the mass-based and volume-based energy density for several battery technologies. [2]

The basic unit in every battery is an electrochemical cell which composed of three components: an anode (negative electrode-reductant), a cathode (positive electrode- oxidant) and an electrolyte which establishes ionic contact between the two electrodes by allowing ion transport, but not the electrons. The amount of the

total energy which can be acquired from a battery with a voltage V(q) at the state of charge (SOC) q and current I flowing through it can be expressed as:

$$E = \int_0^t V(q).I.dt = \int_0^Q V(q).dq \quad (1\text{-}1)$$

Where Q is the total amount of electrical charge stored in the battery. In the energy storage literature the electrical charge is usually expressed in milliampere hour (mAh) where 1 mAh is equivalent to 0.277 Coulombs.

From a historical point of view the birth of the Lithium Ion Battery (LIB) follows the invention and use of Ni-Cd batteries [3]. The Ni-Cd battery operation is based on the oxidation of metallic Cd and simultaneous H^+ insertion and reduction of the nickel center in the layered NiOOH in aqueous electrolytes at *ca.* 1.5 V, according to equations 1-2 and 1-3:

In cathode: $2NiOOH + 2e + 2H^+ \rightarrow 2Ni(OH)_2$ (1-2)

In anode: $Cd + 2H_2O \rightarrow Cd(OH)_2 + 2H^+ + 2e$ (1-3)

The successful implementation of Ni-Cd secondary batteries fuelled up extensive research for designing other insertion chemistries for energy storage application. In this regard TiS_2 was among one of the most studied systems which has a similar layered structure as NiOOH. In this system, Li^+ can be reversibly inserted between the TiS_2 layers at a potential of 2.2 V vs. Li^+/Li^0.[4]

As the discharge potential of the TiS_2-Li system lies above the decomposition potential of water (1.23 V), non-aqueous solvents are required for the battery function. The ideal solvent should have a lowest unoccupied molecular orbital (LUMO) energy state above the Fermi level of electrons in the lithium metal anode and the highest occupied molecular orbital (HOMO) energy state below the conduction band of the cathode active material to avoid side reactions of the electrolyte with the electrodes. Among the organic solvents, carbonates were known to be able to dissociate lithium containing salts (e.g. $LiPF_6$, $LiClO_4$) and provide sufficient Li^+ mobility (10^{-2} $S.cm^{-1}$). The LUMO of dimethyl carbonate (DMC) lies 1.2 eV lower than the Fermi level of lithium metal (Fig. 1-2); therefore to avoid reduction of DMC in contact with lithium metal ethylene carbonate (EC) is added as a modifier which forms a passivation layer (also called solid-electrolyte interface, SEI) on the surface of the anode. On the other hand the HOMO-LUMO

gap for DMC is 3.0 eV and therefore from a thermodynamic point of view the highest achievable potential limit for DMC-EC solvent is 4.2 V. Additional kinetically impeding factors (over-potentials) make DMC-EC mixture as a suitable electrolyte solvent for safe operations of cells up to 4.5 V.

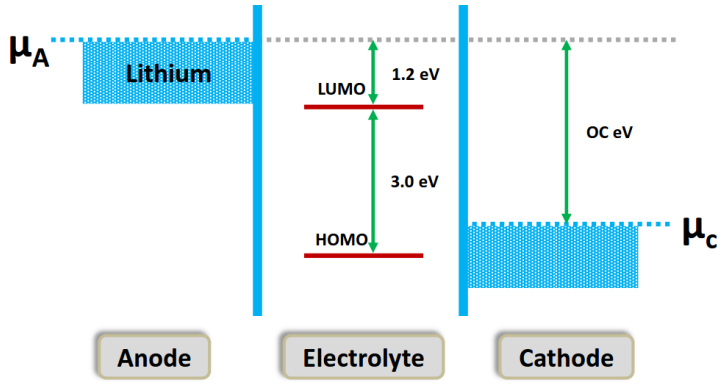

Figure 1-2. Energy level diagram for DMC solvent in a Li-ion cell.

Despite the successful operation of the rechargeable TiS_2-Li battery, the research was discontinued due to a major safety issue: the non-uniform deposition of Li^+ on Li metal creates Li dendrites which can grow toward the cathode and eventually form a short-circuit inside the cell which leads to catastrophic consequences. The problem of Li dendrite formation has been resolved by replacing lithium metal with graphite which can be lithiated at a potential of 0.2 V vs. Li^+/Li^0. However, researchers were looking for chemistries with higher specific energies, as compared to the TiS_2-Li cell.

As a transition to higher specific energy batteries one may consider increasing the cell potential. The conduction band energy of the cathode active material determines the discharge potential of a cell; hence the conduction band of MO_2 (with a mixture of oxygen 2p and metal 3d bands) lies at a lower energy level (and thus higher voltage) compared to the MS_2 (metal 3d and sulfur 3p bands) as oxygen 2p orbitals are harder bases compared to the sulfur 3p orbitals. This opened up the investigation window toward $LiCoO_2$ which is a layered compound similar to $LiTiS_2$, but differs in their stacking of anion layers, cubic stacking in the former and hexagonal stacking in the latter.

Since their introduction to the market by Sony Corporation back in 90's, lithium ion batteries (LIB) revolutionized the electrochemical energy storage concept. With their light weight, acceptable capacity and relatively high voltage LIBs formed a platform for powering up portable electronic devices such as laptops and mobiles, which has revolutionized our lives. The schematic of a typical LIB is shown in Fig. 1-3.

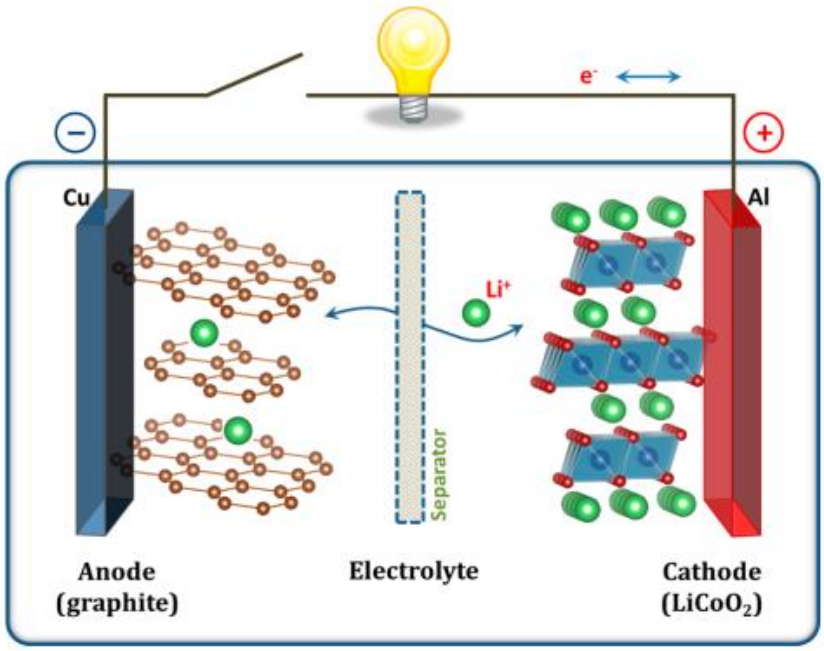

Figure 1-3. Schematic representation of a LIB.

In a fresh LIB system based on $LiCoO_2$ chemistry and with the cell initially in the discharged state, the redox active cobalt center is in the lower oxidation state of +3. $LiCoO_2$ composed of layered network of CoO_2 sheets formed from edge sharing CoO_6 octahedral units with the octahedrally coordinated lithium ions located in the interlayer space (Fig. 1-4). On the anode side the graphitic carbon (C) is in the higher oxidation state of 0. As the battery is connected to a charger electrons are pumped through the external circuit from the cathode to the anode, thus oxidizing the cobalt in the cathode active material from the oxidation state of +3 to +4 and reducing the carbon on the graphite anode from the oxidation state of 0 to -1/6.

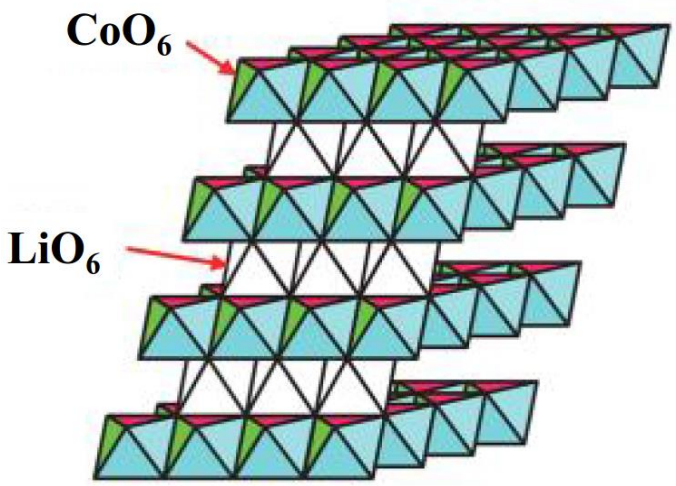

Figure 1-4. The layered crystal structure of $LiCoO_2$.

Meanwhile to balance the charge, lithium ions deintercalate from the $LiCoO_2$ cathode into the electrolyte and an equivalent number of Li^+ intercalate from the electrolyte into the anode to form LiC_6. The whole electrochemical reaction can be expressed according to equations 1-4 and 1-5:

In cathode: $LiCoO_2 \rightarrow CoO_2 + e + Li^+$ (1-4)

In anode: $C_6 + e + Li^+ \rightarrow LiC_6$ (1-5)

Theoretically the battery is fully charged when all the cobalt centers in the cathode have been oxidized to the higher oxidation sate of +4 and there is no Li^+ left in the cathode. Under this situation the LIB has a state-of-charge of 100% (SOC 1.0) and is ready to be discharged (theoretical capacity: 273.8 $mAh.g^{-1}$). Upon discharge the reverse of the above electrochemical reaction occurs during which the CoO_2 will be reduced and intercalated with Li^+ at an average voltage of 3.7 V vs graphite, LiC_6 is deintercalated oxidatively and Li^+ ions will have a net flow from the anode toward the cathode through the electrolyte, according to equations 1-6 and 1-7.

In cathode: $CoO_2 + e + Li^+ \rightarrow LiCoO_2$ (1-6)

In anode: $LiC_6 \rightarrow C_6 + e + Li^+$ (1-7)

Even though Lithium cobalt oxide showed outstanding success for energizing small electronic devices, it suffers from a number of issues for large scale

applications. First, only half of the theoretical specific capacity can be utilized practically. This is due to the fact that the CoO_2 layers in $LiCoO_2$ crystal structure are separated by the Li^+ ions; extraction of more than 50% (practical capacity: 137 $mAh.g^{-1}$) of those ions causes collapse of the structure and irreversible transformation into other phases which are not electrochemically active. This also imposes overcharge protection devices to be implemented into the battery system to avoid capacity loss. Secondly, from a chemical point of view the nature of the transition metal cation–oxide anion bond in a transition metal oxide compound is highly ionic due to the large difference in the electronegativity of the participating atoms in the bonding. This can lead to electrolytic bond cleavage of the oxygen–metal bond and release of the oxygen gas from the cathode. This has been demonstrated schematically in Fig. 1-5; when the cell voltage increases to oxidize Co^{3+} to Co^{4+}, partial overlap of the metal 3d band and oxygen 2p band causes electrons to be stripped from O 2p band, resulting in oxygen gas release.

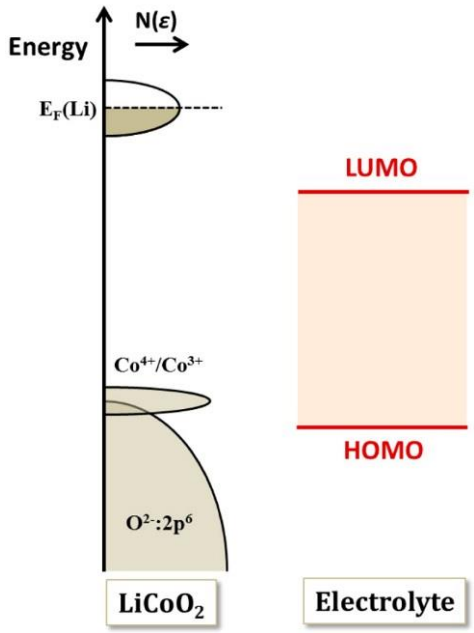

Figure 1-5. Energy level diagram indicating the relative ordering of metal and oxygen energy bands in Li_xCoO_2. [5]

As the battery is a closed system and accumulation of the oxygen gas in contact with the organic-based electrolyte, and heat generated during the battery

operation can cause onset of spontaneous exothermic reaction which leads to further release of oxygen gas and thermal runaways. Introduction of secondary and tertiary transition metals in Co site (e.g. $Li_{1-x}[Ni_{0.5-y}Co_{2y}Mn_{0.5-y}]O_2$) has been found to be effective in bringing down the oxygen 2p band energy lower than that of the transition metal 3d band so that almost complete oxidation of the metal center can occur before O_2 gas release.[6]

Apart from $LiCoO_2$ there are currently other transition metal oxides in which the LIB operation is based on the reversible Li^+ insertion followed by a change in the oxidation state of the central transition metal atom, similar to the former case. Some of these provide considerable improvement over $LiCoO_2$ in terms of capacity and operating voltage. Among these $LiMn_2O_4$ and its nickel substituted version, $Li[Ni_{0.5}Mn_{1.5}]O_4$ can be mentioned which can provide a discharge voltage of 4.7 V vs. Li^+/Li^0 with the extraction of one Li^+ from the formula unit.[7]

1.2. POLYANION BASED CATHODE MATERIALS

By definition, transition metal polyanion compounds are a class of materials which are composed of polyhedral XO_n moieties connected with MO_6 octahedral units (mostly) and less frequently MO_5 bi-pyramidal or MO_4 tetrahedral units, through the bridging oxygen atoms. The X atoms in the polyanion, XO_n, encompasses a wide range of non-metals (X: P, S, B, C, and N) and occasionally semi-metallic or metallic (X: Si, Ge, Se, As, Sb, Nb, Mo, W, etc.) elements. Within the polyanion, the X— O bond has a high degree of covalency due to either non-metal-oxygen electronegativity difference or high order bond formation between metals in high oxidation states and oxygen. This ensures that the oxygen atoms are tightly bound to the material framework imparting higher thermal and mechanical stability to the material compared to the pure transition metal oxides. On the other hand the M — O bond becomes more ionic in nature due to the ample electronegativity differences in the X – O bond, a phenomena known as inductive effect, which helps to improve the redox potential of the active material upon change of oxidation state on the metal center.

Following the introduction of transition metal oxides in LIB, Goodenough *et al* pioneered the idea of electrochemical Li^+ insertion into a solid-state host of a polyanionic compound of iron, olivine $LiFePO_4$ [8]. This marked a big step in LIB research and development and brought several promises with it:

- The polyanion chemistry creates a basis for iron based compounds to be used as cathode in LIB. The inductive effect of the polyanion increases the redox potential so much that low insertion voltage of pure iron-oxides increases manifold in iron polyanion compounds and they become good candidates for cathode. Unlike cobalt, iron is a low cost earth abundant element with no toxicity on living organisms and has less environmental issues;
- The existence of covalent bonds within the polyanion moiety eliminates the chance of electrolytic O_2 gas release and makes these compounds inherently safe;
- Due to strong covalent bonds, the polyanion compounds offer solid-state materials with higher structural stability in which structural rearrangement due to Li^+ extraction/insertion are minimized and often the full capacity given by theoretical calculations can be achieved;
- Unlike the oxide chemistry where the structures are formed by the limited number of close packed anion array, various 2D, 3D and open-framework structures can be formed by mixing different polyanions and transition metal centers;

The possibility to tune the band structure of the solid-state compound through using different polyanionic moieties, as well as addition of secondary (poly)anion, through adjusting the iono-covalency nature of the metal-ligand bond serves as a tool for tuning the cell voltage in the polyanionic cathode materials.

A typical cathode based on olivine $LiFePO_4$ can provide a flat discharge potential at 3.4 V vs. Li^+/Li^0 and a practical specific capacity close to 170 $mAh.g^{-1}$. The crystal structure of the olivine $LiFePO_4$ is shown in Fig. 1-6(a). The structure composed of FeO_6 octahedral units alternatively edge and corner-shared with PO_4 tetrahedral units which leads to formation of a rigid structure with effectively 1D diffusion channels along the b-axis of the crystal, hosting the Li^+ ions [9]. Loaded in a cell as cathode, $LiFePO_4$ is initially in the discharged state; charging the cell

against Li anode causes oxidative delithiation of the cathode electrode to $FePO_4$ which is structurally similar to $LiFePO_4$, although they constitute two different thermodynamic phases. For any electrochemical process one may use the Nernst equation to follow the cell potential as the electrochemical reaction occurs. Therefore, treating the olivine cathode charging reaction as an example the respective cell potential in terms of the activities of the redox reaction components are given in equations 1-8 through 1-10:

$$LiFePO_4 \rightarrow FePO_4 + e + Li^+ \quad (1\text{-}8)$$

$$Li^+ + e \rightarrow Li \quad (1\text{-}9)$$

$$E_{cell} = E^0_{cell} - \frac{RT}{F} ln \frac{a_{FePO_4}.a_{Li}}{a_{LiFePO_4}} \quad (1\text{-}10)$$

Where E^0_{cell} is the cell potential at standard thermodynamic conditions, F is the Faraday's constant, T the absolute temperature and a_i is the activity of chemical species i. Since by definition the activity of a pure solid is equal to unity, for an electrochemical reaction which contains a redox couple in two different phases the above fraction simplifies to unity, and the cell potential remains at the E^0_{cell} throughout the electrochemical process irrespective of the change in the composition of electrode (Fig. 1-6(b)). As will be shown later in the results section this is not always the case, as the oxidized and reduced forms of a cathode normally are such similar in crystal structure that they become thermodynamically indistinguishable, with no phase boundary separating the two components and forming a solid solution of mixed oxidation states. Under this condition the activities of the redox forms of the cathode are not unity anymore and hence the overall cell potential follows a sloppy sigmoid-shaped curve with a center roughly at E^0_{cell}.

A very intuitive demonstration of the capability of the polyanion chemistry can be visualized by substituting the active metal center with other metals of the first row of the d-block of the periodic table in the olivine $LiMPO_4$. As the redox potential of the M(II)/M(III) couple increases in the first row of transition metals, so does the cell potential (Figure 1-7).

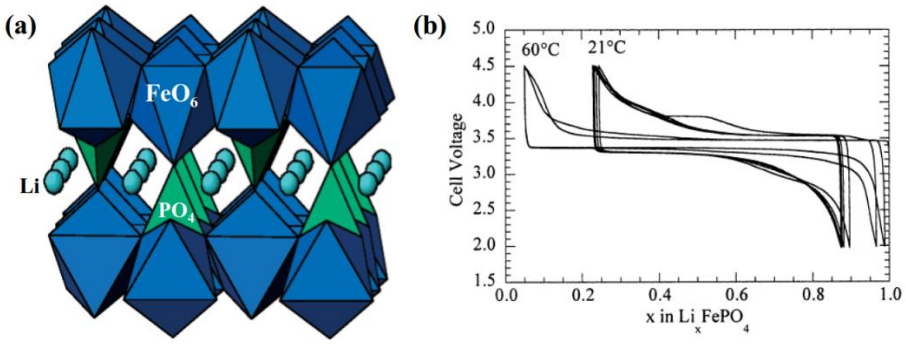

Figure 1-6. (a) Crystal structure of the olivine $LiFePO_4$; (b) Voltage-composition profiles of $LiFePO_4$ as cathode in a typical LIB at various temperatures [10].

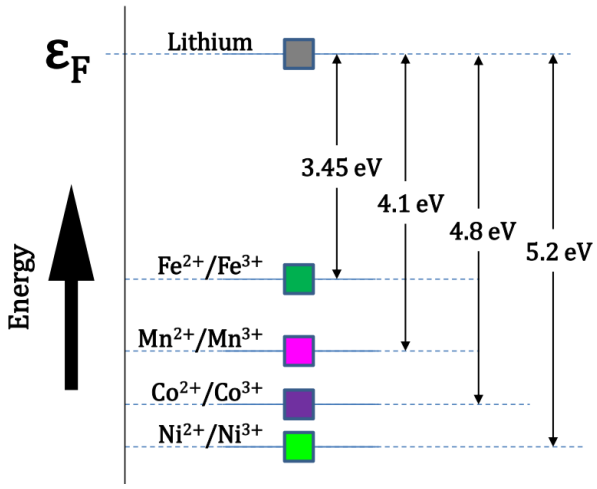

Figure 1-7. Energy diagram of M(II)/M(III) redox energy in phospho-olivines ($LiMPO_4$).

Following the discovery of electrochemical activity in $LiFePO_4$ there was a burst of scientific reports studying the electrochemical activity in already known or newly discovered metal polyanion compounds. Apart from the already discussed phosphates, other compounds based on SO_4, SiO_4, BO_3 were reported. The effect of the electronegativity of the central atom of polyanion on the iono-covalency nature of the metal-ligand bond and their effect on the cell voltage has been demonstrated (Fig. 1-8).

Fig. 1-8 clearly demonstrate the effect of electron withdrawing power of the central atom in the polyanion on the redox potential of different transition metal centers, indicating the numerous compositional combinations which may be used

for tuning the cell potential. Moreover, addition of a secondary anion to the primary polyanion adds new structural and chemical dimensions to the polyanion-based compounds of transition metals. In this regard mixed oxide-phosphate, fluoride-phosphate and carbonate-phosphate in $LiVOPO_4$, $LiVPO_4F$, $LiFeSO_4F$ and $Li_3FePO_4CO_3$ demonstrate the immense possibilities to discover new opportunities in this field. Table 1-1 provides an overview of the major polyanionic cathode materials discovered along with their figures of merit.

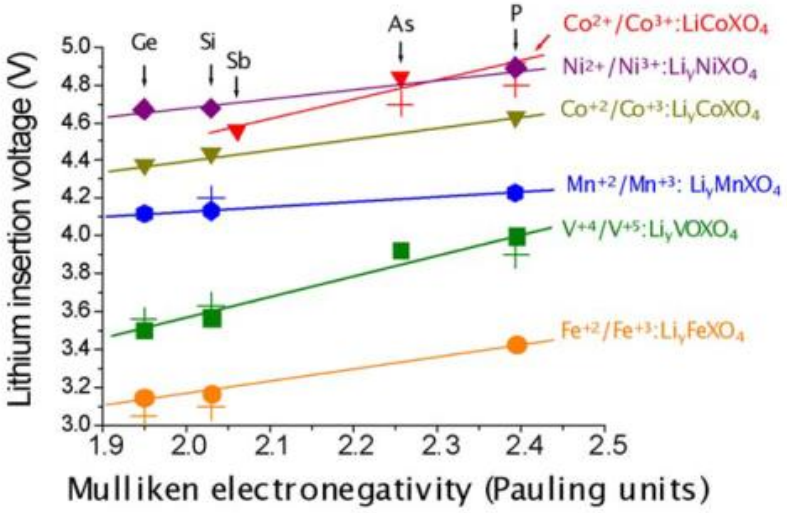

Figure 1-8. Calculated (solid symbols) and experimental (+ symbol) cell voltage for a fixed composition $LixMXO_4$ as a function of the Mulliken electronegativity of the X atom in the polyanion. [11]

Table 1-1. Summary of the most important polyanion-based cathodes, with their nominal cell voltage and specific capacity

Composition	Structure type	Potential vs. Li^+/Li^0	Theoretical capacity ($mA.h.g^{-1}$)	Practical capacity ($mA{\cdot}h.g^{-1}$)	Ref.
$LiFePO_4$	Olivine	3.5	170	155 – 165	[8]
$Li_3Fe_2(PO_4)_3$	NASICON	2.8	128	116	[12]
$LiVOPO_4$	New	3.98	158	90	[13]
α-$Li_3V_2(PO_4)_3$	NASICON-related	4.5	N/A	200	[14]
$LiFeP_2O_7$	$LiInP_2O_7$	2.9	113	113	[15]
$LiVPO_4F$	Tavorite	4.1	156	155	[16]

Table 1-1. Summary of the most important polyanion-based cathodes, with their nominal cell voltage and specific capacity (cont.)

$LiFeBO_3$	$LiCoBO_3$	2.9	200	156	[17]
$Fe_{1.8}(PO_4)(OH)_{0.52}(H_2O)_{0.43}$	Lipscombite	2.5	N/A	85 - 110	[18]
Li_2FeSiO_4	β-Li_3PO_4	2.8	166	140	[19]
$Li_5V(PO_4)_2F_2$	New	4.15	170	88	[20]
$Fe(OH)SO_4$	New	3.2	159	110	[21]
$LiFeSO_4F$	Tavorite	3.6	151	140	[22], [23]
$LiFeSO_4F$	Triplite	3.9	151	121	[24], [25]
$LiFeSO_4OH$	New	3.6		80%	[26]
$FePO_4.H_2O$	$MnPO_4 \cdot H_2O$	2.8	159	125	[27]
$LiFePO_4(OH)$	Tavorite	2.6	153	100	[28]
$LiFePO_4F$	Tavorite	3	152	145	[29], [30]
$Li_2FeP_2O_7$	$Li_2MnP_2O_7$	3.5	110	110	[31]
Li_2MnPO_4F	$Na_2ZrOSiO_4$	3.9	147	140	[32]
Li_2CoPO_4F	Li_2NiPO_4F	4.85	143	60	[33]
$Li_9V_3(P_2O_7)_3(PO_4)_2$	$Li_9Al_3(P_2O_7)_3(PO_4)_2$	4.46, 3.74	116	110	[34]
$Li_3FeCO_3PO_4$	$Na_3MnPO_4CO_3$	2.8	115	110	[35]
$Li_2Fe(SO_4)_2$	Marinite	3.83	102	88	[36]

The list of cathode materials in Table 1-1 is not meant to be comprehensive by any intention. However, they have been presented to demonstrate the huge potential and diversity one may expect from various transition metal polyanionic materials.

1.3. SYNTHESIS PROTOCOLS FOR TRANSITION METAL POLYANIONIC COMPOUNDS

As one may expect, synthetic chemistry contributed a huge role to the ever growing area of transition metal-polyanion compounds. This is mainly due to the numerous available polyanionic moieties and transition metals, which gives rise to several possible combinations. Moreover, solid-state chemists may use different synthetic strategies to form polymorphs of the same composition, which are not necessarily identical from an electrochemical point of view; $LiFeSO_4F$ is probably one of the best examples in this regard. Pure $LiFeSO_4F$ crystallizes in two different

phases, tavorite (triclinic, space group, $P\bar{1}$) and triplite (monoclinic, space group *C2/c*) through different synthesis methods. The difference in the crystal structure (though same composition) leads to surprising results in lithiation voltages, 3.9 V and 3.6 V for triplite and tavorite, respectively (Table 1-1). The lithiation voltage of triplite currently holds the record as the highest observed redox potential of Fe^{2+}/Fe^{3+} couple among all solid-state materials. The change in crystal structure created by different ordering and connectivity of polyhedral units not only affects the cell voltage through thermodynamic stability factors, but also greatly affects the power rating of the active material *via* altering the diffusion path geometry and kinetics of Li^+ ion mass transfer during the cell performance.

With the above argument forming a platform to emphasize the importance of synthetic methods to make solid-state inorganic materials, the following discussion briefly list the mostly used synthetic methods for the synthesis of battery active materials. Different methods have been sorted according to the normally used temperature regime. [37]

- Solid-state and ceramic reactions:

The direct solid-state methods has been used traditionally for making oxides and other materials with high thermal stability. The method works based on simple enhanced ionic diffusion at high temperatures through intimate contact between the starting materials particles. Typically the reagents first milled extensively for an extended period of time to achieve uniformity and small particle size, followed by pressing into a pellet and subsequent heating at 600-900 °C for a few hours to several days. The reaction environment are generally controlled by passing reactive or inert gases to stabilize the desired oxidation state of the transition metal center. For a given set of conditions, normally the most thermodynamically stable phase forms as a result of high activation energy given as thermal energy. This limits the solid-state and ceramic methods to effectively study the polymorphism and also exclude the synthesis of more thermally labile compounds. Moreover, the appearance of impurity phases due to intrinsic inhomogeneity of reagents and formation of large agglomerates with long Li^+ diffusion path lengths are very common in these synthetic methods.

- Sol-gel processes:

The sol-gel process is a multi-step synthetic method which offers better homogeneity and smaller particle sizes compared to the solid-state synthesis route. In this method the reagents are first dissolved and mixed into a solvent to form a homogenized mixture; the solvent is then evaporated, leaving the solid residue which is pulverized and pyrolyzed at high temperatures, similar to the ceramic methods. Since the mixing is performed on an atomic scale, the products present higher degrees of pureness. Moreover conductive carbon layers can be formed on the product particles if carbon-based precursors are used during the synthesis.

- Precipitation processes:

The precipitation methods can be used for making those materials which form as a precipitate as a result of low solubility constants. The method involves mixing the reagents in a solvent and forming the precipitate by adjusting the pH. The precipitate is normally heated at high temperatures (400—700 °C, providing thermal stability) to remove the solvent and possible crystalline disorders.

- Polyol processes:

High boiling point polyols play the role of solvent and reaction medium in polyol based synthesis. The reaction is conducted at the boiling point of the solvent and under isobaric conditions over a hot oil bath, hence eliminating the need to sophisticated reactors. The commonly used polyols are tetraethylene glycol (T_b=314 °C), triethylene glycol (T_b=285 °C) and diethylene glycol (T_b=245 °C).

- Hydrothermal and solvothermal processes:

These two processes encompass the widest range of syntheses due to the low cost of solvents used, relatively low temperatures required and the high degree of control on the reaction conditions. In a typical reaction the reactants are dissolved/dispersed in the solvent (water in the case of hydrothermal reactions) taken into a teflon cup, which is then sealed into an autoclave steel jacket and placed in an oven at a temperature higher than the boiling point of solvent (normally <250 °C). The combination of high temperature and high autogenous pressure leads to the formation of high purity product with good yield.

- Ionothermal processes:

These methods are based on the dissolution of reagents in the ionic solvents with very low vapor pressure. These reactions are based on the organic ionic liquids which are generally expensive, especially for large-scale applications though eliminates the need of elaborate reactors, it imposes recycling of the ionic liquid.

- Inorganic fluxes and eutectic salt mixtures:

These are based on eutectic mixtures or pure compounds with relatively low melting points and are generally much cheaper compared to the ionic liquids. This category can have a wide range of melting points and stability windows, covering the temperature range required for making transition metal polyanion compounds.

Among the above methods, the hydrothermal and flux-based methods have been used extensively in this work. This is mainly due to the low-cost and scalability requirements of battery manufacturing process. Moreover, due to the low to moderate temperatures involved in hydrothermal and flux based reactions, they unlock access to a vast area of metastable compounds with interesting structural and performance features, which cannot be formed by other methods. This is more promising in the case of inorganic fluxes, where the flux acts not only as a medium to dissolve the precursors, but also takes part as a reagent, affecting the final composition of the material. Some examples of the latter is presented in the results sections.

Given the vast studies done so far on the role of the polyanion chemistry for designing cathode materials for LIB application, the innovation has finally reached a plateau. The aim of this work was to focus more on the unexplored areas of the polyanion chemistry and to inspect the possibility of discovering new combination which may be technologically important for energy storage applications. This has been done partly by focusing on flux-based reactions using phosphorous acid, H_3PO_3, which has a low melting point of 94 °C. Moreover, a major volume of the work has been done to study the role and effect of phosphite (HPO_3^{2-}) as a polyanion which was not investigated previously. On the transition metal side, the focus has been narrowed down to iron, to keep the cost, toxicity and abundance of the cathode active material at an optimum level, especially for very large scale applications (e.g. grid scale energy storage). This led to the

formation of two new compounds, $Li_3Fe(HPO_3)_3Cl$ and $LiFe(HPO_3)_2$ as discussed in the relevant chapters. Moreover the idea of combining two polyanions and studying the structural and electrochemical effects of these mixings led to the formation of $LiFe(H_2O)_2B[P_2O_8] \bullet H_2O$ and $AFePO_4NO_3$ via hydrothermal and flux-based syntheses, respectively. The latter is closely related to the carbonophosphates discovered recently. [35] Finally new hydrothermal and flux-based syntheses have been employed to demonstrate alternative synthetic methods for the formation of tavorite $LiFePO_4(OH)_xF_{1-x}$ ($0 \leq x \leq 1$) and to emphasize the role of synthesis, and its effect on controlling composition and eventually cell performance.

Despite the high success rate of current Li-ion batteries, unfortunately they cannot be still be treated as an energy storage technology for the future. This is mainly due to the global shortage of lithium resources and ever increasing use of Li-ion batteries may pose a serious risk of extinction at the end of current or the early decades of the next century. This problem should be addressed by substituting the electrodes with materials which can intercalate sodium, a widely available alkali ion. The principles of lithiation and sodiation follow similar routes, and hence some of the cathode materials can intercalate Na^+ as well as Li^+ ions, provided there is enough crystal stability of the corresponding sodiated phase. For such systems, the observed cell voltage and power rating is, however, inferior to the Li-ion counter parts, as a result of lower Fermi level in sodium and larger ionic radii of Na^+ compared to the Li^+ ion, which makes the diffusion of Na^+ sluggish. Due to the importance of studying Na-ion batteries, we have also evaluated the performance of $Fe(H_2O)_2B[P_2O_8] \bullet H_2O$ and $AFePO_4NO_3$ as cathode materials in Na-ion cells and the results for each case are reported accordingly.

1.4. EXPERIMENTAL

The target of this research was to discover new polyanionic compounds based on iron which can be used as cathode materials in LIBs. The idea here was to incorporate desirable features of iron i.e. high abundance and low cost, with economical synthesis approaches to design cost effective solutions for energy storage at a stationary level. Unlike the mobile applications where a high power density battery system is crucial for successful realization of the technology,

stationary state applications demand lower battery costs and durability as the primary criteria of interest.

The details of the experimental synthesis will be outlined in the respective chapters. Briefly various exploratory synthetic techniques mainly based on solvent free or low melting point fluxes have been used along with low cost starting substances. After heating the reaction mixture at various temperatures and times, the reaction products were retrieved from the mixture and subjected to the post-synthesis analysis and comprehensive characterization techniques.

As these solid-state products are all crystalline, crystallography played the primary and central role in materials characterization. For products formed as large and high quality crystals, single-crystal X-ray diffraction (SC-XRD) was used to collect the diffraction data and solve the crystal structure while powder X-ray diffraction (PXRD) was used for sample purity assessment. On the contrary where the new product obtained only as powder (i.e. micro crystallites) high resolution synchrotron X-ray diffraction was used for solving the crystal structure.

The solved crystal structure is often the starting point for many complementary chemical analysis techniques to expand our understanding of the material properties under study. These include the Mössbauer spectroscopy for assessing the oxidation state of the iron and its coordination sphere. Mössbauer spectroscopy was also used as a quantitative tool for quantification of the proportions of Fe(II) and Fe(III) in cases where a mixing of oxidation states occurred, either through synthesis or as a result of electrochemical treatment. DC magnetization measurements were used for characterization of magnetic interactions and magnetic phase transitions in samples and also to confirm the oxidation state assignments. Thermogravimetric analysis (TGA) was used for thermal stability determination and also to follow thermally induced structural changes leading to a change in the formula unit. Fourier-transformed infrared spectroscopy (FTIR) was used as a general tool for functional group characterization, while SEM/EDS analyses utilized for morphological and elemental analysis studies. Occasionally, elemental analysis using atomic

absorption spectroscopy (AAS) was employed for the exact determination of alkali ions concentration.

Followed by comprehensive characterization of materials, the materials were processed for loading as composite cathodes in the test cells. The processing normally comprises milling with conductive carbon to reduce the active material's particle size and increase the inter-particle electrical conductivity. Furthermore polyvinylidene fluoride (PVDF) dissolved in N-methyl-2-pyrrolidone (NMP) is added to the active material/carbon mixture and the resulting slurry was dispersed on the surface of carbonized aluminum current collector. Upon evaporation of NMP, PVDF acts as a binder for sticking the cathode mix to the current collector. Followed by the preparation of the composite cathode, a disk was cut and assembled in a coin cell versus metallic lithium anode, as depicted in Fig. 1-10.

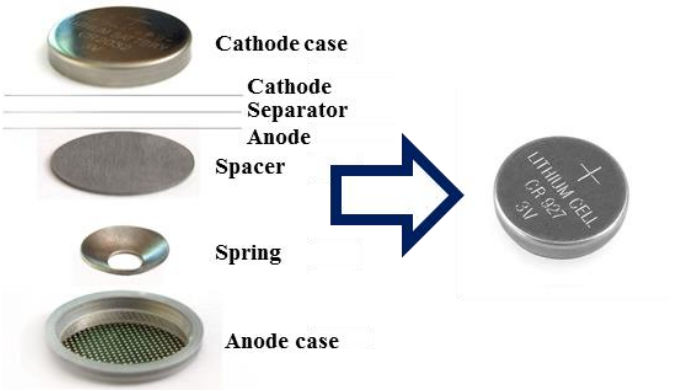

Figure 1-9. Coin cell structures.

Finally for Li-ion cells few droplets of electrolyte (a 1M solution of $LiPF_6$ in 1:1 mixture of ethylene carbonate (EC) and dimethyl carbonate (DMC)) is added to the cell and the cell is crimped to seal. The procedure for fabricating Na-ion cells is similar to the Li-ion ones, with the exception that fresh cuts of Na layer is placed as anode and a 1M solution of $NaClO_4$ in DMC/EC has been used as the electrolyte. Later, the cells were aged for few hours for stabilization and the anode SEI formation, as discussed previously. The cells were then subjected to various electrochemical tests to study the details of the battery performance. Cyclic voltammetry (CV) was employed as a preliminary screening

technique to evaluate the electrochemical activity of the as-prepared cathode material, determination of its redox potentials and the reversibility of the charge-discharge process.

Galvanostatic charge-discharge tests were used as a quantitative technique for obtaining the voltage-composition profiles during the cell operation, as well as measurement of the practical specific capacity. The galvanostatic tests were initially started at slow charge-discharge current rates (C-rate), denoted as C/n where n is the time required for complete oxidation/reduction of the active material in hours. Following the slow charge-discharge tests the C-rate was increased stepwise to evaluate the cell performance and capacity retention at higher charge and discharge rates.

As battery is a complicated multicomponent system, obtaining specific information on individual components is very difficult. Electro-impedance spectroscopy (EIS) was used as a technique of choice for studying the responses of various components of a cell separately. This is done by applying a variable frequency alternating current (AC) voltage input and recording the AC current output; provided that different components of the cell have different time-constant, their current response can be separated in frequency domain.

EIS was also used on candidate samples selected based on crystal structures for measurement of Li^+ ionic conduction in the as-synthesized materials. This has been done by coating the sides of a pelletized sample by conductive silver paint (blocking electrodes) and obtaining the impedance spectra at various temperatures. Details of the synthesis and experimental procedures are provided in the respective paper sections.

PAPER

I. Phosphorous acid route synthesis of iron tavorite phases, $LiFePO_4(OH)_xF_{1-x}$ [0≤ x ≤1] and comparative study of their electrochemical activities

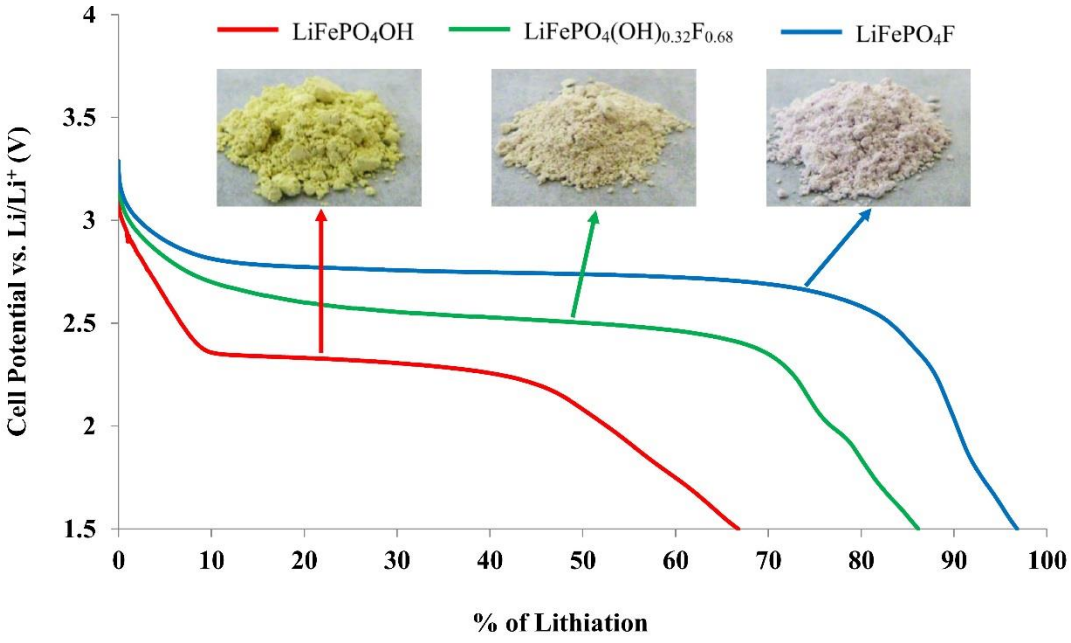

Hooman Yaghoobnejad-Asl [a] and Amitava Choudhury [a,*]

[a,*] Department of Chemistry, Missouri University of Science and Technology, Rolla, MO 65409, USA.

[a] Department of Chemistry, Missouri University of Science and Technology, 400 W 11th Street, Rolla, MO 65409, USA.

Fax: (573)341-6033; Tel:(573)341-6332.

* E-mail: choudhurya@mst.edu

Abstract

New synthesis routes were employed for the synthesis of three derivatives of iron hydroxo-, fluoro-, and mixed hydroxo-fluoro phosphates $LiFePO_4(OH)_xF_{1-x}$ where $0\leq x \leq 1$ with tavorite structure type, and their detail electrochemical activities have been presented. The hydrothermal synthesis of pure hydroxo- derivative, $LiFePO_4OH$, using phosphorous acid as a source of phosphate yielded good

quality crystals from which the crystal structure was solved for the first time using SC-XRD (single crystal X-ray diffraction). The fluoro derivative, $LiFePO_4F$, was prepared as very fine powder at low temperature in a solvent-less flux-based method employing phosphorous acid and mixed alkali metal nitrates. A mixed anionic hydroxo-fluoro iron tavorite phase, $LiFePO_4(OH)_{0.32}F_{0.68}$, was also synthesized by a hydrothermal route. The electrochemical performance of the three phases was studied with galvanostatic charge/discharge tests, cyclic voltammetry, and electrochemical impedance spectroscopy. All three phases showed facile Li-insertion through the reduction of Fe^{3+} to Fe^{2+} at an average voltage in the range of 2.4 – 2.75 volt, through the variation of anion from pure OH to pure F. An increase of 0.35 volt was observed as a result of F substitution in OH position. Also, good cyclability and capacity retention was observed for all three phases and a reversible capacity of more than 90% was achieved for $LiFePO_4F$. The results of EIS indicated that lithium ion mobility is highest in the mixed anion.

Introduction

Polyanion-based compounds of transition metals are being actively investigated as cathode materials for Li-ion battery since the discovery of electrochemical activity in $LiFePO_4$ by Goodenough's group.[1] The polyanions especially phosphates, sulfates, silicates and borates are capable of forming a wide variety of 2-dimensional (2D) and 3-dimensional (3D) structures with transition metals, which are stable and amenable for facile electrochemical Li-ion insertion.[2] There are several other advantages of polyanion based materials over simple oxides. The electronegativity of the central atom of the polyanion due to its inductive effect increases the potential of the transition metal redox couple $M^{n+}/M^{(n-1)+}$ with respect to Li^+/Li compared to pure oxides.[3] Secondly, the polyanion-based cathodes are inherently safer due to the strong covalent bond between the central atom (P, Si, S, and B) and the oxygen, which prevents them from dissociation when the cell is fully charged or fully de-lithiated. All these characteristics have made these materials excellent candidates for motor vehicle application where safety is of utmost importance. In this regard olivine $LiFePO_4$ has been touted as an excellent

candidate for hybrid electric vehicle application due to its reasonably high energy density with an average voltage of 3.5 volt vs Li^+/Li and a theoretical capacity of 170 mAh/g.[4] However, olivine $LiFePO_4$ also suffers from limitations due to poor electronic conduction and 1-dimensional Li-ion diffusion channel.[5] To overcome this drawback, carbon coating and nano-structuring are essential to achieve near theoretical capacity at fast discharge rate, which eventually reduces the cost effectiveness of the material.[6,7] Recently, attention has been paid to another structure type namely, tavorite, with 3-D intersecting channels conducive for facile Li-ion transport.[8] The sulfate version of iron tavorite, $LiFeSO_4F$, showed excellent performance which can potentially outperform olivine $LiFePO_4$.[9] The iron tavorite phosphate phases show an average voltage of 2.6 – 2.8 volts for the hydroxo and fluoro derivatives, which is lower than $LiFePO_4$ and is caused by the structural differences with $LiFePO_4$.[10-15] However, iron tavorite phases can be competitive for stationary application such as in smart grid, where safety, long cycle and calendar life, environmentally friendliness and low cost of the cathode materials supersede the need of high specific energy and energy density constraints of mobile applications.[16] Although tavorite iron phosphate, especially the fluoro derivative, fulfils all the above criteria, they still require an inexpensive and scalable synthesis route for large scale industrial production. High temperature ceramic methods,[12] ionothermal,[11] and solvothermal[13] routes reported so far for the synthesis of iron phosphate fluoro tavorite are cost prohibitive. In this article we report an innovative synthesis of fluoro ($LiFePO_4F$) and hydroxo ($LiFePO_4(OH)$) iron tavorite phases employing phosphorous acid as a source of phosphate in a low temperature flux and hydrothermal reactions, respectively. In addition we also report the synthesis of mixed fluoro/hydroxo phase, $LiFePO_4(OH)_{0.32}F_{0.68}$, by a hydrothermal reaction. The products were characterized by powder and single-crystal X-ray crystallography, IR and Mössbauer spectroscopic techniques and thermogravimetric analysis. Although structure of full hydroxo tavorite has been reported from powder X-ray- and neutron diffraction data,[10] the single-crystal X-ray structure determination is reported here for the first time. Finally we present a comparison of the electrochemical Li-ion activities of the three phases with respect

to charge-discharge, cyclic voltammetry, and electrochemical impedance measurements.

Experimental

Materials

$LiNO_3$, KNO_3, LiOH and H_3PO_3 were purchased from Acros Organics, Fe(NO3)3.9H2O from Alfa Aesar and Li foil from Sigma-aldrich. All the chemicals used without further purification.

Synthesis

$LiFePO_4F$ has been synthesized employing a low melting flux consisting of KNO_3-$LiNO_3$ eutectic mixture and phosphorous acid (H_3PO_3). In a typical synthesis 8.08 g of $Fe(NO_3)_3{\cdot}9H_2O$ (20 mmol), 0.52 g (20 mmol) of LiF, and 1.64 g (20 mmol) H_3PO_3 were added in 14 g of KNO_3-$LiNO_3$ mixture (0.56:0.44) in a 23 mL Teflon-lined stainless steel Parr acid digestion bomb. The Parr reactor containing the reaction mixture was placed in a 200 °C oven and heated at that temperature for 72 h, after that the bomb was removed from the oven and allowed to cool naturally. The product which consisted of white fine powder was washed with chilled water several times to remove LiF completely and then dried in air.

$LiFePO_4(OH)$ was prepared hydrothermally employing H_3PO_3 as source of phosphate. In a typical synthesis 16.16 g (40 mmol) of $Fe(NO_3)_3{\cdot}9H_2O$, 2.87 g (120 mmol) of LiOH, and 9.84 g (120 mmol) of H_3PO_3 were added in a beaker containing 40 mL of deionized water. The reaction mixture was stirred for several minutes to form a homogeneous solution. The reaction mixture was then transferred to a 120 mL capacity Teflon-lined stainless steel Parr reaction vessel. The reaction vessel was then placed in a 200 °C oven and heated at that temperature for 96 h, after that it was removed from the oven and allowed to cool naturally. This process yielded bright green color product containing good quality crystals suitable for single-crystal X-ray structure determination.

$LiFePO_4(OH)_{0.32}F_{0.68}$ was prepared by hydrothermal method from a well homogenized reaction mixture of 1.35 g (5.0 mmol) of $FeCl_3{\cdot}6H_2O$, 1.04 g (25 mmol) of $LiOH{\cdot}H_2O$, 0.34 mL (5.0 mmol) H_3PO_4 (85%), 0.35 mL (10 mmol) HF

(49-51%) and 9 mL of deionized water in a 23 mL Teflon-lined stainless steel Parr reaction vessel. The Parr reaction vessel was heated at 175 °C for 72 h. The product, pale green powder was filtered, washed with hot water and acetone and subsequently dried in air.

Material Characterization

Single-crystal X-ray diffraction. Single-crystal X-ray diffraction studies of $LiFePO_4(OH)$: Crystal structure of $LiFePO_4(OH)$ was solved from single-crystal intensity data sets collected on a Bruker Smart Apex diffractometer with monochromated Mo Kα radiation (λ = 0.7107 Å). Suitable crystal was selected and mounted on a glass fiber using epoxy-based glue. The data were collected at room temperature employing a scan of 0.3° in ω with an exposure time of 20 s/frame. The data sets were collected using SMART[17] software, the cell refinement and data reduction were carried out with SAINT,[18] while the program SADABS[18] was used for the absorption correction. The structure was solved by direct methods using SHELX-97[19] and difference Fourier syntheses. Full-matrix least-squares refinement against $|F^2|$ was carried out using the SHELXTL-PLUS[19] suit of programs. The structure of $LiFePO_4(OH)$ was solved in $P\bar{1}$ space group. The positions of two Fe atoms, Fe1 and Fe2 were located in 1*c* and 1*a* Wyckoff positions, respectively; one P and 5 O atoms were located in 2*i* positions from the difference Fourier maps. These positions were then refined isotropically and immediately the position of Li (2*i*) clearly appeared around 2 Å away from the oxygen atoms. At this point anisotropic refinement was carried out and a *q* peak appeared around 1 Å away from the oxygen (O3), which was bridging the two Fe-atoms. This peak was assigned as hydrogen and refined isotropically without any constraints. After the refinement O – H bond distances changed to 0.778 Å. Details of the final refinements and the cell parameters for $LiFePO_4(OH)$ are given in Table 1. The final atomic coordinates and the isotropic displacement parameters are given in Table 2. Selected inter-atomic distances are listed in Table 3.

Powder X-ray diffraction (PXRD). Phase purity for all samples was evaluated by X-ray powder diffraction patterns obtained from a PANalytical X'Pert Pro diffractometer over a 2θ range of 5 to 90 ° with scanning rate of $0.0236°s^{-1}$.

Mössbauer spectroscopy. ^{57}Fe Mössbauer experiments were performed in transmission geometry at room temperature using a conventional constant acceleration spectrometer. The data were collected using a ^{57}Co (50 mCi) gamma-ray source embedded in a Rh matrix. Velocity calibration and isomer shifts are given with respect to alpha-Fe foil at room temperature. The Mössbauer data was analyzed by Lorentzian line fitting using RECOIL software.[20]

Table 1. Crystal Data and structure refinement for $LiFePO_4OH$

Empirical formula	$LiFePO_4OH$	V	174.81(6) Å^3
Formula weight	174.77 g.mol^{-1}	Z	2
Crystal system	Triclinic	ρ_{calc}	3.320 g.cm^{-3}
Space group	$P\bar{1}$	F(000)	170
a	5.3506(10) Å	Temperature	293 K
b	7.2877(14) Å	GOF on F^2	1.265
c	5.1174(10) Å	R factors	R1 = 0.0393
α	109.237(2)˚	[I>2σ(I)]	wR2 = 0.1126
β	97.878(2)˚	R factors [all	R1 = 0.0437
γ	106.397(2)˚	data]	wR2 = 0.1145

Thermo-gravimetric analysis. Thermo-gravimetric analysis of the samples was done using a TA instrument Q50 TGA from room temperature up to 800 °C with a heating rate of 10 °C.min^{-1} in N_2 atmosphere.

IR spectroscopy. IR spectra were obtained using a Thermo Nicholet Nexus 470 FT-IR spectrometer on KBr pellets in the wavenumber range of 400 to 4000 cm^{-1}.

SEM. The morphology of the powders was studied by scanning electron microscopy (Hitachi S570) at 10 KV with a LaB_6 thermionic electron gun.

Fluorine analysis. For determination of fluorine content in the mixed hydroxo-fluoro iron tavorite, $LiFePO_4(OH)_{1-x}F_x$, a dried and accurately weighed sample was digested in acid and the fluoride ion concentration was subsequently measured with fluoride ion selective electrode calibrated against different concentrations of a standard (NaF) solutions; Accordingly x found to be 0.68.

Electrochemical testing. For electrochemical studies cathode mixture was prepared by mixing the active cathode material (tavorite) with Super P conductive

carbon and poly vinylidene fluoride (PVDF) as binder in 75:15:10 weight ratio. First, the mixture of active material and carbon was ball milled in a SPEX 8000D ball mill for 1 to 2 h. PVDF was then added to this fine mixture followed by an appropriate amount of N-Methyl-2-pyrrolidone (NMP) to dissolve the PVDF.

Table 2. Atomic coordinates and equivalent isotropic displacement parameters for $LiFePO_4OH$

Atoms	*x*	*Y*	*z*	*U*(eq) [Å^2]	SOF
Fe(1)	0	0.5	0	0.0064(3)	0.5
Fe(2)	0	0	0	0.0062(3)	0.5
P(1)	0.6373(3)	0.7688(2)	0.3245(3)	0.0055(3)	1
O(1)	0.6588(7)	0.8802(6)	0.1146(8)	0.0082(10)	1
O(2)	0.3397(7)	0.6626(6)	0.3103(8)	0.0086(10)	1
O(3)	0.9529(8)	0.2774(6)	0.1579(8)	0.0086(10)	1
O(4)	0.7869(8)	0.6160(6)	0.2682(8)	0.0088(10)	1
O(5)	0.2456(7)	0.0689(6)	0.3670(7)	0.0075(10)	1
Li(1)	0.613(2)	0.1826(19)	0.254 (2)	0.024(3)	1
H(1)	1.027(14)	0.326(10)	0.319(16)	0.007(16)	1

This slurry was then further ball milled for about 15 minutes to form a uniform mixture. The resulting paste was spread into a uniform film on aluminum current collector foil manually with the help of a glass rod. The prepared composite cathode sheet was kept in vacuum oven at 90 °C for 12 h. Circular disks of 3/8 inch diameter were then cut from the composite cathode film and moved to argon filled glove box (oxygen level below 3 ppm) for cell assembly. The loading of the active cathode materials in the disk was about 4 – 4.5 mg. CR2032 type coin cells were assembled with the prepared composite cathode disks as positive electrode and lithium foil (thickness 0.75 mm) as the anode. A Celgard® 2325 sheet was placed between cathode and anode to act as a separator and 1 M $LiPF_6$ dissolved in ethylene carbonate (EC) and dimethyl carbonate (DMC) solution in 1:1 ratio was used as an electrolyte. The whole assembly was pressed using a coin cell crimper to fabricate the cell and aged for 12 h before electrochemical charge-discharge experiments.

A PAR EG&G potentiostat/galvanostat model 283 was used for recording the CV over the range of 1.5 to 4.0 V *vs* Li/Li^+ with a scan rate of 0.02 $mV.s^{-1}$.

Table 3. Selected bond lengths for $LiFePO_4OH$

Bonds	Distances (Å)	Bonds	Distances (Å)
Fe1 – O2	1.996(4)	Fe2 - O5[e]	1.959(3)
Fe1 – O3[b]	2.009(4)	Fe2 – O3[g]	2.018(4)
Fe1 – O4[b]	2.027(4)	Fe2 – O1[h]	2.042(4)
Fe1 – O2[f]	1.996(4)	P1 – O1	1.543(4)
Fe1 – O3[h]	2.009(4)	P1 – O2	1.541(4)
Fe1 – O4[h]	2.027(4)	P1 – O4	1.523(5)
Fe2 – O5	1.959(3)	P1 – O5[i]	1.538(4)
Fe2 – O1[a]	2.042(4)	O3 – H1	0.78(8)
Fe2 – O3[b]	2.018(4)		

[a] -1 + x, -1 + y, z; [b] -1 + x, y, z; [e] –x, -y, -z; [f] –x, 1 - y, -z; [g] 1 - x, -y, -z; [h] 1 - x, 1 - y, -z; [i] 1 - x, 1 - y, 1 - z

Galvanostatic charge/discharge experiments were carried out on an Arbin Instruments battery tester model BT2043. Electrochemical impedance spectra were collected with an Ivum Stat Impedance Analyzer at 30 °C in a frequency range of 10 mHz to 100 KHz with AC signal amplitude of 5 mV and the resulting Nyquist plots were analyzed with ZView software.

Results and discussion

Synthesis, Structure and Morphology

The method of synthesis is very important for the application of the material as cathode in Li-ion battery. Different synthesis methods produce different morphologies, particle sizes, and crystallinities. The hydrothermal synthesis of $LiFePO_4(OH)$ reported by Marx et al.[10] and Ellis and Nazar[14] are very similar and yielded product with platelet morphology. On the other hand our hydrothermal synthesis reported here starting with completely different starting precursors yielded good quality single crystals. Similarly, synthesis of $LiFePO_4F$, which was so far achieved by three different methods namely ionothermal, high temperature solid-state, and solvothermal synthesis. The ionothermal synthesis of $LiFePO_4F$ reported by Tarascon group, involves expensive ionic liquids, has produced

nanometer sized particles. A high temperature (575 – 750 ° C) ceramic method, which is not energy efficient, has produced highly crystalline phase of $LiFePO_4F$ with micron sized particles often requiring extensive ball-milling to produce fine particles for electrochemical application. The solvothermal route reported by Nazar group also requires careful drying of the ethanol to produce OH free $LiFePO_4F$ phase of elongated particles. In this manuscript we are reporting for the first time a flux based solvent free method for the synthesis of $LiFePO_4F$ starting with H_3PO_3, iron nitrate, and mixed alkali metal nitrates at relatively low temperature (200 °C). It is to be noted here that in these reactions the phosphorous acid is acting as a precursor for phosphate moiety; aided by the strong oxidizing nature of the reaction mixture due to the presence of nitrate anions in solution (in the case of $LiFePO_4OH$) or in the molten salt mixture (in the case of $LiFePO_4F$). The following redox reaction (1) appears to occur as evident by the evolution of yellow-orange NO2 gas on opening the reaction vessel after completion of the reaction:

$$2NO_3^- + H_3PO_3 \rightarrow 2NO_2 + H_2O + HPO_4^{2-} \quad (1)$$

To compare the electrochemical activities of the two end members, pure hydroxo and pure fluoro, we have also synthesized a mixed anionic solid solution, $LiFePO_4(OH)_{0.32}F_{0.68}$. The hydrothermal synthesis reported is different from Ellis and Nazar14 and produces micrometer long bar-shaped crystallites. Genkina et al first reported the single-crystal structure of a synthetic tavorite of the composition $LiFePO_4(OH,F)$.[21] Yakubovich on the other hand reported a single-crystal study of a tavorite related phase with an additional Fe-sites and a mixed valency of Fe with the composition $LiFe^{3+}Fe^{2+}_x[PO_4][(OH)_{1-2x}O_{2x}]$.[22] In the former Li-site has been described as 6-coordinate, while the latter has two partially occupied 5 coordinate Li-sites. To our knowledge there is no report of single-crystal structure solution of pure $LiFePO_4(OH)$ from X-ray data. Recently, high quality X-ray and neutron powder data has been used to solve the structure of pure $LiFePO_4(OH)$ phase by Marx et al.[10] and our single-crystal structure determination fully corroborates with that report. Both Fe1 and Fe2 adopt octahedral geometry, where Fe – O distances are in the range 1.995(3) – 2.0274(4) Å and 1.958(2) – 2.042(3) Å, respectively,

for Fe1 and Fe2. The Li ion is surrounded by 5 oxygen atoms in an irregular polyhedron, with Li – O distances in the range 1.944(4) – 2.177(5) Å. Both Fe – O and Li – O distances are in very good agreement with Marx et al's neutron solution. Fe1 and Fe2 are located on the center of inversion at (0, 0.5, 0) and (0, 0, 0), respectively, and Fe1O6 and Fe2O6 octahedra are connected through the corner (O3) to form a one-dimensional corner-shared chain along the a-lattice vector. These chains of octahedra are then cross-linked by the phosphate tetrahedra to form the three-dimensional structure. Such connectivity also leads to channels in all the three crystallographic directions (Fig. 1). The Li-ions are located in channels along the c-axis; on the other hand hydrogen attached to the bridging oxygen (O3) protrudes in the channels along the a-axis. It is also interesting to note that anisotropic thermal parameters for Li (U11 = 21, U22 = 31, and U33 = 17 Å x 10^3) indicate more vibrations of Li along ab-plane compared to c-axis, an observation similar but less pronounced compared to the data from neutron refinement.[10]

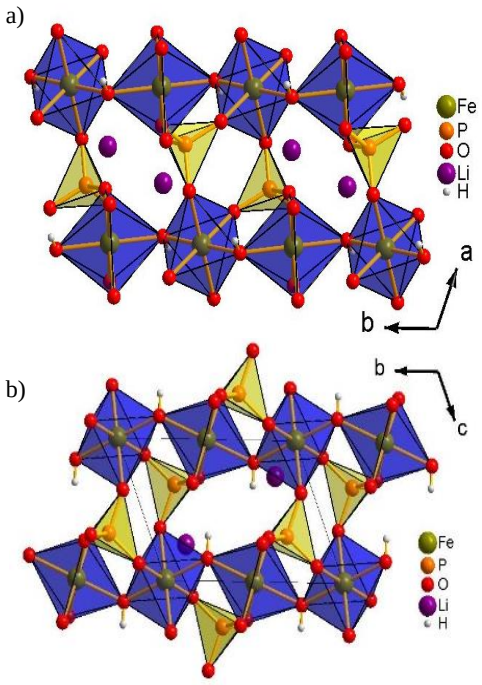

Fig. 1. Polyhedral representation of LiFePO4(OH) structure with Fe1 and Fe2 at the center of blue octahedra; a) view along the c- axis; b) view along the a- axis.

The powder XRD patterns of two as prepared tavorite phases are shown in Fig. 2. The experimental powder patterns for $LiFePO_4(OH)$ and $LiFePO_4(OH)_{0.32}F_{0.68}$ were compared with the simulated powder X-ray pattern from the single-crystal coordinates of $LiFePO_4(OH)$.

The excellent agreement between the simulated and the experimental patterns indicate phase purity of $LiFePO_4(OH)$, however, a small amount of LiF impurity phase can be seen in the as synthesized mixed anion phase, which goes away on repeated washing with chilled water.

For the full fluoro derivative, LiFePO4F, a Rietveld refinement has been performed using GSAS-II software on a high resolution PXRD data.[23]

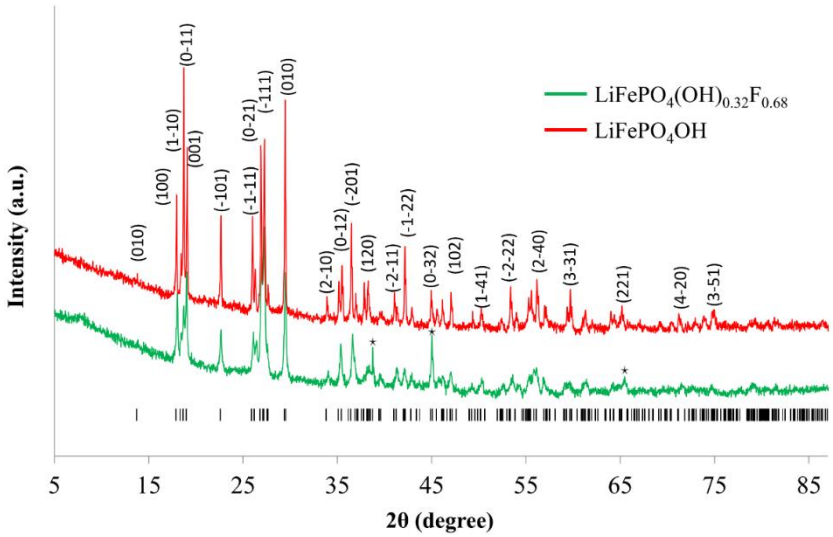

Fig. 2. Observed and calculated XRD patterns for the two prepared tavorite phases. LiF impurity phase is marked with star.

Unit cell parameters, space group ($P\bar{1}$), and atomic coordinates for the starting model were taken from Nazar group publication.[13] Unit cell parameters, fractional atomic coordinates, isotropic thermal displacement parameters, and site occupancy for lithium ion were subsequently refined. Accordingly, the occupancy of two disordered lithium sites was refined to a value of each having 50% occupancy, which is slightly different from that reported by Nazar group. The refinement was converged with Rw = 2.11% (Fig. 3) and the resulting cell parameters [a = 5.296(2) Å, b = 7.256(5) Å, c = 5.140(3) Å, α = 108.43(7)°, β =

98.05(6)°, γ = 107.16(1)°, V = 173.05(2) Å3] are in good agreement with that reported by Nazar group.[13]

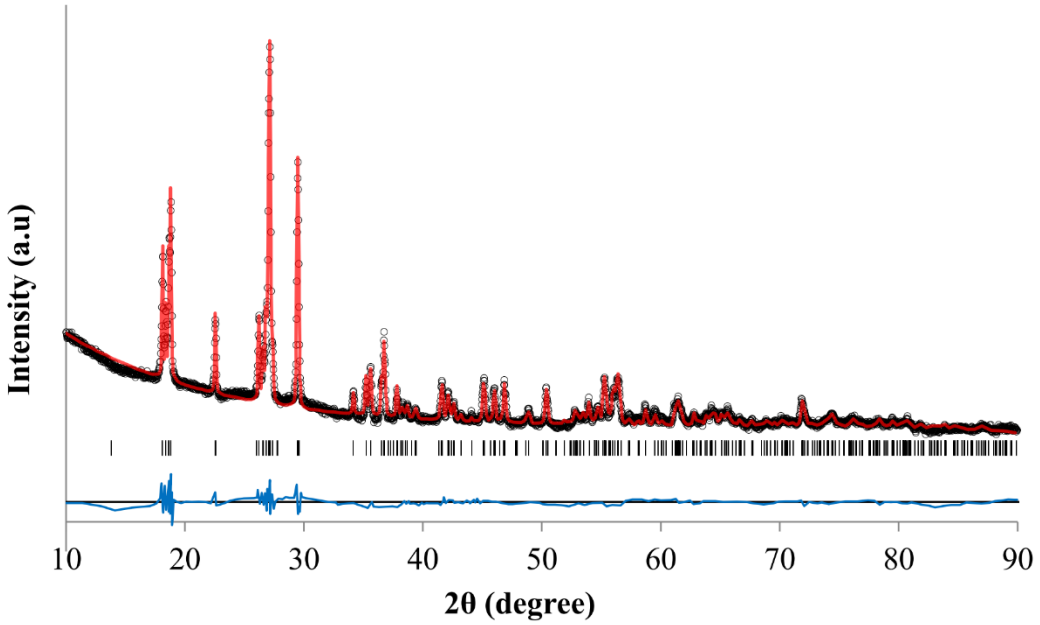

Fig. 3. Calculated (red line) and experimental (open circles) curves after Rietveld refinement on XRD pattern of $LiFePO_4F$.

Fig. 4 demonstrates the typical SEM micrographs of the samples. The SEM images reveal great differences in the morphology between the three samples. As synthesized $LiFePO_4(OH)$ particles are composed of polyhedral crystals of various sizes fused together to form secondary particles, several tens of micrometers in diameter. $LiFePO_4(OH)_{0.32}F_{0.68}$ on the other hand includes strip like crystals with submicron width and thickness and the synthesis procedure for $LiFePO_4F$ yields small plate-like crystals which are several hundred nanometers in thickness.

Spectroscopic and thermo-gravimetric analysis

Fig. 5 shows the FTIR spectra of the three samples with vibrational modes for phosphate in the range of 940-1160 cm^{-1}. The -OH bending and stretching modes are clearly observed at 795 and 3270 cm^{-1}, respectively, for the $LiFePO_4OH$ phase. As expected the intensity of the -OH vibrational modes decreased in $LiFePO_4(OH)_{0.32}F_{0.68}$ compared to $LiFePO_4(OH)$ and disappear completely in $LiFePO_4F$.

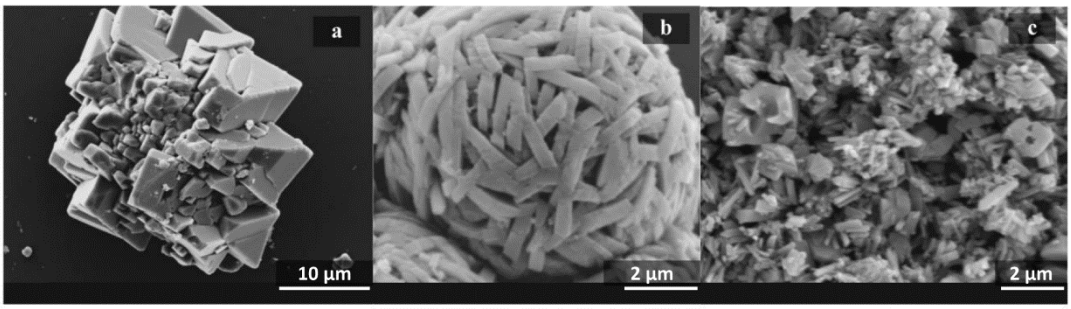

Fig. 4. SEM images of $LiFePO_4OH$ (a); $LiFePO_4(OH)_{0.32}F_{0.68}$ (b) and $LiFePO_4F$ (c).

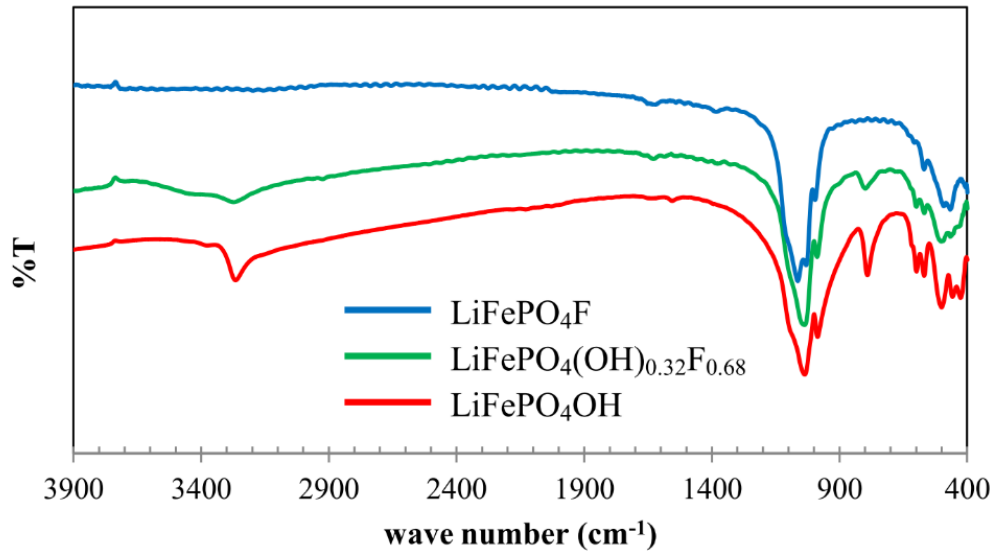

Fig. 5. FTIR spectra of the three phases of $LiFePO_4(OH)_xF_{1-x}$ where $0 \leq x \leq 1$.

Fig. 6 exhibits the Mössbauer spectra for the three different samples, along with the fit parameters in Table 4.

The Mössbauer spectra provide valuable information about the chemical nature of Fe in the compound. Two important parameters in Mössbauer spectrum, isomer shift (IS) and quadruple splitting (QS), are directly related to the total electron density at the Fe center which in turn gives sensitive information about valence and spin state of Fe.

For each compound, the Mössbauer spectrum has been fitted with two doublets corresponding to Fe1 and Fe2. The ratio of the two doublets (1:1)

determined from the fitting is in agreement with ratio derived from crystal structure of $LiFePO_4(OH)$. The values of the isomer shift and quadruple splitting are signature of Fe in +3 oxidation state and octahedral coordination. The fitted values of IS and QS corroborates well with that reported by Delmas and Nazar groups.[13, 10]

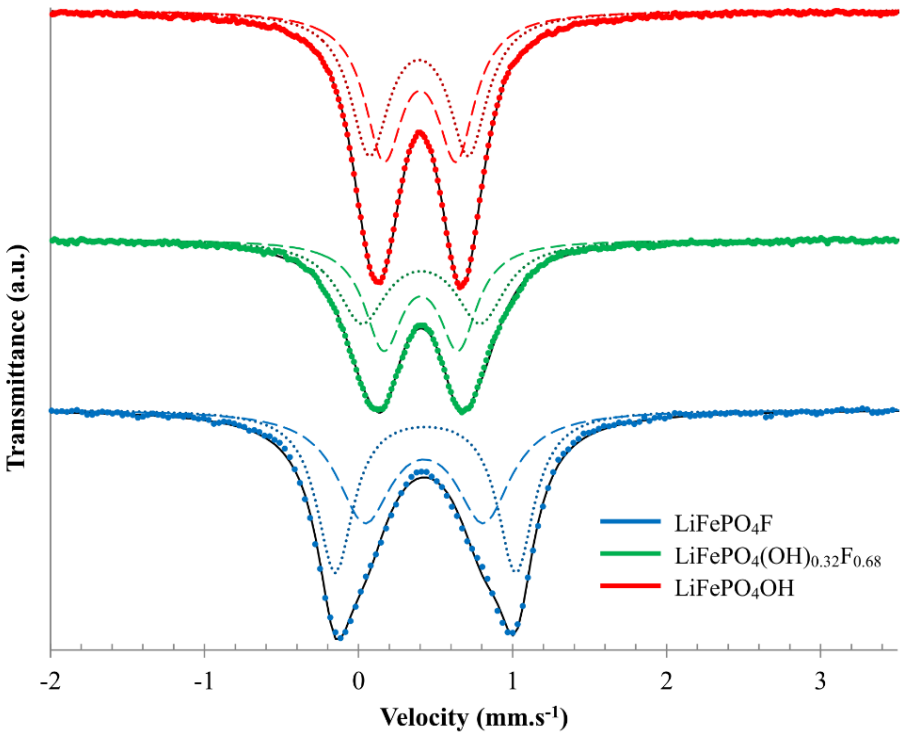

Fig. 6. Mössbauer spectra of three prepared iron tavorite phases; experimental data: dots; doublets 1 and 2: dashed and dotted line; solid line: fitted curve.

More importantly it can be seen that the isomer shift as well as quadrupole splitting between the doublets increases as the F-/OH- ratio increase. This can be explained based on the reduction of the covalency of the Fe – X (X = O, F) bond with increase of fluoride anion[24,25] and that is reflected in the higher cathode potential in the case of $LiFePO_4F$ (vide infra).

Mössbauer spectra was also indicative of the fact that there was no other iron-containing impurities in any of the compounds as evident in the spectra collected over the entire velocity range spanning from -10 to +10 mm.s-1 (data not shown).

Mössbauer spectrum for $LiFePO_4(OH)_{0.32}F_{0.68}$ also supports the substitutional solid solution of F and OH in the same crystallographic site and is statistically distributed throughout the structure.

Table 4. Values of fit parameters for Isomer Shift (δ), Quadrupole Splitting (ΔE) and site percentage for $LiFePO_4OH$, $LiFePO_4(OH)_{0.32}F_{0.68}$ and $LiFePO_4F$

		Doublet 1	Doublet 2
$LiFePO_4OH$	δ ($mm.s^{-1}$)	0.398(9)	0.392(6)
	ΔE ($mm.s^{-1}$)	0.469(2)	0.641(1)
	%Fe	50.016(4)	49.983(6)
$LiFePO_4(OH)_{0.32}F_{0.68}$	δ ($mm.s^{-1}$)	0.404(4)	0.406(4)
	ΔE ($mm.s^{-1}$)	0.483(3)	0.769(4)
	%Fe	50.000(4)	49.999(6)
$LiFePO_4F$	δ ($mm.s^{-1}$)	0.425(8)	0.434(6)
	ΔE ($mm.s^{-1}$)	0.772(4)	1.173(1)
	%Fe	49.947(8)	50.052(2)

If $LiFePO_4(OH)_{0.32}F_{0.68}$ was a heterogeneous mixture of 32% pure hydroxo and 68% of pure fluoro derivative or if there were fluoro or hydroxo rich regions in the structure then signature of both end member would have been found in the Mössbauer spectra.

TGA was conducted to assess the thermal stability of each compound and the results are presented in Fig. 7.

$LiFePO_4OH$ decomposes at 450 °C to $Li_3Fe_2(PO_4)_3$, Fe_2O_3, and H2O in agreement with previous results,[13] $LiFePO_4F$ is stable up to 550 °C, about 50 °C lower than that reported by Nazar et al.[14] This lower thermal stability can be assigned to smaller particle sizes of our sample. It is expected that $LiFePO_4F$ ($2FeF_3 + 3H_2O = Fe_2O_3 + 6HF$). $LiFePO_4(OH)_{0.32}F_{0.68}$ shows a trend in between that of the other two end members of the group with two major mass loss steps. The first mass loss occurs at 450 °C, which we speculate, is due to the loss of HF according to the following equation, $3LiFe(OH)_{0.32}F_{0.68}PO_4 = Li_3Fe_2(PO_4)_3 + 1/3FeF_3 + 1/3Fe_2O_3 + HF$. Above 530 °C the sluggish weight loss may be due to

the decomposition of FeF_3 due to the presence of impurity moisture similar to $LiFePO_4F$.

Electrochemistry

Cyclic voltammetry. Fig. 8 shows the first cycle of cyclic voltammograms of composite electrodes made from these tavorite phases. The open circuit voltage (OCV) values for $LiFePO_4(OH)$, $LiFePO_4(OH)_{0.32}F_{0.68}$, and $LiFePO_4F$ are 3.05, 3.15, and 3.06 V, respectively. The cathodic (Li-insertion) and anodic (Li-extraction) peaks are observed at 2.29 and 2.59 V for LiFePO4(OH), 2.43 and 2.94 V for $LiFePO_4(OH)_{0.32}F_{0.68}$, and 2.65 and 3.19 V for $LiFePO_4F$.

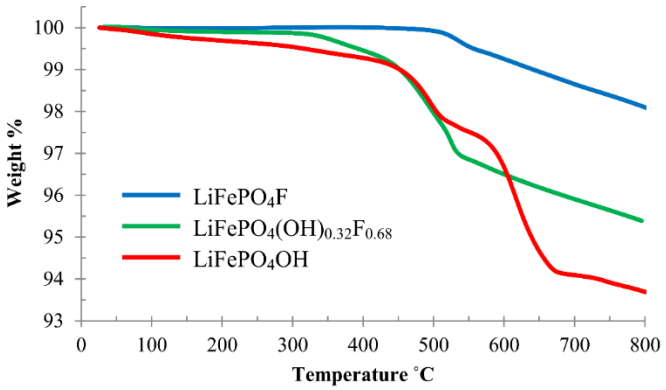

Fig. 7. TGA plots of three iron tavorite phases.

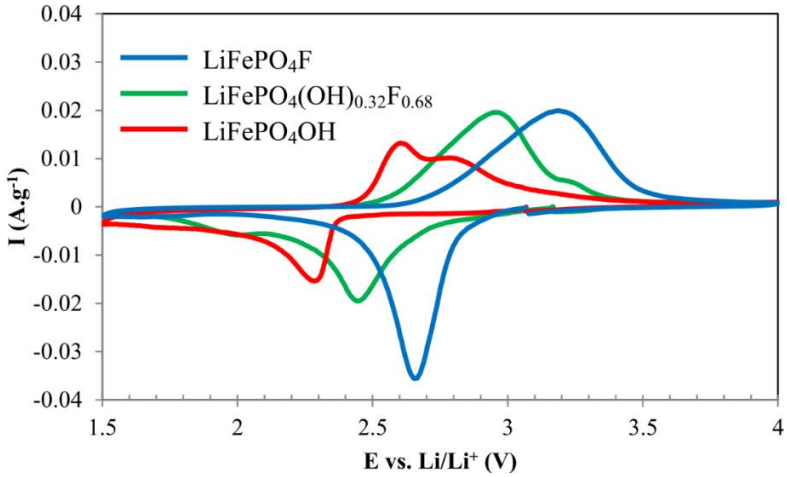

Fig. 8. First cylce of cyclic Voltammograms for the three tavorite phases at 0.02 $mV.s^{-1}$. Cathodic current is negative.

Besides the main anodic and cathodic peaks, $LiFePO_4(OH)$ shows an additional broad anodic peak centered at 2.78 V, which may indicate phase transformation during oxidation. On the other hand $LiFePO_4(OH)_{0.32}F_{0.68}$ shows low intensity shoulders in both anodic and cathodic peaks at higher and lower voltages than the main peaks, respectively. Upon successive cycling the shoulder peaks as well as the main anodic and the cathodic peaks shift to higher and lower potentials, respectively, indicating increased electrode polarization due to cycling (supplementary information). The increasing trend of discharge potential with increasing fluoride content in conjunction with the results from Mössbauer spectra suggests that incorporation of fluoride anion leads to the increased cell potential in the full fluoro tavorite version. Also notably, the area under cathodic curve is considerably larger for $LiFePO_4F$ compared to $LiFePO_4(OH)$, suggesting higher overall discharge kinetic capabilities of the former.

Galvanostatic charge/discharge. Based on the results from CVs, cutoff potentials were set at 4.0 and 1.5 V for running galvanostatic charge/discharge experiments. The voltage profile for $LiFePO_4OH$, $LiFePO_4(OH)_{0.32}F_{0.68}$, and $LiFePO_4F$ are given in Fig. 9.

As can be observed, $LiFePO_4OH$ delivers a specific capacity 102 $mAh.g^{-1}$ during the first discharge at C/50, which is 67% of the theoretical capacity (153 $mAh.g^{-1}$) followed by an irreversible capacity loss of about 6 $mAh.g^{-1}$ (6 %) on the second cycle but stabilizes to almost constant capacity on subsequent cycles.

It is to be noted here that during the 1st discharge the voltage drop was gradual from 3 volt (OCV) to 2.37 volt and then discharge curve shows a plateau at 2.32 volt till 0.45 Li insertion (69 $mAh.g^{-1}$). However, on the subsequent cycles the discharge plateau is observed at 2.5 V.

This gain of 0.13 V in the discharge voltage has also been observed by Nazar group[13] and has been attributed to the fact that reductive Li-insertion into $LiFePO_4OH$ leads to an amorphous phase of Li_2FePO_4OH, which remains amorphous upon oxidation. Therefore, subsequent discharge/charge cycles take place from an amorphous phase and results in an increase of discharge voltage. For

assessing the cell capacity retention, it has been subjected to multiple charge/discharge cycles at higher C-rates.

The results given in inset of Fig. 9(a) demonstrate that essentially there is a loss of capacity at higher C-rate due to electrode polarization. However, upon slowing down the C-rate, the initial capacity can be fully recovered at 96 $mAh.g^{-1}$ at C/50.

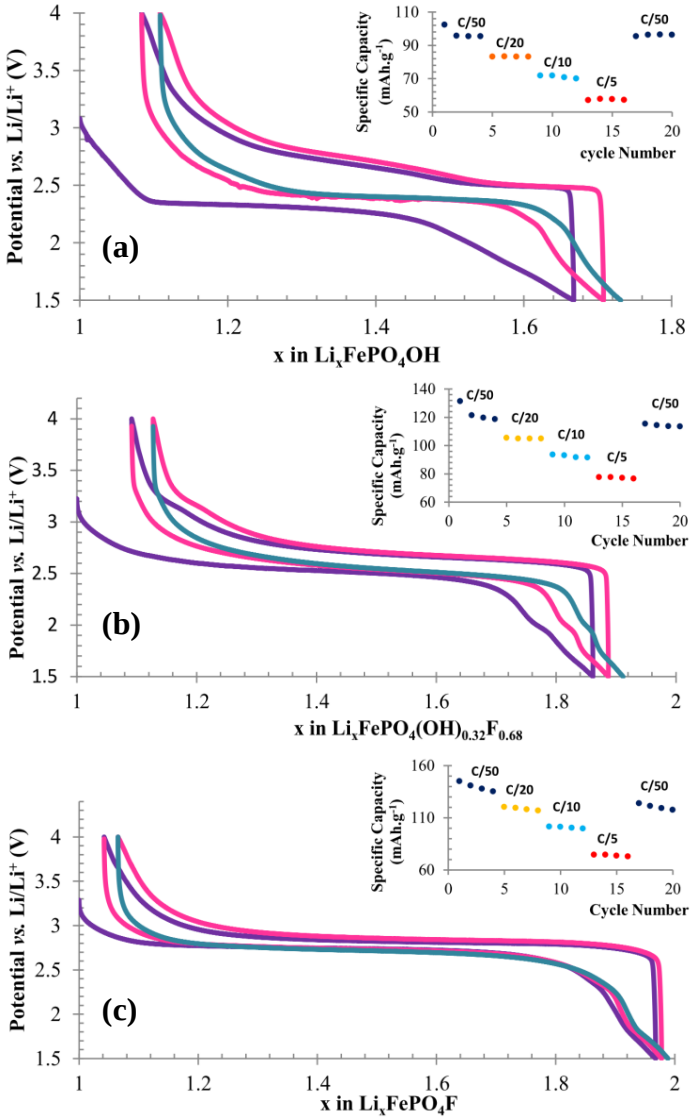

Fig. 9. Voltage-composition profiles for the first 3 discharge curves of: $LiFePO_4OH$ a); $LiFePO_4(OH)_{0.32}F_{0.68}$ (b) and $LiFePO_4F$ (c) at C/50. First discharge and charge: —; second discharge and charge: —; Third discharge: —. Inset in each Figure shows the achievable specific discharge capacity at different C-rates on consecutive cycles.

This suggests that the capacity loss due to fast C-rate was limited by the kinetics of Li-diffusion and electron transfer through the poorly conducting tavorite material and not due to any cathode degradation. On the other hand, for $LiFePO_4(OH)_{0.32}F_{0.68}$ and $LiFePO_4F$ the discharge/charge behavior is different. These two phases demonstrate good specific capacity achievement for the first cycle at 131 (74% of theoretical capacity) and 146 $mAh.g^{-1}$ (97% of theoretical capacity), respectively, at C/50 followed by an irreversible capacity fading of 10 $mAh.g^{-1}$ for $LiFePO_4(OH)_{0.32}F_{0.68}$ and 4 $mAh.g^{-1}$ for $LiFePO_4F$ in the second cycle. The difference in achievable specific capacity for the three phases may be due to the different particle sizes as can be seen from SEM images. During the first discharge for $LiFePO_4F$ the voltage gradually drops from 3.2 (OCV) to 2.90 volts which accounts for 0.1 Li insertion and then the discharge curve shows a flat plateau at 2.65 volt up to 0.7 Li insertion. After this point the voltage gradually drops to the lower cutoff point (1.5 volt). However, earlier report from Nazar group on $LiFePO_4F$ prepared by ceramic method has shown solid solution type sloping discharge curve up to 0.4 Li insertion.[12] Although a good initial specific capacity was observed for $LiFePO_4F$, it undergoes some irreversible capacity losses as a result of cycling at different fast C-rates (inset of Fig. 9(c)). At 20th cycle the capacity reduces to a value of 118 $mAh.g^{-1}$ when discharge is repeated again at the initial rate of C/50. On the contrary, $LiFePO_4(OH)_{0.32}F_{0.68}$ exhibit a gradual sloping profile in the entire discharge/charge curve, which may indicate solid-solution type behavior during the discharge and charging. Again this discharge slope is not as steep as it was reported for $LiFePO_4(OH)_{0.4}F_{0.6}$,[14] which may be due to higher fluoride content in the current one. Capacity fading has been observed when cycled at different fast C-rates, however, the overall irreversible capacity loss after 20 cycles of charge/discharges at various C-rates is less than 8 $mAh.g^{-1}$ when the discharge is repeated again at the initial rate of C/50 (inset Fig. 9(b)). More importantly the capacity appears to decrease upon cycling only slightly in the case of $LiFePO_4(OH)_{0.32}F_{0.68}$.

The derivative voltage-composition curves for the three phases are shown in Fig. 10. $LiFePO_4OH$ shows two distinct phenomena close to 2.4 V during the

discharge and sharp peak at 2.5 V due to the plateau arising from two phase behavior and broad peak centered around 2.6 V due to sloping charging curve. On the other hand LiFePO4F demonstrate rather sharp peaks in the derivative plot, indicative of two-phase lithium insertion reactions.

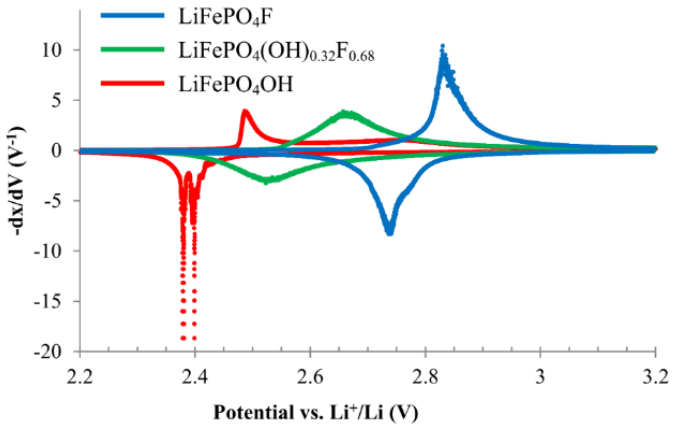

Fig. 10. Derivatives of voltage-composition curves for the three tavorite phases.

For $LiFePO_4(OH)_{0.32}F_{0.68}$, the case is made complicated by the fact that insertion and extraction curves are broadened considerably and there is potential overlap of reduction and oxidation peaks indicating a solid-solution type behavior during Li-insertion and extraction.

The effect of polarization (η) for the three phases as a function of C-rate is presented in Fig. 11.

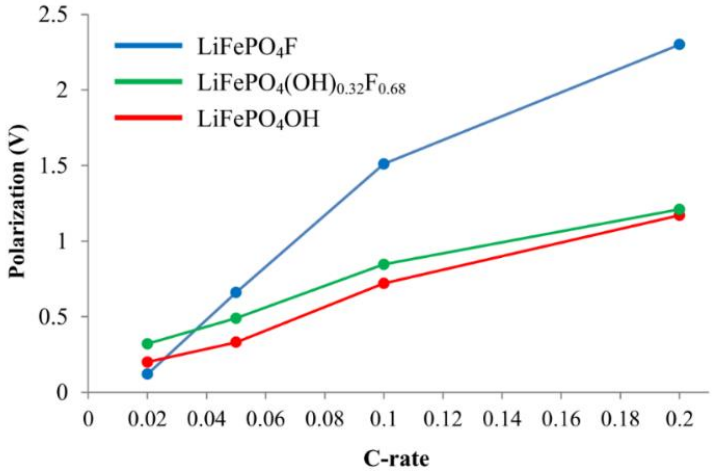

Fig. 11. Polarization as a function of C-rate for the three phases.

Polarization was measured from voltage-composition curves as the separation between charge and discharge plateaus at their flattest point. $LiFePO_4F$ shows the least polarization in C/50 rate, however, as the C-rate increases polarization increases abruptly suggesting the slow kinetics of lithium ion transfer in this phase. However, $LiFePO_4(OH)_{0.32}F_{0.68}$ exhibit least polarization followed by $LiFePO_4OH$ and both exhibit similar sluggish increase in polarization with increasing C-rates. The relationship between polarization (defined as E-E_{OCV}) and current density (J) treated according to porous electrode theory can be approximated as:[26]

$$J \propto Fk\left[x\exp\left(\frac{\alpha_A F}{RT}(E-E_{OCV})\right)-(1-x)exp\left(-\frac{\alpha_C F}{RT}(E-E_{OCV})\right)\right] \quad (2)$$

Where F is the Faraday constant, k is the adjusted electrochemical reaction rate constant, αA and αC are the respective transfer coefficients for cathodic and anodic reactions on the working electrode, and x is the fraction of lithiation. Furthermore, according to the Fick's first law of diffusion:

$$J = -zFD(\nabla c) \quad (3)$$

Where z is the number of charges per charge carrier (z =1 for lithium ion) and ∇c is the concentration gradient across the cathode solid particle. Inspection of (2) and (3) suggests that η should have an inverse logarithmic relationship with diffusivity and concentration gradient of the lithium ion in the cathode, and should not depend on particle size, as can be seen in the work of Kang et al.27 Therefore, the higher polarization of $LiFePO_4F$ compared to $LiFePO_4(OH)$ or $LiFePO_4(OH)_{0.32}F_{0.68}$ at higher C-rate can be attributed to the difference in lithium ion diffusion coefficients although the particle sizes are larger for $LiFePO_4OH$ and smaller for $LiFePO_4F$.

Electroimpedance spectroscopy: Electroimpedance spectroscopy (EIS) was used for further studying the lithium ion mobility in the three cathode materials and the results of experimental data and fitted curves using a general lithium-ion battery equivalent circuit model are shown in Fig. 12.[28]
In the case of $LiFePO_4OH$ and $LiFePO_4(OH)_{0.32}F_{0.68}$ two parallel R|CPE elements are required to describe the medium to high frequency region which are usually

assigned to solid-electrolyte interface (SEI) film and charge-transfer resistances while for $LiFePO_4F$ the above two processes have very close time constant so that they are merged together and only one parallel R|CPE is sufficient for modelling.

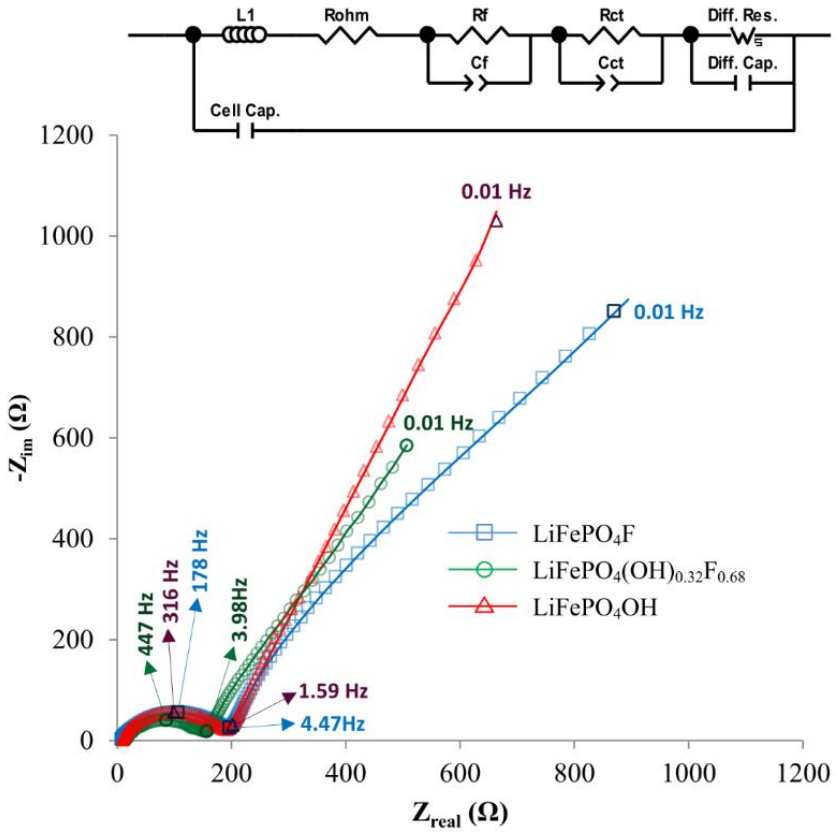

Fig. 12. Nyquist plot for $LiFePO_4OH$, $LiFePO_4(OH)_{0.32}F_{0.68}$ and $LiFePO_4F$ cells with solid lines representing the fitted curve; inset: equivalent circuit model used for fitting.

Note that the low frequency tail of the impedance spectra in all cases is characteristic of the ionic nature of conductivity. Interestingly, of the three derivatives $LiFePO_4(OH)_{0.32}F_{0.68}$ phase exhibits the highest lithium ion mobility and smallest combined charge transfer and film resistance, consistent with polarization studies mentioned above. However, low frequency part of the spectra for $LiFePO_4F$ and $LiFePO_4OH$ has comparable absolute impedance magnitudes. The reason for comparable absolute impedances for $LiFePO_4OH$ and $LiFePO_4F$ at lowest frequencies is that although $LiFePO_4OH$ exhibits a higher lithium ion

diffusion coefficient, it has a higher average particle size as well and the corresponding relaxation time (τ) defined as:

$$\tau = \frac{L^2}{D} \quad (4)$$

(where L is the diffusion length and D is the diffusion coefficient), becomes comparable to that of $LiFePO_4F$.

The values of fit parameters for the two systems are given in Table 5. The combined value for Rct+Rf and their related capacitance obtained for $LiFePO_4F$ are consistent with those reported by Prabu et. al.[15]

Conclusions

Novel synthesis routes presented in this work could be used to expand the inventory of available methods for production of the iron tavorite family of materials. The crystal structure found from single crystal X-ray diffraction confirmed the accepted models which were previously based mainly on powder diffraction techniques. Moreover, the low temperature, solvent free phosphorous acid based synthesis route proposes an economical and scalable way for mass production of $LiFePO_4F$ as a cheap cathode material for lithium ion batteries.

Table 5. Impedance Equivalent circuit Fit parameters for LiFePO4OH, LiFePO4(OH)0.32F0.68 and LiFePO4F cells

							Warburg Short*				
	L_1 (μH)	R_{ohm} (Ω)	R_f (Ω)	R_{ct} (Ω)	C_f (μF)	C_{ct} (μF)	R_w (Ω)	τ (s)	P	Diff. Cap. (mF)	Cell Cap. (nF)
$LiFePO_4OH$	4.5	9.7	83.9	98.2	12.5	89.5	7719	215	0.72	0.20	27.2
$LiFePO_4(OH)_{0.32}F_{0.68}$	3.6	9.1	53.2	99.9	2.93	20.9	2565	134	0.54	3.11	19.9
$LiFePO_4F$	2.6	5.8	199.6		56.8		4404	211	0.46	2.93	31.6

$* \ Z_{ws} = \frac{R_W \times tanh(j\omega\tau)^P}{(j\omega\tau)^P}$ where $\tau = L^2/D$ and L and D are effective diffusion length and diffusion coefficients, respectively.

The results of electrochemical tests indicate the importance of the anion on cell performance; coordination of F^- anion increases the cell potential relative to

OH^- anion by inductive effects. Both full fluoro and full hydroxo tavorite show a two phase behavior while the mixed anionic $LiFePO_4(OH)_{0.32}F_{0.68}$ shows a solid solution like behavior during the Li-insertion and extraction. On the other hand, in terms of charge and discharge dynamics the mixed anion phase exhibited the highest lithium ion mobility.

Acknowledgements

The authors acknowledge the funding from Materials Research Centre (Missouri S&T) and University of Missouri Research Board. The authors are also grateful to Professors Nick Leventis and Pericles Stavropoulos for the donation of a potentiostat and a glovebox, respectively.

Notes and references

Electronic Supplementary Information (ESI) available: Details of crystal structure in the CIF format and extended CVs for each phase are available. See DOI: 10.1039/b000000x/

1 A. K. Padhi, K. S. Nanjundaswamy, J. B. Goodenough, *J. Electrochem. Soc.*, 1997, **144**, 1188 - 1194.

2 C. Masquelier, L. Croguennec, *Chem. Rev.,* 2013, **113**, 6552 - 6591.

3 A. K. Padhi, V. Manivannan, J. B.Goodenough, *J. Electrochem. Soc.* 1998, **145**, 1518 – 1520.

4 B. Dunn, H. Kamath, J. –M. Tarascon, *Science*, 2011, **334**, 928-935.

5 R. Amin, J. Maier, P. Balaya, D. P. Chen, C. T. Lin, *Solid State Ionics*, 2008, **179**, 1683 – 1687.

6 H. Huang, S. -C. Yin, L. F. Nazar, *Electrochem. Solid-State Lett.* 2001, **4**, A170 – A172.

7 C. Delacourt, P. Poizot, S. Levasseur, C. Masquelier, *Electrochem. Solid-State Lett.*, 2006, **9**, A352 – A355.

8 J. Barker, M. Y. Saidi, J. L. Swoyer, *J. Electrochem. Soc.*, 2003, **150**, A1394 – A1398.

9 N. Recham, J. -N. Chotard, L. Dupont, C. Delacourt, W. Walker, M. Armand, J. -M. Tarascon, *Nat. Mater.*, 2010, **9**, 98-74

10 N. Marx, L. Croguennec, D. Carlier, A. Wattiaux, F. Le Cras, E. Suard, C. Delmas, *Dalton Trans.*, 2010, **39**, 5108-5116.

11 N. Recham, J. –N. Chotard, J. –C. Jumas, L. Laffont, M. Armand, J. –M. Tarascon, *Chem. Mater.*, 2010, **22**, 1142-1148.

12 T. N. Ramesh, K. T. Lee, B. L. Ellis, L. F. Nazar, *Electrochem. Solid-State Lett.*, 2010, **13**, A43-A47.

13 B. L. Ellis, T. N. Ramesh, W. N. Rowan-Weetaluktuk, D. H. Ryan, L. F. Nazar, *J. Mater. Chem.*, 2012, **22**, 4759-4766.

14 B. L. Ellis, L. F. Nazar, *Chem. Mater.*, 2012, **24**, 966-968.

15 M. Prabu, M. V. Reddy, S. Selvasekarapandian, G. V. Subba Rao, B. V. R. Chowdari, *Electrochim. Acta*, 2012, **85**, 572-578.

16 Z. Yang, J. Zhang, M. C. W. Kintner-Meyer, X. Lu, D. Choi, J. P. Lemmon, J. Liu, *Chem. Rev.*, **2011**, 111, 3577 – 3613.

17 Bruker- SMART. Bruker AXS Inc., Madison, Wisconsin, USA. 2002.

18 Bruker- SAINT and SADABS. Bruker AXS Inc., Madison, Wisconsin, USA, 2008.

19 G. M. Sheldrick. *Acta Cryst.*, 2008, **A64**, 112–122.

20 K. Lagarec and D. G. Rancourt, *Nucl. Instrum. Meth. Phys. Res. B 1997, **129**, 266-280.*.

21 E. A. Genkina, Y. K. Kabalov, B.A. Maksimov and O.K. Mel'Nikov, *Kristallografiya*, 1984, **29**, 50-55.

22 O.V. Yakubovich and V. S. Urusov, *Geochem. Int.*, 1997, **35**(7), 630-638.

23 B. H. Toby and R. B. Von Dreele, *J. Appl. Cryst.*, 2013, **46**, 544-549.

24 F. Menil, *J. Phys. Chem. Solids*, 1985, **46**, 763 – 789.

25 F. Neese, *Inorg Chim Acta*, 2002, **337**, 181 – 192.

26 M. Doyle, T. F. Fuller and J. Newman, *J. Electrochem. Soc.*, 1993, **140**, 1526 – 1533.

27 J. Dou, X. Kang, T. Wumaier, N. Hua, Y. Han, G. Xu, *J. Solid State Electrochem.*, 2012, **16**,1925 – 1931.

28 D. Andre, M. Meiler, K. Steiner, H. Walz, T. Soczka-Guth, D.U. Sauer, *J. Power Sources*, 2011, **196**, 5349 – 5356.

II. $Li_3Fe_2(HPO_3)_3Cl$: an electroactive iron phosphite as a new polyanionic cathode material for Li-ion battery

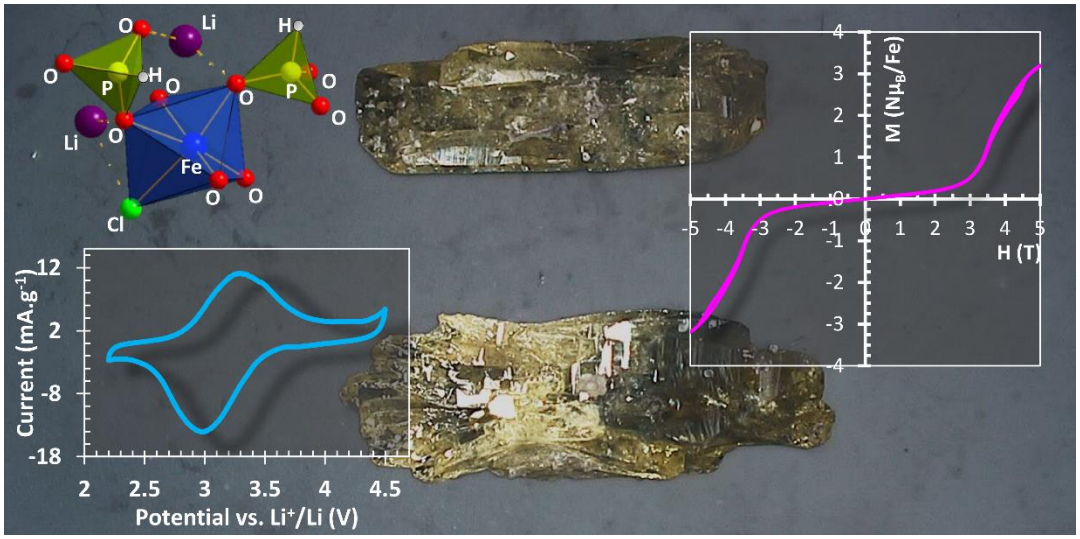

Hooman Yaghoobnejad Asl,[a] Kartik Ghosh,[b] Melissa P. Vidal Meza[c] and Amitava Choudhury[a,*]

[a,*] Department of Chemistry, Missouri University of Science and Technology, Rolla, MO 65409, USA.

[b] Department of Physics, Astronomy and Materials Science and Center for Applied Science and Engineering, Missouri State University, Springfield, MO 65897, USA

[c] Department of Chemical and Biological Engineering, Missouri University of Science and Technology, Rolla, MO 65409, USA

Corresponding author: Fax: (573)341-6033; Tel:(573)341-6332.

* E-mail: choudhurya@mst.edu

Abstract

A novel lithium containing iron-chlorophosphite, $Li_3Fe_2(HPO_3)_3Cl$ has been synthesized by employing low melting phosphorous acid flux. The single-crystal X-ray structure determination established that the compound has a 3-dimensional structure built up by edge-shared octahedral dimer and phosphite moiety that create narrow channels along *a*- and *b*-axis. Two crystallographically independent Li-ions are located in those channels. The compound was further characterized by TGA, IR, magnetic measurements, and Mössbauer spectroscopy. Magnetic

measurements indicate that the compound has a field-induced metamagnetic transition. In this article we report for the first time an iron chlorophosphite, $Li_3Fe_2(HPO_3)_3Cl$, as the new polyanion-based cathode with a promising electrochemical activity that shows an average voltage of 3.1 V vs Li^+/Li for the Fe^{2+}/Fe^{3+} redox couple and a reversible capacity of 70 $mAhg^{-1}$. Details of electrochemical studies including cyclic voltammetry, galvanostatic charge-discharge, and electro-impedance spectroscopy are reported here.

Introduction

In recent years the Li-ion battery technology has seen a dramatic increase in its demand as the idea of implementation of Li-ion battery in hybrid electric vehicles (HEVs), electric vehicles (EVs) and smart grid is getting more and more attention.[1, 2] Sustainable energy needs demand more efficient battery technology in terms of manufacturing costs, materials safety, environmental friendliness, cycle life, good rate capability, and capacity.[3, 4] Cathode or positive electrode material plays a prominent role for achieving these goals. As a result there has been an ongoing effort to synthesize and identify new cathode materials.[5] In this context polyanion-based materials, for examples, phosphates, sulfates, silicates, and borates of iron have taken a center stage in recent years challenging the purely oxide based materials.[6] This burst of research activity in polyanion-based cathodes is due to one pioneering discovery by the Goodenough group that olivine $LiFePO_4$ is electrochemically active with a reasonably high operating voltage (3.5 V vs $Li^+/Li0$) and with a reasonably good theoretical specific capacity of 170 $mAh.g^{-1}$.[7] It was soon realized that there is a huge potential of the polyanionic cathode specially for the solid state chemist who can use innovative synthesis techniques and take advantage of the ability of polyanions to form different 3-dimensional (3-D) and two-dimensional (2-D) networks amenable for lithium ion insertion.[8] More importantly, the ability to tune the redox potential of the host cathode based on the iono-covalency of the metal-ligand bond through the influence of inductive effect of the central atom of the polyanion moiety has become an essential tool for design strategy of cathode materials.[9] Thus a variety of polyanion-based compounds

including those previously known as well as newly discovered structures and compositions have been tested for Li-ion battery. These include borate ($LiFeBO_3$),[10] silicate (Li_2FeSiO_4),[11] carbono-phosphates, ($AMPO_4CO_3$, A = Li, Na; M = Fe, Mn),[12, 13] iron sulfates[14] besides a large number of phosphates. Further tuning of the cell voltage has been achieved by introduction of fluoride into the structure, especially in iron- fluoride sulfate (Tavorite and Triplite phases)[15, 16] and iron fluoride phosphate (Tavorite).[17, 18] Some of the recently discovered iron sulfate cathodes are becoming strong contender to become an alternate to the most noteworthy polyanion cathode, olivine $LiFePO_4$.[16]

Among the various polyanions, phosphite with three P – O bonds, one P – H bond and P in +3 oxidation state is known to form 2-D, 3-D or open framework structures with transition metals.[19] These structures are quite stable and their redox chemistry as an insertion host for Li-ion battery has not been exploited thus far. Only recently Rojo's group has shown small amount electrochemical activity in an open framework iron phosphite, $Li_{1.43}[Fe^{II}_{4.43}\ Fe^{III}_{0.57}(HPO_3)_6]\cdot 1.5H_2O$, in the potential range of 2.0 – 4.0 V vs Li+/Li with a specific capacity of 12 $mAh.g^{-1}$.[20]

In this article we describe the synthesis, structure determination, and magnetic properties of a new polyanion compound, $Li_3Fe_2(HPO_3)_3Cl$, based on phosphite moiety and demonstrate its application as a cathode material for Li-ion batteries. The electrochemical activity has been investigated by a variety of techniques and the results reported here exhibit an effective reversible capacity equivalent to 70 $mAh.g^{-1}$ (about 53% of the theoretical capacity) between 2.2 – 4.5 V vs Li^+/Li and good high-current performance of this phase.

Experimental

Materials

$FeCl_2\cdot 4H_2O$ (reagent grade, purity 98%) was purchased from Fisher Scientific, $LiOH\cdot H_2O$ (reagent grade, purity 98%) and H_3PO_3 (Extra pure, 98%) from Across Organics and Li foil (purity 99.9%) from Sigma-Aldrich. All the chemicals were used as-purchased and without further purification.

Synthesis

$Li_3Fe_2(HPO_3)_3Cl$ has been synthesized by mixing 2.9823 g of $FeCl_2 \cdot 4H_2O$ (15 mmol), 1.2591 g $LiOH \cdot H_2O$ (30 mmol) and 1.2300 g H_3PO_3 (15 mmol) in a 23 mL Teflon-lined stainless steel Paar acid digestion bomb. The reactants were first mixed in a Teflon beaker, which form a highly viscous flux upon mixing due to the water released in the course of acid-base reaction. The Teflon beaker with a lid was then placed in the steel autoclave, sealed tightly, and placed in an oven in the temperature range of 175 to 200 °C for 6 days, followed by cooling down naturally to room temperature. The product of the reaction composed of millimeter size crystals of green-jade color mixed with some impurity powder and/or minor needle like crystals, depending on the synthesis temperature. Variation of synthesis temperature and mole ratios did not yield a pure phase of the product in our hands. However, due to the ample crystal size difference between the main product and those of impurity phase(s) we were able to easily separate the product by first washing the reaction product with hot water to remove the unreacted reagents and subsequently sonication/decantation in deionized water. After purification the crystals were filtered, washed several times with water and ethanol and dried in air.

Material Characterization

Single-crystal X-ray diffraction. Crystal structure of $Li_3Fe_2(HPO_3)_3Cl$ was solved from single-crystal intensity data sets collected on a Bruker Smart Apex diffractometer with monochromated Mo Kα radiation (λ = 0.7107 Å). Suitable crystal was selected and mounted on a glass fiber using epoxy-based glue. The data were collected using SMART[21] software at 200 K employing a scan of 0.3° in ω with an exposure time of 10 s/frame. The cell refinement and data reduction were carried out with SAINT,[22] while the program SADABS[22] was used for the absorption correction. The structure was solved by direct methods using SHELX-97[23] and difference Fourier syntheses. Full-matrix least-squares refinement against $|F^2|$ was carried out using the SHELXTL-PLUS[23] suit of programs. The structure of $Li_3Fe_2(HPO_3)_3Cl$ was solved in *Pnma* space group. The positions of one Fe, one Cl, two P, and 5 O atoms were located from the difference Fourier maps. These positions were then refined isotropically and immediately two more Li positions

clearly appeared approximately 2 Å away from the oxygen atoms. At this point anisotropic refinement was carried out and finally peaks of the intensity of 1 e/A^3 close to 1.3 Å away from the two P atoms appeared in the difference Fourier maps. These peaks were assigned as phosphite hydrogen and refined isotropically without any constraints. Details of the final refinements and the cell parameters for $Li_3Fe_2(HPO_3)_3Cl$ are given in Table 1. The final atomic coordinates and the isotropic displacement parameters are given in Table 2. Selected inter-atomic distances are listed in Table 3.

Table 1. Crystal Data and structure refinement for $Li_3Fe_2(HPO_3)_3Cl$

Empirical formula	$Li_3Fe_2(HPO_3)_3Cl$	*Z*	4
Formula weight	407.90 g.mol^{-1}	ρ_{calc}	2.737 g.cm^{-3}
Crystal system	Orthorhombic	F(000)	792
Space group	*Pnma*	Temperature	200(2) K
a	9.139(2) Å	GOF on F^2	1.125
b	15.266(4) Å	*R* [I>2σ(I)]	R_1 = 0.0230
c	7.094(1) Å		wR_2 = 0.0654
$\alpha = \beta = \gamma$	90 °	*R* [all data]	R_1 = 0.0240
V	989.8(4) Å^3		wR_2 = 0.0661

Powder X-ray diffraction (PXRD). Phase purity of $Li_3Fe_2(HPO_3)_3Cl$ was evaluated by comparison of PXRD pattern with the simulated pattern generated from the atomic coordinates of single-crystal XRD solution. The powder pattern was obtained from a PANalytical X'Pert Pro diffractometer equipped with a Cu $\mathbf{K_{\alpha_{1,2}}}$ anode and a linear array PIXcel detector over a 2θ range of 5 to 90° with an average scanning rate of 0.0118° sec^{-1}.

Mössbauer spectroscopy. About 70 mg of sample was secured in a lead sample holder and studied by ^{57}Fe Mössbauer experiment at room temperature using a constant acceleration spectrometer in transmission geometry, operated using a ^{57}Co (50 mCi) gamma-ray source embedded in Rh matrix. The Mössbauer spectrum was calibrated for isomer shift with respect to a standard α-Fe foil at room temperature. The collected experimental data was then analyzed for line fitting by Lorentzian function using the RECOIL software.[24] To confirm the electrochemical oxidation of Fe center inside the cell, few cells were subjected to

charge up to 4.5 V vs. Li^+/Li, followed by recovering of about 15 mg of oxidized sample by breaking the charged cells. The oxidized cathode was then washed with NMP and acetonitrile and analyzed with Mössbauer spectroscopy in a manner similar to the as prepared crystals.

Magnetic susceptibility measurements. The DC Magnetic susceptibility of the compound was measured at magnetic field of 0.5 Tesla (1 Tesla = 10,000 Oe) after zero-field cooling over the temperature range 1.8 - 300 K and isothermal magnetization at 2 K was measured in an applied field range of +5 to -5 Tesla with a Quantum Design SQUID magnetometer. Several zero field cooled (ZFC) and field cooled (FC) magnetization data were collected at different applied magnetic field. Variable field magnetization was also measured under ZFC condition at different temperatures.

Thermo-gravimetric analysis (TGA). TGA has been done on the sample with a TA instrument Q50 TGA in a temperature range of 25 to 800 °C with a scan rate of 10 $°C.min^{-1}$ under nitrogen flow.

IR spectroscopy. The IR spectrum was collected using Thermo Nicolet Nexus 470 FT-IR spectrometer over 500 – 4000 cm^{-1} on a sample embedded in KBr pellet.

Electrochemical testing. To assess the electrochemical performance of $Li_3Fe_2(HPO_3)_3Cl$ a standard cathode film was made first. In a typical composite cathode film preparation, the active material, $Li_3Fe_2(HPO_3)_3Cl$ was first milled with super P conductive carbon thoroughly in a SPEX 8000D miller for 3 h to reduce the particle size. Poly-vinylidene fluoride (PVDF) was then added to the active material as the binder and an optimum amount of N-Methyl-2-pyrrolidone (NMP) was added to dissolve the PVDF. The resulting slurry was further ball milled for another 20 min until a homogeneous viscous mixture was obtained. The ratio of the active material, conducting carbon, and the binder in cathode mix was 60:30:10. The cathode mix was then spread as a film of uniform thickness onto a flat sheet of aluminium current collector with a glass rod and transferred into a vacuum oven and dried for 12 h at 85 °C.

For electrochemical tests CR2032 type coin cells were fabricated. The composite cathode film was cut into circular disks (3/8 inch diameter) with 3.5 – 4.0 mg of active material loading and transferred into an argon filled glove box with an oxygen concentration below 2.0 ppm.

Table 2. Final Atomic Coordinates and Equivalent Isotropic Displacement Parameters of the non-Hydrogen and hydrogen atoms. U_{eq} = 1/3rd of the trace of the orthogonalized U Tensor

Atom	Wyckoff	Site	Occu-pancy	x/a	y/b	z/c	U_{eq} [Å^2]
Fe1	8*d*	1	1	0.62631(4)	0.63532(2)	0.48115(5)	0.0081(1)
P1	8*d*	1	1	0.60170(6)	0.45227(4)	0.22508(8)	0.0081(2)
P2	4*c*	.m.	1	0.39091(9)	¾	0.19558(12)	0.0084(2)
O1	8*d*	1	1	0.75611(18)	0.45578(10)	0.1447(2)	0.0119(5)
O2	8*d*	1	1	0.55165(18)	0.54337(10)	0.2834(2)	0.0106(4)
O3	8*d*	1	1	0.58452(17)	0.38610(11)	0.3872(2)	0.0106(4)
O4	8*d*	1	1	0.29833(18)	0.66721(10)	0.1918(2)	0.0130(5)
O5	4*c*	.m.	1	0.4923(2)	¾	0.3676(3)	0.0098(6)
Cl1	4*c*	.m.	1	0.66554(9)	¾	0.72893(11)	0.0131(2)
Li1	8*d*	1	1	0.3491(4)	0.5690(3)	0.3526(6)	0.0144(11)
Li2	4*c*	.m.	1	0.3929(7)	¾	0.6221(10)	0.0193(17)
H1	8*d*	1	1	0.510(3)	0.420(2)	0.101(5)	0.0290
H2	4*c*	.m.	1	0.475(5)	¾	0.036(6)	0.0290

The cathode disk and Li anode (0.75 mm thickness Li ribbon cut into circular disk) were assembled in the coin cell casing with a Celgard® 2325 circular sheet placed between the two electrodes as the separator. The electrolyte, 1 M solution of $LiPF_6$ in DMC-EC (1:1) was then added and the cell was sealed with a coin cell crimper. The prepared cells were aged for equilibration for about 12 hours before electrochemical testing.

Cyclic voltammograms were obtained using a PAR EG&G potentiostat/galvanostat model 283 in the potential range of 2.2 – 4.5 V (vs. Li^+\Li) with a scan rate of 0.05 mV.sec^{-1}. Voltage-composition profiles were obtained using galvanostatic charge/discharge experiments on an Arbin Instruments battery tester, model BT2043, on the same potential limits as CV with a constant current constant voltage (CCCV) charge and constant current discharge modes and at various C-rates. An Ivium Stat potentiostat/galvanostat with built-in impedance

analyzer was used for running electrochemical impedance spectroscopy (EIS) analyses on the assembled cells in a frequency range of 10 mHz – 100 kHz over the temperature range of 23 - 50 °C with an AC amplitude of 10 mV and the acquired experimental data were fitted to an equivalent circuit with ZView software.

Table 3. Selected bond lengths for $Li_3Fe_2(HPO_3)_3Cl$

Bonds	Distances (Å)	Bonds	Distances (Å)
Fe(1) – O(4)$^{\#1}$	2.052(9)	P(2) – O(4)$^{\#4}$	1.521(1)
Fe(1) – O(2)	2.098(5)	P(2) – H(2)	1.37(4)
Fe(1) – O(1)$^{\#2}$	2.105(9)	Li(1) – O(1)$^{\#5}$	1.926(4)
Fe(1) – O(3)$^{\#3}$	2.166(1)	Li(1) – O(2)	1.955(4)
Fe(1) – O(5)	2.283(3)	Li(1) – O(3)$^{\#3}$	2.061(5)
Fe(1) – Cl(1)	2.506(6)	Li(1) – O(4)	1.940(4)
P(1) – O(2)	1.521(3)	Li(2) – O(3)$^{\#7}$	2.089(1)
P(1) – O(1)	1.523(1)	Li(2) – O(3)$^{\#3}$	2.089(1)
P(1) – O(3)	1.538(6)	Li(2) – O(5)	2.021(7)
P(1) – H(1)	1.31(3)	Li(2) – Cl(1))$^{\#6}$	2.331(6)
P(2) – O(4)	1.521(1)	Li(2) – Cl(1)	2.605(7)
P(2) – O(5)	1.532(2)		

$^{\#1}$ x +1/2, y, - z + 1/2; $^{\#2}$ – x + 3/2, - y + 1, z + 1/2; $^{\#3}$ – x + 1,- y + 1,- z + 1; $^{\#4}$ x, - y + 3/2, z; $^{\#5}$ x - 1/2, y, - z + 1/2; $^{\#6}$ x + 1/2, y, -z + 3/2; $^{\#7}$ –x + 1, y + 1/2, -z + 1.

Results and discussion

Synthesis

While $Li_3Fe_2(HPO_3)_3Cl$ can be synthesized in the temperature range 175 to 205 °C, the nature of impurity phases varies with the temperature. The major impurity phase was $Li_{1.43}[Fe^{II}_{4.43}\ Fe^{III}_{0.57}(HPO_3)_6]\cdot 1.5H_2O$,[20] when the reaction was carried out below 200 °C and above 200 °C an unknown impurity phase was observed as evident from the PXRD and Mössbauer spectroscopy. This difference in impurity phases based on reaction temperature can be explained from the chemistry of phosphite group, which undergo decomposition (disproportionation) at 200 °C to phosphate and phosphine gas according to equation (1):

$$4H_3PO_3 \xrightarrow{\Delta} 3H_3PO_4 + PH_3 \qquad (1)$$

In both cases the reaction yields large crystals of $Li_3Fe_2(HPO_3)_3Cl$ which can be readily separated and analyzed with single-crystal XRD. The powder XRD pattern of $Li_3Fe_2(HPO_3)_3Cl$ obtained from purified phase along with the calculated pattern from the atomic coordinates of single-crystal data are represented in Fig. 1. A good match between the acquired and theoretical patterns suggests that the separated crystals are mostly pure and only minor amount of unknown impurity phase remains in the sample whose peak is indicated with an asterisk. From the Mössbauer spectroscopic analysis the percentage of impurity has been determined to be 3.6 % and isomer shift and quadrupole moment value point to some Fe(II) containing phase (discussed later).

Structural description

The asymmetric unit (Fig. 2a) contains 11 non-hydrogen atoms (1 Fe, 2 P, 2 Li, 1 Cl, and 5 O) and two hydrogen atoms. Each phosphorous atom is coordinated to 3 oxygen atoms and one hydrogen atom, exhibiting a distorted tetrahedral unit (or pseudo-trigonal) with P1 – O and P2 – O bond distances in the range 1.521(3) – 1.538(6) and 1.521(1) – 1.532(2) Å, respectively.

The two P — H distances for P1 and P2 are 1.31(3) and 1.37(4) Å, respectively, which are in good agreement with the reported values.[25] There is only one crystallographically distinct Fe atom which adopts an octahedral coordination surrounded by five oxygen atoms and one chlorine atom. The Fe — O distances are in the range 2.052(9) – 2.283(3) Å, which corroborates well with the reported Fe – O distances where Fe is in 2+ oxidation state.[26] A Fe — Cl distance of 2.506(6) Å is similar to Fe – Cl distances reported in Fe_2PO_4Cl.[25] There are two crystallographically distinct Li sites, Li1 and Li2, in the asymmetric unit located in a general and special position with site occupancy factors (SOFs) of 1 and 0.5, respectively. Li1 is four coordinated by oxygen atoms from the two different phosphite groups with Li1 – O bond lengths in the range 1.926(4) – 2.061(5) Å. Li2, on the other hand, is five coordinated surrounded by 3 oxygen and two chlorine atoms with Li2 – O and Li2 – Cl bond lengths in the range 2.021(7) – 2.089(1) and 2.331(6) – 2.604(8) Å, respectively.

The structure is composed of dimers of edge-shared FeO_5Cl octahedra connected through a common edge O5 – Cl1 along the b-axis and these edge-shared dimers are further connected through the participation of eight phosphite groups to form the three-dimensional structure (Fig. 2b).

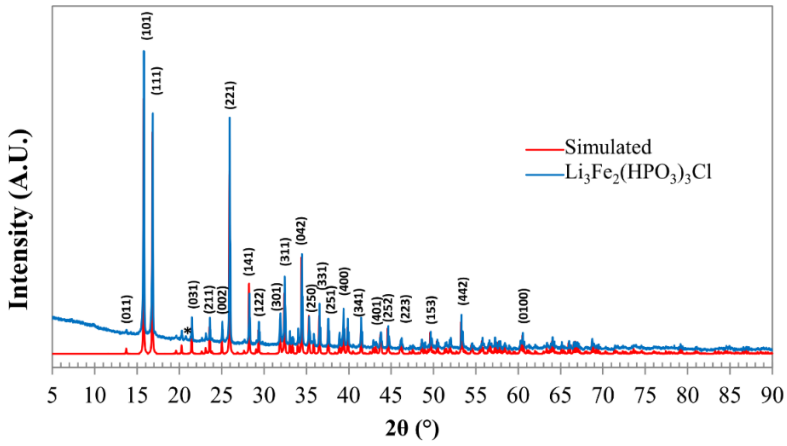

Fig. 1. PXRD pattern of $Li_3Fe_2(HPO_3)_3Cl$ compared with the simulated pattern reconstructed from SC-XRD. The impurity peak is marked with an asterisk.

Out of the eight phosphite groups that are connected to the dimer, seven are corner-shared and the remaining one bridges the octahedral dimer through the two apical oxygen atoms from the same P_2O_3 group (Fig. 2b). Li sites fill the space between the adjacent iron octahedral dimers and when viewed along the a-axis Li ions can be seen located in narrow zig-zag channels intercepted by chloride in case of Li2 and by oxygen in case of Li1, respectively (Fig. 3a).

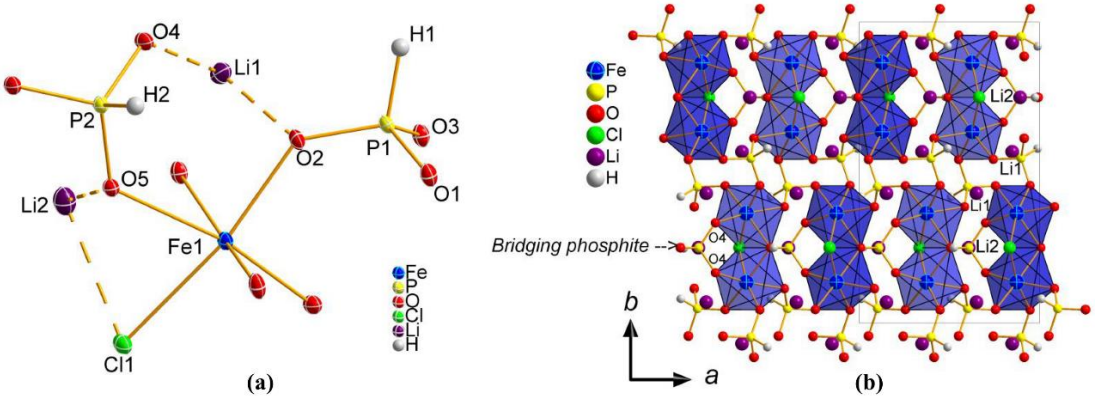

Fig. 2. Asymmetric unit of $Li_3Fe_2(HPO_3)_3Cl$ as refined from SC-XRD (a); packing diagram as viewed along the *c*-axis (b).

This arrangement creates empty helical channels along the b-axis of the crystals where P — H apices are protruding into the channels alternatively through the length of the channel (Fig. 3b). It is also interesting to note that anisotropic thermal parameters for the two Li atoms are different, with Li2 (U11 = 21, U22 = 15, and U33 = 22 $Å^2$ x 10^3) having higher vibrations in all three directions compared to Li1 (U11 = 13, U22 = 11, and U33 = 19 $Å^2$ x 10^3). These differences in the anisotropic thermal parameters may have important implications in Li-ion mobility (vide infra). Existence of chloride anion in the asymmetric unit was further confirmed through EDS analysis and the result is in good agreement with that calculated from single-crystal X-ray data (9.17% wt/wt vs. 8.69% from SC-XRD).

Spectroscopic and thermogravimetric analyses

The IR spectrum of $Li_3Fe_2(HPO_3)_3Cl$ as shown in Fig. 4 mainly consists of strong absorption peaks due to P—H and P—O bonds of the phosphite moiety in the structure. The strong, sharp peak located at 2428 cm^{-1} is the signature of P—H stretching mode while the corresponding bending mode is merged with the strong PO_3 symmetric and asymmetric stretching modes in the range of 950 – 1150 cm^{-1}.[25]

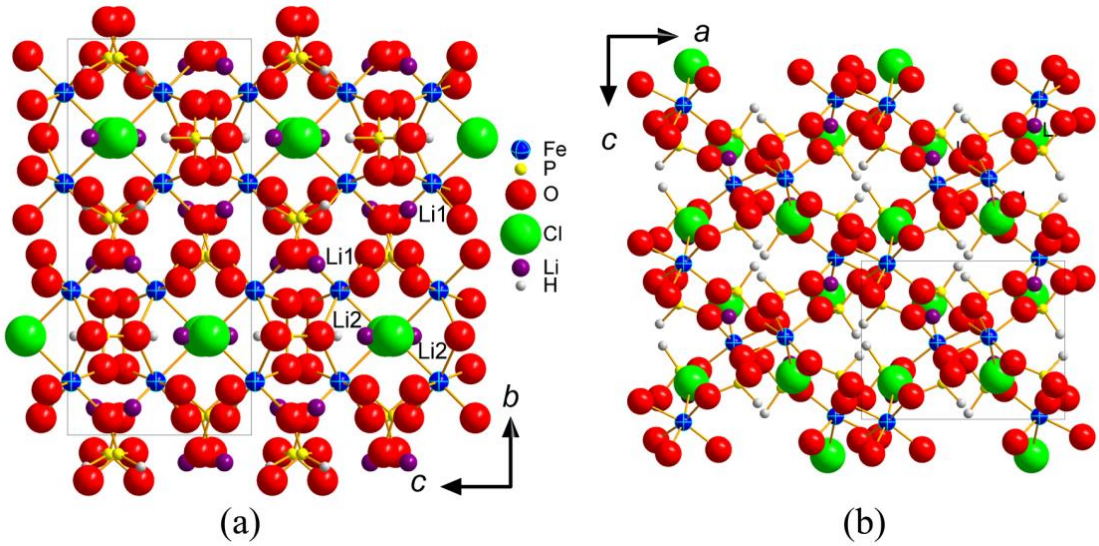

Fig. 3. Packing diagram of $Li_3Fe_2(HPO_3)_3Cl$ phase as views along *a*-axis (a); and *b*-axis (b).

The asymmetric PO_3 bending mode is visible at 594 cm^{-1}. Except for a few low intensity peaks the spectral region above 3000 cm^{-1} is almost flat; this (as well as the single-crystal XRD data) confirms that there is no partial oxidation of P—H bond to P – OH bond as commonly seen in phosphite chemistry.[27]

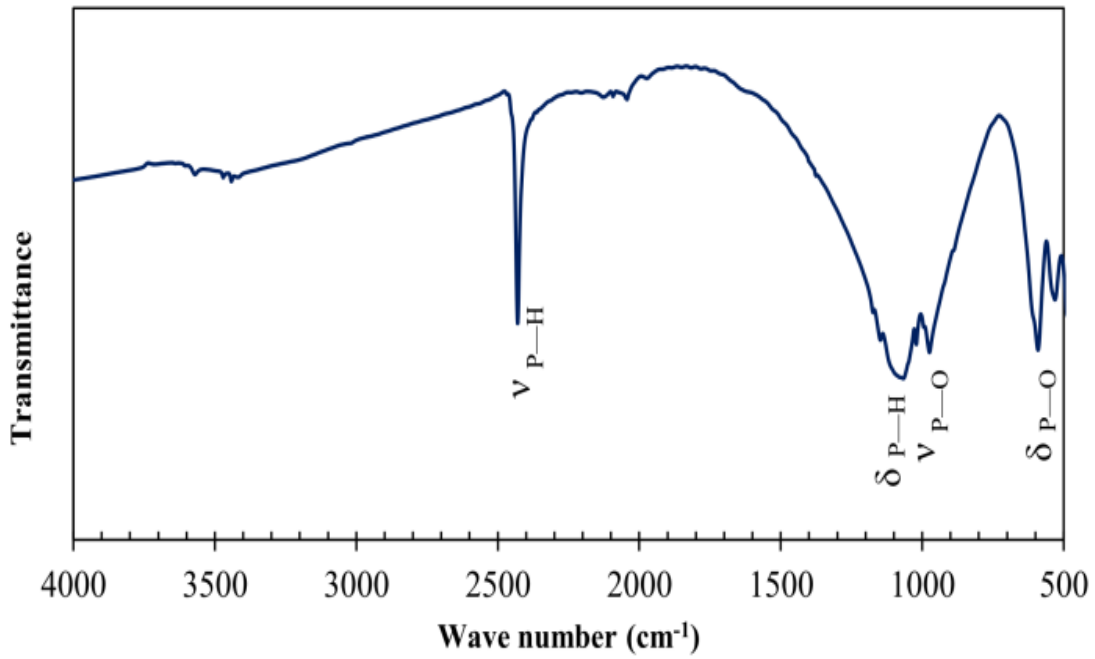

Fig. 4. FT-IR spectrum of $Li_3Fe_2(HPO_3)_3Cl$.

TGA of $Li_3Fe_2(HPO_3)_3Cl$ was conducted to assess the thermal stability of the compound and represented in Fig. 5. The TGA reveals about 0.6% mass loss starting from room temperature up to 300 °C which can be assigned to the adsorbed moisture. The $Li_3Fe_2(HPO_3)_3Cl$ phase is stable until 420 °C where it decomposes abruptly with a mass loss of 9.1% which matches perfectly well with the loss of one HCl unit from the formula (theoretical = 9.0 %).

At higher temperatures there are two constant positive slopes of mass gain processes which can be assigned to the oxidation of both Fe(II) and P(III) in the compound to Fe(III) and P(V), respectively, due to the existence of oxygen and moisture impurities in the nitrogen purge gas, as observed also in the work of Rojo *et. al.*[20]

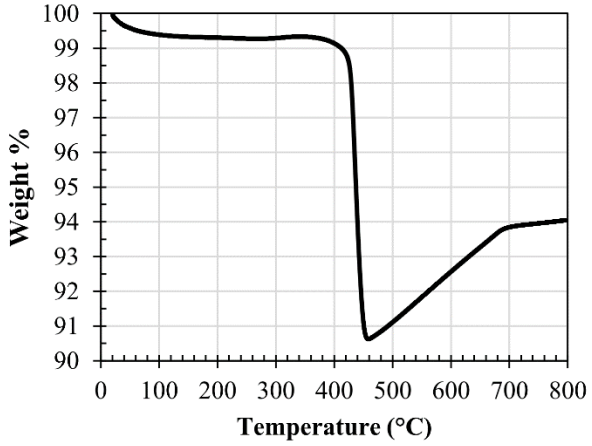

Fig. 5. TGA curve of $Li_3Fe_2(HPO_3)_3Cl$.

Magnetic property

The magnetic measurements were performed on powdered sample (finely ground manually separated pure crystals) to validate the oxidation states of Fe and to verify the presence of any magnetic phase transition. The temperature dependence of the magnetic susceptibility and inverse susceptibility of $Li_3Fe_2(HPO_3)_3Cl$ measured in an applied field of 0.5 T from 2 K to room temperature under zero-field cooled (ZFC) condition are given in Fig. 6. The molar magnetic susceptibility increases asymptotically as the temperature decreases from 300 K and reached a maximum at 9.5 K in the $\chi M(T)$ plot and after that there is a sharp fall of molar susceptibility indicating an onset of antiferromagnetic ordering below 9.5 K. The plot of thermal variation of inverse susceptibility, $\chi M^{-1}(T)$, shows linear behavior between 100 – 300 K and can be fitted to Curie-Weiss law yielding a Curie constant of 3.8 emu K/mol and a Curie-Weiss constant (θp) of -6.9 K, respectively (Fig. 6).

The experimental effective magnetic moment per iron ion derived from Curie constant (μeff (experimental) = 5.5 μB) is higher than the spin-only value (4.9 μB) due to contribution from unquenched orbital magnetic moment. The observed μeff found in different Fe(II) compounds are in the range 5.1 – 5.5 μB.[28] The negative value of the Weiss constant reflects the antiferromagnetic interactions between the Fe centers, which forms an edge-shared octahedral dimer.

Temperature variation of χMT shows a very sluggish decrease in χMT upon cooling from 3.72 emu K mol^{-1} at 300 K to 3.10 emu K mol^{-1} at 40 K followed by a sharp fall below 40 K to a value of 0.139 emu K mol^{-1} at 2 K (Supplementary information, Fig. S1).

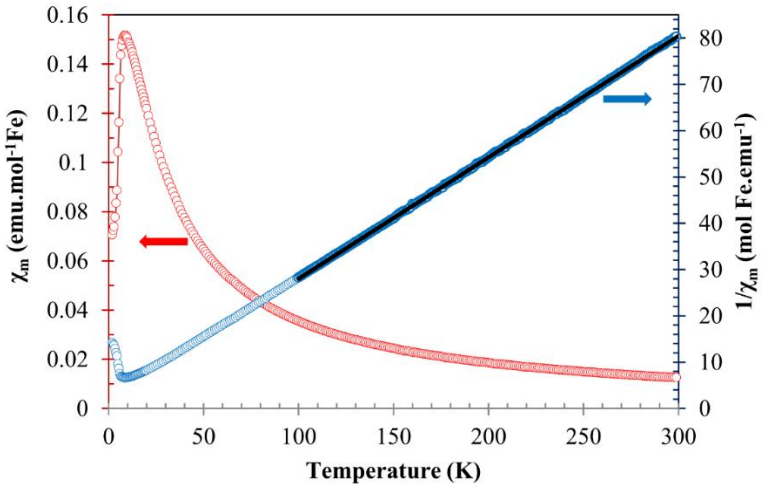

Fig. 6. Temperature dependent molar and inverse molar magnetic susceptibility of $Li_3Fe_2(HPO_3)_3Cl$ acquired at an applied field of 0.5 T.

To further investigate the nature of the antiferromagnetic transition, low-temperature magnetic behavior was studied by dc magnetization measurements under field cooled (FC) and zero field cooled (ZFC) conditions under low fields and several ZFC measurements at several increments of applied field (Fig. 7). The ZFC and FC magnetic susceptibilities measured at low fields 0.01, 0.05, and 0.1 T show another transition at 4.75 K, which exhibits irreversibility in the FC and ZFC data.

This irreversibility between the FC-ZFC data also decreases as the applied field increases from 0.01 to 0.11 T (inset of Fig. 7). However, the broad peak at 9.5 K (seen at 0.5 Tesla data) shows reversibility indicating an onset of a 3-D antiferromagnetic ordering. The transition at 4.75 K is not pronounced in ZFC data especially at higher applied fields.

Increasing the applied field in the ZFC data to various higher fields shift the antiferromagnetic maxima to lower temperatures (for example, from 9.5 K at 0.5 T

to 6.9 K at 3 Tesla) and disappears completely at 4 T, indicating a field-induced metamagnetic transition.

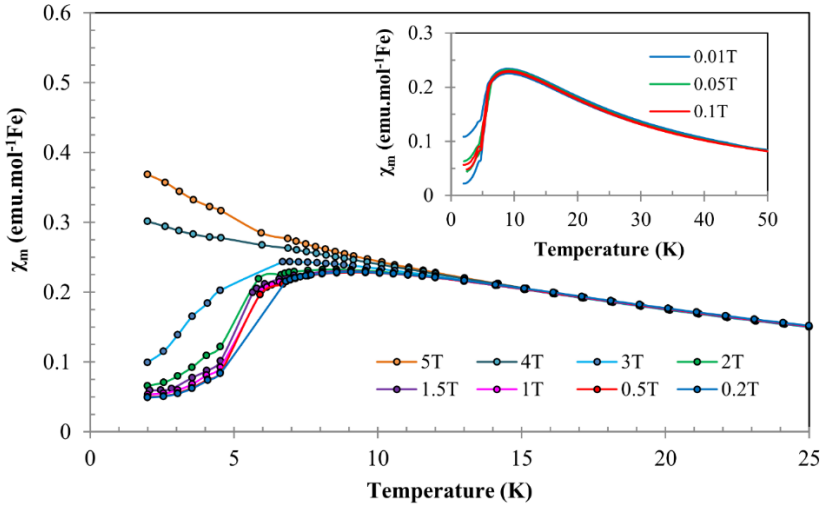

Fig. 7. Depiction of field induced variation of the molar magnetic susceptibility of $Li_3Fe_2(HPO_3)_3Cl$ as a function of temperature; inset shows ZFC-FC curves at different field strengths.

The variable field isothermal magnetization (M) measured at 2 K shows a very sluggish linear increase of magnetization till 3 T and after that there is a sharp jump in magnetization from 0.50 to 3.20 NμB/Fe between 3 and 5 T, respectively, confirming the metamagetic transition from an antiferromagnetic phase to a ferromagnetic like phase (Fig. 8). Such metamagnetic transitions have been observed previously in transition metal coordination polymers involving azido and cyanide bridges. [29, 30]

The hysteresis scan at 2 K also exhibit a small remnant magnetization and an interesting history dependent loops at higher field regions at both positive and negative field after the metamagnetic transition. Hysteresis scan at 50 and 300 K are completely linear and no signature of any remnant magnetization or field induced transition. M-H measurements at higher temperatures, 8 - 50 K, show linear increase of magnetization reminiscent of antiferromagnetic interactions.

Electrochemistry

The first three cyclic voltammograms (CV) of the cell with $Li_3Fe_2(HPO_3)_3Cl$ as cathode is represented in Fig. 9. The CVs indicate that the phase is

electrochemically active and also the broadness of cathodic and anodic peaks reveal that the oxidized and reduced phases may be following a solid-solution type behavior.

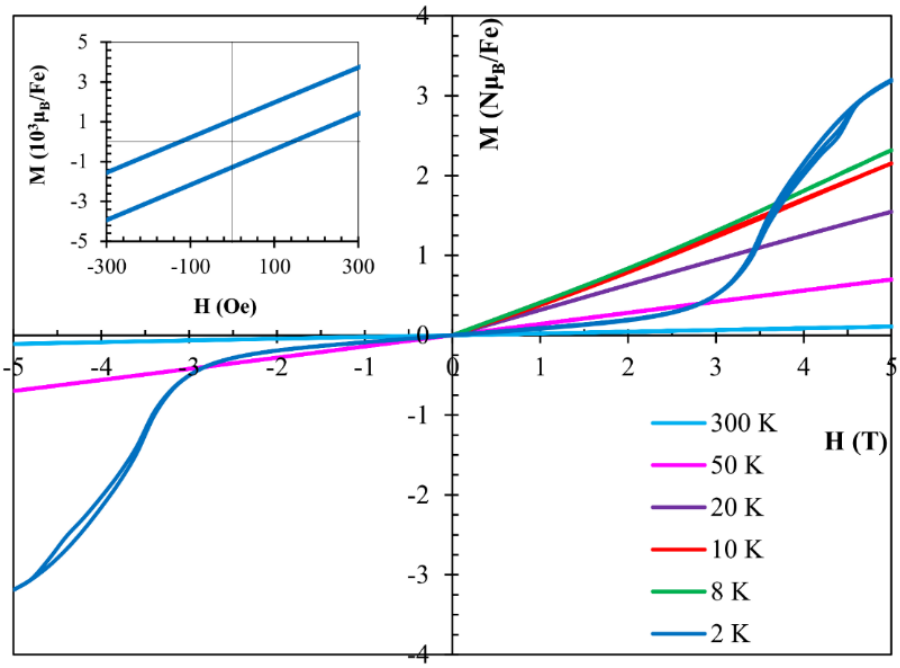

Fig. 8. Magnetization vs. field variation hysteresis loop for $Li_3Fe_2(HPO_3)_3Cl$ along with M-H scans at different temperatures. Inset shows an enlargement view of the remanent magnetization at 2 K around the zero field strength.

The open circuit voltage (OCV) is located at 2.74 V and the cathodic and anodic peak potentials are observed at 3.026 and 3.334 V, respectively. The oxidation and reduction peak potentials do not shift with cycling suggesting the high reversibility of the redox process. Since there are two iron(II) and three Li atoms per unit formula, one may expect to be able to extract and insert up to two Li ions upon oxidation (charging) and reduction (discharging) of iron atoms, respectively, which leads to a theoretical capacity of 131.41 $mAh.g^{-1}$ of active material.

Galvanostatic charge/discharge tests were employed for evaluating the cell performance of $Li_3Fe_2(HPO_3)_3Cl$ as cathode in a Li-ion cell and the results are given in Fig. 10. Since the oxidation state of Fe is +2 in the active material, the cell was charged first with de-insertion of Li^+ ions.

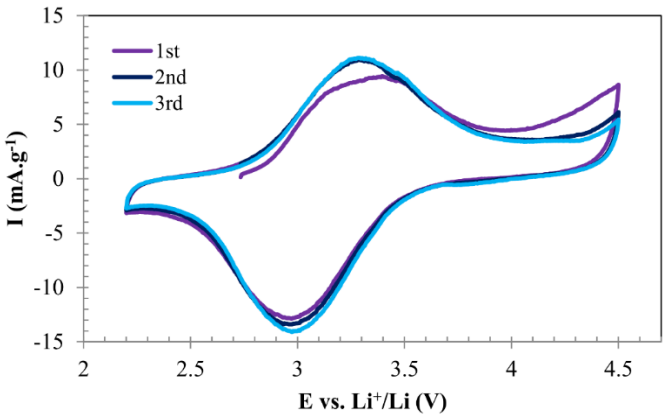

Fig. 9. CV of $Li_3Fe_2(HPO_3)_3Cl$. The cathodic current is negative.

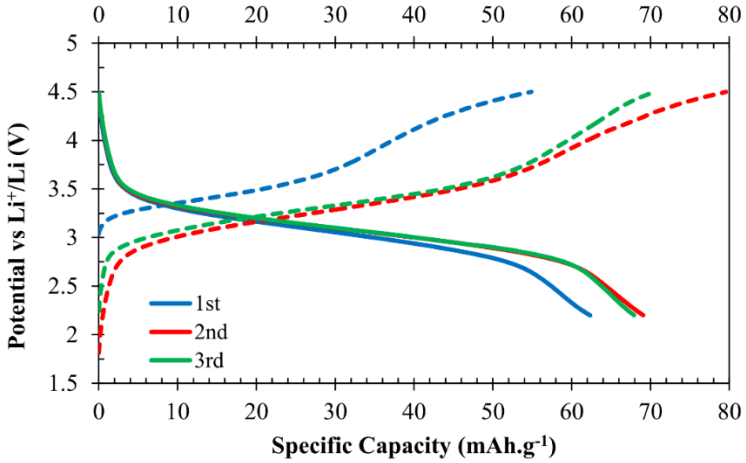

Fig. 10. First three cycles of galvanostatic charge\discharge test. Dashed and solid lines represent the charge and discharge curves, respectively.

As is obvious from the first cycle of charge-discharge curve, the discharge capacity is greater than the corresponding charge capacity, which may indicate that a fraction of Fe(II) sites in the crystal structure was oxidized to Fe(III) before charging. The Mössbauer results (vide infra), however, rules out the existence of any Fe(III) in the as-synthesized materials; therefore, this oxidation can be due the extensive milling during the composite cathode preparation. This observation is also supported by cyclic voltammetry studies when the cathode was initially subjected to charge (reductive lithiation) in the first cycle (supplementary information, Fig. S2), a cathodic peak around 2.87 V was observed, which disappeared upon further cycling and only one reduction peak can be observed at

3.028 V in the CV. Also to be noted here that first charge curve lies at 0.25 volt higher than the successive charge curves, which confirms that initially a fraction of the active material has been oxidized to Fe(III). The partial oxidation of Fe(II) centers and consequent extraction of Li^+ by air and moisture has been previously observed for some cathode materials and the effect is severe when the initial voltage (i.e. cell OCV) is below 3.0 V.10 The so-called air poisoning of the particles has been reported to cause irreversible capacity loss by accumulating inactive Fe(III) impurities on the surface of the active particles. However, in our case the Fe(III) phase recovery is evident from the higher charge capacity in the second and third cycles, which indicates that the initially oxidized phase has reduced to Fe(II) at the end of the first cycle and contributing to the subsequent charging steps in a reversible manner.

The voltage composition profile as shown in Fig. 10 exhibits a sloppy curve which in conjunction with the broad peaks of CV and the voltage charge derivative curves (Supplementary information, Fig. S3) confirm the solid-solution formation of Fe(II) and Fe(III) ions in the structure as the cathode was subjected to charge and discharge. Neither curves exhibit sharp changes in voltage especially in the charge regime and consequently the charge cut-off potential was set at 4.5 vs Li^+/Li with constant current charging to avoid extensive electrolyte oxidation followed by constant voltage charging (CCCV charge) at the same potential until the current drops to 10 % of the value at C/50 to maximize Fe(II) oxidative delithiation. Similarly the lower cut-off potential was set to 2.2 V vs Li^+/Li (CC discharge) to limit the cell performance only to the reversible capacity. With the above routines the first discharge delivered a capacity of about 62 $mAh.g^{-1}$ which accounted for 47% of the theoretical capacity; upon the second and third discharge, the discharge capacity increased to 69 $mAh.g^{-1}$ (52% of the theoretical capacity) and became stable at this value, equivalent to the removal of only one Li^+ ion per formula unit. The de-intercalation Li^+ could be accomplished either through complete extraction of Li2 with site occupancy of 0.5, or 50 % removal of Li1 sites (site occupancy 1), or a mixture of both. Discharging the cells at a slower rate of C/100 didn't show capacities higher than that at C/50 where this issue could be the

result of a fundamental limitation or may be resolved by increasing the sample conductivity or further decrease in the particle size.

The $Li_3Fe_2(HPO_3)_3Cl$ cathode was tested for capacity retention upon successive cycling at C/5 rate after the cell has been cycled several times at different C-rates. The results given in Fig. 11 indicate the acceptable stability of this phase after 60 cycles. The specific capacity decays only with a slight slope, but there are some higher frequency fluctuations in specific capacity which are due to the change in environmental conditions, most notably the temperature.

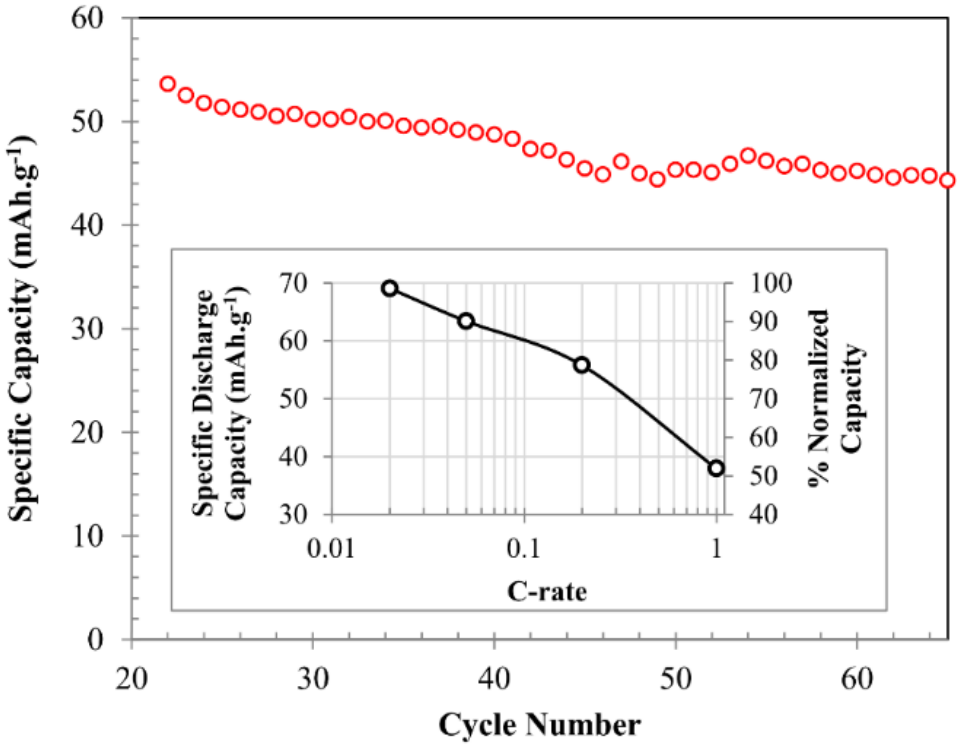

Fig. 11. Capacity retention of $Li_3Fe_2(HPO_3)_3Cl$ cathode at C/5 rate. Inset shows the effect of variation of discharge rate on the cathode specific capacity.

Increasing the discharge rates reveal some interesting kinetic properties of $Li_3Fe_2(HPO_3)_3Cl$ phase, as shown in the inset of Fig. 11. Upon increasing the discharge rate from C/50 to C/5 (10 fold increase in current) the cell can still deliver a specific capacity of 56 $mAh.g^{-1}$ which accounts for 80% of the value at C/50; moreover even at a discharge rate of 1C (50 times increase in the current) still 38 $mAh.g^{-1}$ (55% of the normalized value) can be reversibly delivered.

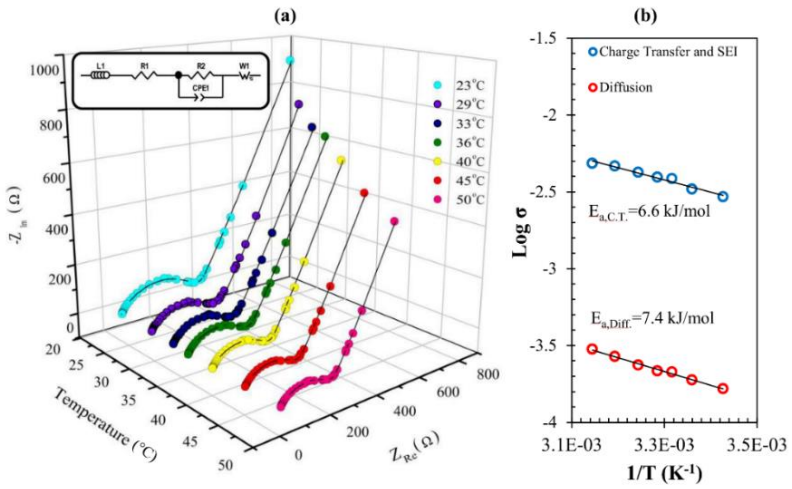

Fig. 12. a) Nyquist plots of $Li_3Fe_2(HPO_3)_3Cl|LiPF_6|Li$ cell at different temperatures; filled circles and the line represents the experimental data and fitted curve, respectively. Inset shows the equivalent circuit. b) The corresponding Arrhenius plots for the two main resistive processes.

These results suggest a high Li^+ mobility in the $Li_3Fe_2(HPO_3)_3Cl$ lattice, even though the channels are not very wide. Electroimpedance spectroscopic technique was employed at multiple temperatures below the electrolyte decomposition temperature to calculate the activation energies involved in the different processes inside the cell in the measured temperature range, and the results are shown in Fig. 12 and the fitted impedance parameters using the equivalent circuit (see inset of Fig. 12) are supplied as supplementary information (Table S1)

The Nyquist plot has the general shape of a Li-ion cell with a low-frequency tail and a high frequency depressed semi-circle representing the Li^+ diffusion inside the cathode active material and the combined charge transfer/SEI resistances, respectively. The value for the two main resistive processes was then extracted from the fit parameters and converted to conductance values which were utilized for construction of the respective Arrhenius plots, as given in Fig. 12b. The results shown in Fig. 12b suggest that both ionic diffusion and the combined charge transfer and SEI film resistances are thermally activated. The interestingly small activation energy of 7.4 kJ/mol (0.077 eV) associated with the ionic diffusion process as well as low activation energy for the charge transfer process

(6.6 kJ/mol) may be attributed to the facile kinetics of electrochemical reactions observed during successive charge-discharge tests at high C-rates. This low activation energy of Li-ion diffusion can be compared to 6.57 kJ/mol previously observed in the case of a $Li_3V_2(PO_4)_3$ cathode.[31] In general the apparent activation energy of the Li-ion diffusion in different materials in composite cathodes range between 30 – 60 kJ/mol, as has been reported to be 35.2 and 50.9 kJ/mol for LiV_3O_8,32 44.7 kJ/mol for $Li_3V_2(PO_4)_3$/C,33 47.48 kJ/mol for $LiFePO_4$@C.[31] The Arrhenius activation energy for the charge transfer process in the present case is much lower than observed in $LiFePO_4$@C cathode (59.35 kJ/mol).[34]

Ex-situ Mössbauer and PXRD

To gain further insight into electrochemically oxidized phase, we carried out ex-situ Mössbauer spectroscopic measurements and powder X-ray diffraction after removing the cathode active material from the cell after the first charge cycle and compared with Mössbauer and PXRD of pure cathode. Mössbauer spectrum of pristine $Li_3Fe_2(HPO_3)_3Cl$ has been fitted with two quadrupolar doublets, one major and one minor. The isomer shift (δ) and quadrupole splitting (Δ) values (δ = 1.20(1) mm/s, Δ = 1.97(7) mm/s; δ = 1.19(8) mm/s, Δ = 2.87(8) mm/s) reveal the existence of two different Iron(II) octahedral sites with site population of about 96 and 4%, respectively, as shown in Fig. 13a and Table 4. Since there is only one crystallographically unique Fe atom in the structure, the minor doublet can be assigned to the impurity phase, where Fe is in 2+ oxidation state. The Mössbauer spectrum also rules out other possible Fe-containing impurity phases in the sample as evident in the spectra collected over the entire velocity range spanning from -10 to +10 $mm.s^{-1}$ (data not shown).

The Mössbauer spectrum for the electrochemically oxidized sample is shown in Fig. 13b along with the deconvoluted curves representing three iron sites; typical spectra for Fe^{2+} site as in pristine sample along with a new quadrupole doublets for Fe^{3+} as in $Li_{3-x}Fe^{II}_{2-x}Fe^{III}_x(HPO_3)_3Cl$ and the impurity doublet. The results of fitting are shown in Table 4 suggest that after charging the cells up to 4.5 V vs. Li^+/Li, almost 40% of the Fe(II) sites are oxidized to Fe(III).

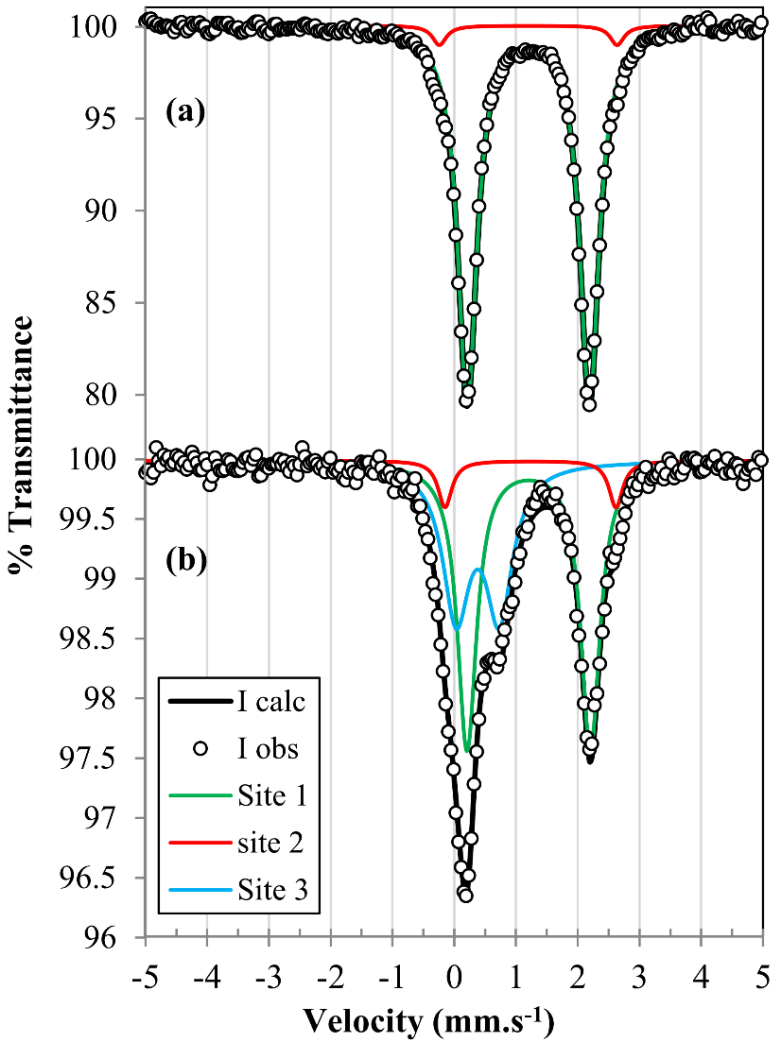

Fig. 13. Mössbauer spectrum of purified crystals of $Li_3Fe_2(HPO_3)_3Cl$ (a), and cathode powder retrieved from a charged cell up to 4.5 V vs Li^+/Li (b).

The relative increase in the impurity site percentage with respect to the as prepared crystals can be assigned to the addition of one doublet and a consequent increase in the degrees of freedom (or uncertainty) in the fitting process. The isomer shift and quadrupole splitting values are typical for Fe^{2+} and Fe^{3+} octahedral coordination surrounded by oxo donors.[35] The ex-situ PXRD of the electrochemically oxidized sample shows crystalline nature and pattern is in good agreement with the pristine sample except some line broadening. The lattice constants refinement indicates no appreciable change with respect to the pristine material (supplementary information, Fig. S4).

Table 4. Values of isomer shift (δ), Quadrupole Splitting (Δ) and site population derived from fit parameters of Mössbauer spectra of $Li_3Fe_2(HPO_3)_3Cl$ and its electrochemically oxidized form

Pristine $Li_3Fe_2(HPO_3)_3Cl$			
Site	δ ($mm.s^{-1}$)	Δ ($mm.s^{-1}$)	Site (%)
Doublet 1, Fe^{2+}(1)	1.20(1)	1.97(7)	96.3(6)
Doublet 2, Fe^{2+} impurity	1.19(8)	2.87(8)	3.6(4)
$Li_3Fe_2(HPO_3)_3Cl$ electrochemically oxidized by charging to 4.5 V			
Doublet 1, Fe^{2+}(1)	1.20(1)	1.99(8)	54.2(3)
Doublet 2, Fe^{3+}(1)	0.38(1)	0.69(7)	39.4(1)
Doublet 2, impurity	1.23(2)	2.76(7)	6.3(2)

Which Li ion is active?

Since only one Li-atom from $Li_3Fe_2(HPO_3)_3Cl$ can be removed, it will be interesting to know which one of the two crystallographically distinct Li-atoms is electrochemically active or part of both (two Li1 and one Li2) are active. In the absence of solid-state 7Li NMR before and after the oxidation, it will not be possible to conclude unambiguously which Li is active. Based on the anisotropic thermal parameters it may be possible that the Li2 is electrochemically active because it has higher vibrations in all three directions. Also Li2 has coordination with three oxygen atoms in a plane and two chlorine atoms in axial positions with Cl – Li2 – Cl angle of 136.6°. Chlorine is less electronegative than oxygen and weaker Cl – Li interactions may favor facile Li mobility. It will be also interesting to find out the Li-ion conduction path in this structure since only open channel along the b-axis has hydrogen atoms protruding into it, and oxygen and chlorine intercepts the channel along a-axis. A theoretical investigation will be required to find out the Li diffusion path.

Conclusions

In this article we have shown that a newly synthesized and structurally characterized phosphite-based compound of iron, $Li_3Fe_2(HPO_3)_3Cl$, is electrochemically active with respect to Li-ion (de)-insertion. Though it cannot compete with $LiFePO_4$, the average voltage of 3.1 volt vs Li^+/Li for an iron-based

compound is reasonably high and with the full theoretical capacity achievement can turn it to an attractive cathode. The compound also exhibits interesting field-induced metamagnetic transition. This example will open up new exploration in phosphite chemistry for new cathode materials for Li-ion battery.

Acknowledgements

The authors acknowledge the funding from Materials Research Centre (Missouri S&T) and University of Missouri Research Board. The authors are also grateful to Professors Nick Leventis and Pericles Stavropoulos for the donation of a potentiostat and a glovebox, respectively.

Notes and references

Electronic Supplementary Information (ESI) available: Details of crystal structure in the CIF format, figures of $\chi_m T$ *vs* T plot, CV, Voltage-charge derivative curve *vs* potential, and PXRD of the oxidized phase of $Li_3Fe_2(HPO_3)_3Cl$ and a table of impedance fit parameters are available. See
DOI: 10.1039/b000000x/

1 M. S. Whittingham, *Chem. Rev.* 2004,**104**, 4271.

2 B. Dunn, H. Kamath and J.-M. Tarascon, *Science*, 2011, **334**, 928.

3 M. Armand and J.-M. Tarascon, *Nature*, 2008, **451**, 652.

4 J. B. Goodenough and Y. Kim, *Chem. Mater.*, 2010, **22**, 587.

5 B. Ellis, K. T. Lee and L. F. Nazar, *Chem. Mater.*, 2010, **22**, 691.

6 C. Masquelier and L. Croguennec, *Chem. Rev.*, 2013, **113**, 6552.

7 A. K. Padhi, K. S. Nanjundaswamy and J. B. Goodenough, *J. Electrochem. Soc.*, 1997, **144**, 1188.

8 J.-M. Tarascon, N. Recham, M. Armand, J.-N. Chotard, P. Barpanda, W. Walker and L. Dupont, *Chem. Mater.*, 2010, **22**, 724.

9 A. K. Padhi, V. Manivannan and J. B. Goodenough, *J. Electrochem. Soc.*, 1998, **145**, 1518.

10 A. Yamada, N. Iwane, Y. Harada, Sh.-I Nishimura, Y. Koyama and I. Tanaka, *Adv. Mater.*, 2010, **22**, 3583.

11 M. Saiful Islam, R. Dominko, C. Masquelier, C. Sirisopanaporn, A. R. Armstrong and P. G. Bruce, *J. Mater. Chem.*, 2011, **21**, 9811.

12 H. Chen, Q. Hao, O. Zivkovic, G. Hautier, L. Du, Y. Tang, Y. Hu, X. Ma, C. P. Grey and G. Ceder, *Chem. Mater.*, 2013, **25**, 2777.

13 H. Chen, G. Hautier and G. Ceder, *J. Am. Chem. Soc.*, 2012, **134**, 19619.

14 G. Rousse and J. M. Tarascon, *Chem. Mater.*, 2014, **26**, 394.

15 N. Recham, J.-N Chotard, L. Dupont, C. Delacourt,, W. Walker, M. Armand and J.-M Tarascon, *Nat. Mater.*, 2010, **9**, 68.

16 P. Barpanda, M. Ati, B. C. Melot, G. Rousse, J-N. Chotard, M-L. Doublet, M. T. Sougrati, S. A. Corr, J-C. Jumas and J-M. Tarascon, *Nat. Mater.*, 2011, **10**, 772.

17 B. L. Ellis and L. F. Nazar, *Chem. Mater.*, 2012, **24**, 966.

18 H. Yaghoobnejad Asl and A. Choudhury, *RSC Adv.*, 2014, **4**, 37691.

19 T. Rojo, J. L. Mesa, j. Lago, B. Bazan, J. L. Pizarro and M. I. Arriortua, 2009, **19**, 3793.

20 U. Chung, J. L. Mesa, J. L. Pizarro, I. de Meatza, M. Bengoechea, J. R. Fernandez, M. I. Arriortua and T. Rojo, *Chem. Mater.*, 2011, **23**, 4317.

21 Bruker- SMART. Bruker AXS Inc., Madison, Wisconsin, USA. 2002.

22 Bruker- SAINT and SADABS. Bruker AXS Inc., Madison, Wisconsin, USA, 2008.

23 G. M. Sheldrick. *Acta Cryst.* 2008, **A64**, 112–122.

24 Recoil software: K. Lagarec and D. G. Rancourt, *Nucl. Instrum. Meth. Phys. Res. B, 1997, **129**, 266.*

25 U. Chung, J. L. Mesa, J. L. Pizarro, V. Jubera, L. Lezama, M. I. Arriortua and T. Rojo, *J. Solid State Chem.*, 2005, **178**, 2913.

26 J. B. Anderson, J. R. Rea and E. Kostiner, *Acta Crystallogr. B*, 1986, **42**, 95.

27 S. Fernández-Armas, J. L. Mesa, J. L. Pizarro, J. S. Garitaonandia, M. I. Arriortua and T. Rojo, *Angew. Chem., Int. Ed.*, 2004, **43**, 977.

28 F. A. Cotton and G. Wilkinson, *Advanced Inorganic Chemistry*, Fourth edition, John Wiley and Sons, New York, **1980.**

29 T. Liu, Y. Zhang, Z. Wang, and S. Gao, *Inorg. Chem.*, 2006, **45**, 2782.

30 Y. –Z. Zhang, Z. –M. Wang and S. Gao, *Inorg. Chem.* 2006, **45**, 10404.

31 X. H. Rui, Y. Jin, X. Y. Feng, L. C. Zhang and C. H. Chen, *J. Power Sources*, 2011, **196**, 2109.

32 H. Ma, Z. Yuan, F. Cheng, J. Liang, Z. Tao and J. Chen, J. Alloys Compd., 2011, **509**, 6030.

33 Y. Q. Qiao, J. P. Tu, X. L. Wang, and C. D. Gu, *J. Power Sources*, 2012, **199**, 287.

34 J. Fan, J. Chen, Y. Chen, H. Huang, Z. Wei, M. –S. Zheng and Q. Dong, *J. Mater. Chem. A*, 2014, **2**, 4870.

35 F. Menil, *J. Phys. Chem. Solids*, 1985, **46**, 763 – 789.

III. Phosphite as Polyanion-based Cathode for Li-ion Battery: Synthesis, Structure and Electrochemistry of $LiFe(HPO_3)_2$

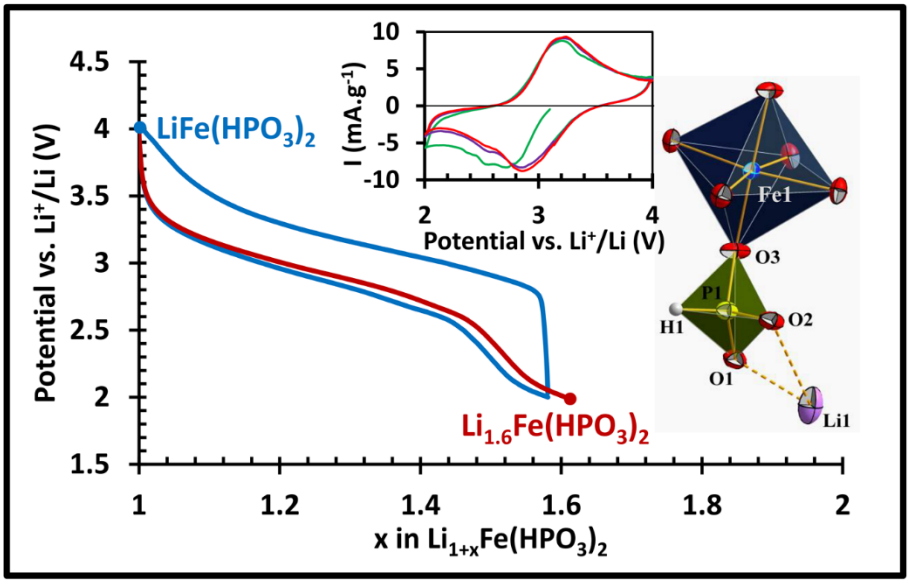

Hooman Yaghoobnejad Asl [a] and Amitava Choudhury [a,*]

[a,*] Department of Chemistry, Missouri University of Science and Technology, Rolla, MO 65409, USA.

ABSTRACT: A new lithium containing iron(III) phosphite, $LiFe(HPO_3)_2$, has been synthesized via a solvent-free, low temperature, solid-state synthesis route. The crystal structure of this material has been determined employing single-crystal X-ray diffraction, which indicates that the compound has a 3-dimensional structure formed by isolated FeO_6 octahedral units joined together via bridging HPO_3 pseudo-pyramidal moieties. This arrangement leads to the formation of channels along all the three crystallographic directions, where channels along the *a*- and *b*-axes host Li^+ ions. The compound was further characterized by TGA, IR, and Mössbauer spectroscopic techniques. Additionally, it has been demonstrated that this phase is electrochemically active towards reversible intercalation of Li^+ ions and thus can be used as a cathode material in Li-ion cells. An average discharge potential of 2.8 V and a practical capacity of 70 $mAh.g^{-1}$ has been achieved as indicated by the results of cyclic voltammetry and galvanostatic charge-discharge tests.

INTRODUCTION

In today's world, there are plenty of avenues of applications where Li-ion battery has been envisaged as a prime source of energy storage or power supply.[1-4] For all the applications safety is the primary concern but different qualities of batteries are sought after based on whether the application is focused on mobile or stationary devices. For example, a battery for vehicular application has to be high in energy density while for smart grid application, a low cost, long cycle life and fast charge-discharge battery will take precedence over the high energy density.[5] Thus one may expect to have different materials in Li-ion battery to fulfil different requirements of applications and in this race cathode component merits most attention since it determines the voltage and the specific capacity.

In this respect polyanion compounds of the transition metals are being actively investigated as cathode materials for Li-ion batteries.[6, 7] Due to the strong covalent bonding between the main group element in the center of the polyhedron and oxygen atoms in the polyanion moiety, the oxygen atoms are held tightly in the structure. This imparts structural stability to the compound and chances of oxygen release upon charging to high potentials are minimized thus improving the safety features of the cathode. Moreover, by changing the electronegativity of the central atom in a polyanion one can vary the iono-covalency of the metal-ligand bond in X – O – M (X = B, S, P, Si etc.; M = transition metal) linkage through the inductive effect of X thereby tuning the redox potential on the transition metal center.[8] This ability of tuning redox potential makes polyanion chemistry unique when compared to pure oxides. Another feature of this polyanion chemistry is the propensity of forming a wide variety of 2-dimensional (2-D) and 3-dimensional (3-D) structures through different types of connectivity between the polyanion and the transition metals.[9] These structures are stabilized under different synthetic conditions as employed by chemists.[10]

In this context various compounds of transition metals have been synthesized incorporating PO_4^{3-},[7, 11] SO_4^{2-},[12-14] SiO_4^{4-},[15, 16] BO_3^{3-},[17, 18] mixed PO_4^{3-}- CO_3^{2-},[19, 20] etc. Among the various newly discovered polyanion cathodes,

Triplite, $LiFeSO_4F$ (3.9 V) is emerging as a strong contender of cathode for Li-ion battery,[21] challenging the most outstanding polyanion cathode, Olivine $LiFePO_4$.[11]

Despite the enormous efforts devoted towards polyanion compounds for their electrochemical properties, phosphite-based compounds received little or no attention. The only example was that of Rojo *et al*. showing very small electrochemical activity in $Li_{1.43}[Fe_{4.43}^{II}Fe_{0.57}^{III}(HPO_3)_6]1.5H_2O$ with a specific capacity of 12 $mAh.g^{-1}$.[22] Recently we have shown that a new phosphite polyanion based material, $Li_3Fe_2(HPO_3)_3Cl$, is electrochemically active with a practical specific capacity of 70 $mAh.g^{-1}$ (theoretically 131.4 $mAh.g^{-1}$) and an average discharge voltage above 3.0V.[23] The relatively high voltage observed for this compound can be assigned to the inductive effects of the phosphite and chloride groups coordinated to the iron center.

With the above encouraging results we have focused more on the synthesis and electrochemical activity of other possible phosphite-based compounds of iron. In this article we report for the first time the synthesis and structural details of a new lithium iron(III) phosphite, $LiFe(HPO_3)_2$ and demonstrate its activity towards reversible intercalation of Li^+ ions. This new phase has a theoretical capacity 120.3 $mAh.g^{-1}$ and exhibits extremely good capacity retention upon successive cycling.

EXPERIMENTAL SECTION

Materials. γ-Fe_2O_3 (99+% metal basis) was purchased from Alfa Aesar, $LiOH{\cdot}H_2O$ (98% reagent grade) and H_3PO_3 (98% extra pure) are obtained from Acros Organics. All the chemicals were used as received without further purification.

Synthesis. 0.80 g of γ-Fe_2O_3 (5 mmol), 0.94 g of $LiOH{\cdot}H_2O$ (23 mmol) and 2.46 g of H_3PO_3 (30 mmol) were mixed and ground in an agate mortar pestle and the resulting high viscosity paste was then transferred to a Teflon cup. The cup was then closed with a Teflon cap, placed in a stainless steel Paar reaction vessel and heated for 7 days in an oven at 150 °C. After removal from the oven, the reaction vessel was allowed to cool down to room temperature and the product, which

composed of uniform small clear crystals, was washed with hot water followed by filtration to remove the unreacted reagents and dried overnight in open air.

Single-Crystal X-ray Diffraction. Crystal structure of $LiFe(HPO_3)_2$ was solved from single-crystal intensity data sets collected on a Bruker Smart Apex diffractometer with monochromated Mo Kα radiation (λ = 0.7107 Å). A suitable crystal was selected and mounted on a glass fiber using epoxy-based glue. The data were collected using SMART[24] software at 298 K employing a scan of 0.3° in ω with an exposure time of 10 s/frame. The cell refinement and data reduction were carried out with SAINT,[25] while the program SADABS[25] was used for the absorption correction. The structure was solved by direct methods using SHELX-97[26] and difference Fourier syntheses. Full-matrix least-squares refinement against $|F^2|$ was carried out using the SHELXTL-PLUS[26] suit of programs. The structure of $LiFe(HPO_3)_2$ was solved in tetragonal system in a non-centrosymmetric space group, $\boldsymbol{I\,\bar{4}\,2\,d}$. The electron densities of Fe, P and O atoms were located from Fourier difference maps and refined isotropically. Subsequently, electron density for the Li^+ ion appeared at a distance of 2 Å from the oxygen atoms. An anisotropic refinement performed on the located atoms revealed one more electron density peak, approximately 1.2 Å away from the phosphorous atom. The latter has been assigned as the phosphite hydrogen and subsequently refined isotropically after adding soft constrains to fix P – H bond distance close to the theoretical value. Details of the final refinement and crystallographic information for $LiFe(HPO_3)_2$ is provided in Table 1.

The fractional atomic coordinates along with the isotropic thermal displacement parameters are given in Table 2. Selected inter-atomic distances are listed in Table 3.

Powder X-ray Diffraction: For assessing the sample purity powder XRD pattern of the as synthesized product was collected on a PANalytical X'Pert Pro diffractometer equipped with a Cu $\mathbf{K}_{\boldsymbol{\alpha_{1,2}}}$ anode and a linear array PIXcel detector over a 2θ range of 5 to 90° with an average scanning rate of 0.025° sec^{-1}. The acquired pattern was then subjected to quantitative phase analysis via the Rietveld

method using the single-crystal structure solution as the starting model for $LiFe(HPO_3)_2$ to calculate the amount of impurity phase(s).

Table 1. Crystal data and structure refinement parameters for $LiFe(HPO_3)_2$

Empirical formula	$LiFe(HPO_3)_2$	Z	8
Formula weight	222.75 $g.mol^{-1}$	ρcalc	2.644 $g.cm^{-3}$
Crystal system	Tetragonal	F(000)	872
Space group	$I\bar{4}2d$	Temperature	298(2) K
a	10.593(6) Å	GOF on F^2	1.159
b	10.593(6) Å	R [I>2σ(I)]	R1 = 0.0250
c	9.971(4) Å		wR2 = 0.0675
α = β = γ	90 °	R [all data]	R1 = 0.0259
V	1119.0(3) $Å^3$		wR2 = 0.0679

Mössbauer Spectroscopy. 75 mg of the as prepared sample was mounted on a Pb sample holder and subjected to analysis by ^{57}Fe Mössbauer spectroscopy at room temperature using a constant acceleration spectrometer in transmission geometry. The spectrometer was equipped with a ^{57}Co (50 mCi) gamma-ray source embedded in Rh matrix and calibrated for isomer shift with respect to a standard α-Fe foil at room temperature. The collected experimental data were fitted to Lorentzian function using the Recoil software.[27]

Table 2. Atomic coordinates and equivalent isotropic displacement parameters of the atoms. U_{eq} = 1/3rd of the trace of the orthogonalized U tensor

Atom	Wyckoff	Site	Occ.	x/a	y/b	z/c	U_{eq} [$Å^2$]
Fe1	8d	.2.	1	0.2819(1)	0.2500	0.1250	0.008(1)
P1	16e	1	1	0.4463(1)	0.2511(1)	0.4013(1)	0.011(1)
O1	16e	1	1	0.3444(2)	0.1902(2)	0.4886(2)	0.014(1)
O2	16e	1	1	0.4259(2)	0.2121(2)	0.2543(2)	0.013(1)
O3	16e	1	1	0.5774(2)	0.2164(3)	0.4483(2)	0.015(1)
Li1	8d	.2.	1	0.5627(8)	0.2500	0.1250	0.024(2)
H1	16e	1	1	0.4440(4)	0.3736(2)	0.4090(4)	0.007(1)

Thermo-Gravimetric Analysis (TGA). TGA has been done on about 15 mg of manually separated crystals of pure $LiFe(HPO_3)_2$ using a TA instrument

Q50 TGA in a temperature range of 25 to 800 °C with a scan rate of 10 °C.min^{-1} under nitrogen flow.

IR Spectroscopy. The IR spectrum was collected using Thermo Nicolet Nexus 470 FT-IR spectrometer over 500 – 4000 cm^{-1} on manually separated pure sample embedded in KBr pellet.

Table 3. Selected Bond lengths for $LiFe(HPO_3)_2$[a]

Bonds	Distances (Å)	Bonds	Distances (Å)
Fe1 – O3 x2[#1]	1.969(2)	P1 – O3	1.511(2)
Fe1 – O1 x2[#2,#3]	2.010(3)	P1 – H1	1.299(2)
Fe1 – O2 x2[#4,#5]	2.037(2)	Li1 – O1 x 2[#8]	2.026(6)
P1 – O1	1.529(3)	Li1 – O2 x 2 [#6.#7]	1.982(7)
P1 – O2	1.539(2)		

[a] [#1] x + 0, - y + 1/2, - z + 1/4; [#2] - y, x, - z; [#3] – y + 0, - x + 1/2, z + 1/4; [#4] y + 1/2, - x + 1/2, - z + 1/2; [#5] y + 1/2, x, z - 1/4; [#6] – y + 1/2, x - 1/2, - z + 1/2; [#7] – y + 1/2, - x, z - 1/4; [#8] x + 0, - y - 1/2, - z + ¼

Electrochemical Testing. For electrochemical studies of $LiFe(HPO_3)_2$, a cathode film was prepared. In this regard the active material, $LiFe(HPO_3)_2$, was first milled with super P conductive carbon vigorously in a SPEX 8000 miller for 2 h followed by addition of Poly-vinylidene fluoride (PVDF) as binder dissolved in N-Methyl-2-pyrrolidone (NMP). The resulting mixture was further ball milled for 20 min until a homogeneous, viscous slurry was obtained. The ratio of the active material, conducting carbon, and the binder in cathode mix was 65:25:10. The cathode mix was then spread as a film of uniform thickness onto a flat sheet of aluminum current collector with a glass rod and dried in a vacuum oven for 12 h at 80 °C. The milled cathode mix was also tested for structural stability by powder X-ray diffraction and the XRD pattern clearly showed the retention of the crystal structure during the cathode mix preparation (supporting information, Figure S1). The SEM images of the pulverized (ball-milled) sample mixed with carbon after 2 h milling are presented in the supporting information (Figure S2). The sizes of the particles as estimated from the SEM images range from submicron particulates to particles of several micron in diameters. However, the size distribution of the majority of particles is approximately in the range 2 - 5 μm in diameter.

For electrochemical tests, CR2032 type coin cells were fabricated using the above composite cathode film cut into circular disks (3/8 inch diameter) with 5.0 – 6.0 mg of active material loading. The cells were assembled in an argon filled glove box with oxygen concentration below 2.0 ppm. The cathode disk and Li anode (0.75 mm thickness Li ribbon cut into circular disk) were mounted in the cell using a Celgard® 2325 circular sheet placed between the two electrodes as the separator. The electrolyte, 1 M solution of $LiPF_6$ in DMC-EC (1:1) was then added and the cell was sealed with a coin cell crimper. The prepared cells were aged for equilibration for several hours before electrochemical testing.

Cyclic voltammograms were obtained using a PAR EG&G potentiostat/galvanostat model 273 in the potential range of 2.0 – 4.0 V (vs. $Li^+\backslash Li$) with a scan rate of 0.05 $mV.sec^{-1}$. Voltage-composition profiles were obtained using galvanostatic charge-discharge experiments on an Arbin Instruments battery tester, model BT2043, in the potential range 2.0 – 4.0 V with a constant current charge and discharge modes at various C-rates.

RESULTS AND DISCUSSION

Synthesis. The initial ratio of the reactants had a crucial role on the percentage yield of the major product and identity of the by-products formed in this reaction. It has been found that the highest purity of $LiFe(HPO_3)_2$ could be obtained when Fe_2O_3:$LiOH{\cdot}H_2O$:H_3PO_3 were mixed in 1:4:6 molar ratio, with $Fe_2(HPO_3)_3$ as the only major impurity phase. Ratios of acid to base greater than the above increases the $Fe_2(HPO_3)_3$ mass fraction in the final product while smaller ratios yield an unknown impurity phase (supporting information, Figure S3). A quantitative phase analysis via Rietveld refinement performed on the reaction products obtained under optimized conditions revealed that the product contained 85% $LiFe(HPO_3)_2$ and 15% $Fe_2(HPO_3)_3$ by mass, as demonstrated in Figure 1.

It is to be noted here that *ex-situ* time-dependent PXRD evolution of the reaction product(s) indicated that the optimized synthesis of 85% $LiFe(HPO_3)_2$ and 15% $Fe_2(HPO_3)_3$ can be achieved in 72 hours. In fact, $LiFe(HPO_3)_2$ as the major product can be formed during the first 6 hours of the synthesis, further heating was

required to remove/reduce the intensity of impurity peaks (supporting information, Figure S4) . However, 7 days of reaction was required to grow crystals suitable for single-crystal X-ray diffraction. Since the identity of the impurity phase was known, this sample was used for electrochemical studies rather than the one with unknown impurities (Figure S3).

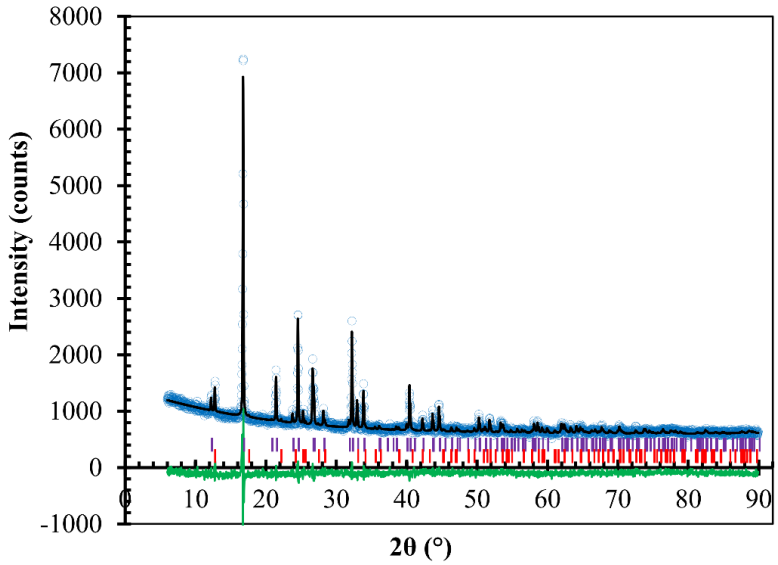

Figure 1. Rietveld refinement on the powder XRD of the as-synthesized product. Open circles: observed intensity; black line: calculated intensity; green line: difference curve; diffraction position indicator: $LiFe(HPO_3)_2$- purple tick mark; $Fe_2(HPO_3)_3$- red tick mark.

Crystal Structural Description. $LiFe(HPO_3)_2$ is a three-dimensional open-framework structure made from vertex-shared FeO_6 octahedra and HPO_3 pseudo-pyramidal units incorporating Li-ions within its channels. The structure of $LiFe(HPO_3)_2$ is isostructural to a recently published vanadium analogue, $LiV(HPO_3)_2$.[28] The asymmetric unit of $LiFe(HPO_3)_2$ contains 6 non hydrogen atoms and 1 hydrogen atom (Figure 2a). There is one crystallographically distinct iron center, located at the special position, 8*d*, and adopts an octahedral coordination with oxygen atoms from phosphite groups. The Fe – O distances fall in the range 1.969(2) – 2.037(2) Å which agree well with the reported Fe^{3+}– O bond lengths.[29]

The phosphorous of the phosphite group is in +3 oxidation state and bonded to 3 oxygen atoms and 1 hydrogen atom in a distorted tetrahedral (or pseudo-pyramidal) unit.

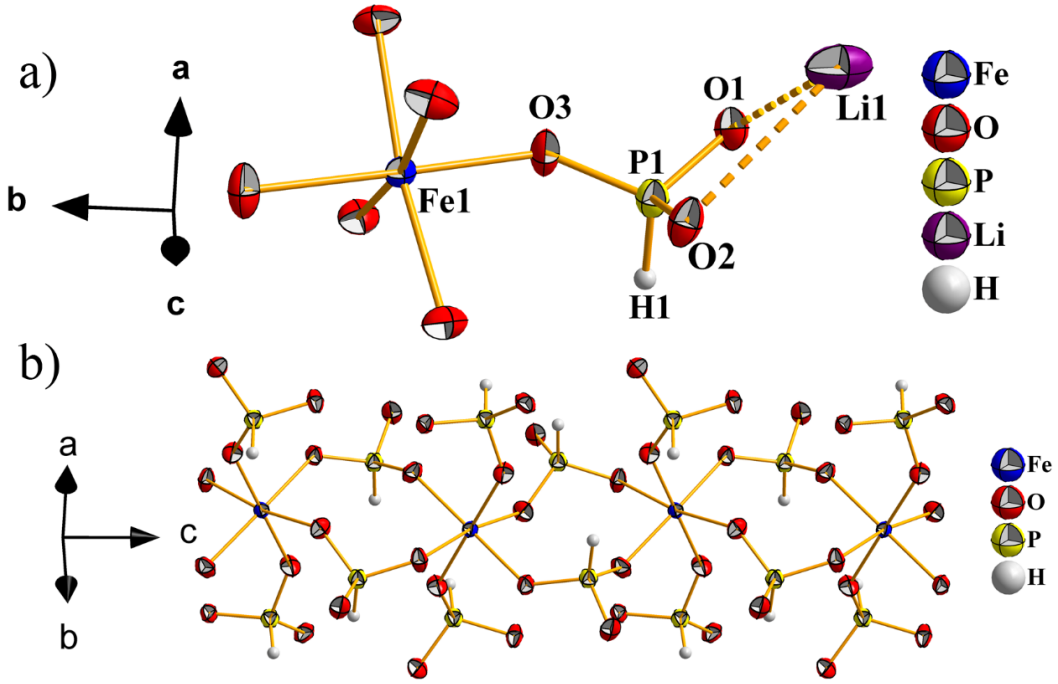

Figure 2. Connectivity pattern and coordination spheres of atoms in $LiFe(HPO_3)_2$ as obtained from single-crystal X-ray structure solution. Thermal ellipsoids are given at 80% probability. Only atoms present in the asymmetric unit are labelled (a); connectivity pattern of FeO_6 and HPO_3 units along the *c*-axis (b).

The P – O distances are in the range 1.511(2) – 1.539(2) Å and the P – H bond length is 1.29(4) Å (constrained), all corroborating well with the reported values for P – O and P – H distances in many reported metal phosphites.[22, 29, 30] The Li atom is located in the special position, 8*d*, and is coordinated by 4 oxygen atoms (from two crystallographically distinct O atoms) in an irregular non-planar geometry with Li1 – O1 and Li1 – O2 bond lengths of 2.026(6) and 1.982(7) Å, respectively. The results of the bond valence sum calculations (BVS)[31] for Fe1 (BVS = 3.09) and P1 (BVS = 3.97, disregarding hydrogen) confirms the oxidation states Fe and P as 3+. It is to be noted that the proof of oxidation state of +3 for P in phosphite group from BVS value is indirect, because of the lack of reliable bond valence parameters for pure P(III) – O bonds.[32] The BVS calculation actually

represents the oxidation state of $(PH)^{4+}$ group rather than P in HPO_3 moiety as also noted by Rojo *et al.* in an iron phosphite compound.[29]

Each Fe atom makes six Fe – O – P linkages and similarly each P atom makes three P – O – Fe linkages. Thus the crystal structure is composed of strictly alternating FeO_6 octahedra and HPO_3 units sharing vertices. The vertex linking polyhedra form 4-membered rings (connecting only P and Fe atoms) through the two bridging HPO_3 units between the two FeO_6 octahedra, these four membered rings are further corner-shared along the *c*-axis to form a chain (Figure 2b). These chains are further connected through HPO_3 units laterally along *a*- and *b*-axes, creating interconnected channels in all three crystallographic directions (Figure 3).

Two types of channels are formed when viewed along the *a*- or *b*-axes. Li^+ ions can be seen occupying the slightly elongated zig-zag channels while the straight hexagonal-shaped channels are left empty. On the other hand, channels along the *c*-axis are also empty and have larger diameter formed by 8-membered ring and the hydrogen atoms of the phosphite moiety are protruding into the channel. It is to be noted here that Li-ions prefer the channels where inner walls are exclusively built by oxygen atoms.

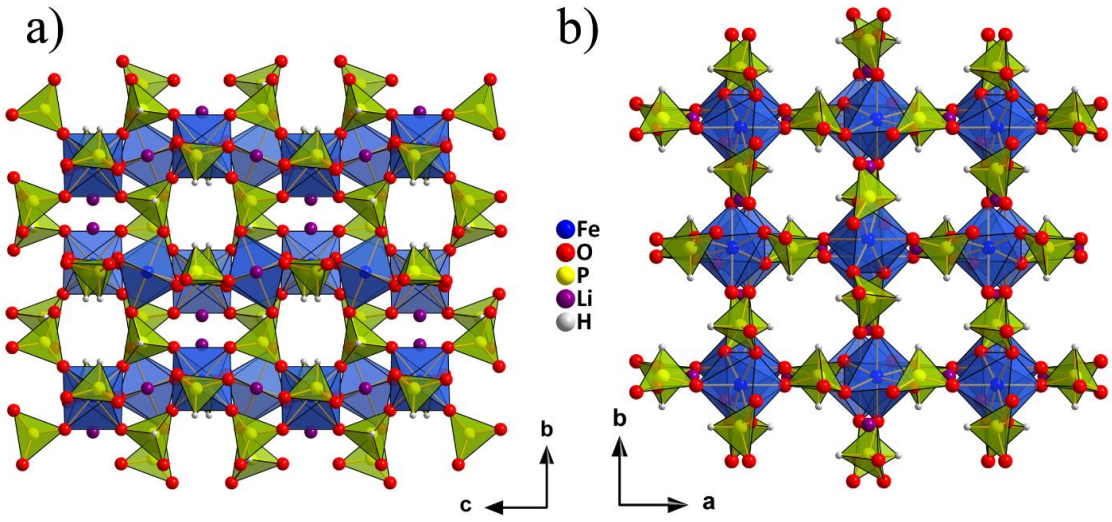

Figure 3. Perspective view of the packing diagram of the crystal structure of $LiFe(HPO_3)_2$ as viewed along the *a*-axis (a) and *c*-axis (b). Blue: FeO_6 octahedra; Green: HPO_3 pseudo pyramidal units.

Thermogravimetric and Spectroscopic Characterization. The TGA plot of the pure sample exhibits an initial mass loss of 0.15% up to a temperature of 300 °C, which can be assigned to the removal of adsorbed moisture (Figure 4). The structure remains stable up to 320 °C, after which it loses 3 % of its mass, indicating the decomposition of the delicate HPO_3 groups. As the temperature increases from 450 to 800 °C a considerable mass gain can be observed, which can be assigned to the oxidation of P(III) to P(V) to form a phosphate or pyrophosphate as a result of oxygen impurity in the N_2 purge gas, similar to other phosphite based materials reported in the literature.[22, 33]

Figure 5 depicts the FT-IR spectrum of $LiFe(HPO_3)_2$. The spectrum is composed of the signature sharp P–H stretching mode at 2450 cm^{-1} and the P – O stretching modes prevailing in the region 900 –1100 cm^{-1} overlapping with the bending vibrations of P – H bond.[22] The low frequency part of the spectrum shows moderate absorption peaks assigned to the bending modes of P – O bonds. The absence of strong absorption peaks in the 3200 – 3500 cm^{-1} region indicates that the P – H bond is preserved during the synthesis and there is no sign of oxidation of P – H bond to P–O–H.

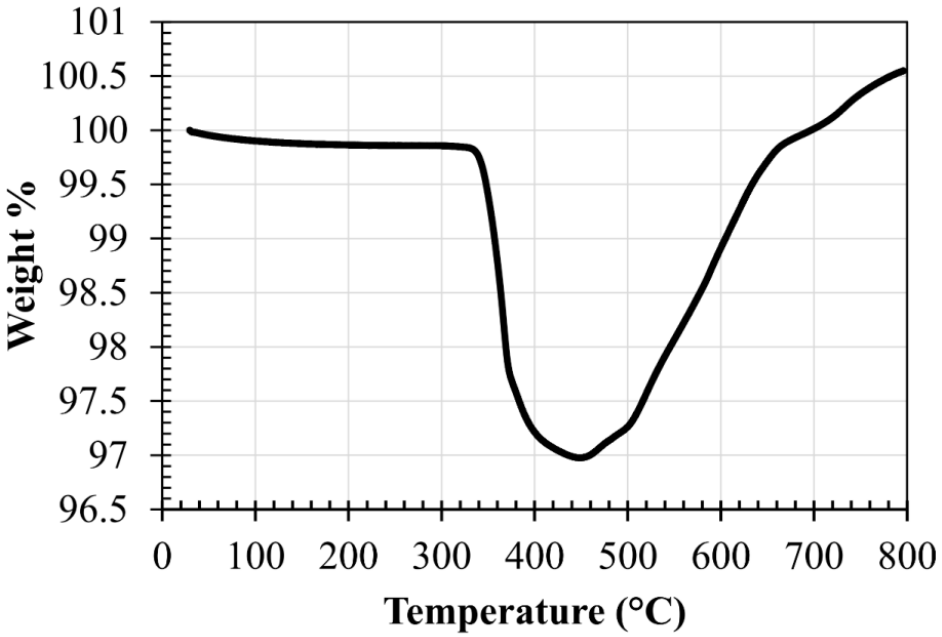

Figure 4. TGA curve for $LiFe(HPO_3)_2$.

The Mössbauer spectrum of the as-synthesized product is given in Figure 6 and the isomer shift (IS) and quadrupole splitting (QS) parameters derived from the curve fitting are given in Table 4. The observed spectrum has been fitted with two quadrupolar doublets, consistent with the results of powder XRD, with each doublet representing one crystallographically distinct Fe(III) in octahedral coordination as in $LiFe(HPO_3)_2$ and $Fe_2(HPO_3)_3$, respectively.

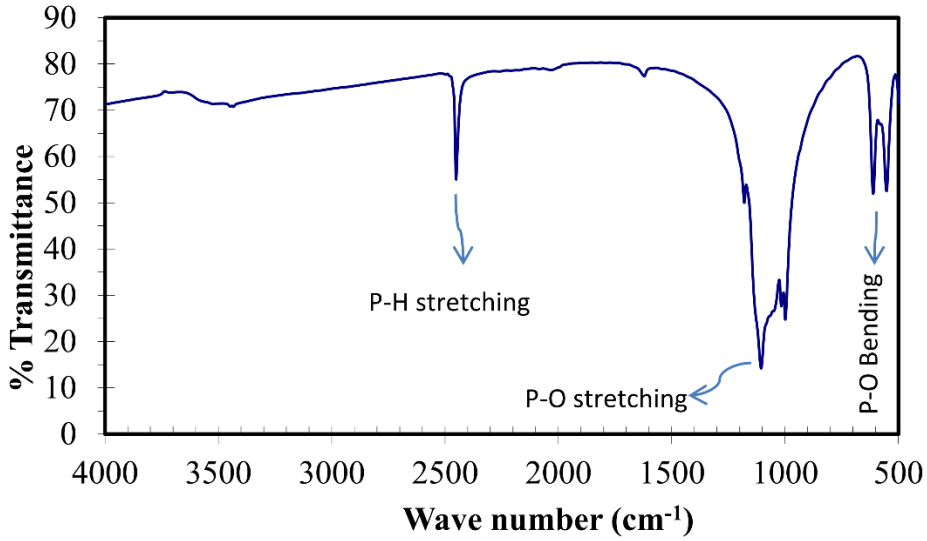

Figure 5. FT-IR spectrum of $LiFe(HPO_3)_2$.

Site population analysis as obtained through the Lorentzian fit suggests that $LiFe(HPO_3)_2$ and $Fe_2(HPO_3)_3$ each contributes 87 and 13% to the area, respectively, corroborating well with the quantitative phase analysis results achieved via powder XRD refinement. The IS values are consistent with Fe(III) ions in octahedral coordination.[34] The Mössbauer spectrum also rules out the existence of other iron containing impurity species as evident from the spectra collected over the velocity range from -8.5 to +8.5 $mm.s^{-1}$.

Electrochemistry. To evaluate the basic electrochemical properties of the prepared composite cathode, cyclic voltammetry (CV) tests were performed on the coin-cells (Figure 7) which demonstrate that the phase is active with respect to Li intercalation/deintercalation. The cell exhibits an initial open circuit potential of 3.1 V upon scanning to the potential of 2.0 V. The reductive lithiation peak for

$LiFe(HPO_3)_2$ appears at 2.71 V with a weak shoulder at 2.5 assigned to the reduction of $Fe_2(HPO_3)_3$ phase. On reversing the scan toward 4.0 V the corresponding oxidative delithiation peak can be observed at 3.22 V.

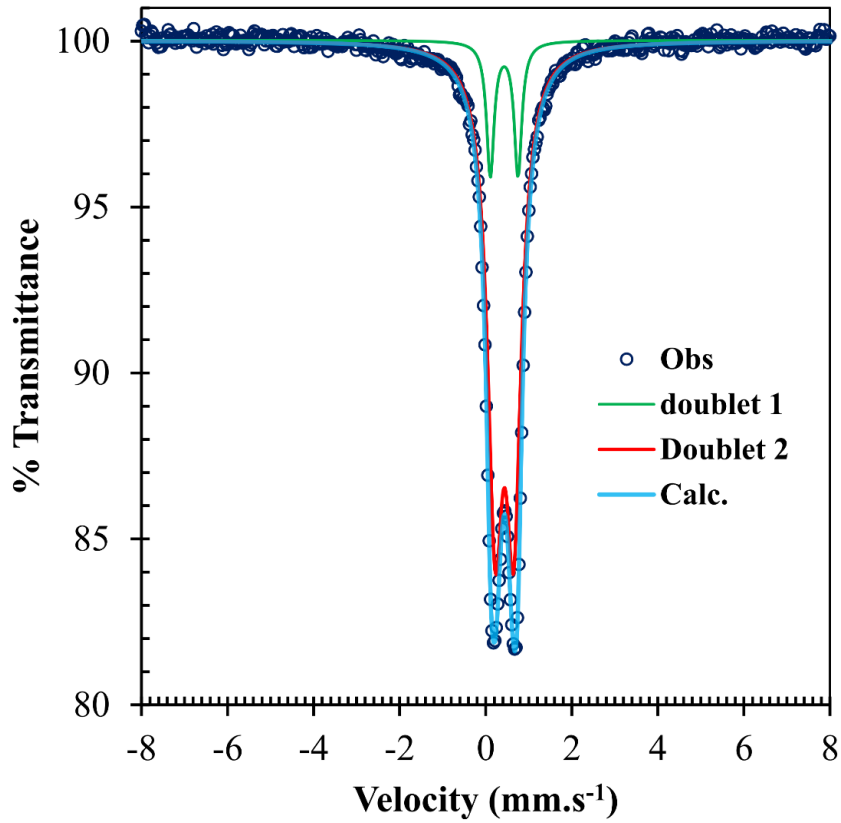

Figure 6. Mössbauer spectrum of the as-synthesized product, $LiFe(HPO_3)_2$ (85%) and $Fe_2(HPO_3)_3$ (15%).

Table 4. Lorentzian deconvolution fit parameters of the Mössbauer spectrum

	IS ($mm.s^{-1}$)	QS ($mm.s^{-1}$)	Site population
Doublet 1	0.429 (2)	0.644(2)	12.9(7)
Doublet 2	0.434(6)	0.431(1)	87.1(7)

Repeating the cycling shows two obvious events: firstly, a shift in the $LiFe(HPO_3)_2$ reduction peak toward more positive direction (2.86 V), indicating an increase in the cell discharge potential; and secondly, decrease in $Fe_2(HPO_3)_3$ phase reduction current. Additional cycling reveals that the position of oxidation

and reduction peaks for $LiFe(HPO_3)_2$ do not shift anymore and the magnitude of the cathodic and anodic currents at the peak potentials is very reproducible, evidencing the high reversibility of the redox process.

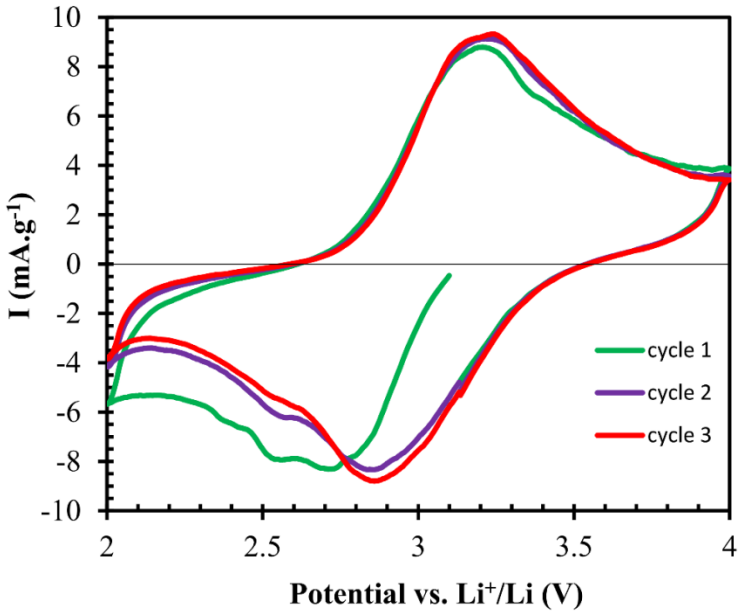

Figure 7. Cyclic voltammograms of the composite cathode with respect to Li^+/Li. Cathodic current is negative.

The galvanostatic charge discharge curves at C/50 rate for the $LiFe(HPO_3)_2$ phase at room temperature and 40 °C are shown in Figure 8. In order to assess the contribution of the $Fe_2(HPO_3)_3$ impurity phase toward the total discharge capacity, coin cells of pure $Fe_2(HPO_3)_3$ phase was fabricated in the same manner and the specific discharge capacity was found to be negligible and also rapidly decaying with cycling. Therefore, the observed specific capacity can be assigned to the active $LiFe(HPO_3)_2$ phase reliably, *albeit* corrections were made to account for the inactive/less-active mass of the $Fe_2(HPO_3)_3$ phase in the composite cathode mix.

As the iron center in $LiFe(HPO_3)_2$ is in +3 oxidation state, the as-fabricated cells are already in charged state. The cells were initially subjected to discharge by reductive lithiation at room temperature (dotted lines) shows sloppy voltage profiles, indicating solid-solution formation between the oxidized and reduced phases. At this condition the discharge terminates after insertion of 0.3 Li^+ ion per

formula unit (36 mAh.g^{-1}). Repeating the test at 40 °C, however, shows considerable improvement in capacity achievement with intercalation of 0.6 Li^+ ion per formula unit (72 mAh.g^{-1}), revealing the existence of polarization effects which can be thermally activated. Such findings suggest that the limited achievable capacity may be due to the poor electronic and/or ionic conductivity of the material which can be improved by reducing the particle size and applying more efficient carbon coating procedures.

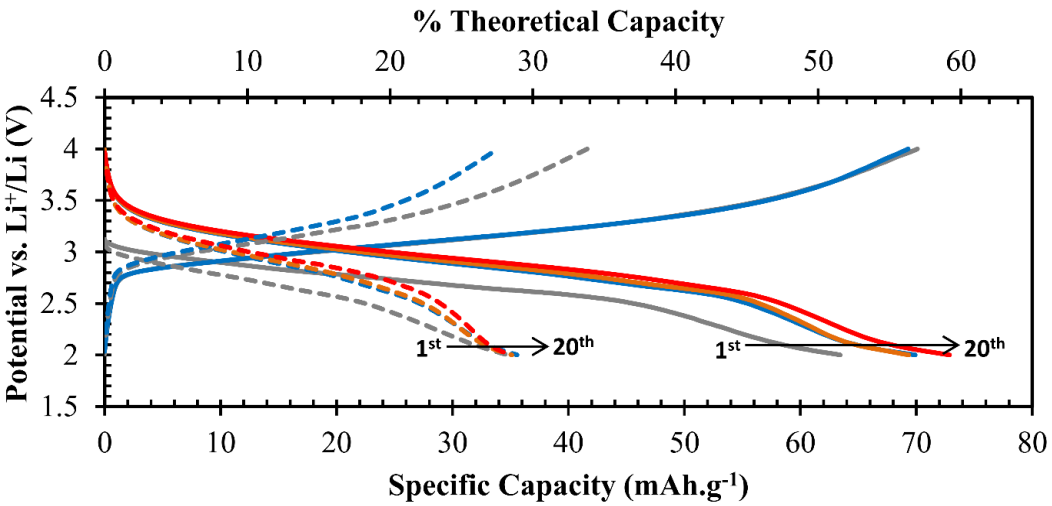

Figure 8. The C/50 voltage-composition profiles of $LiFe(HPO_3)_2$. Dotted line: Room temperature; solid line: 40 °C; gray: 1st, blue: 2nd; orange: 3rd and red: 20th cycles.

The first discharge curve for both room temperature and 40 °C cycled cells starts from the open circuit potential, 3.1 V, while for the subsequent cycles the discharge starts at a higher potential of 3.4 V *vs.* Li^+/Li redox couple, in agreement with the cyclic voltammetry results. In addition, Li^+ intercalation for $LiFe(HPO_3)_2$ during the discharge occurs at an average potential of 2.82 V which stands higher than some phosphate based materials, e.g. fluoro tavorite $LiFePO_4F$.[35, 36]

Despite the limited capacity achievement, $LiFe(HPO_3)_2$ exhibit outstanding capacity retention when cycled at different C-rates for prolonged amounts of time (Figure 9). The cell cycled at 40 °C exhibits a steady specific capacity of about 70 mAh.g^{-1} during the first 5 cycles at C/50. Increasing the C-rate to C/20 causes a

corresponding decrease in the specific capacity by 15 mAh.g^{-1}. Further increase in discharge rate to C/10 and C/5 reduces the specific capacity to 50 and 43 mAh.g^{-1}, respectively. However, returning the discharge rate back to C/50 recovers the original value of 70 mAh.g^{-1}, indicating that the drop in capacity at higher C-rates is reversible and associated with different polarization mechanism inside the cell.

As expected the cell cycled at 40 °C shows higher specific capacity for all C-rates, but for both systems virtually no capacity fading can be detected even after 200 cycles. These results indicate the stability of $LiFe(HPO_3)_2$ crystal structure and the reversible nature of Li^+ ion intercalation. The retention of the structural integrity after electrochemical cycling has been confirmed by ex-situ XRD of the reduced cathode material retrieved after breaking the button cell (supporting information, Figure S5).

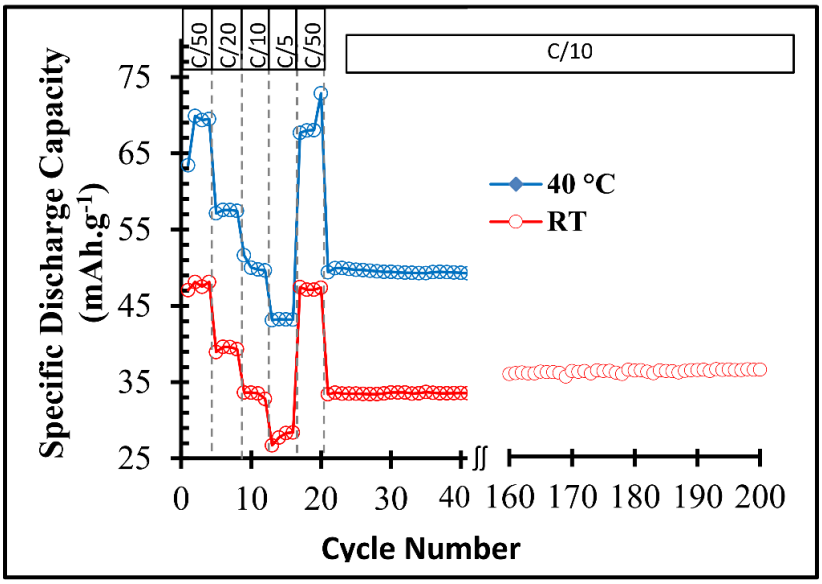

Figure 9. Capacity retention at various C-rates for $LiFe(HPO_3)_2$ cathode.

However, it was not possible to refine the powder pattern or locate the position of the inserted Li-ion due to the poor quality of the diffraction data. The excellent capacity retention may be related to the 3-dimensional interconnected channels of the crystal structure. It is well-known that cathode materials where Li^+ diffusion is restricted to 1-D channels, for example, in Olivine $LiMPO_4$ (M = Fe

and Mn), are susceptible to blockage of Li^+ diffusion path due to defects and impurities.[37] This blockage eventually causes capacity fading and reduced cycle-life. This problem is less likely to occur in materials with 3-D interconnected network of ionic diffusion paths and thus capable of showing good cycling stability as in the case of Tavorite.[38]

CONCLUSIONS

In this article we demonstrated that a novel phosphite with iron, the most abundant and environmentally benign transition metal, $LiFe(HPO_3)_2$, can be synthesized in a solvent-less low temperature synthesis route. The phase has been shown to be electrochemically active for reversible intercalation of Li^+ ions, with an average discharge voltage of 2.8 V and an experimental capacity of about 70 $mAh.g^{-1}$ has been achieved at 40 °C. Simple synthesis, low cost materials and excellent capacity retention of this phase may find applications where energy density is not a concern.

ACKNOWLEDGMENT

The authors acknowledge the funding from Materials Research Centre (Missouri S&T) and University of Missouri Research Board. The authors are also grateful to Professors Nick Leventis and Pericles Stavropoulos for the donation of a potentiostat and a glovebox, respectively.

ASSOCIATED CONTENT

Supporting Information

X-ray crystallographic data for compound, $LiFe(HPO_3)_2$, in CIF format, PXRD patterns of (i) ball-milled sample with carbon, (ii) sample with the unknown impurity, (iii) discharged cathode (reductively lithiated) and (iv) time-dependent evolution of synthesis products as well as the SEM images of ball milled sample are available free of charge via the Internet at http://pubs.acs.org.

AUTHOR INFORMATION

To whom correspondence should be addressed.

E-mail: choudhurya@mst.edu

REFERENCES

(1) Whittingham, M. S. *Chem. Rev.* **2004**, *104*, 4271 - 4302.

(2) Armand, M.; Tarascon, J. -M. *Nature*, **2008**, *451*, 652 - 657.

(3) Dunn, B.; Kamath, H.; Tarascon, J. -M. *Science*, **2011**, *334*, 928 - 935.

(4) Larcher, D.; Tarascon, J. -M. *Nature Chem.*, **2014**, *7*, 19 - 29.

(5) Yang, Z.; Zhang, J.; Kintner-Meyer, M. C. W.; Lu, X.; Choi, D.; Lemmon, J. P.; Liu, J. *Chem. Rev.* **2011**, *111*, 3577 - 3613.

(6) Ellis, B.; Lee, K. T.; Nazar, L. F. *Chem. Mater.*, **2010**, *22*, 691 - 714.

(7) Masquelier, C.; Croguennec, L. *Chem. Rev.*, **2013**, *113*, 6552 - 6591.

(8) Padhi, A. K.; Manivannan, V.; Goodenough, J. B. *J. Electrochem. Soc.*, **1998**, *145*, 1518 - 1520.

(9) Murugavel, R.; Choudhury, A.; Walawalkar, M. G.; Pothiraja, R.; Rao, C. N. R. *Chem. Rev.* **2008**, *108*, 3549 - 3655.

(10) Tarascon, J. -M.; Recham, N.; Armand, M.; Chotard, J.-N. ; Barpanda, P.; Walker, W.; Dupont, L. *Chem. Mater.*, **2010**, *22*, 724 - 739.

(11) Padhi, A. K.; Nanjundaswamy, K. S.; Goodenough, J. B. *J. Electrochem. Soc.*, **1997**, *144*, 1188 - 1194.

(12) Anji Reddy, M.; Pralong, V.; Caignaert, V.; Varadaraju, U. V.; Raveau, B. *Electrochem. Commun.*, **2009**, *11*, 1807 - 1810.

(13) Recham, N.; Chotard, J. -N.; Dupont, L.; Delacourt, C.; Walker, W.; Armand, M.; Tarascon, J. –M. *Nature Mater.*, **2010**, *9*, 68 - 74.

(14) Rousse, G.; Tarascon, J. -M. *Chem. Mater.*, **2014**, *26*, 394 - 406.

(15) Nytén, A.; Abouimrane, A.; Armand, M.; Gustafsson, T.; Thomas, J. O. *Electrochem. Commun.* **2005**, *7*, 156 - 160.

(16) Islam, M. S.; Dominko, R.; Masquelier, C.; Sirisopanaporn, C.; Armstrong, A. R.; Bruce, P. G. *J. Mater. Chem.*, **2011**, *21*, 9811 - 9818.

(17) Legagneur, V.; An, Y.; Mosbah, A.; Portal, R.; Le Gal La Salle, A.; Verbaere, A.; Guyomard, D.; Piffard, Y. *Solid State Ionics*, **2001**, *139*, 37 - 46.

(18) Yamada, A.; Iwane, N.; Harada, Y.; Nishimura, Sh.-I; Koyama, Y.; Tanaka, I. *Adv. Mater.*, **2010**, *22*, 3583 - 3587.

(19) Chen, H.; Hautier, G.; Ceder, G. *J. Am. Chem. Soc.*, **2012**, *134*, 19619 - 19627.

(20) Chen, H.; Hao, Q.; Zivkovic, O.; Hautier, G.; Du, L.; Tang, Y.; Hu, Y.; Ma, X.; Grey, C. P.; Ceder, G. *Chem. Mater.*, **2013**, *25*, 2777 - 2786.

(21) Barpanda, P.; Ati, M.; Melot, B. C.; Rousse, G.; Chotard, J. -N.; Doublet, M. -L.; Sougrati, M. T.; Corr, S. A.; Jumas, J. -C.; Tarascon, J. -M. *Nature Mater.*, **2011**, *10*, 772 - 779.

(22) Chung, U.; Mesa, J. L.; Pizarro, J. L.; de Meatza, I.; Bengoechea, M.; Fernandez, J. R.; Arriortua, M. I.; Rojo, T. *Chem. Mater.*, **2011**, *23*, 4317 - 4330.

(23) Yaghoobnejad Asl, H.; Ghosh, K.; Vidal Meza, M. P.; Choudhury, A. *J. Mater. Chem. A.* **2015**, *3*, 7488 - 7497.

(24) Bruker- SMART. Bruker AXS Inc., Madison, Wisconsin, USA. **2002**.

(25) Bruker- SAINT and SADABS. Bruker AXS Inc., Madison, Wisconsin, USA, **2008**.

(26) Sheldrick, G. M. *Acta Cryst.* **2008**, *A64*, 112 - 122.

(27) Recoil software: Lagarec, K.; Rancourt, D. G., Nucl. Instrum. Meth. *Phys. Res. B*, **1997**, *129*, 266 - 280.

(28) Huang, H. –L.; Huang, S. –H.; Lai, C. –W.; Wu, J. –R. Lii, K. –H.; Wang, S. -L., *J. Chin. Chem. Soc.* **2013**, *60*, 691 – 694.

(29) Chung, U. -C.; Mesa, J. L.; Pizarro, J. L.; Fernández, J. R.; Marcos, J. S.; Garitaonandia, J. S.; Arriortua, M. I.; Rojo, T. *Inorg. Chem.*, **2006**, *45*, 8965 - 8972.

(30) Chung, U.; Mesa, J. L.; Pizarro, J. L.; Jubera, V.; Lezama, L.; Arriortua, M. I.; Rojo, T. *J. Solid State Chem.*, **2005**, *178*, 2913 - 2921.

(31) Brown, I. D.; Altermatt, D. *Acta Crystallogr.* 1985, *B41*, 244 - 247.

(32) Loub, J. *Acta Crystallogr.* **1991**, *B47*, 468 - 473.

(33) Hamchaoui, F.; Alonzo, V.; Venegas-Yazigi, D.; Rebbah, H.; Fur, E. L. *J. Solid State Chem.* **2013**, *198*, 295 – 302.

(34) Menil, F. *J. Phys. Chem. Solids*, **1985**, *46*, 763 - 789.

(35) Ellis, B. L.; Ramesh, T. N.; Rowan-Weetaluktuk, W. N.; Ryan, D. H.; Nazar, L. F. *J. Mater. Chem.*, **2012**, *22*, 4759 - 4766.

(36) Yaghoobnejad Asl, H.; Choudhury, A. *RSC Adv.*, **2014**, *4*, 37691 - 37700.

(37) Morgan, D.; Van der Ven, A.; Ceder, G. *Electrochem. and Solid-State Lett.* **2004**, *7*, A30 - A32.

(38) Ramesh, T. N.; Lee, K. T.; Ellis, B. L.; Nazar, L. F. *Electrochem. and Solid-State Lett.* **2010**, *13*, A43 - A47.

IV. Iron Borophosphate as Potential Cathode for Lithium- and Sodium-ion Batteries

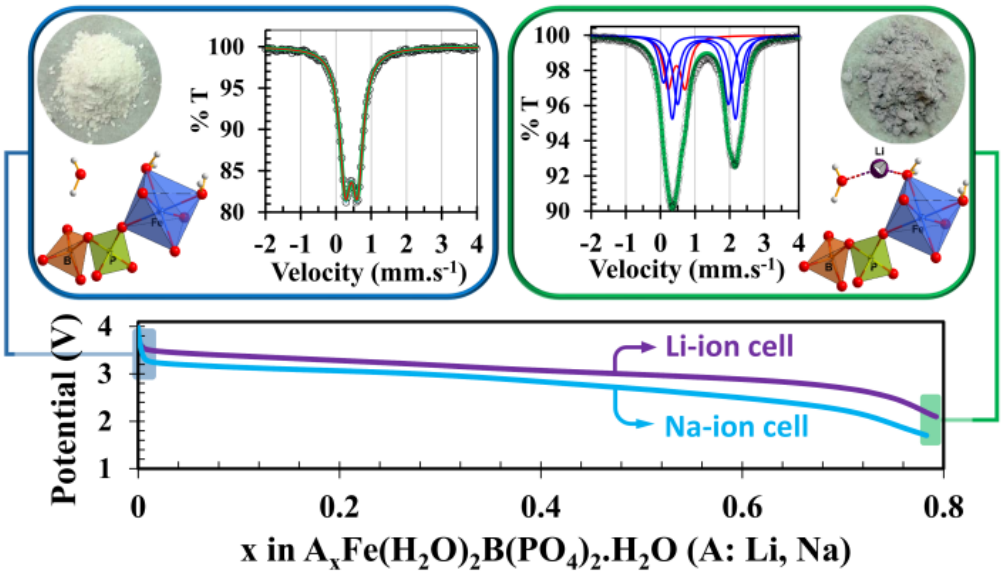

Hooman Yaghoobnejad Asl,[a] Patrick Stanley,[a, b] Kartik Ghosh,[c] and Amitava Choudhury[a,*]

[a]Department of Chemistry, Missouri University of Science and Technology, Rolla, MO 65409, USA.

[b]Department of Chemical and Biological Engineering, Missouri University of Science and Technology, Rolla, MO 65409, USA

[c]Department of Physics, Astronomy and Materials Science and Center for Applied Science and Engineering, Missouri State University, Springfield, Missouri 65897, USA.

ABSTRACT: Lithium iron borophosphate, $Li_{0.8}Fe(H_2O)_2[BP_2O_8]\cdot H2O$, with a chiral 6_5 helical channel structure has been shown to be electrochemically active as cathode for both Li- and Na-ion batteries. We report here for the first time synthesis of the illusive Li-containing iron borophosphate of a well-known structure type by employing hydrothermal synthesis route. The compound has been characterized by single-crystal X-ray diffraction, magnetic measurement and Mössbauer spectroscopy, which unequivocally prove the mixed valency of $Fe^{2+/3+}$. The compound exhibits a sloppy voltage profile reminiscent of single phase solid solution type behavior on electrochemical lithium and sodium insertion in the voltage range 2.1 – 4.0 and 1.6 – 4.0 V, respectively. The pure single phase oxidized end member $Fe(H_2O)_2[BP_2O_8]\cdot H_2O$ was synthesized by chemical de-

lithiation of the as-synthesized compound, and the structure was solved by ab-initio method followed by Rietveld refinement of the synchrotron X-ray powder diffraction data, showing a volume change of 3% with retention of the parent lattice. The oxidized phase was also characterized with magnetic and Mössbauer spectroscopy, which besides proving the 3+ oxidation state of Fe, showed long-range anti-ferromagnetic ordering. The electrochemical performance of $Li_{0.8}Fe(H_2O)_2[BP_2O_8]\cdot H_2O$ was studied with galvanostatic charge/discharge tests, cyclic voltammetry, and electrochemical impedance spectroscopy. The compound showed facile Li- and Na- (de)-insertion with an average voltage of 3.06 and 2.76 V for Li- and Na-ion cell, respectively, with almost 80% of the theoretical capacity achieved and a reasonable capacity retention was observed. The results of EIS in the fabricated cells indicated higher impedances for the Na-ion cell compared to Li-ion cell. Variable temperature EIS studies on pressed pellet of $Li_{0.8}Fe(H_2O)_2[BP_2O_8]\cdot H_2O$ showed high Li-ion conduction ($3.0x10^{-8}$ $S.cm^{-1}$ at room temperature) with low activation energy (0.20 eV/Li^+).

INTRODUCTION

Polyanion chemistry has taken a center stage in the search for new cathode materials in lithium- and sodium-ion batteries.[1] This strong surge in research activity of polyanionic materials is catalyzed by a pioneering discovery from the Goodenough group in 1997 that Olivine structure type $LiFePO_4$ can act as viable cathodes for Li-ion batteries.[2] Subsequent realization that iono-covalency of the metal-ligand bond caused by the inductive effect of the central atoms of the polyanion moiety can tune the redox potential with respect to Li^+/Li has fueled chemists to look out for polyanions beyond phosphates.[3, 4]

Thus a large number of polyanionic materials in phoshphates,[1, 2] silicates,[5, 6] sulfates,[7 - 9] and borates[10 - 11] are being investigated as viable cathodes for Li-ion batteries. We have recently shown that phosphite (HPO_3^{2-}) can also act as cathode for Li-ion batteries. [12, 13] The focus is also shifting towards Na-ion batteries as well, as limited global Li abundance may cause Li-ion batteries to become cost-prohibitive in the future.[14 - 16] Similarly, our focus from mono-polyanionic material

is shifting to mixed polyanionic materials. It was recently predicted from high throughput computation that mixed polyanionic compounds of transition metals could be attractive cathode materials for Li-ion batteries both in terms of average voltage and specific capacity.[17] Subsequently, it was shown by the Ceder group that carbono-phosphates, ($AMPO_4CO_3$, *A* = Li, Na; *M* = Fe, Mn) are indeed versatile cathodes for Li- and Na-ion batteries as predicted from the theoretical studies.[18, 19] In the same article some borophosphate composition predicted from substitutional chemistry showed very impressive computed Li-ion battery property.[17] Encouraged by this finding we wanted to explore borophosphate family in search of a suitable cathode for Li- and Na-ion batteries. The chemistry of borophosphate is very rich, because of the ability of the borate and phosphate unit to polymerize through P – O – B linkages to form a large variety of oligomeric species.[20, 21] Borophosphates have already been touted for several potential applications in optical materials[22 - 24] and catalysis because of their propensity to form non-centrosymmetric and zeolitic structure, [25-27] respectively. However, borophosphates as potential cathode materials for Li-ion batteries have not been tested so far. Towards this goal we have synthesized and structurally characterized a new mixed valent iron borophosphate composition, $Li_{0.8}Fe(H_2O)_2[BP_2O_8]\cdot H_2O$, which is electrochemically active with respect to both Li- and Na-ion (de)insertion with high reversibility at an average voltage of 3.06 and 2.76 V, with respect to Li^+/Li and Na^+/Na, respectively. During the preparation of this manuscript we have noticed a paper showing electrochemical activity in the already known phases, $(NH_4)_{0.75}Fe(H_2O)_2[BP_2O_8]\cdot 0.25H_2O$[28] and $NaFe(H_2O)_2[BP_2O_8]\cdot H_2O$[29] as cathode in Na-ion battery.[30] The framework structure of the reported ammonium- and sodium phases and the current Li-phase is same, only difference exists in the handedness of the helical channels. This class of compounds has been found to crystallize in both the enantiomorphic space groups, $P6_122$ or $P6_522$ and $P6_1$ or $P6_5$.[25, 28, 31, 32] Though the crystal structure belongs to a well-known structure-type, $M^IM^{II}(H_2O)_2[BP_2O_8]\cdot H_2O$ (M^I = Na, K; M^{II} = Mg, Mn, Fe, Co, Ni, Zn), first reported by Kniep et al.[25] and later by others,[28, 29, 31 - 41] the combination of Li-Fe in this structure type was not reported until now. Successful synthesis of the Li-phase

has direct relevance to the Li-ion battery study, since it enables direct chemical and electrochemical Li-extraction. Herein we report the synthesis, structure solution of $Li_{0.8}Fe(H_2O)_2[BP_2O_8]\cdot H_2O$ via single-crystal X-ray diffraction, confirmation of the oxidation state of Fe by magnetic measurements and Mössbauer spectroscopy, and details of electrochemical studies including cyclic voltammetry, galvanostatic charge-discharge and impedance spectroscopy in Li- and Na-ion batteries using $Li_{0.8}Fe(H_2O)_2[BP_2O_8]\cdot H_2O$ as a cathode. Moreover, we report the first structural solution of the fully oxidized end member, $Fe(H_2O)_2[BP_2O_8]\cdot H_2O$, from synchrotron powder X-ray diffraction data and elucidate the oxidation state of Fe by magnetic and Mössbauer spectroscopy.

EXPERIMENTAL SECTION

Reagents. Reagent grade $FeCl_2\cdot 4H_2O$, H_3PO_4, and H_3BO_3 were purchased from Fisher Scientific. $LiOH\cdot H_2O$ (reagent grade, purity 98+%) was purchased from Acros Organics. Li foil (purity 99.9%) and Na cubes (purity 99.9%) were purchased from Aldrich. Anhydrous $NaClO_4$ (98%) was purchased from Strem Chemicals and battery grade Selectilyte ethylene carbonate (EC) and dimethyl carbonate (DMC) were purchased from BASF. All the chemicals were used as-purchased and without further purification.

Synthesis. $Li_{0.8}Fe(H_2O)_2[BP_2O_8]\cdot H_2O$ has been synthesized by employing hydrothermal method. Initially a homogeneous solution was prepared by dissolving 2.9820 g $FeCl_2\cdot 4H_2O$ (15 mmol), 46.5 mL concentrated (85% w/w, density = 1.68 $g.cm^{-3}$) H_3PO_4 (0.675 mol), 6.1830 g H_3BO_3 (0.100 mol), and 18.8820 g $LiOH\cdot H_2O$ (0.450 mol) in 20 mL of deionized water under continuous stirring for an hour. The solution was then transferred into a Teflon lined Parr stainless-steel reaction vessel (120 ml capacity), sealed, and kept in an oven at 175 °C for two weeks for the reaction to occur under autogenous pressure. The reaction product was composed of large well-defined dark-purple hexagonal crystals. The crystals were separated from the solution of unreacted reagents by filtration and washed several times with copious amounts of hot water, cold water, and finally by ethanol. The product was allowed to dry naturally in air, weighed for the

measurement of yield (reaction yield: ~70% with respect to Fe) and subsequently used for characterization and property studies.

Chemical Oxidation. The above material was subjected to chemical oxidation (oxidative de-insertion) by mixing 0.4880 g of milled $Li_{0.8}Fe(H_2O)_2[BP_2O_8]\cdot H_2O$ (1.53 mmol) and 0.5200 g of NO_2BF_4 (3.90 mmol) in 5 mL acetonitrile in an argon filled glovebox. The reaction was continued for 5 days at room temperature under continuous stirring while color of the powder changed from purple to white as the oxidation proceeded to completion. The reaction mixture was then removed from glovebox, filtered and washed with acetonitrile and dried overnight in a vacuum oven at 65 °C.

Material Characterization. *Single-crystal X-ray diffraction.* Crystal structure of $Li_{0.8}Fe(H_2O)_2[BP_2O_8]\cdot H_2O$ was solved from single-crystal intensity data sets collected on a Bruker Smart Apex diffractometer with monochromated Mo Kα radiation (λ = 0.7107 Å). Suitable crystal was selected and mounted on a glass fiber using epoxy-based glue. The data were collected using SMART[42] software at room temperature employing a scan of 0.3° in ω with an exposure time of 20 s/frame. The cell refinement and data reduction were carried out with SAINT,[43] while the program SADABS[43] was used for the absorption correction. The structure was solved by direct methods using SHELX-97[44] and difference Fourier syntheses. Full-matrix least-squares refinement against $|F^2|$ was carried out using the SHELXTL-PLUS[44] suite of programs. The hexagonal crystal system and the unit cell parameters, immediately revealed that the crystal structure belongs to a well-known structure-type, $M^IM^{II}(H_2O)_2[BP_2O_8]\cdot H_2O$ (M^I = Na, K; M^{II} = Mg, Mn, Fe, Co, Ni, Zn), first reported by Kniep *et al.*[25] The structure of $Li_{0.8}Fe(H_2O)_2[BP_2O_8]\cdot H_2O$ was solved in $P6_522$ space group. The positions of one Fe, one P, and 5 O atoms were located from the difference Fourier maps. These positions were then refined isotropically and immediately one more peak clearly appeared approximately 1.4 Å away from the O1 atom, which was assigned as boron atom (B1). At this point anisotropic refinement was carried out and two additional peaks separated by a distance of 2.16 Å appeared. These peaks were refined as Li, which was ~2 Å away from O5, and water of crystallization (O1w),

respectively. Both Li1 and O1w had high thermal parameters and, therefore, checked for partial occupancy. Refinement of occupancies revealed that Li1 has an occupancy of 66%, however, Li being a light atom such occupancy refinement may not be meaningful. Therefore, Li occupancy was fixed at 80% based on the Mössbauer spectroscopic study, which indicated ~20% of Fe^{3+} in the unique Fe site. Determination of lithium content was also carried out by atomic absorption spectroscopy (AAS) and the amount of lithium was found to be 1.67%. This value yielded the fraction of the Li^{+} to be 0.76(3) in the formula, $Li_{0.76}Fe(H_2O)_2[BP_2O_8].H_2O$, corroborating well with the Mössbauer spectroscopic results. The water of crystallization did not show any partial occupancy. The hydrogen atoms on the bound as well as free water could be located in the Fourier maps but could not be refined without using the restraints. Details of the final refinements and the cell parameters for $Li_{0.8}Fe(H_2O)_2[BP_2O_8]\cdot H_2O$ are given in Table 1. The final atomic coordinates and the isotropic displacement parameters are given in Table 2. Selected inter-atomic distances are listed in Table 3.

Powder X-ray diffraction (PXRD) and Thermo-diffractometry. The powder XRD pattern of the as-prepared phase was recorded on a PANalytical X'pert Pro diffractometer with a Cu $K\alpha_{1,2}$ tube for evaluation of phase purity over a 2θ range of 5–90 ° with a step width of 0.026 ° and step exposure duration of 3.3 sec. Thermo-diffractometry was utilized for in-situ study of thermal stability of the crystal structure of the as-prepared material in a 2θ range of 10 – 26 ° and a temperature window of 25–450 °C with 25 °C temperature intervals in an Anton-Paar HTK 2000 high-temperature strip heater chamber in N_2 gas flow.

For structural characterization after oxidative delithiation, synchrotron powder X-ray diffraction data has been collected from Argonne National Laboratory (ANL) Advanced Photon Source (APS) 11-BM beam line. The data collection was performed in ambient conditions using a monochromated parallel X-ray beam of 0.4139 Å wavelength over a 2θ range of 0.5 - 50°.The acquired data were then used for structure solution and refinement, initial atomic coordinates were found using FOX[45] software and Rietveld refinement was performed employing GSAS-II.[46]

Magnetic measurements. The DC Magnetic susceptibility of the compounds (as-prepared and chemically oxidized) were measured at 0.5 Tesla (1 Tesla = 10,000 Oe) after zero-field cooling over the temperature range 1.8 - 300 K with a Quantum Design SQUID magnetometer.

Table 1. Crystal data and structure refinement for $Li_{0.8}Fe(H_2O)_2[BP_2O_8]\cdot H_2O$

Empirical formula	$Li_{0.8}Fe(H_2O)_2[BP_2O_8]\cdot H_2O$
Formula weight	316.20 $g.mol^{-1}$
Crystal system	Hexagonal
Space group	$P\,6_522$
a = b	9.47(6) Å
c	15.76(1) Å
$\alpha = \beta$	90 °
γ	120 °
V	1225.4(3) $Å^3$
Z	6
ρ_{calc}	2.563 $g.cm^{-3}$
F(000)	944
Temperature	296(2) K
GOF on F^2	1.125
R [I>2σ(I)]	$R_1 = 0.0266$, $wR_2 = 0.0703$
R [all data]	$R_1 = 0.0286$, $wR_2 = 0.0719$

Further magnetic measurements including isothermal magnetization at various temperatures were carried out in an applied field range of +5 to -5 Tesla. Zero field cooled (ZFC) and field cooled (FC) magnetization data were collected at a low applied field (.01 T) for the chemically oxidized phase.

Mössbauer spectroscopy. ^{57}Fe Mössbauer spectroscopy was performed on the as-prepared, chemically oxidized, and different state-of-charge cathode materials in transmission geometry using a constant acceleration spectrometer equipped with a ^{57}Co (25 mCi) gamma source embedded in Rh matrix. The instrument was calibrated for velocity and isomer shifts with respect to α-Fe foil at

room temperature. The resulting Mössbauer data were analyzed using Lorentzian profile fitting by RECOIL software.[47]

Table 2. Atomic coordinates and equivalent isotropic displacement parameters of the atoms. U_{eq} = 1/3rd of the trace of the orthogonalized U tensor

Atom	x/a	y/b	z/c	U_{eq} [Å^2]
Fe(1)	0.5522(1)	0.4478(1)	0.0833	0.012(1)
P(1)	0.1683(1)	0.3866(1)	0.0814(1)	0.010(1)
B(1)	-0.1517(2)	0.1517(2)	0.0833	0.011(1)
O(1)	0.1789(2)	0.4154(2)	0.1791(1)	0.014(1)
O(2)	0.0209(2)	0.2132(2)	0.0648(1)	0.015(1)
O(3)	0.1409(3)	0.5173(3)	0.0433(1)	0.019(1)
O(4)	0.3149(2)	0.3825(3)	0.0478(1)	0.020(1)
O(5)	0.4806(3)	0.1924(3)	0.0483(2)	0.028(1)
O(1W)	0.1957(9)	0.0978(4)	-0.0833	0.085(2)
Li(1)	0.4830(3)	0.2414(1)	-0.0833	0.075(4)

Table 3. Selected bond lengths for $Li_{0.8}Fe(H_2O)_2[BP_2O_8]\cdot H_2O$

Bonds	Distances (Å)	Bonds	Distances (Å)
Fe1—O3$^{\#1,\#2}$	2.081(6)	P1—O1	1.558(3)
Fe1—O4$^{\#0,\#3}$	2.088(3)	B1—O2$^{\#0,\#6}$	1.465(3)
Fe1—O5$^{\#0,\#3}$	2.233(2)	B1—O1$^{\#7,\#8}$	1.473(3)
P1—O4	1.506(1)	Li1—O3$^{\#1,\#4}$	2.086(1)
P1—O3	1.511(7)	Li1—O5$^{\#5}$	2.124(2)
P1—O2	1.557(9)	O1W—Li1	2.36(2)

$^{\#0}$ x, y, z; $^{\#1}$ x – y + 1, -y + 1, -z; $^{\#2}$ y, -x + y, z + 1/6; $^{\#3}$ –y + 1, -x + 1, -z + 1/6; $^{\#4}$ x – y + 1, x, z - 1/6; $^{\#5}$ x, x – y, -z - 1/6; $^{\#6}$ -y, -x, -z + 1/6; $^{\#7}$ x – y, x, z - 1/6; $^{\#8}$ -x, -x + y, -z + 1/3

Thermogravimetry. The thermogravimetric analysis on the as-prepared sample along with the chemically oxidized samples were acquired using a TA instrument Q50 TGA in the temperature range of 25 – 800 °C under flowing nitrogen atmosphere with a heating rate of 10 °C.min^{-1}.

IR spectroscopy. Infrared spectra of the crystalline $Li_{0.8}Fe(H_2O)_2[BP_2O_8]\cdot H_2O$ and the chemically oxidized phases were recorded using a Thermo Nicolet Nexus 470 FT-IR spectrometer on KBr pellets in the wavenumber range of 400 – 4000 cm^{-1}.

Electrochemical tests. Electrochemical analyses of $Li_{0.8}Fe(H_2O)_2[BP_2O_8]\cdot H_2O$ were performed on composite cathodes made from the synthesized compound as the active material, conductive carbon and poly-vinylidenefluoride (PVDF) (binder) in 75:15:10 weight ratio in Li- and Na-ion cells. In a typical cathode preparation the active material was ball milled with super P conductive carbon for 2 hours in a SPEX 8000 mixer/milling machine to reduce the particle sizes. PVDF dissolved in N-methyl-2-pyrrolidone (NMP) was then added to the fine powder and milling continued for another 15 min to form a homogenous suspension which was applied subsequently on the surface of aluminum current collector with a uniform thickness by means of a glass rod. The composite cathode was then transferred to the vacuum oven where NMP was evaporated by drying at 85 °C for 12h.

CR2032 button cells were assembled in the argon glove box (oxygen concentration < 2.0 ppm) with circular disks (3/8”) cathodes cut from the above composite with active material loadings of about 4 mg. The cathodes were mounted with a Celgard 2325 as separator and Li-foil as the anode and 1M solution of $LiPF_6$ dissolved in DMC-EC (1:1) as the electrolyte for the Li-ion cells. For Na-ion cells the above cathodes were assembled with Whatman GF/A glass microfiber separators cut to the size, freshly prepared slices of Na metal as the anode and a 1M solution of $NaClO_4$ in DMC-EC (1:1) as the electrolyte. The assembled Li or Na-ion cells were crimped and aged for at least 12 h before the electrochemical analyses.

A PAR EG&G potentiostat/galvanostat model 273 was used for running cyclic voltammetry tests on the cells with a scan rate of 0.05 $mV.sec^{-1}$ in the potential range 1.8–4.2 V and 1.2–4.3 V *vs.* Li^+/Li and Na^+/Na, for Li- and Na-ion cells, respectively. Galvanostatic charge/discharge experiments were executed on an Arbin Instruments battery testing station model BT2403 under various C-rates.

Ionic conductivity measurements. About 600 mg of the as-prepared material was pressed into a pellet under a hydrostatic force of 7 tons for 5 min. The two sides of the obtained pellet were then coated with silver paint to form the blocking electrode and the complex impedance plots were obtained in a frequency range of 0.1 Hz - 100 kHz in the temperature windows 25 - 65 °C.

RESULTS AND DISSCUSSION

Crystal Structure Characterization. The asymmetric unit of $Li_{0.8}Fe(H_2O)_2[BP_2O_8]\cdot H_2O$ contains 10 non-hydrogen atoms (Figure 1). There is one crystallographically distinct Fe center located in 6*b* site, adopting an octahedral coordination with 4 oxygen atoms from the phosphate groups and two oxygen atoms from the coordinated water molecules where all the oxygen atoms coordinated to Fe are located at the general position, 12*c*.

The Fe — O bond lengths are in the range 2.081(6) — 2.233(2) Å, which are in good agreement with Fe(II) – oxygen bonds reported in the literature.[28, 29]. The P atom is located in a general position (12*c*) surrounded by 4 oxygens in a tetrahedral environment with P — O distances in the range 1.506(1) — 1.558(3) Å. The boron atom is located in a special position, 6*b*, and adopts a tetrahedral coordination with B — O distances in the range 1.465(3) — 1.473(3) Å. O1 and O2 act as the bridging oxygens between the phosphate and borate tetrahedral units. There is also one free water molecule, O1W located at the special position, 6*b*, coordinating only to the Li ion. The only Li site at the position, 6*b*, is partially occupied, implying mixed-valency in the Fe center. The Li atom is 5-coordinated adopting an irregular LiO_5 polyhedron with two oxygens from phosphate, two from coordinated water, and one from free water molecule with Li — O distances in the range 2.086(1) — 2.124(2) Å and a weaker bond with the free water molecule through a longer interatomic distance equal to 2.36(2) Å.

A bond valence sum (BVS) calculation yields a BVS value +2.070 for Fe reveals that the oxidation state of iron is mostly 2+ with some contribution from Fe^{3+} as well.

The remarkable feature of the structure of $Li_{0.8}Fe(H_2O)_2[BP_2O_8]\cdot H_2O$ is the polymerization of borate and phosphate units to form helical chains that run along the *c*-axis of the crystal (Figure 2a). These 6_5 helical chains form inner walls of the spiral channels which are filled with the free water molecules (Figure 2b). These chains are further connected by $FeO_4(H_2O)_2$ octahedral units and such arrangements create empty pores which are hosting Li^+ ions when viewed along the *a*-axis (Figure 2b and Figure 2c).

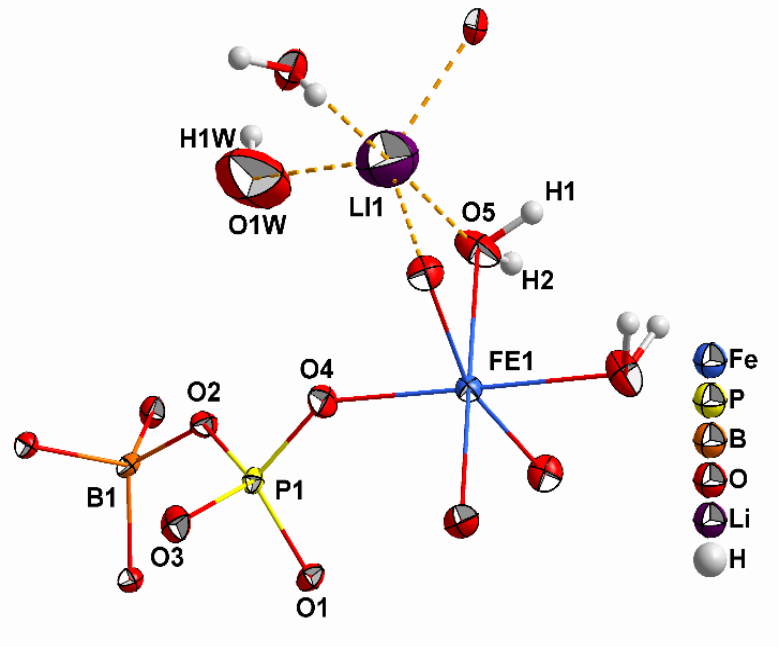

Figure 1. Connectivity pattern and coordination sphere of different atoms in $Li_{0.8}Fe(H_2O)_2[BP_2O_8]\cdot H_2O$. The atoms that appear in the asymmetric unit are labelled.

The Li^+ ions show large displacements in the *ab*-plane compared to *c*-axis as indicated by the respective thermal displacements of the ellipsoid. This may have implications towards high ionic conductivity of this phase, as studied by electro-impedance technique (discussed later). Comparison of the acquired powder X-ray diffraction pattern of the as-prepared $Li_{0.8}Fe(H_2O)_2[BP_2O_8]\cdot H_2O$ against the simulated pattern obtained from the single-crystal XRD suggests pure phase formation by the employed synthesis procedure (Supplementary Information, Figure S1).

In order to verify the existence of fully oxidized end member of $Li_{0.8}Fe(H_2O)_2[BP_2O_8]\cdot H_2O$, the obtained material was treated with NO_2BF_4, a strong oxidizer, which mimics the electrochemical oxidative delithiation.

The powder X-ray diffraction pattern of the chemically oxidized phase, $Fe(H_2O)_2[BP_2O_8]\cdot H_2O$, can reveal the crystal structure stability upon extraction of Li^+ ions. To follow the structural changes induced by chemical oxidation, synchrotron powder XRD of the sample was collected and used for structure solution (Figure 3).

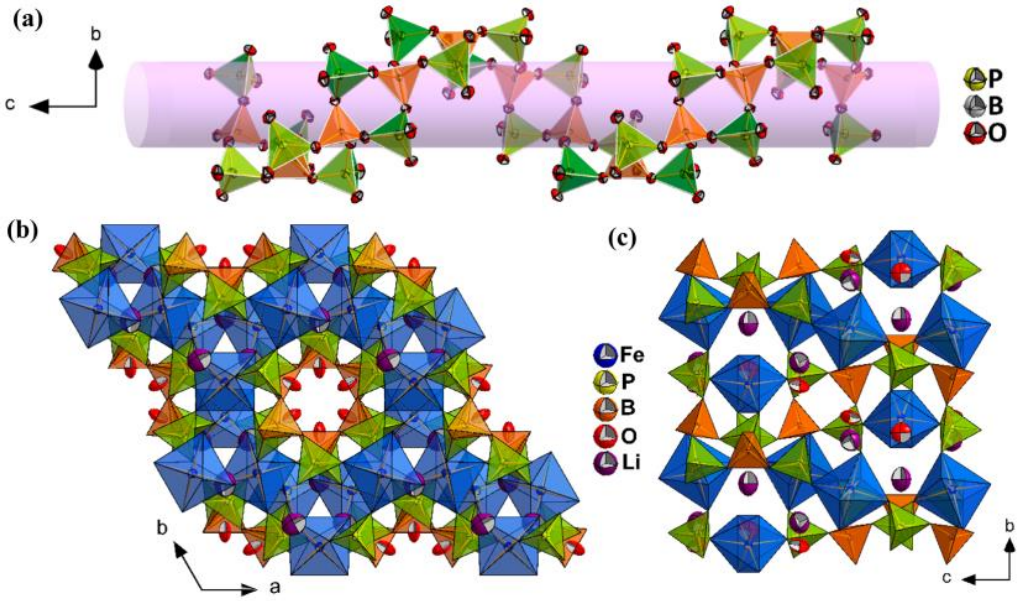

Figure 2. Demonstration of 6_5 helix forming the channel wall (a); Polyhedral connectivity of structure of $Li_{0.8}Fe(H_2O)_2[BP_2O_8]\cdot H_2O$ as viewed along the *c*-axis (b) and *a*-axis (c) with FeO_6 octahedra: blue, PO_4 tetrahedra: light green, BO_4 tetrahedra: orange. The red and purple ellipsoids with large thermal displacement represent the free water and Li^+, respectively.

The pattern was indexed in $P6_522$ space group using the FOX software,[45] similar to the as-prepared material. Intensity extraction by LeBail method followed by reconstruction of observed Fourier maps after the *ab-initio* Monte-Carlo simulation technique incorporated in FOX revealed the position of 9 non-hydrogen atoms, including: 1 Fe, 1 P, 1 B and 6 O atoms. These coordinates were used for the final Rietveld refinement using GSAS II.[46] Apart from the absence of the Li^+ ion, the free water molecule showed a high degree of disorder, as is evident from

its large thermal displacement parameter (Figure 4 and Table S1). However, the structure remains more or less the same after carrying out the chemical oxidation, suggesting a topotactic de-intercalation of Li^+ ions and high degree of structural stability.

Moreover, comparison of the unit cell parameters in the as-synthesized and chemically delithiated phase shows approximately -3.0% volume change after the oxidation. Refined lattice constants and agreement parameters of refinement for the oxidized phase are given in Table 4 and the atomic coordinates are supplied as supplementary information (Table S1). A bond valence sum (BVS) calculation yields a value of +3.06 for iron, which confirms complete oxidation of the Fe center in $Fe(H_2O)_2[BP_2O_8]\cdot H_2O$ to 3+.

Spectroscopic and Thermal Analyses. IR spectra of as-prepared and chemically oxidized phases of $Li_{0.8}Fe(H_2O)_2[BP_2O_8]\cdot H_2O$ are given in supporting information (Figure S2). The spectrum in each case is dominated by the strong P – O stretching modes in the range 900 – 1100 cm^{-1} overlapping heavily with the strong B – O stretching vibrations in the range 800 – 1200 cm^{-1}.[48] Strong O – H stretching (broad) and bending modes can be observed around 3400 and 1625 cm^{-1}, respectively.

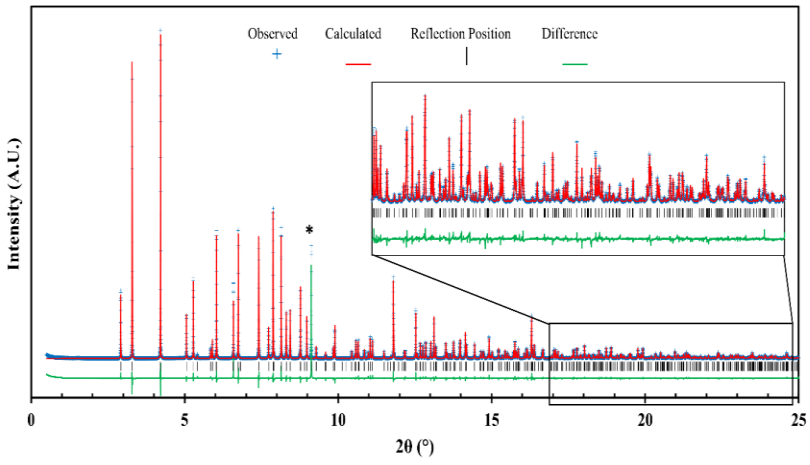

Figure 3. Rietveld refinement of synchrotron XRD data of $Fe(H_2O)_2[BP_2O_8]\cdot H_2O$. Blue cross: observed intensity, red line: calculated intensity; green line: difference curve. The impurity peak is indicated with an asterisk. Inset shows an enlarged view of the high 2θ segment of the pattern.

Similar to the powder XRD studies, the IR spectrum of the chemically oxidized sample matches fairly well with the as-prepared product, indicating the bonds remain intact after oxidative removal of the Li^+ from the channels or in other words a topotactic de-intercalation.

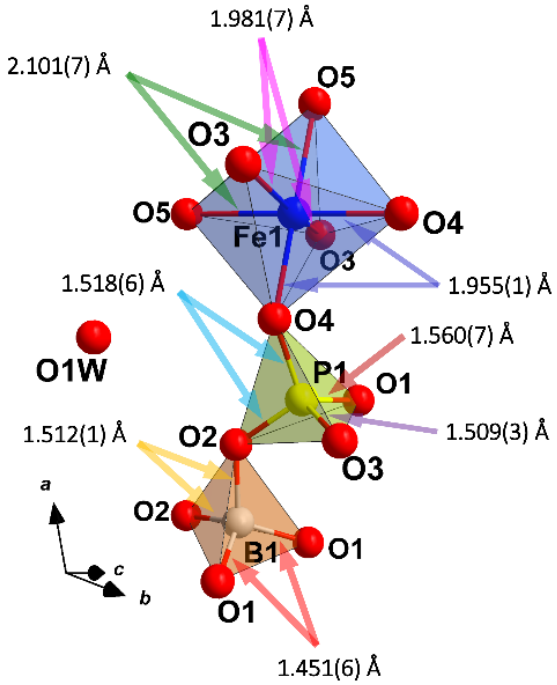

Figure 4. Connectivity pattern in $Fe(H_2O)_2[BP2O8]\cdot H_2O$ after chemical oxidation.

Table 4. Lattice parameters and goodness of the powder XRD refinement of $Fe(H_2O)_2[BP_2O_8]\cdot H_2O$

$a = b$	9.372(7) (Å)
c	15.606(7) (Å)
$\alpha = \beta$ (°)	90
γ (°)	120
V	1187.33(1) ($Å^3$)
Space group	$P6_522$
Number of reflections	327
R_w	12.04%
R_F^2	8.9 %
Number of data points	23928

TGA results of the ground crystals of $Li_{0.8}Fe(H_2O)_2[BP_2O_8]\cdot H_2O$ along with the oxidized phase are given in Figure 5. The as-prepared phase shows two major weight losses; in the first step 12% mass loss occurs in the temperature range 100 - 210 °C corresponding to loss of two H_2O molecules from the formula leading to a flat plateau, where weight remains stable between 210 – 320 °C. Afterwards, a second major weight loss is observed between 340 to 450 °C where the last coordinated water molecule is removed from the structure and no further weight loss is observed from 500 to 800 °C.

The final observed mass of 83.5% matches well with the theoretical value of 82.9% due to the mass of de-hydrated compound, $Li_{0.8}FeB(PO_4)_2$. The thermal behavior of the chemically oxidized phase is different as the first and second mass loss processes have merged together so that no flat profile can be recognized and conversion to the dehydrated final product occurs at a much lower temperature of 260 °C. Thermo-diffraction tests were performed in order to gain further information regarding the crystal structure stability upon removal of water molecules and the result is given in Figure 6.

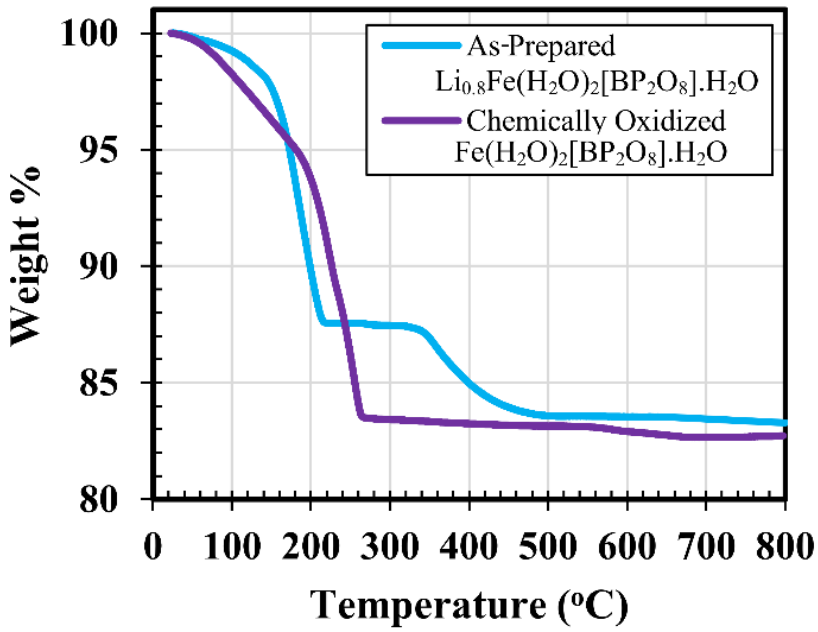

Figure 5. TGA curves for $Li_{0.8}Fe(H_2O)_2[BP_2O_8]\cdot H_2O$ and $Fe(H_2O)_2[BP_2O_8]\cdot H_2O$.

An initial peak intensity degradation is observed as the temperature increases from 25 to 75 °C, however, the main peak intensities can be clearly observed up to 150 °C (prior to the rapid weight loss as seen in TGA) after which an amorphous product forms. The results of TGA and thermo-diffraction studies indicate that the crystal structure remains stable after partial removal of the water of crystallization which accounts for 2% of mass loss corresponding to the removal of 0.33% of free water molecule. Further heating results in the simultaneous extraction of the remaining water of crystallization and one of the coordinated water molecules leading to the collapse of the crystal structure. This observation is in sharp contrast to some of the isostructural Na analogues, where removal of the water of crystallization and one of the coordinated water molecules led to microporosity with the retention of structural integrity.[25, 35] This is also in contrast to ammonium analogue, $(NH_4)_{0.75}Fe(H_2O)_2[BP_2O_8]\cdot 0.25H_2O$, where heating at 300 °C for 10 h does not remove the water of crystallization, nor does it destroy the crystal structure.[30]

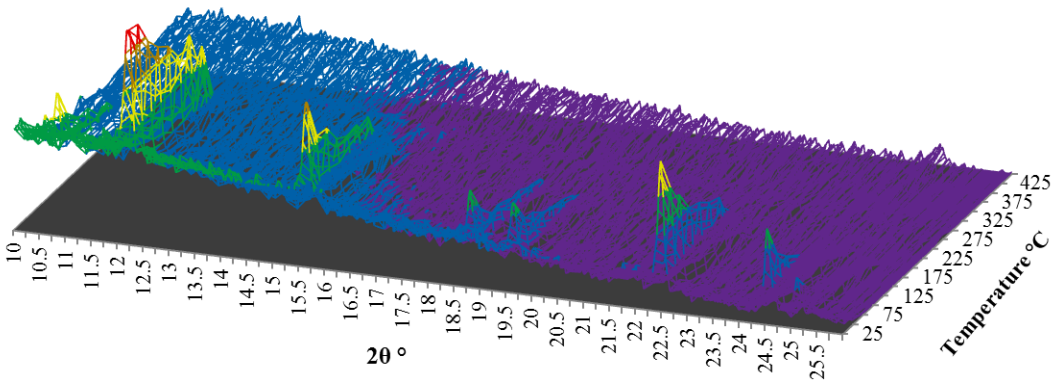

Figure 6. Themo-diffraction pattern of $Li_{0.8}Fe(H_2O)_2[BP_2O_8]\cdot H_2O$.

Magnetic Characterization. Magnetic property measurement is an important characterization for the cathode materials for alkali-ion batteries because it gives important information about the oxidation state of the transition metal besides any magnetic ordering. The ZFC magnetic susceptibility (χ_M) and the corresponding inverse (χ_M^{-1}) molar susceptibility as a function of temperature for

the as-synthesized and oxidized compounds are given in Figure 7 as a function of temperature.

The χ_M-T plots reveal that as-synthesized compound has no magnetic ordering and is asymptotic in the entire temperature range, while the chemically oxidized phase shows an onset of an antiferromagnetic transition at 5.16 K.

The χ_M-T plots reveal that as-synthesized compound has no magnetic ordering and is asymptotic in the entire temperature range, while the chemically oxidized phase shows an onset of an antiferromagnetic transition at 5.16 K. The χ_M^{-1}-T plots are perfectly linear between 25 to 300 K and data above 100 K can be fitted to Curie-Weiss law yielding a Curie constant C of 3.97(1) and 4.26(1) emu K/mol and θ_p of –4.9(4) K and –4.2 (3) K, respectively, for the as-synthesized and chemically oxidized phases. The effective magnetic moment calculated from the Curie constants are 5.64 and 5.84 μ_B for as-prepared and chemically oxidized phases, respectively, agree well with the presence of 20% Fe^{3+} in as-prepared material (theoretical 5.66 μ_B) and full Fe^{3+} in the oxidized phase (theoretical 5.9 μ_B).

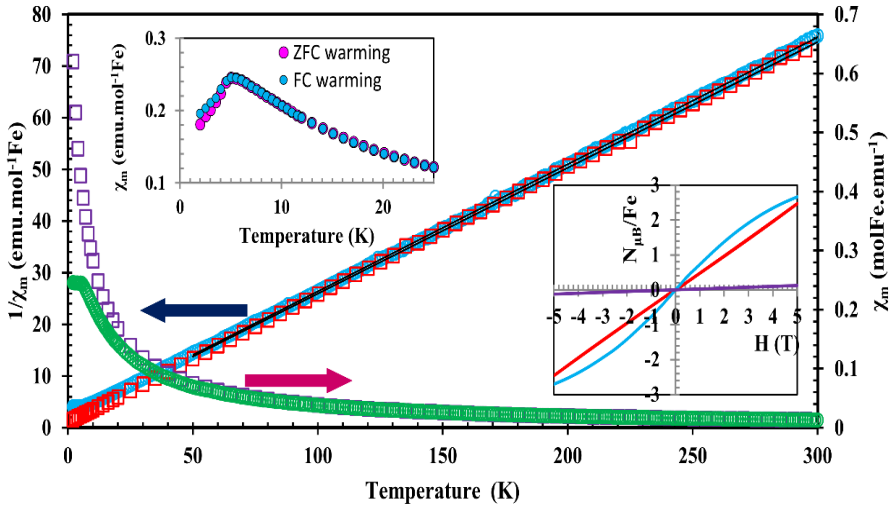

Figure 7. The temperature dependence of inverse and molar susceptibility of as-prepared (squares) and chemically oxidized (circles) samples of $Li_{0.8}Fe(H_2O)_2[BP_2O_8]\cdot H_2O$. Upper left inset: temperature dependence of χ_m of chemically oxidized sample under ZFC-FC (0.01T) conditions. Lower right inset shows the M-H curves of the two phases at different temperatures: as-prepared at 300 K (purple) and 5 K (blue), and oxidized sample at 2 K (Red).

The effective magnetic moment of 5.64μ_B for the as-prepared sample can be easily explained by taking into account 80 % of Fe in 2+ (assuming μ_{eff} (Fe^{2+}) = 5.6 μ_B) and remaining Fe in 3+ oxidation state, these values also corroborates with the Mössbauer experiment *(vide infra*). The observed magnetic moment for Fe^{2+} in high spin state is always higher than the spin only value (4.89 μ_B) because of the contribution from unquenched orbital moment and lies in the range (5.1 – 5.6 μ_B).[49] The negative values of the Weiss constant for both phases indicate predominant antiferromagnetic interactions between the Fe-centers. However, this exchange interactions between the Fe centers through the phosphate moiety in the case of high spin Fe(III) is strong enough to induce an antiferromagnetic ordering, while in the case of mixed valency (or predominant Fe^{2+}) there is no such ordering. The non-divergence of low field FC-ZFC magnetization measurements for the chemically oxidized phase also points to a long range three-dimensional antiferromagnetic ordering. The isothermal magnetization measurement at 2 K, which is below the T_N for the oxidized phase, shows a perfect straight line with no hysteresis, once again reinforcing the 3D antiferromagnetic ordering. Similar *M-H* scan for the as-synthesized compound at low and room temperature also indicate linear nature reminiscent of antiferromagnetic interactions.

Mössbauer Spectroscopy. Figure 8 demonstrates the Mössbauer spectra for the as-prepared compound along with its chemically oxidized form recorded over a velocity range of -10 to 10 $mm.s^{-1}$ (limited range shown here) with the fit parameters given in Table 5. According to SC-XRD there is only one crystallographically distinct iron site in the asymmetric unit and hence the observed spectrum should be one simple symmetrical doublet for any single oxidation state of Fe with definite isomer shift (IS) and quadrupolar splitting (QS). However, the observed asymmetry in the Mössbauer peak intensities and widths suggest inclusion of another doublet site in the low velocity peak, representing Fe in 3+ oxidation state. The compound is, therefore, in a mixed oxidation state with a certain ratio of Fe^{2+}:Fe^{3+}, which can be determined through the Lorentzian curve fitting. Another important characteristic of the Mössbauer spectrum of the as-synthesized compound is that the peaks have very broad linewidths reflecting a

distribution of the quadrupolar splitting due to different degree of distortion of FeO_6 octahedra. However, the exact reason for varying degree of octahedral distortion is not clear to us but may have to do with mixed valency and charge disorder. For this reason we have used multiple doublets with different quadrupolar splitting values to fit the higher quadrupole value peaks and one doublet for the smaller quadrupole value peak. However, we report here the average IS and the average magnitude of the QS for the doublet with larger quadrupolar splitting.

The fitted parameters given in Table 5 indicate that part of the iron ions are trivalent with a high-spin configuration and are located in octahedral environments and the remaining Fe ions are in divalent state with high spin octahedral coordination as expected from the structure and also corroborates with magnetic data. The ratio of the population of Fe^{2+} and Fe^{3+} is 4:1 and hence the formula $Li_{0.8}Fe^{2+}_{0.8}Fe^{3+}_{0.2}[BP_2O_8]\ (H_2O)_2{\cdot}H_2O$.

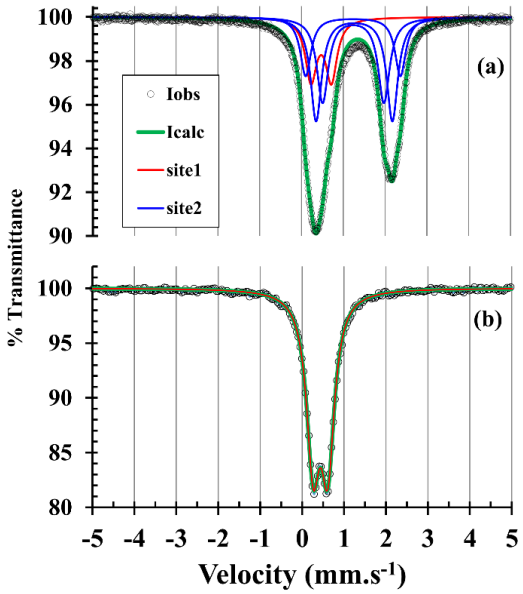

Figure 8. Mössbauer spectra for $Li_{0.8}Fe(H_2O)_2[BP_2O_8]{\cdot}H_2O$ (a), and $Fe(H_2O)_2[BP_2O_8]{\cdot}H_2O$ (b).

On the other hand, the curve fitting of the Mössbauer spectrum for the chemically oxidized phase requires only one doublet (Figure 8 b), with IS and QS values signature of Fe^{3+} in octahedral coordination. The isomer shift of the

oxidized phase matches perfectly with the isomer shift observed for Fe(III) in the as-synthesized compound (see Table 5). The absence of any Fe^{2+} impurity peak indicates complete conversion of Fe^{2+} centers to Fe^{3+} as a result of oxidative delithiation using NO_2BF_4. IS and QS values reported here are typical of Fe^{2+} and Fe^{3+} in high spin octahedral configuration in an oxide environment.[50]

Electrochemistry. As mentioned above, topotactic oxidative chemical de-intercalation of Li^+ can be achieved from the host structure $Li_{0.8}Fe(H_2O)_2[BP_2O_8]\cdot H_2O$. Accordingly, we tried electrochemical oxidation/reduction of this phase to assess its electrochemical properties as a cathode material in rocking-chair alkali-ion batteries. Reversible electrochemical intercalation of Li^+ and Na^+ ions into the host structure was studied by running cyclic voltammetry experiments on the coin cells, whose results are presented in Figure 9.

Table 5. Values of Mössbauer isomer shift (IS), quadrupole splitting (QS) and site percentage for the as-synthesized and chemically oxidized samples

	IS ($mm.s^{-1}$)	QS ($mm.s^{-1}$)	site %
$Li_{0.8}Fe(H_2O)_2[BP_2O_8].H_2O$			
Site 1 (Fe^{3+})	0.468(1)	0.487(9)	20.1(4)
Site 2(Fe^{2+})[a]	1.240(2)	1.853(3)	79.9(1)
$Fe(H_2O)_2[BP_2O_8]\cdot H_2O$			
site 1	0.438(8)	0.348(3)	100

a Average IS and QS.

The open circuit potential for Li- and Na-ion cells fabricated with Li0.8Fe(H2O)2[BP2O8]·H2O as cathode are essentially the same, 3.0 and 3.1 V, respectively. The cells were first subjected to oxidation by scanning the potential towards the higher voltage, followed by reversing the potential scan to the lower voltage limit. The anodic and cathodic peaks for the Li-ion cell occur at 3.65 V and 2.70 V, respectively. Moreover, the peak positions do not move following further cycling, implying the high degree of reversibility and the stability of the redox process for this cathode material as will be discussed later.

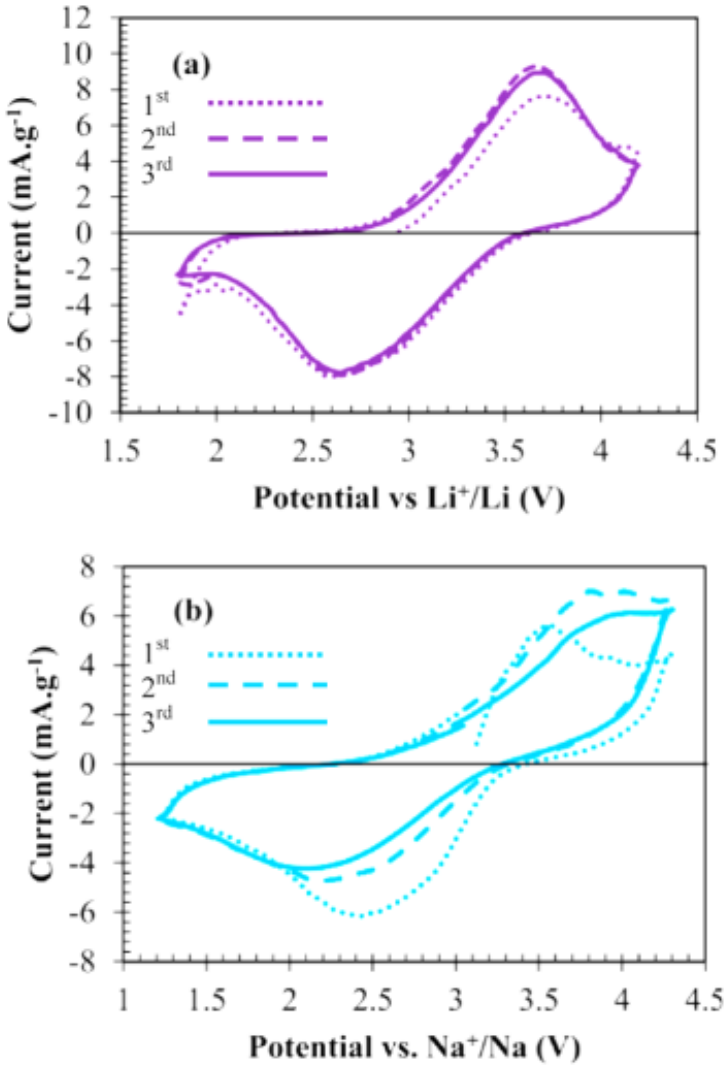

Figure 9. Cyclic voltammetry curves of $Li_{0.8}Fe(H_2O)_2[BP_2O_8]\cdot H_2O|LiPF_6|Li$ (a) and $NaFe(H_2O)_2[BP_2O_8]\cdot H_2O|NaClO_4|Na$ (b).

The anodic and cathodic peaks for the Na-ion cell can be observed at 3.50 V and 2.45 V, respectively. The anodic peak potential for the Na-ion cell is broad in comparison to the Li-ion cell, implying a higher polarization compared to the Li-ion cell. However, the cathodic (discharge) potential is lower than the latter, as expected. The observed shifts in the position of the cathodic and anodic peaks towards extreme values upon cycling, as well as comparatively lower peak current can be related to the slower dynamics of Na^+ diffusion rates as discussed later (see the impedance part).

The results of the CV experiments reveal the electrochemical activity of the $Fe(H_2O)_2[BP_2O_8]\cdot H_2O$ host towards reversible intercalation of alkali ions. Assuming one electron transfer the $LiFe(H_2O)_2[BP_2O_8]\cdot H_2O$ and $NaFe(H_2O)_2[BP_2O_8]\cdot H_2O$ active materials give rise to a theoretical specific capacity of 84.4 and 80.33 $mAh.g^{-1}$, respectively.

Figure 10 shows the first 3 cycles of the galvanostatic charge/discharge cycling test performed on the Li-ion cells in the potential window of 2.1 - 4.0 V *vs.* Li^+/Li at the C-rate of C/50.

The charge capacity (oxidative delithiation) achieved in the first cycle is smaller than the subsequent charge/discharge cycles, since a fraction of the material is already in +3 oxidation state. For the first discharge, initially Li^+ intercalates into the $Li_xFe(H_2O)_2[BP_2O_8]\cdot H_2O$ (x ~0.24) host at 3.5 V, which appears relatively high for an iron-based cathode material. The voltage-composition profile reduces monotonically up to an intercalation of 0.7 Li^+ into the structure (60 $mAh.g^{-1}$) reaching a value of 2.7 V, after which the potential drops rapidly to the lower voltage cut-off value of 2.1 V achieving 80% of the theoretical capacity (67.5 $mAh.g^{-1}$) with an average redox potential of 3.06 V *vs* Li^+/Li.

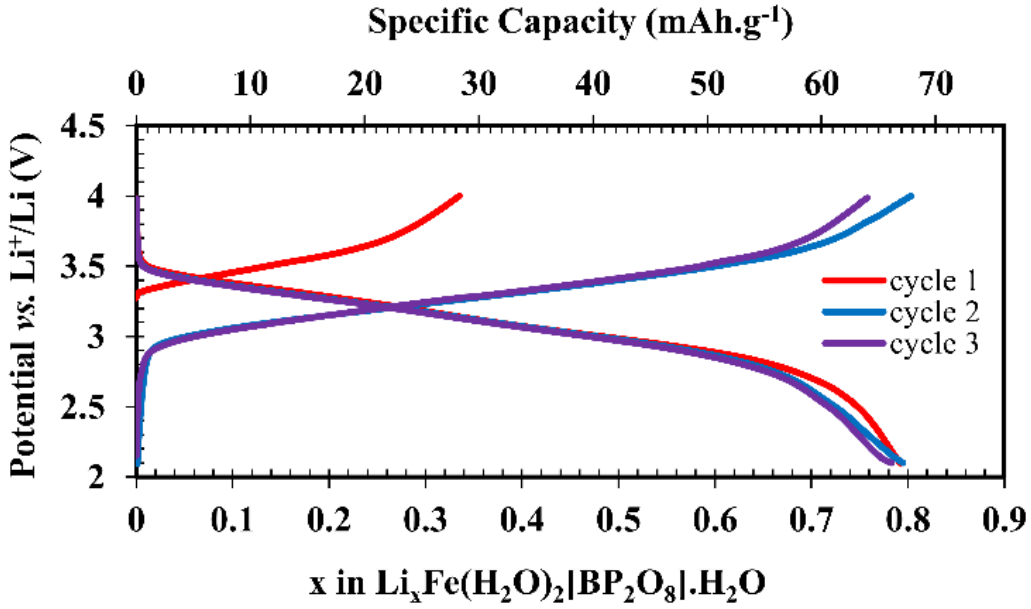

Figure 10. First three galvanostatic charge-discharge tests on $Li_{0.8}Fe(H_2O)_2[BP_2O_8]\cdot H_2O|LiPF_6|Li$ cell.

Further examination of discharge curves indicates high reversibility of the redox process and small capacity loss on subsequent cycles.

Mössbauer spectroscopy was employed as an *ex-situ* technique to keep track of oxidation state and environment change of iron as the cells were cycled between charge and discharge state at C/20 rate. The Mössbauer spectra of the cathode has been obtained from fresh cells charged to 4.0 V and subsequently discharged to 3.0 and 2.0 volts corresponding to the fully charged, half-way discharged and fully discharged states, respectively. For each state-of-charge the cathode materials for Mössbauer study were retrieved from 3-4 cells after breaking the cells apart. The Mössbauer spectrum of the 4.0 V charged state shows that 68.8% of iron is in +3 oxidation state, while the percentage of +3 state drops to 47.7% and 34.0% as the cell potential decreases to 3.0V and 2.0V, respectively, during the discharge process (Supplementary information, Figure S3 and Table S2). This trend demonstrates the change in the oxidation state of iron center as a function of potential and state-of-charge as expected from the charge-discharge-composition curve and reinforces the fact that the mechanism of charge and discharge is associated with oxidative de-intercalation and reductive insertion, respectively.

Minimal changes (Table S2) in the isomer shift and quadrupole splitting of the +2 state of iron indicate that there is no change in the coordination environment of Fe supporting the intactness of the bound water during the charge-discharge. On the other hand, there is some small variation of the isomer shift and quadrupole splitting of the Fe(III), the isomer shift decreases from 0.40 mms^{-1} to 0.36 $mm \cdot s^{-1}$ and quadrupole splitting increases from 0.62 to 0.85 $mm \cdot s^{-1}$) as the cell is discharged (Table S2). These changes in IS and QS of Fe(II) and Fe(III) compared to as-synthesized and chemically oxidized form are related to changes in the particle sizes, defect, and different degree of distortions of Fe-centers introduced during electrochemical charge-discharge and also consistent with the solid solution mechanism. Since the isomer shift value lower than 0.30 $mm \cdot s^{-1}$ was not observed, which is a signature of Fe(III) in the tetrahedral coordination, it can be safely assumed that octahedral coordination of Fe(III) remained intact.[51] Therefore, we

conclude that bound water molecules are intact during the charge-discharge processes.

Similar to Li-ion cells, the voltage-composition profiles were obtained for Na-ion cells at the C-rate of C/50 and the results are shown in Figure 11.

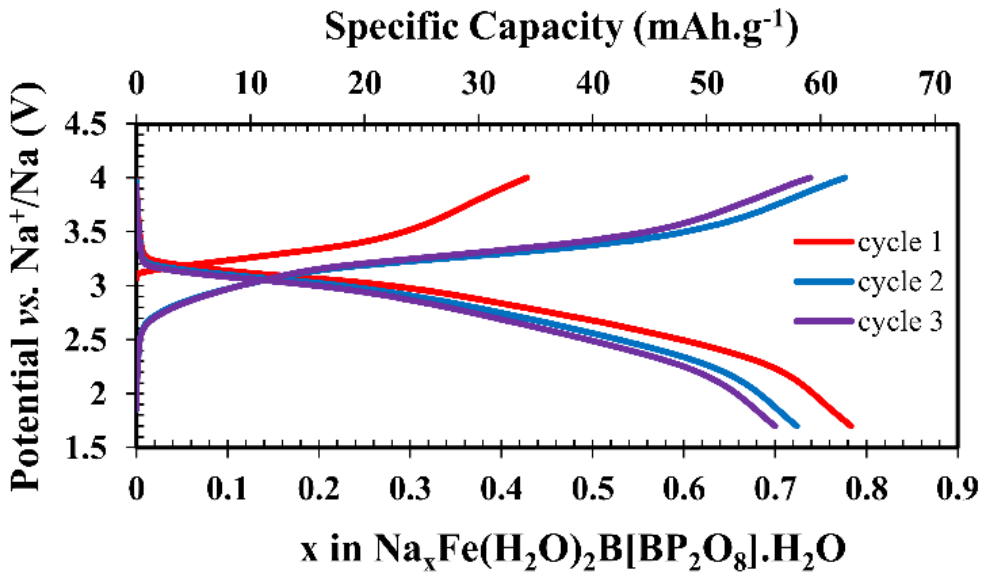

Figure 11. First three galvanostatic charge-discharge tests on $NaFe(H_2O)_2[BP_2O_8]\cdot H_2O|NaClO_4|Na$ cell.

In the course of the first charge cycle Li^+ ions are removed from the host structure with concomitant oxidation of most of the Fe(II) centers into Fe(III). During the first discharge cycle Na^+ intercalate into the $Li_xFe(H_2O)_2[BP_2O_8]\cdot H_2O$ (x~ 0.2) host with simultaneous reduction of Fe(III) species into Fe(II). The Na^+ intercalation is accompanied by a unit cell expansion from the original value 1225.4 $Å^3$ in the lithiated phase to 1240.1 $Å^3$ in the sodiated phase as determined through a Pawley refinement of the XRD pattern from the cathode of a discharged Na-ion cell following the first discharge cycle (Supplementary Information, Figure S4 and Table S3). It is worth mentioning that the observed cell volume in this case is slightly larger than that reported in the literature for $NaFe(H_2O)_2[BP_2O_8].H_2O$ by 0.73 %.[29] The intercalation of Na^+ into the host structure has also been confirmed from the EDS microanalysis elemental maps acquired from the discharged Na-ion

cell after removing the electrolyte by continuous washing using acetone (Supplementary Information, Figure S5).

The process of Na-ion cell discharge starts to occur at a lower voltage, 3.2 V *vs* Na^+/Na, compared to the Li-ion cell (3.5 V), as a result of smaller redox potential for the sodium redox couple compared to the lithium (-2.71 V and -3.04 V *vs* S.H.E., respectively). Analogous to the previous case, the Na-ion cell exhibits a sloppy voltage-composition profile indicative of solid solution formation between the oxidized and reduced phases. The voltage constantly decreases until 75% of the theoretical capacity has been achieved (60.2 $mAh.g^{-1}$), after which it drops with a higher slope to the lower voltage cut-off potential of 1.7 V, yielding a total specific capacity of 66.5 $mAh.g^{-1}$ (82% of the theoretical capacity) at an average potential of 2.76 V at the end of the first cycle. Upon further cycling around 9% capacity loss can be observed at the end of third cycle of discharge indicating somewhat lower degree of reversibility in comparison to the Li-ion cell. The results of capacity retention for both the Li-ion and Na-ion cells as a function of C-rate are given in Figure 12.

Due to the different ionic and electronic polarization effects the specific discharge capacity degrades as the C-rate increases for both Li- and Na-ion cells. However, the decrease in Na-ion cell is more pronounced due to the added ionic diffusion energy barrier as the Na^+ ion has a considerably larger ionic radii compared to the agile Li^+ ion. For both systems, however, the results indicate that the achieved capacity is stable for a given C-rate, which is in sharp contrast to the recently reported results on $NaFe(H_2O)_2[BP_2O_8]\cdot H_2O$ cathode by Masquelier group, which shows a fast decaying capacity.[30]

Upon returning to the slow discharge at C/50 following the higher rate charge discharge cycles, subtle differences can be observed for the Li- and Na-ion cells. While the Li-ion cell recovers its capacity approximately to the initial C/50 value the Na-ion cell suffers from capacity loss. This signifies the low mobility of Na^+ during the charge-discharge processes and the limited higher current rate capability of this phase, opposed to the lithiated phase.

To further characterize the of Li^+/Na^+ ion-exchange and their respective cell dynamics electro-impedance spectroscopy was utilized on the assembled cells and the results are given in Figure 13.

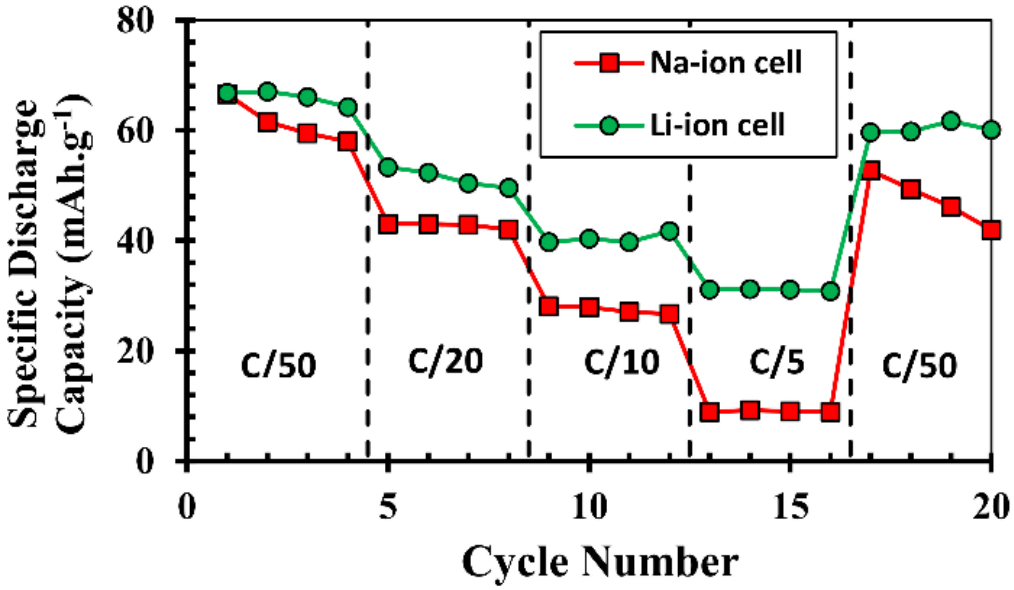

Figure 12. Capacity retention versus C-rate for Li-ion and Na-ion cells assembled with $Li_{0.8}Fe(H_2O)_2[BP_2O_8]\cdot H_2O$ cathode.

The composition of the cathode is same initially in both Li- and Na-ion cells. Therefore, the two cells were charged to 4.0 V to remove most of the Li^+ ions from the cathode host structure by oxidative extraction and impedance spectra were collected for the delithiated cathode compound.

Subsequently the Li- and Na-ion cells were subjected to discharge to 2.0 and 1.5 V, respectively, to insert Li^+ and Na^+ ions into the respective cathode and another set of impedance curves were acquired to observe the change in cell resistance induced by intercalation of respective ions. In each case the impedance curve composed of three semi-circles corresponding to anodic and cathodic processes (i.e. solid-electrolyte interface (SEI) and charge-transfer resistances), except for the Na-ion cell discharged to 1.5 V where only two semi-circles can be observed in the frequency range employed (Bode plots and fit parameters are provided for comparison in the Supplementary Information, Figure S6 and Table S4).

Comparable cell impedances for the two charged cells is quite expected as in both cases the cathode is in the higher oxidation state with no (or less) Li^+ ion in the structure. However, the impedance curves of the two discharged cells demonstrate enormous difference in the cell impedances, with the Na-ion cell impedance larger by more than three times than the Li-ion counterpart indicating the Na^+/Li^+ ion-exchange takes place from the first discharge. Additionally, the increased cell impedance in Na-ion battery explains the lower rate capability of this cell compared to the Li-ion cell as observed also in CVs and capacity-retention experiments.

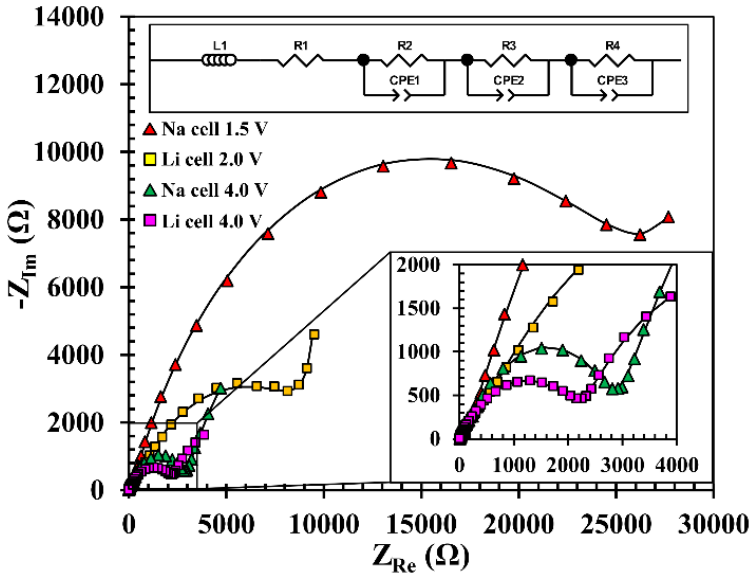

Figure 13. Electro-impedance spectra of Li-ion and Na-ion cells fabricated with $Li_{0.8}Fe(H_2O)_2[BP_2O_8]\cdot H_2O$ cathode. Top inset shows the equivalent circuit used for fitting the curves.

Following the discussion regarding mobility of Li^+ ions in the lattice from the anisotropic thermal displacement parameters, the pelletized as-synthesized material was studied by electro-impedance spectroscopy for evaluation of ion conduction and the determination of corresponding activation energy (Figure 14 a). The spectra show inclined line at the low frequency region followed by a medium and a high frequency semi-circle. The low frequency tail indicates that the mechanism of the conductivity is mainly ionic in nature and depicts the typical

behavior of blocking electrodes (silver) towards mobile Li^+ ions. The medium and high frequency semicircles are assigned to the ionic conductivity impedance within the grain boundary and the grains/bulk, respectively. This allows separation of the additive contribution of resistance and extraction of pure ionic conductivity through the bulk of the material. Extractions of the respective resistance values by fitting indicate that the material has an ionic conductivity value equal to $3.0x10^{-8}$ $S.cm^{-1}$ at room temperature. Collecting the conductivity values at different temperatures allows one to construct an Arrhenius type plot and extract the activation energy for Li^+ ion hopping from one site to the other (Figure 14b). The activation energy yielded in the selected temperature range has a value of 0.20 eV per Li^+, which is comparable to or smaller than some ionic conductors, e.g. $Li_{10}SnP_2S_{12}$[52] or Nalipoite Li_2NaPO_4.[53] However, the total conductance in $Li_{0.8}Fe(H_2O)_2[BP_2O_8]\cdot H_2O$ is considerably smaller than the commercial ionic conductors due to the smaller attempt frequency (Arrhenius pre-exponential factor). Details of the fit parameters are given in supplementary information (Table S5) .

CONCLUSIONS

In this work we have shown that iron borophosphate with tunnel structure is a good host for reversible Li- and Na-ion (de)-insertion and can act as cathode materials for Li- and Na-ion batteries with reasonable average voltage. Besides electrochemistry, we have also demonstrated that the Li-ion deintercalation/intercalation is topotactic and fully de-lithiated phase is highly crystalline and preserve the structural framework of the parent lithiated phase supporting a solid-solution mechanism. The structural and compositional variation in borophosphate chemistry will open up new area to explore mixed polyanion-based cathodes for alkali-ion batteries.

ASSOCIATED CONTENT

Supporting Information.

Details of single-crystal X-ray diffraction of $Li_{0.8}Fe(H_2O)_2[BP_2O_8]\cdot H_2O$ in the form of CIF format, comparison of the observed and calculated powder XRD

patterns of the as-synthesized $i_{0.8}Fe(H_2O)_2[BP_2O_8].H_2O$, atomic coordinates of the chemically oxidized phase,

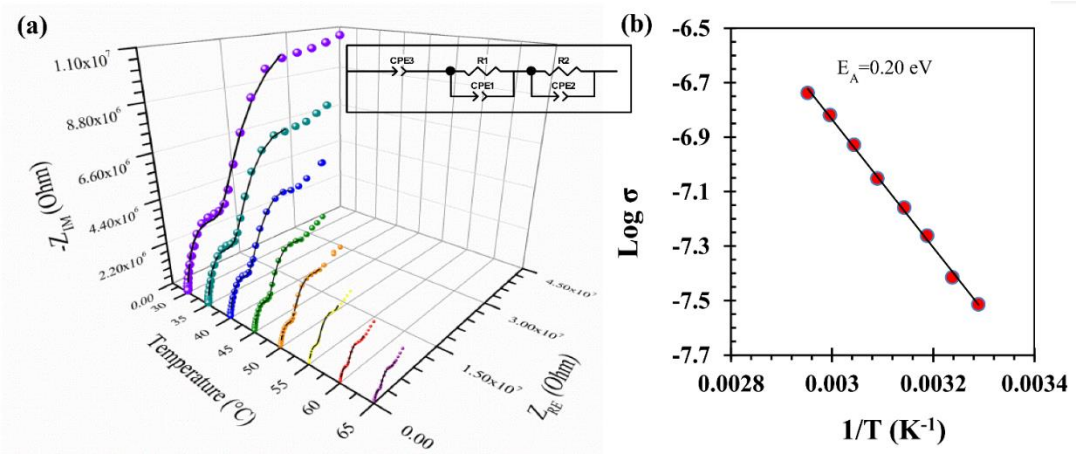

Figure 14. Nyquist plots of the complex impedance data points (spheres) with the fit (solid line) and the equivalent circuit (inset) (a); Arrhenius plot for the bulk ionic conductivity of $Li_{0.8}Fe(H_2O)_2[BP_2O_8]\cdot H_2O$ (b).

Mössbauer spectra of the cathode at different state-of-charge and their corresponding isomer shift and quadrupole splitting values, Pawley refinement of the reduced cathode phase in Na-ion cell and the corresponding EDS elemental mapping, impedance phase Bode plot and impedance fit parameters for the cell and the pellet. These materials are available free of charge via the Internet at http://pubs.acs.org.

AUTHOR INFORMATION

Corresponding Author

choudhurya@mst.edu

* Department of Chemistry, Missouri University of Science and Technology, Rolla, MO 65409, USA.

ACKNOWLEDGMENT

The authors acknowledge the funding from Materials Research Centre (Missouri S&T) and University of Missouri Research Board. The authors are also grateful to Professors Nick Leventis and Pericles Stavropoulos for the donation of a

potentiostat and a glovebox, respectively. Use of the Advanced Photon Source at Argonne National Laboratory was supported by the U. S. Department of Energy, Office of Science, Office of Basic Energy Sciences, under Contract No. DE-AC02-06CH11357.

REFERENCES

(1) Masquelier, C.; Croguennec, L. Polyanionic (Phosphates, Silicates, Sulfates) Frameworks as Electrode Materials for Rechargeable Li (or Na) Batteries *Chem. Rev.* **2013**, *113*, 6552 −6591.

(2) Padhi, A. K.; Nanjundaswamy, K. S.; Goodenough, J. B. Phospho-olivines as Positive-Electrode Materials for Rechargeable Lithium Batteries *J. Electrochem. Soc.* **1997**, *144*, 1188-1194.

(3) Padhi, A. K.; Manivannan, V.; Goodenough, J. B. Tuning the Position of the Redox Couples in Materials with NASICON Structure by Anionic Substitution *J. Electrochem. Soc.* **1998**, *145*, 1518-1520.

(4) Recham, N.; Chotard, J.-N.; Dupont, L.; Delacourt, C.; Walker, W.; Armand, M.; Tarascon, J.-M. A 3.6 V lithium-based fluorosulphate insertion positive electrode for lithium-ion batteries *Nature Mater.* **2010**, *9*, 68-74.

(5) Nytén, A.; Abouimrane, A.; Armand, M.; Gustafsson, T.; Thomas, J. O. Electrochemical performance of Li_2FeSiO_4 as a new Li-battery cathode material. *Electrochem. Commun.* **2005**, *7*, 156 - 160.

(6) Saiful Islam, M.; Dominko, R.; Masquelier, C.; Sirisopanaporn, C.; Armstrong, A. R.; Bruce, P. G. Silicate cathodes for lithium batteries: alternatives to phosphates? *J. Mater. Chem.* **2011**, *21*, 9811-9818.

(7) Anji Reddy, M.; Pralong, V.; Caignaert, V.; Varadaraju, U. V.; Raveau, B. Monoclinic iron hydroxy sulphate: A new route to electrode materials. *Electrochem. Commun.*, **2009**, *11*, 1807 - 1810.

(8) Barpanda, P.; Ati, M.; Melot, B. C.; Rousse, G.; Chotard, J. -N.; Doublet, M. -L.; Sougrati, M. T.; Corr, S. A.; Jumas, J. -C.; Tarascon, J. -M. A 3.90 v iron-based fluorosulphate material for lithium-ion batteries crystallizing in the triplite structure. *Nature Mater.* **2011**, *10*, 772 - 779.

(9) Rousse, G.; Tarascon, J.-M. Sulfate-Based Polyanionic Compounds for Li-Ion Batteries: Synthesis, Crystal Chemistry, and Electrochemistry Aspects *Chem. Mater.* **2014**, *26*, 394-406.

(10) Legagneur, V.; An, Y.; Mosbah, A.; Portal, R.; Le Gal La Salle, A.; Verbaere, A.; Guyomard, D.; Piffard, Y. LiMBO3 (M = Mn, Fe, Co): Synthesis, crystal structure and lithium deinsertion/insertion properties. *Solid State Ionics*, **2001**, *139*, 37 - 46.

(11) Yamada, A.; Iwane, N.; Harada, Y.; Nishimura, Sh.-I; Koyama, Y.; Tanaka, I. Lithium Iron Borates as High-Capacity Battery Electrodes *Adv. Mater.* **2010**, *22*, 3583-3587.

(12) Yaghoobnejad Asl, H.; Ghosh, K.; Vidal Meza, M. P.; Choudhury, A. $Li_3Fe_2(HPO_3)_3Cl$: an electroactive iron phosphite as a new polyanionic cathode material for Li-ion battery *J. Mater. Chem. A* **2015**, *3*, 7488-7497.

(13) Yaghoobnejad Asl, H.; Choudhury, A. Phosphite as Polyanion-based Cathode for Li-ion Battery: Synthesis, Structure and Electrochemistry of $LiFe(HPO_3)_2$. *Inorg. Chem.* **2015**, 54, 6566–6572.

(14) Palomares, V.; Serras, P.; Villaluenga, I.; Hueso, K. B.; Carretero-González, J.; Rojo, T. Na-ion batteries, recent advances and present challenges to become low cost energy storage systems *Energy Environ. Sci.* **2012**, ***5***, 5884-5901.

(15) Kim, S.-W.; Seo, D.-H.; Ma, X.; Ceder, G., Kang, K. Electrode Materials for Rechargeable Sodium-Ion Batteries: Potential Alternatives to Current Lithium-Ion Batteries *Adv. Energy Mater.* **2012**, *2*, 710-721.

(16) Han, M. H.; Gonzalo, E.; Singh, G.; Rojo, T. A comprehensive review of sodium layered oxides: powerful cathodes for Na-ion batteries *Energy Environ. Sci.*, **2015**, ***8***, 81-102.

(17) Hautier, G.; Jain, A.; Chen, H.; Moore, C.; Ping Ong, S.; Ceder, G. Novel mixed polyanions lithium-ion battery cathode materials predicted by high-throughput ab initio computations *J. Mater. Chem.*, **2011**, *21*, 17147-17153.

(18) Chen, H.; Hautier, G.; and Ceder, G. Synthesis, computed stability, and crystal structure of a new family of inorganic compounds: carbonophosphates. *J. Am. Chem. Soc.*, **2012**, *134*, 19619-19627.

(19) Chen, H.; Hao, Q.; Zivkovic, O.; Hautier, G.; Du, L.; Tang, Y.; Hu, Y.; Ma, X.; Grey, C. P.; Ceder, G. Sidorenkite ($Na_3MnPO_4CO_3$): A New Intercalation Cathode Material for Na-Ion Batteries *Chem. Mater.*, **2013**, *25*, 2777-2786.

(20) Kniep, R.; Engelhardt, H.; Hauf, C. A First Approach to Borophosphate Structural Chemistry *Chem. Mater.* **1998**, *10*, 2930-2934.

(21) Ewald, B.; Huang, Y. –X.; Kniep, R. Structural Chemistry of Borophosphates, Metalloborophosphates, and Related Compounds *Z. Anorg. Allg. Chem.* **2007**, *633*, 1517.

(22) Li, H.; Zhao, Y.; Pan, S.; Wu, H.; Yu, H.; Zhang, F.; Yang, Z.; Poeppelmeier, K. Synthesis and Structure of $KPbBP_2O_8$ – A Congruent Melting Borophosphate with Nonlinear Optical Properties R. *Eur. J. Inorg. Chem.* **2013**, 3185.

(23) Shi, Y.; Pan, S.; Dong, X.; Wang, Y.; Zhang, M.; Zhang, F.; Zhou, Z. $Na_3Cd3B(PO_4)_4$: A New Noncentrosymmetric Borophosphate with Zero-Dimensional Anion Units *Inorg. Chem.* **2012**, *51*, 10870-10875.

(24) Zhao, D.; Cheng, W.-D.; Zhang, H.; Huang, S.-P.; Xie, Z.; Zhang, W.-L.; Yang, S.-L. $KMBP_2O_8$ (M = Sr, Ba): A New Kind of Noncentrosymmetry Borophosphate with the Three-Dimensional Diamond-like Framework *Inorg. Chem.* **2009**, *48*, 6623-6629.

(25) Kniep, R.; Will, H. G.; Boy, I.; Roehr, C. 6_1 Helices from Tetrahedral Ribbons $1^{\infty}[BP_2O_8^{3-}]$: Isostructural Borophosphates $M^IM^{II}(H_2O)_2[BP_2O_8] \cdot H_2O$ (M^I = Na, K; M^{II} = Mg, Mn, Fe, Co, Ni, Zn) and Their Dehydration to Microporous Phases $M^IM^{II}(H_2O)[BP_2O_8]$ *Angew. Chem. Int. Ed.*, **1997**, *36*, 1013-1014.

(26) Zhou, Y.; Hoffmann, S.; Menezes, P. W.; Carrillo-Cabrera, W.; Huang, Y.-X.; Vasylechko, L.; Schmidt, M.; Prots, Y.; Deng, J.-F.; Mi, J.-X.; Kniep, R. Nanoporous titanium borophosphates with rigid gainesite-type framework structure *Chem. Commun*. **2011**, *47*, 11695-11696.

(27) Feng, Y.; Li, M.; Fan, H.; Huang, Q.; Qiu, D.; Shi, H. A novel open-framework copper borophosphate containing 1-D borophosphate anion with 10-MR windows and 12-MR channels *Dalton Trans.*, **2015**, *44*, 894 - 897.

(28) Huang, Y.-X.; Schaefer, G.; Carrillo Cabrera, W.; Cardoso, R.; Schnelle, W.; Zhao, J.-T.; Kniep, R. Open-Framework Borophosphates: $(NH_4)_{0.4}Fe^{II}_{0.55}Fe^{III}_{0.5}(H_2O)_2[BP_2O_8]\cdot 0.6H_2O$ and $NH_4Fe^{III}[BP_2O_8(OH)]$ *Chem. Mater.*, **2001**, *13*, 4348-4354.

(29) Boy, I.; Schaefer, G.; Kniep, R. Crystal structure of sodium iron(II) diaquacatena-(monoboro-diphosphate) monohydrate $NaFe(H_2O)_2(BP_2O_8).(H_2O)$ and potassium iron(II) diaquacatena-(monoboro-diphosphate) hemihydrate, $KFe(H_2O)_2(BP_2O_8).0.5(H_2O)$ *Z. Kristallogr.*, **2001**, *216*, 13-14.

(30) Tao, L.; Rousse, G.; Sougrati, M. T.; Chotard, J.-N.; Masquelier, C. $(NH_4)_{0.75}Fe(H_2O)_2[BP_2O_8]\cdot 0.25H_2O$, a Fe^{3+}/Fe^{2+} Mixed Valence Cathode Material for Na Battery Exhibiting a Helical Structure *J. Phys. Chem. C* **2015**, *119*, 4540-4549.

(31) Menezes, P.W.; Hoffmann, S.; Prots, Yu.; Kniep, R. Crystal structure of lithium diaquacobalt(II) catena-(monoboro-diphosphate) monohydrate, $LiCo(H_2O)_2[BP_2O_8].H_2O$ *Z. Kristallogr.*, **2008**, *223*, 333-334.

(32) Boy, I.; Kniep, R. Crystal structure of lithium zinc diaqua catena-(monoborodiphosphate)-monohydrate $LiZn(H_2O)_2(BP_2O_8).H_2O$ *Z. Kristallogr.*, **2001**, *216*, 9-10.

(33) Boy, I.; Schaefer, G.; Kniep, R. Crystal structure of sodium nickel diaqua catena(monoboro-diphosphate) monohydrate, $NaNi(H_2O)_2(BP_2O_8).(H_2O)$, at 293 K and 198 K *Z. Kristallogr.*, **2001**, *216*, 11-12.

(34) Boy, I.; Schaefer, G.; Kniep, R. Crystal structure of sodium iron(II) diaquacatena-(monoboro-diphosphate) monohydrate $NaFe(H_2O)_2(BP_2O_8).(H_2O)$ and potassium iron(II) diaquacatena-(monoboro-diphosphate) hemihydrate, $KFe(H_2O)_2(BP_2O_8).0.5(H_2O)$ *Z. Kristallogr.*, **2001**, *216*, 13-14.

(35) Boy, I.; Stowasser, F.; Schaefer, G.; Kniep, R. $NaZn(H_2O)_2(BP_2O_8).(H_2O)$: A novel open framework borophosphate with CZP-Topology and its reversible dehydration to microporous sodium zincoborophosphate Na $(ZnBP_2O_8).(H_2O)$ *Chem.-Eur. J.,* **2001**, *7*, 834-839.

(36) Shi H.; Shan Y.; Dai L.; Liu Y.; Weng L. Crystal structure of borophosphate with 6_1 screw axis helices *Jiegon Huaxue*, **2003**, *22*, 391-394.

(37) Zhuang R.; Chen X.; Mi Lithium manganese diaquaborophosphate monohydrate, $LiMn(H_2O)_2[BP_2O_8].H_2O$ J. *Acta Crystallogr. E* **2008**, *64*, i46-i46.

(38) Yakubovich, O.V.; Steele, I.; Dimitrova, O.V. $Na(H_2O)[Mn(H_2O)_2(BP_2O_8)]$: Crystal structure refinement *Kristallografiya* **2009**, *54*, 20-25.

(39) Zheng, J.; Zhang, A. Lithium diaqua-nickel(II) catena-borodiphosphate(V) monohydrate *Acta Crystallogr. E* **2009**, *65*, i42-i42.

(40) Mingzhen, W. Crystal structure of potassium diaquamanganese(II) borophosphate monohydrate, $K[Mn(H_2O)_2(BP_2O_8)].H_2O$ *Z. Kristallogr.* **2012**, *227*, 3-4.

(41) Guesmi, A.; Driss, A. $KCo(H_2O)_2BP_2O_8.0.48H_2O$ and $K_{0.17}Ca_{0.42}Co(H_2O)_2BP_2O_8.H_2O$: two cobalt borophosphates with helical ribbons and disordered (K,Ca)/H_2O schemes *Acta Crystallogr. C* **2012**, *68*, i55-i59.

(42) Bruker- SMART. Bruker AXS Inc., Madison, Wisconsin, USA. **2002**.

(43) Bruker- SAINT and SADABS. Bruker AXS Inc., Madison, Wisconsin, USA, **2008**.

(44) Sheldrick, G. M. A short history of SHELX *Acta Cryst.* **2008**, *A64*, 112.

(45) Favre-Nicolin; V.; Cerny, R. FOX, 'free objects for crystallography': a modular approach to ab initio structure determination from powder diffraction *J. Appl. Cryst.* **2002**, *35*, 734-743.

(46) Toby, B. H.; Von Dreele, R. B. GSAS-II: the genesis of a modern open-source all-purpose crystallography software package *J. Appl. Cryst.* **2013**, *46*, 544-549.

(47) Lagarec, K.; Rancourt, D. G. Extended Voigt-based analytic lineshape method for determining N-dimensional correlated hyperfine parameter distributions in Mössbauer spectroscopy Nucl. Instrum. *Meth. Phys. Res. B* **1997**, 129, 266.

(48) Ciceo-Lucacel, R.; Radu, T.; Simon, P. V. Novel selenium containing boro-phosphate glasses: Preparation and structural study *Mater. Sci. Eng. C* **2014**, *39*, 61-66.

(49) Cotton, F. A.; Wilkinson, G. *Advanced Inorganic Chemistry*, Fourth edition, John Wiley and Sons, New York, **1980.**

(50) F. Menil, Systematic trends of the ^{57}Fe Mössbauer isomer shifts in (FeO_n) and (FeF_n) polyhedra. Evidence of a new correlation between the isomer shift and the inductive effect of the competing bond T-X (→ Fe) (where X is O or F and T any element with a formal positive charge) *J. Phys. Chem. Solids* **1985**, *46*, 763–789.

(51) Kuzmann, E.; Nagy, S.; Vértes, A.;Critical review of analytical applications of Mössbauer spectroscopy illustrated by mineralogical and geological examples *Pure Appl. Chem.*, **2003**, *75*, 801–858.

(52) Born, P.; Johansson, S.; Zick, K.; auf der Günne, J. S.; Dehnen, S.; Roling, B. $Li_{10}SnP_2S_{12}$: An Affordable Lithium Superionic Conductor *J. Am. Chem. Soc.* **2013**, *135*, 15694-15697.

(53) López, M. C.; Ortiz, G. F.; Dompablo, E. M. A.-d.; Tirado, An Unnoticed Inorganic Solid Electrolyte: Dilithium Sodium Phosphate with the Nalipoite Structure *J. Inorg. Chem.* **2014**, *53*, 2310-2316.

V. Combined Theoretical and Experimental Approach to the Discovery of Electrochemically Active Mixed Polyanionic Phosphatonitrates, $AFePO_4NO_3$ (A = NH_4/Li, K)

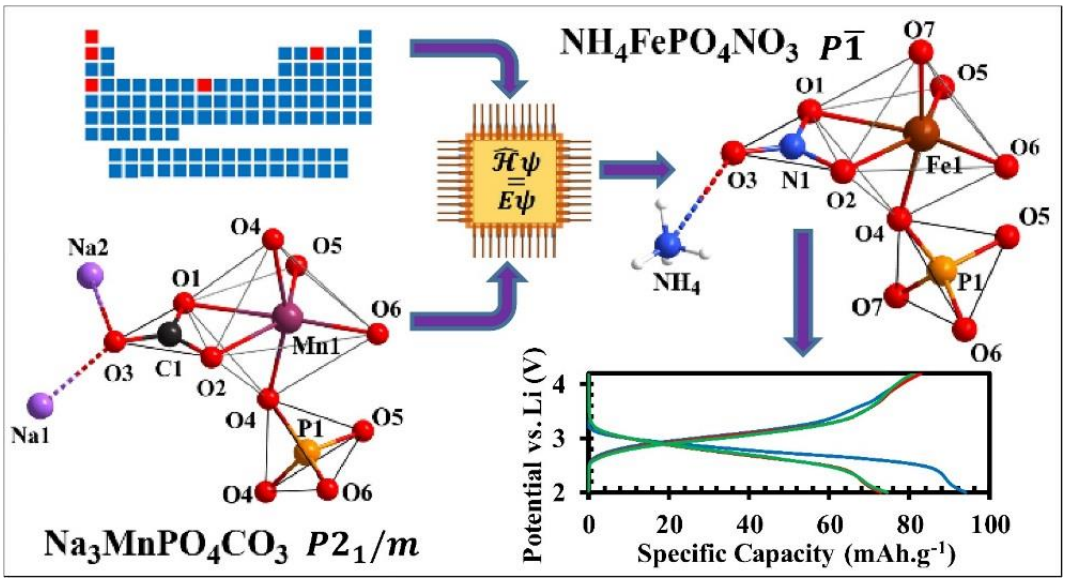

Hooman Yaghoobnejad Asl and Amitava Choudhury*

* Department of Chemistry, Missouri University of Science and Technology, Rolla, Missouri 65409, United States.

ABSTRACT: A new class of mixed polyanionic transition metal phosphatonitrate with the general formula $AFePO_4NO_3$ (A = NH_4/Li, K) has been synthesized following a computational predictive study based on DFT calculations. Structures of the crystalline products have been solved through synchrotron powder XRD and single-crystal XRD techniques. This class of materials exhibits the rare coordination of PO_4^{3-} and NO_3^- to a single transition metal center and is structurally related to the rare mineral bonshtedtite ($Na_3FePO_4CO_3$), which has been used as the initial model for predicting phosphatonitrates. $(NH_4)_{1-x}Li_xFePO_4NO_3$ has been found to be capable of reversible electrochemical Li- and Na-ion intercalation in the potential range 2.0—4.2 V at a theoretical capacity of ca. 116 $mAh.g^{-1}$. Various aspects of structural, chemical/electrochemical and spectroscopic features of $AFePO_4NO_3$ have been discussed in this article

INTRODUCTION

Recently great deal of efforts are being invested in high throughput (HT) calculation to discover new materials.[1–3] These computer led searches are inexpensive and good at determining the best material from the existing database and at the same time can predict new hypothetical composition and structure for a particular application.[4] Such HT searches for new cathode materials for Li-ion battery led by the Ceder group has helped in identifying new materials and discovering unknown compounds, thereby accelerating the pace of discovery.[5–9] This approach of combining computation and experiments especially in the case of cathode materials often narrows down the vast space of exploration to a very focused new chemistries, which can overcome the shortcomings of cost, energy density, safety and so on. In this search polyanionic chemistry is playing a crucial role because of the large inventory of polyanions, high degree of flexibility in crystal structure and composition, and wide range of Li^+ insertion voltage and capacities.[8, 9] More importantly, the idea of incorporation of a secondary polyanion in the metal polyanion compound adds another dimension to the rich chemistry of this class of materials and provides a tool for exploring new structures. Recently Ceder group has identified through HT computation a family of mixed polyanionic compounds related to the mineral sidorenkite, $Na_3MnPO_4CO_3$, and bonshtedtite, $Na_3FePO_4CO_3$, as potential two electron candidates.[10] These compounds have been experimentally realized[11–13] and $Na_3MnPO_4CO_3$ did show a two electron process in a Na-ion battery.[14] Inspired by this finding we designed a new class of compounds, namely phosphatonitrates, with no known natural mineral analogue. For the predicted new compounds we assumed that NO_3^- with planar trigonal geometry the same as CO_3^{2-} with one less negative charge keeping rest of the constituents the same will stabilize compositions with one less alkali ion in the formula unit when compared to the carbonate analogue at the same oxidation state of transition metals, *cf.* $A_3MPO_4CO_3$ and $A_2MPO_4NO_3$ (A = alkali ions), thus providing a higher theoretical capacity by keeping optimum number of alkali ions for a potential two electron process. A Further increase of the Li-insertion voltage can also be expected by virtue of inductive effect due to more electronegative nitrogen atom of

the nitrate in phosphatonitrate compared to a carbon atom in the carbonophosphate.[10] It is to be noted here that there are only a handful of compounds known where a nitrate and a phosphate coexist in the same structure.[15–17] The structural stability of these predicted composition was then validated through density functional theory (DFT), which also guided the synthesis of DFT-determined most stable targeted phases of Fe^{3+}, $AFePO_4NO_3$ (A = NH_4 and K) and subsequent structure determination using synchrotron powder and single-crystal X-ray diffraction data. For our initial efforts we chose Fe in +3 oxidation state for the ease of synthesis and to validate the model. The metastable Li/Na phases were synthesized *via* ion-exchange of the ammonium phase. This class of compounds may not only be interesting for alkali-ion intercalation battery applications, but also attractive from the chemical point of view as the coexistence of two mismatched polyanions, nitrate with planar geometry and phosphate with tetrahedral geometry in the asymmetric unit are expected to form more open structure amenable for host-guest chemistry. In this article we are reporting theoretical prediction and experimental development of a highly rare class of solids in the chemical inventory of transition metal compounds and their use as cathodes for lithium and sodium ion batteries.

EXPERIMENTAL SECTION

Methodology. The *ab initio* calculations for energy and geometry optimizations have been carried out with Quantum Espresso plane wave-based (PW) code.[18] Calculations were based on the nonlinear core corrected UltraSoft Pseudo-Potentials (USPPs) with Generalized Gradient Approximation (GGA) exchange-correlation functional parametrized according to the Perdew-Burke-Ernzerhof (PBE) method.[19] For systems containing Fe, all calculations have been performed in spin polarized mode with an antiferromagnetic ordering of the magnetic moments. The starting atomic coordinates have been taken from the mineral bonshtedtite, $Na_3FePO_4CO_3$ (ICSD no.77053) and geometry optimizations for the derived phosphatonitrate compounds have been performed with no constrain to the parent compound's space group. The variable cell relaxation

achieved in this way (via BFGS quasi-newton algorithm) is free to adopt lower or higher symmetries, as compared to the parent compound. For self-consistency calculations, an energy cutoff of 544 eV for wave function (and 5.4 keV for charge density) calculations has been set. The unit cell integrals have been evaluated by applying 90 k-points generated automatically by the Monkhorst-Pack method, [20] with a fixed k-point density of 0.216 $Å^{-1}$ along the reciprocal axes.

Details regarding evaluation of the accuracy of the employed functionals and other simulation parameters have been elaborated in the associated supporting information.

Reagents. NH_4NO_3 (certified ACS) has been purchased from Fisher Scientific, amorphous $FePO_4·4H_2O$ from Sigma-Aldrich, LiF (98.5%) and $Fe(NO_3)_3·9H_2O$ (ACS 98.0-101%) from Alfa Aesar, $LiNO_3$ (99+% extra pure), KNO_3 (99+% extra pure) and H_3PO_3 (98% extra pure) from Acros Organics, and Li foil (99.9%) and Na cubes (99.9%) from Aldrich. All the chemicals used as received without further purification.

Synthesis. Caution: Reactions involving solid NH_4NO_3 will explode if the mixture is heated above 200 °C. Close control of the temperature is required for safety reason.

$NH_4FePO_4NO_3$ has been synthesized by mixing 0.6686 g of $FePO_4·4H_2O$ (3 mmol) and 4.0020 g of NH_4NO_3 (50 mmol) which serves as both reagent and flux (T_m = 169 °C). The reaction was carried out in an open glass beaker and placed directly in an oven at 183 °C for a duration of 2 to 48 h. $(NH_4)_{0.96}Li_{0.06}FePO_4NO_3$ has been synthesized similarly as above, but with further addition of 0.0778 g (3 mmol) of LiF to the reaction mixture. The product in both cases consisted of finely divided yellow powder, which was then removed from the oven and cooled down to room temperature, washed thoroughly with cold water to remove the unreacted reagents, filtered and dried in air.

$KFePO_4NO_3$ has been formed as an impure phase by mixing 0.2419 g of (0.6 mmol) $Fe(NO_3)_3·9H_2O$, 0.0820 g of H_3PO_3 (1.0 mmol), and 0.0259 g of LiF (1.0 mmol) in a 3.5 g of KNO_3-$LiNO_3$ (0.56:0.44 mole ratio) eutectic mixture, which was used as the reactive molten salt flux and as a source of K^+ and NO_3^-

ions. The mixture was sealed in a Teflon-lined Paar reaction vessel and placed in an oven at 145 °C for 21 days. The product, which consisted of clear flat crystals of $KFePO_4NO_3$, white powders of tavorite, $LiFePO_4F$, and some other unidentified phase(s); was washed with hot water, filtered, and dried in air. Except for single-crystal structure solution the K-analogue was not used for any electrochemical experiments.

Ion-exchange. In a conical flask about 1 g of the $(NH_4)_{0.96}Li_{0.06}FePO_4NO_3$ powder was dispersed in 20 mL of water, following which 6.25 g of LiNO3 was dissolved in the suspension (1:20 mol ratio) and the conical flask was placed in an oven at 75 °C for a duration of 2 to 40 h. The resultant ion-exchanged powder was filtered and then thoroughly washed with deionized water and dried in a vacuum oven at 80 °C. The amount of Li+ loading in the formula unit was measured with atomic absorption spectroscopy as a function of time (vide infra).

Material Characterization. *Synchrotron Powder X-ray Diffraction.* The crystal structure of $(NH_4)_{0.96}Li_{0.06}FePO_4NO_3$ was solved from powder XRD pattern collected from the Argonne National Laboratory (ANL) Advanced Photon Source (APS) 11-BM beamline in a capillary holder. The Pattern was collected under ambient conditions using a parallel monochromated X-ray beam with a calibrated wavelength of 0.4139 Å over the Bragg angle range of 0.5—50 °.

The pattern was indexed in the $P\bar{1}$ space group and the intensities were extracted employing the LeBail method and subsequently used to solve the crystal structure by Monte-Carlo method using the FOX *ab initio* crystal structure solution package.[21]

The acquired atomic coordinates were then refined by Rietveld method employing Bruker DIFFRAC.SUITE TOPAS software, [22] to get the final crystal structure. Due to the existence of intensity mismatch induced by stacking faults and also peak broadening which leads to the rapid intensity loss at higher 2θ portion of the pattern, refinement of individual thermal displacement parameters was not possible. Therefore, all the atomic positions have been refined with the individual thermal parameters constrained to the average value for all the atoms (0.0127 $Å^2$). The observed intensity mismatch caused by stacking fault of the

layered structure as well as flaky nature of the crystallites, both induces a slight lack of long-range ordering in directions along and normal to the plane stacking and subsequent loss of diffraction intensity in those crystal directions. Note that the Li position could not be detected from the synchrotron powder X-ray diffraction data due to poor scattering power of lightweight lithium present in small percentage. Therefore, an analytically measured value of Li (6 %) was introduced in the ammonium site just for the sake of completion of the structure solution. Details of cell parameters and refinement residuals as well as atomic coordinates derived from Rietveld refinement are presented in Tables 1 and 2, respectively.

Single-Crystal X-ray Diffraction. The crystal structure of $KFePO_4NO_3$ was solved from single-crystal intensity data obtained from a Bruker Smart Apex diffractometer equipped with monochromated Mo Kα radiation (λ = 0.7107 Å). The single crystal of interest was glued to a glass fiber and the diffraction data were collected at room temperature through ω scan with step sizes of 0.3° at four equally spaced φ orientations.

Table 1. Crystal Data and Refinement Results for $(NH_4)_{0.94}Li_{0.06}FePO_4NO_3$

Empirical Formula		$(NH_4)_{0.94}Li_{0.06}FePO_4NO_3$	
a	9.67(8) Å	V	303.9(9) Å^3
b	6.22(2) Å	Space group	$P\bar{1}$
c	5.14(1) Å	number of reflections	630
α	91.2(4) °	R_p	0.061
β	79.6(8) °	R_{wp}	0.078
γ	93.1(9) °	number of data points	22503

The SMART software[23] was used for collecting the diffraction data while SAINT[24] was used for cell refinement, intensity extraction and data reduction. SADABS[24] was used for absorption correction and the crystal structure was solved employing direct methods using SHELX-97[25] software using difference Fourier syntheses. Full-matrix least squares refinement against $|F^2|$ was carried out using the SHELXTL-PLUS[25] suite of programs.

The unit cell was indexed in the $P\bar{1}$ space group and the atomic coordinates of one iron, one phosphorus and one potassium atom were found immediately following the direct methods. The positions of 7 oxygens and one nitrogen atom in the asymmetric unit have been located from the difference Fourier map.

Table 2. Atomic Coordinates for $(NH_4)_{0.94}Li_{0.06}FePO_4NO_3$

Atom	Wyck.	S.O.F.	x/a	y/b	z/c	Uiso (Å^2)[a]
Fe1	2i	1	0.36882	0.74678	0.25199	0.0127
P1	2i	1	0.42817	0.25207	0.33558	0.0127
O1	2i	1	0.86273	0.26517	0.79252	0.0127
O2	2i	1	0.53749	0.76816	0.38304	0.0127
O3	2i	1	0.33174	0.41658	0.31972	0.0127
O4	2i	1	0.96709	0.75065	0.58420	0.0127
O5	2i	1	0.34954	0.07613	0.23103	0.0127
N1	2i	1	0.08602	0.75143	0.48072	0.0127
O6	2i	1	0.81787	0.22550	0.38780	0.0127
O7	2i	1	0.55399	0.28954	0.11819	0.0127
N2	2i	0.94	0.20384	0.27299	0.90735	0.0127
Li1	2i	0.06	0.20384	0.27299	0.90735	0.0127

[a] Constrained

The iron atom was found to be in a highly distorted octahedral environment with two donor oxygen atoms supplied from a single nitrate group and the other four from the phosphate moiety. The potassium atom can be found in a 9 coordinated environment with K—O distances in the range from 2.82— 3.26 Å. Details of refinement parameters and crystal data along with the atomic coordinates and isotropic thermal displacement parameters are given in Tables 3 and 4, respectively.

Powder X-ray Diffraction. The laboratory X-ray diffraction patterns of the powdered samples have been collected on a PANalytical X'Pert Pro diffractometer using a Cu $K\alpha_{1,2}$ source and a linear array detector over the angular range of 5—90°.

Mössbauer Spectroscopy. The ^{57}Fe Mössbauer spectra of the ion-exchanged $(NH_4)_{0.75}Li_{0.25}FePO_4NO_3$ phase and the electrochemically reduced phase, $(NH_4)_{1-x}Li_{x+\delta}FePO_4NO_3$, have been acquired with a constant acceleration spectrometer equipped with a γ-emitting ^{57}Co source (25 mCi) embedded in Rh matrix. The spectra were obtained at ambient conditions with 60 mg of sample enclosed in a lead sample holder, with the velocity and chemical shifts calibrated against α-Fe foil and were fit by the Lorentzian function using the Recoil software.[26]

Table 3. Crystal Data and Refinement Results for $KFePO_4NO_3$

Empirical formula	$KFePO_4NO_3$	Formula weight	251.93 g.mol^{-1}
Crystal System	Triclinic	Space group	$P\bar{1}$
a	9.514(5) Å	Z	2
b	6.207(4) Å	V	294.4(3) Å^3
c	5.067(3) Å	ρ_{calc}	2.824 g.cm^{-3}
α	91.22(4) °	T	298(2) K
β	80.05(9) °	GOF on F^2	1.096
γ	92.93(7) °	F(000)	246
R [I>2σ(I)]		R1 = 0.0581, wR2 = 0.1405	
R [all data]		R1 = 0.0816, wR2 = 0.1740	

Acquisition of the electrochemically reduced cathode's spectrum has been carried out by assembling the cathode in a homemade pouch cell with 100 mg active material loading. Following the galvanostatic discharge, the cell was disassembled in the glovebox and the cathode film was washed with acetone to remove the electrolyte salt. The active material was then recovered from the current collector, loaded in the lead sample holder and sealed in polyethylene pouches to protect the sample against air oxidation during the data collection.

Atomic Absorption Spectroscopy (AAS). Several fractions of the ion-exchanged products have been removed from the oven at various times to study the rate of Li^+/NH_4^+ ion-exchange and hence determine the optimum reaction time. The powdered samples in contact with the concentrated $LiNO_3$ solution was

collected by filtration and washed with copious amounts of water to remove the unused $LiNO_3$, and dried in a vacuum oven at 80 °C for several hours.

The dried powders were weighed and dissolved in the minimum amount of 1:3 (v:v) solution of HNO_3(c):HCl(c) and diluted in volumetric flasks. Measurements for Li has been carried out with a PerkinElmer 2380 AA spectrometer at 670.8 nm and quantification has been done by standard addition method against standard solutions (Fluka) to eliminate the sample matrix effect. Furthermore, the weight fraction of the Li (0.2%) to the overall solid sample has been converted into mole fraction present in the formula unit (0.06 Li).

Table 4. Atomic Coordinates and Isotropic Thermal Displacement Parameters for $KFePO_4NO_3$

Atom	Wyck.	S.O.F.	x/a	y/b	z/c	Uiso ($Å^2$)[a]
Fe1	2i	1	0.36623	0.25078	0.24958	0.009(1)
P1	2i	1	0.43185	0.75641	0.31307	0.023(2)
O1	2i	1	0.33137	0.94296	0.32585	0.018(2)
O2	2i	1	0.46335	0.72403	0.59881	0.035(2)
O3	2i	1	0.57297	0.80557	0.12518	0.019(1)
O4	2i	1	0.35094	0.55853	0.21814	0.012(1)
N1	2i	1	0.09142	0.25543	0.45663	0.008(1)
O5	2i	1	0.18721	0.28107	0.59893	0.045(1)
O6	2i	1	0.96365	0.25603	0.55180	0.014(1)
O7	2i	1	0.13257	0.23304	0.20466	0.012(1)
K1	2i	1	0.80995	0.20684	0.10422	0.012(1)

[a] Uiso is defined as one third of the trace of the orthogonalized U_{ij} tensor.

Spectral and Thermal Analysis. The FT-IR spectrum of the as-synthesized sample ($(NH_4)_{0.96}Li_{0.06}FePO_4NO_3$) has been acquired with a Thermo Nicolet Nexsus-470 spectrometer with sample embedded in KBr pellet. TGA of the sample has been obtained using a TA Instruments Q50 thermogravimetric analyzer in the temperature range 25—800 °C at a heating rate of 10 °C.min^{-1} under the high-purity N_2 flow.

Coin Cell Fabrication and Testing. For the electrochemical lithiation and sodiation experiments CR2032 coin cells have been fabricated with the compound of interest acting as the cathode active material. In this regard the ion-exchanged sample, $(NH_4)_{0.75}Li_{0.25}FePO_4NO_3$, has been ball milled with conducting carbon and polyvinylidenefluoride (PVDF) binder in 75:15:10 ratio for 0.5 h. N-Methyl-2-pyrrolidone (NMP) then added to the powder mixture to dissolve the binder and resulting high viscosity paste was spread on the carbonized aluminum current collector as a film of uniform thickness using a spacer and glass rod. The obtained composite cathode was then dried in vacuum oven at 80 °C overnight to evaporate the NMP. Circular disk of 3/8 in. in diameter was cut through the cathode film (5 mg of active material loading) and transferred into an Ar filled glovebox (oxygen level < 2 ppm) for coin cell assembly. Li-ion cells were fabricated from the above cathode with Celgard 2325 as the separator, Li foil as the anode and 1 M $LiPF_6$ in (1:1 v:v) dimethyl carbonate-ethylene carbonate (DMC-EC) solution used as the electrolyte. The Na-ion cells were fabricated in the same manner as Li-ion cells, however, a Whatman GF/A glass microfiber sheet was used as the separator and a 1 M $NaClO_4$ in (1:1 v:v) dimethyl carbonate-ethylene carbonate (DMC-EC) solution used as the electrolyte. An Arbin Instruments battery tester (Model BT2403) was employed for running the galvanostatic charge-discharge experiments in a potential range of 4.2— 2.0 V and 4.0— 2.0 V for Li-ion and Na-ion cells, respectively.

RESULTS AND DISCUSSION

DFT predictions, synthesis and structure. In our DFT calculation we initially used the crystal structure of $Na_3FePO_4CO_3$ as the starting model with the carbonate moiety replaced by NO_3^-. The structure has been completed with different monovalent cations (Li^+, Na^+, K^+, and NH_4^+) mainly for iron in the +3 oxidation state, and has been subjected to geometry optimization.

As a first approximation, the stabilization energy for each predicted compound was estimated by comparing the converged total energy of the products with respect to the reactants according to the eq 1:

$$ANO_3 + FePO_4 \rightarrow AFePO_4NO_3 \quad (1);$$

where *A* = Li, Na, K, and NH_4. The resulting stabilization energies and unit cell parameters are presented in Table 5. Although construction of the convex Hull surface may be required for exact determination of the feasibility of a reaction, the above procedure may provide a quick estimate regarding the relative stability of each phase with respect to its reactants.

The results of DFT geometry optimization runs provided in Table 5 suggest that as long as stabilization energies are concerned, except for $NaFePO_4NO_3$, all other phases should be stable. However, given the intrinsic uncertainty in DFT calculations, $LiFePO_4NO_3$ may also fall in the unstable region due to the relatively narrow stabilization energy margin, leaving $KFePO_4NO_3$ and $NH_4FePO_4NO_3$ as the potentially stable compounds with the assumed layered structure as in parent carbonophosphate.[11, 12]

Among the most stable pair of predicted compounds, synthesis of $NH_4FePO_4NO_3$ was attempted first via a direct reaction between amorphous $FePO_4 \cdot 4H_2O$ and NH_4NO_3 through a fast molten salt approach at 185 °C, at which temperature $FePO_4 \cdot 4H_2O$ dehydrates to the disordered $FePO_4$ (the disordered $FePO_4$ phase crystallizes to quartz phase of $FePO_4$ at higher temperatures as shown in the Supporting Information, Figure S1).The product was formed as a finely divided powder with quantitative yield within only 2 h of the reaction initiation (Supporting Information, Figure S2).

Interestingly we found that introduction of a small amount of Li^+ into the structure by adding LiF during the synthesis leads to the formation of solid-solution $(NH_4)_{1-x}Li_xFePO_4NO_3$ phase with considerably improved crystallinity of the product compared to the pure $NH_4FePO_4NO_3$, as observed through XRD peak intensities (Supporting Information, Figure S3).

The chemical (nitrogen and lithium analysis) and spectroscopic (FTIR and Mössbauer) analysis (*vide infra*) of $(NH_4)_{1-x}Li_xFePO_4NO_3$ clearly indicated presence of ammonium, nitrate, phosphate, lithium, and Fe into the structure. Assuming the formation of iron phosphatonitrate crystalline phase, an *ab initio* structure solution from synchrotron powder X-ray diffraction data was initiated.

The crystal structure of the crystalline powder was immediately solved and as expected the composition was determined to be $(NH_4)_{1-x}Li_xFePO_4NO_3$ [x = 0.06]. The compound, $(NH_4)_{1-x}Li_xFePO_4NO_3$, crystallizes in the triclinic crystal system, space group $P\bar{1}$ with lattice parameters; a = 9.67(8) Å, b = 6.22(2) Å, c = 5.14(1) Å, α = 91.2(4)°, β = 79.6(8)°, γ = 93.1(9)°, and V = 303.9(9) Å^3, in an excellent agreement with DFT prediction. The Rietveld refinement of the *ab-initio* solved coordinates from FOX software converged very well (Figure 1).

Table 5. DFT Results of Stabilization Energies and Lattice Parameters for the Predicted $AFePO_4NO_3$ phases

compound	$\Delta E_s^{\dagger}$ (kJ/mol)	crystal system	lattice parameters
$LiFePO_4NO_3$	-21.67	Orthorhombic	a = 9.48, b = 6.40, c = 5.34 Å, V = 324.61 Å^3
$NaFePO_4NO_3$	+10.63	Triclinic	a = 9.02, b = 6.30, c = 4.94 Å, α = 90.01, β = 84.94, γ = 91.06 ° ; V = 279.19 Å^3
$KFePO_4NO_3$	-147.27	Triclinic	a = 9.73, b = 6.06, c = 5.20 Å, α = 89.98, β = 82.09, γ = 91.48 ° ; V = 303.14 Å^3
$NH_4FePO_4NO_3$	-110.08	Triclinic	a = 9.80, b = 6.24, c = 5.12 Å, α = 90.0, β = 78.27, γ = 91.14 ° ; V = 306.57 Å^3

† referred to the reaction outlined in eq 1.

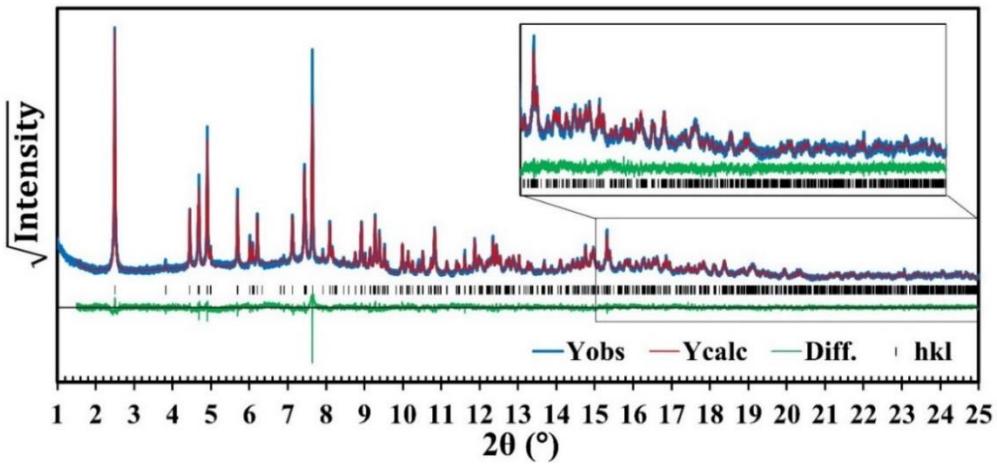

Figure 1. Rietveld refinement of the synchrotron powder XRD pattern of $(NH_4)_{1-x}Li_xFePO_4NO_3$ showing the observed and calculated intensity based on the structure presented in Figure 2.

It is to be noted here that both sidorenkite ($Na_3MnPO_4CO_3$) and bonshtedtite ($Na_3FePO_4CO_3$) crystallize in the monoclinic crystal system (space group, $P2_1/m$). Our efforts to grow single crystal of $(NH_4)_{1-x}Li_xFePO_4NO_3$ by employing different flux failed due to low decomposition temperature caused by the presence of ammonium (discussed later). On the other hand due to the high melting point of KNO_3, formation of the $KFePO_4NO_3$ was not possible through a direct reaction with $FePO_4 \cdot xH_2O$. However, after many attempts very thin plate-like clear crystals of $KFePO_4NO_3$ were obtained in a mixture with tavorite-$LiFePO_4F$, and other impurity phases from a low temperature molten salt synthesis after 3 weeks using nitrate rich KNO_3-$LiNO_3$ eutectic flux (Supporting Information, Figure S4).

Structure of $KFePO_4NO_3$ was solved from single-crystal X-ray diffraction data, which confirmed that $KFePO_4NO_3$ is isostructural with $NH_4FePO_4NO_3$, with lattice parameters a = 9.514(5) Å, b = 6.207(4) Å, c =5.067(3) Å, α = 91.22(4)°, β = 80.05(9)°, γ = 92.93(7)°, and V = 294.4(3) Å^3, consistent with DFT calculations but showing slight deviations from the predicted values. Successful single-crystal solution of the K-analogue also validated the *ab-initio* structure solution of the mixed NH_4/Li phase in the $P\bar{1}$ space group.

Figure 2 shows the asymmetric unit and local environment in the $(NH_4)_{1-x}Li_xFePO_4NO_3$. The iron atom is in highly distorted FeO_6 octahedral coordination receiving four oxygen donors from the phosphate tetrahedral moiety and the remaining two cis-coordinations are filled by oxygen atoms from a single nitrate moiety. The third oxygen of the nitrate has a short O7—N1 bond length of 1.23(4) Å consistent with the terminal N=O bond and participates in the coordination of the monovalent cation, probably through hydrogen-bonding in case of ammonium and ionic interactions in the case of pure alkali ions. It is worth mentioning that our efforts to form pure $LiFePO_4NO_3$ and $NaFePO_4NO_3$ from direct synthesis did not yield any crystalline product, in complete agreement with the stabilization energy calculations outlined above.

The results of bond valence sum (BVS) calculations performed on the monovalent cation site unequivocally prove that the site is majorly occupied by

NH_4^+ ions (BVS = 0.98) and not Li^+ ions (BVS = 0.12). Moreover, BVS analysis confirms the oxidation states of Fe as +3 (BVS=3.02) and P as +5 (BVS=4.92). In addition, the results of atomic absorption spectroscopy (AAS) revealed that the compound contains 6 % Li^+ in the monovalent cation site. As a result, the overall composition of the as-synthesized material can be derived as $(NH_4)_{0.94}Li_{0.06}FePO_4NO_3$. It is worth noting that the Li^+ position could not be located from the Fourier map, presumably due to poor scattering from a small percentage of Li.

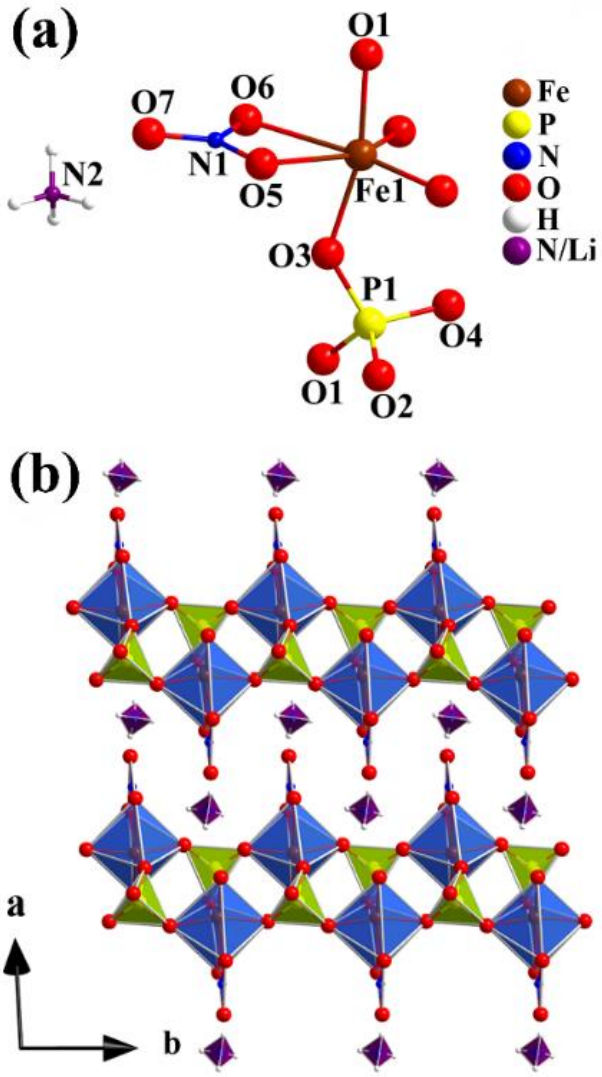

Figure 2. (a) Connectivity pattern in the building block of $(NH_4)_{1-x}Li_x\ FePO_4NO_3$ as determined through ab-initio crystal structure solution of the synchrotron powder XRD. (b) Packing diagram showing the stacking of the layers along [100].

The packing of asymmetric units exhibits the layered nature of the phase similar to carbonophosphates.[10] Corner sharing of alternative FeO_6 and PO_4 polyhedral units forms the $FePO_4$ layer along the (011) plane. The nitrate moiety is coordinated to the iron center and disposed normal to the $FePO_4$ plane. The layers are then stacked along [100] direction (Figure 2b) with the monovalent cations distributed in the interlayer space.

Thermogravimetric analysis performed on vacuum dried samples shows that the as-prepared $(NH_4)_{0.94}Li_{0.06}FePO_4NO_3$ is essentially stable up to 300 °C, after which the structure collapses through an abrupt mass loss of ~ 30% due the loss of delicate nitrate and ammonium moieties, forming majorly $FePO_4$, $Fe_7(PO_4)_6$ and other minority phases (Supporting Information, Figures S5 and S6).

Complementary FT-IR spectroscopic analysis confirms the existence of ammonium N—H stretching and bending modes at 3260 and 1410 cm^{-1}, respectively, while the nitrate N—O stretching modes are visible at 1530 and 1310 cm^{-1}. (Supporting Information, Figure S7).

Electrochemistry. Similar to $Li_3FePO_4CO_3$ and $Na_3MnPO_4CO_3$, the synthesized phosphatonitrate compounds should be able to intercalate alkali ions due to flexibility in the framework.

Accordingly, the first cycle voltage-composition profile for the as-synthesized and ion-exchanged material in a RC2032 type coin cell assembled with Li metal as the reference and counter electrode is depicted in Figure 3(a). The iron center in $(NH_4)_{0.94}Li_{0.06}FePO_4NO_3$ is in the higher oxidation state of +3 and therefore, the cell can be discharged by reductive insertion of Li^+. The discharge profile starts from an OCV value of 3.17 V (vs. Li^+/Li) and reduces monotonically in a sloppy manner as the cathode host material is being lithiated, reminiscent of a single phase solid-solution formation between redox couples.

The discharge continues until insertion of 0.35 Li^+ at which value the discharge ends as it reaches the lower cutoff potential of 2.0 V. Being capable of inserting one complete Li^+ ion per formula unit, it provides a specific discharge capacity of about 116 $mAh.g^{-1}$ for the active material. One possible explanation for the small observed discharge capacity could be the presence of large grain sizes

in the as-synthesized compound and the existence of bulky NH_4^+ ions in the interlayer space. Both these factors have the tendency to hinder the diffusion of Li^+ ions in and out of the crystal during the cell operation (Figure 4). As depicted in Figure 4, the major calculated pathways for Li^+ diffusion according to bond valence sum analysis, using the Bond_Str routine within the FullProf Suite,[27] are located between the layers.

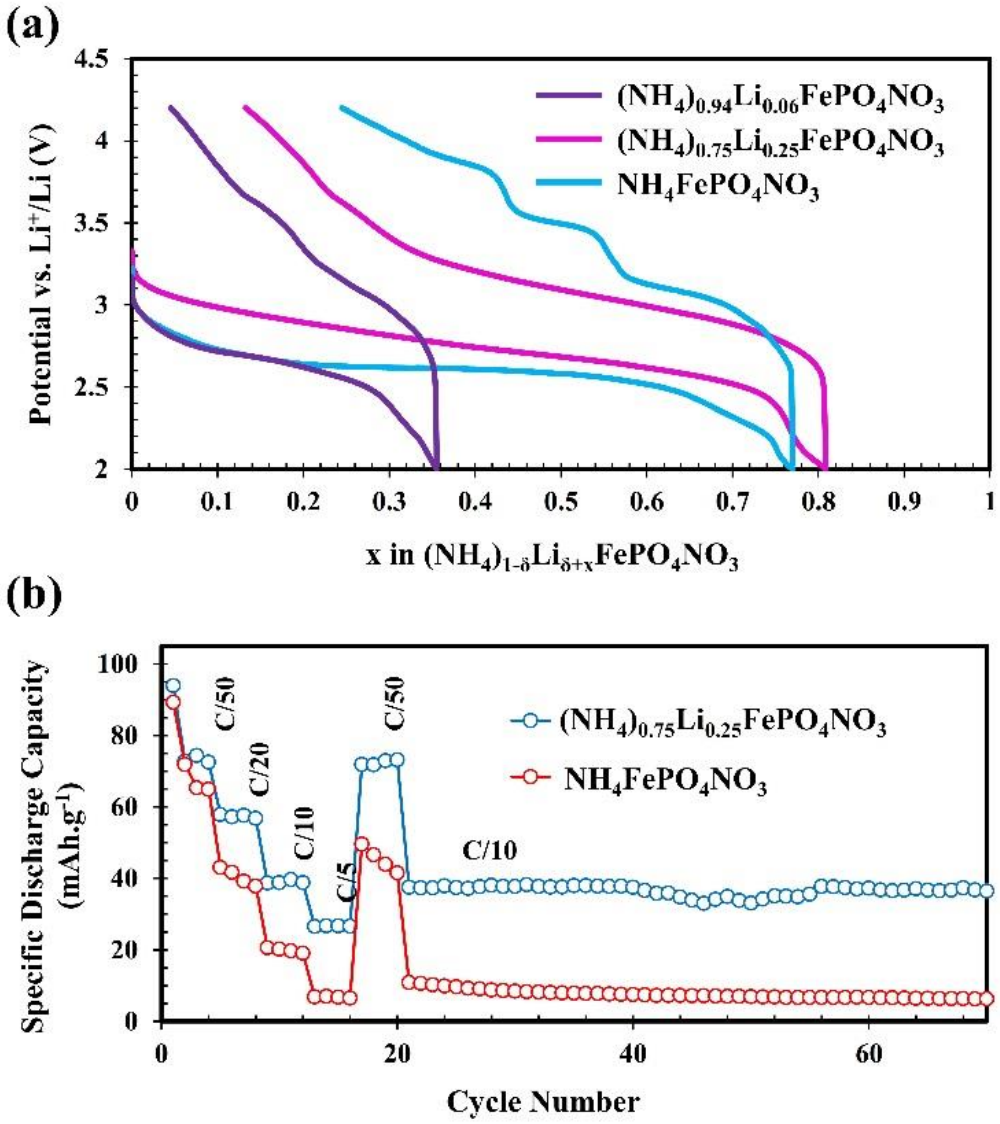

Figure 3. (a) First cycle voltage-composition profiles for: $(NH_4)_{0.94}Li_{0.06}FePO_4NO_3$, $(NH_4)_{075}Li_{0.25}FePO_4NO_3$ and $NH_4FePO_4NO_3$ at C/50. (b)The capacity retention for $(NH_4)_{0.75}Li_{0.25}FePO_4NO_3$and $NH_4FePO_4NO_3$.at various C-rates.

Occupation of these paths by NH_4^+ groups effectively blocks Li^+ diffusion leading to low utilization of theoretical capacity. To alleviate this problem, aqueous ion-exchange (IEX) method was utilized to exchange the ammonium ions topotactically with Li^+. With the employed IEX conditions (see Experimental Section), it was found that the Li content of the compound can be increased rapidly from 6 to 25 % mole fraction in the first 5 h of the IEX (Supporting Information, Figure S8).

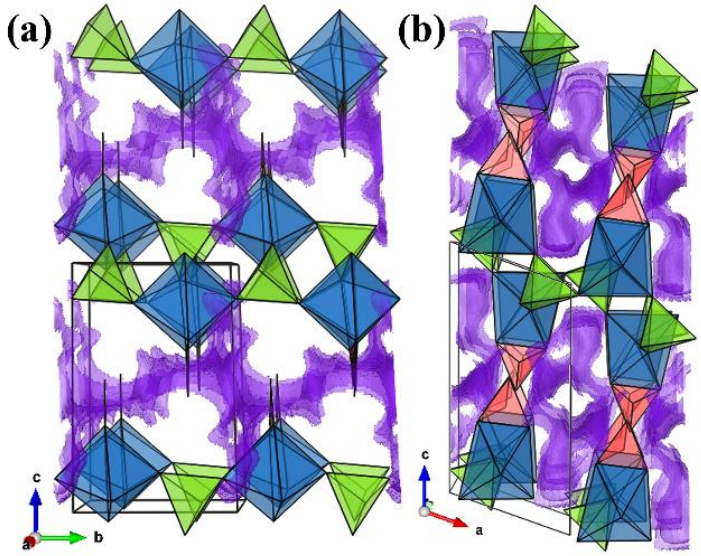

Figure 4. Calculated BVS isosurface at the value 1.0 for Li^+ in $NH_4FePO_4NO_3$ along (a) [100]; and (b) [010]. Polyhedral guide, blue: FeO_6, green: PO_4, red: NO_3. NH_4^+ ions have been removed for clarity of visualization.

However, the material resisted against further ion exchange and extending IEX time decreased the Li content gradually. This has been assigned to the slow dissolution of nitrate and subsequent phase transformation to $Fe_5(PO_4)_4(OH)_3{\cdot}2H_2O$, as it was evident from powder XRD pattern of the IEX sample after 40 h (Supporting Information, Figure S9). The resistance of the $(NH_4)_{0.75}Li_{0.25}FePO_4NO_3$ phase for further exchange of Li^+ with NH_4^+ ions also suggests the instability of pure $LiFePO_4NO_3$ phase as seen in the DFT results.

Despite the incomplete exchange between NH_4^+ and Li^+ ions after 5 h, repeating the charge-discharge studies on the ion-exchanged sample, $(NH_4)_{0.75}Li_{0.25}FePO_4NO_3$, reveals a significant improvement in the discharge

capacity, as almost 80% of the theoretical capacity can be obtained during the first cycle (Figure 3(a)). Moreover, complete capacity utilization has also been observed for the ion-exchanged sample at 40 °C at a C-rate of C/100, implying the existence of thermally activated processes (ionic diffusion and charge transfer). The ion-exchanged sample exhibits an average voltage of 2.9 V, comparable to the $Li_3FePO_4CO_3$.[11]

Study of electrochemical insertion of Li^+ in pure $NH_4FePO_4NO_3$ exhibits a 76% of theoretical capacity utilization during the first cycle (Figure 3(a)). This substantial capacity achievement compared to as-synthesized $(NH_4)_{0.94}Li_{0.06}FePO_4NO_3$ has been assigned to a very fine crystallite formation during the synthesis, as evident from the broad Bragg's peak of the $NH_4FePO_4NO_3$ phase (Supporting Information, Figure S3) and the particle size comparison analyses of the as-synthesized $NH_4FePO_4NO_3$ and $(NH_4)_{0.94}Li_{0.06}FePO_4NO_3$ phases, through SEM imaging (Supporting Information, Figure S10). Moreover, a close inspection of the flat discharge profile indicates that lithiation of pure $NH_4FePO_4NO_3$ follows a two-phase reaction mechanism, as opposed to the ion-exchanged $(NH_4)_{0.75}Li_{0.25}FePO_4NO_3$ phase. However, on the start of the second discharge the voltage-composition curve mimics the sloppy nature of the $(NH_4)_{0.75}Li_{0.25}FePO_4NO_3$ phase (Supporting Information, Fig. S11), indicating an irreversible solid-solution formation during the first cycle. The lower capacity achieved in the case of $(NH_4)_{0.94}Li_{0.06}FePO_4NO_3$ may be also due to formation of more stable Li^+—NH_4^+ ordered mixed cationic phase, compared to the pure $NH_4FePO_4NO_3$ as observed previously for cation ordering in mixed $Na_{1-x}Li_xNi_{0.5}Mn_{0.5}O_2$ and generally in cation-vacancy ordering in alkali transition metal oxides.[28,29] On the other hand breaking of such ordering in $(NH_4)_{0.94}Li_{0.06}FePO_4NO_3$, through compositional change induced by Li^+ ion exchange as in $(NH_4)_{0.75}Li_{0.25}FePO_4NO_3$ may create a phase which suffers less from preferred ordering of cations resulting in improved electrochemical performance. The results for the capacity retention for both phases are given in the inset of Figure 3(b).

The two phases lose some 20% of their capacity irreversibly at the end of the first cycle; however, as the cells are subjected to charge-discharge tests at higher C-rates, both phases lose some capacity due to kinetically induced ionic and electronic polarization factors; however, $NH_4FePO_4NO_3$ loses its capacity much more rapidly compared to the ion-exchanged phase. As the cells are returned to the slow C/50 rate (cycles 17-20), $(NH_4)_{0.75}Li_{0.25}FePO_4NO_3$ recovers the initial second cycle capacity (~73 $mAh.g^{-1}$), unlike the $NH_4FePO_4NO_3$, showing only 38 $mAh.g^{-1}$. The results of capacity retention suggest that even after 70 cycles at C/10, $(NH_4)_{0.75}Li_{0.25}FePO_4NO_3$ exhibits no capacity loss (compared to the cycles 9-12) due to aging processes, while the achievable capacity for the pure ammonium phase becomes negligible under similar condition. This reconfirms the added diffusion resistance induced by ammonium ions, as discussed previously. Another noticeable feature of the ion-exchanged phase is that the discharge voltage is at least 0.15 V higher than the pure ammonium phase.

Following the reversible electrochemical intercalation of Li^+ ions in $(NH_4)_{0.75}Li_{0.25}FePO_4NO_3$ host structure, the activity of the phase has been tested for Na^+ insertion in a Na-ion cell setup (Figure 5).

The voltage-composition curves for sodiation share common features with the lithium insertion experiments. However, sodiation starts at the lower potential of 2.7 V (vs. Na^+/Na) as a result of lower (absolute value) reduction potential of sodium compared to the lithium (-2.71 vs. -3.04 wrt. SHE, respectively).

The (de)intercalation process advances through a sloppy profile, evidencing solid-solution formation between the end members. The capacity retention curve (Figure 5-inset) demonstrates that the Na-ion cell retains 80% of its capacity after going through a series of relatively higher C-rate charge-discharge tests. However, the performance is inferior to Li-ion cell, especially at high C-rates as a result of larger Na^+ ionic radii and consequently slower diffusion kinetics.

Ex Situ Mössbauer Spectroscopy. Mössbauer spectroscopy has been utilized as an ex situ technique to follow the changes in the oxidation state and local environment of redox active iron center in the $(NH_4)_{0.75}Li_{0.25}FePO_4NO_3$ and the electrochemically lithiated materials (Figure 6). The asymmetry observed in

the absorption bands of $(NH_4)_{0.75}Li_{0.25}FePO_4NO_3$ (Figure 6a) indicates large chemical disorder in the local environment of Fe(III) centers, probably due to the mixing of Li^+ and NH_4^+ leading to stacking faults of the layers. In addition, the preferred orientation of the crystallites as also observed in Rietveld refinement can cause asymmetry in the Mössbauer spectrum.[30] Therefore, two doublets were used for Lorentzian fitting of the observed intensity data, but only the overall fit is shown in Figure 6a.

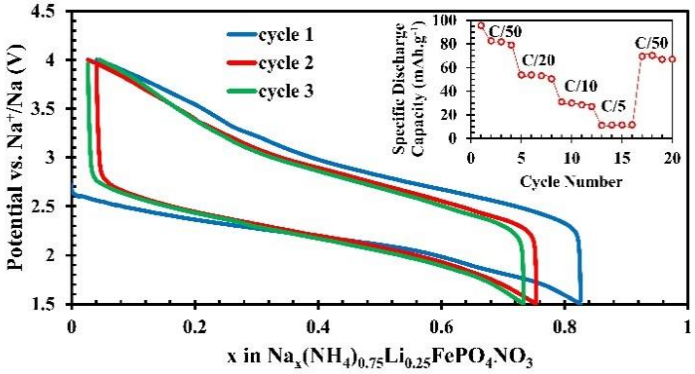

Figure 5. Voltage-composition profiles of $(NH_4)_{0.75}Li_{0.25}FePO_4NO_3$ phase cathode in a Na-ion cell at C/50. Inset shows the capacity retention at various C-rates.

The Mössbauer spectrum of the lithiated phase at the end of C/10 discharge is shown in Figure 6b. The emergence of an absorption band at higher chemical shift and quadrupole splitting confirms the reduction of Fe(III) to Fe(II). Again, the local disorder for Fe(II) is evident from the broadness of the absorption doublet, and suggests that all Fe(III) sites contribute to reduction during cell discharge. Details of the chemical shift and quadrupole splitting for the Mössbauer spectra are provided in Table 6 and the values are typical for Fe(III) and Fe(II) in high-spin configuration in oxidic materials.[31]

CONCLUSION

In conclusion, we have successfully theoretically predicted and experimentally realized a new family of mixed polyanionic solid combining nitrate and phosphate into one structure. Electrochemical studies indicate these phosphatonitrates are electrochemically active with respect to insertion and deinsertion of lithium and sodium ions. Ease of

synthesis, good reversibility and flexible framework, which is able to accommodate different alkali ions will instigate exploration of synthesis with other metals such as Mn, which can improve the insertion voltage and can undergo more facile two electron process for eventual practical applications.

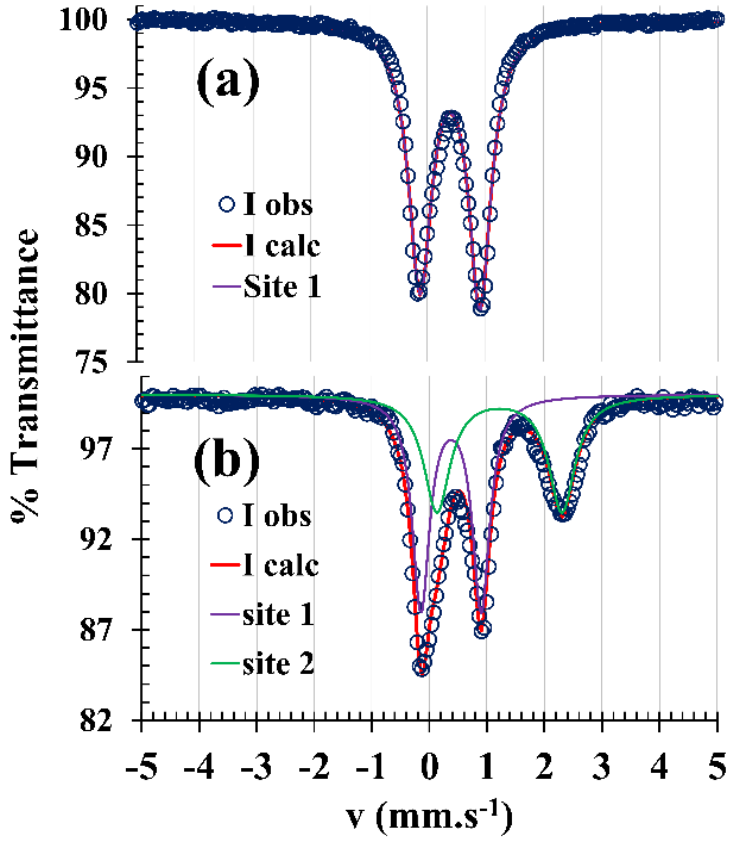

Figure 6. Mössbauer spectrum of $(NH_4)_{0.75}Li_{0.25}FePO_4NO_3$ (a), and electrochemically lithiated $(NH_4)_{1-x}Li_{x+\delta}FePO_4NO_3$ (b).

Table 6. Values of chemical shift (C.S.), quadrupole splitting (Q.S.), and population analysis of the ion-exchanged sample $(NH_4)_{0.75}Li_{0.25}FePO_4NO_3$ and the respective electrochemically reduced phase, $(NH_4)_{0.75}Li_{0.25+x}FePO_4NO_3$

$(NH_4)_{0.75}Li_{0.25}FePO_4NO_3$			
	C.S. ($mm.s^{-1}$)	Q.S. ($mm.s^{-1}$)	Site %
Fe(III) Site 1	0.390(4)	1.121(9)	70.4(3)
Fe(III) Site 2	0.412(9)	0.607(2)	29.6(3)
$(NH_4)_{0.75}Li_{0.25+x}FePO_4NO_3$			

Table 6. Values of chemical shift (C.S.), quadrupole splitting (Q.S.), and population analysis of the ion-exchanged sample $(NH_4)_{0.75}Li_{0.25}FePO_4NO_3$ and the respective electrochemically reduced phase, $(NH_4)_{0.75}Li_{0.25+x}FePO_4NO_3$ (cont.)

	C.S. ($mm.s^{-1}$)	Q.S. ($mm.s^{-1}$)	Site %
Fe(III) site 1	0.376(6)	1.047(3)	54.4(1)
Fe(II) site 2	1.218(1)	2.173(1)	45.6(1)

ASSOCIATED CONTENT

Supporting Information

Details of DFT Functional accuracy testing, CIF file of KFePO4NO3, PXRD of heat-treated $FePO_4 \cdot 4H_2O$, ex-situ time evolution PXRD of synthesis of $(NH_4)_{0.94}Li_{0.06}FePO_4NO_3$, PXRD of as-synthesized $NH_4FePO_4NO_3$ and $KFePO_4NO_3$; IR, TGA, of $(NH_4)_{0.94}Li_{0.06}FePO_4NO_3$, atomic absorption evolution of ion-exchange product of $(NH_4)_{0.94}Li_{0.06}FePO_4NO_3$ and PXRD of the 40 h ion-exchanged product; SEM micrographs of as-synthesized $(NH_4)_{0.96}Li_{0.06}FePO_4NO_3$ and $NH_4FePO_4NO_3$, And voltage composition profiles of $NH_4FePO_4NO_3$ after 2nd cycle. This material is available free of charge via the Internet at http://pubs.acs.org

AUTHOR INFORMATION

Corresponding Author.

* choudhurya@mst.edu

Department of Chemistry, Missouri University of Science and Technology, Rolla, MO 65409, USA.

ACKNOWLEDGMENT

The authors acknowledge the funding from Energy Research and Development Center (ERDC) and University of Missouri Research Board. Use of the Advanced Photon Source at Argonne National Laboratory was supported by the U.S. Department of Energy, Office of Science, Office of Basic Energy Sciences, under Contract No. DE-AC02-06CH11357.

REFERENCES

(1) Hautier, G.; Fischer, C. C.; Jain, A.; Mueller, T.; Ceder, G. Finding Nature's Missing Ternary Oxide Compounds Using Machine Learning and Density Functional Theory. *Chem. Mater.* **2010**, *22*, 3762−3767.

(2) Curtarolo, S.; Hart, G. L. W.; Nardelli, M. B.; Mingo, N.; Sanvito, S.; Levy, O. The high-throughput highway to computational materials design. *Nat. Mater.* **2013**, *12*, 191−201.

(3) Gautier, R.; Zhang, X.; Hu, L.; Yu,L.; Lin, Y.; Sunde, T. O. L.; Chon, D.; Poeppelmeier, K. R.; Zunger, A. Prediction and accelerated laboratory discovery of previously unknown 18-electron ABX compounds. *Nat. Chem.* **2015**, 7, 308−316.

(4) Yan, F.; Zhang, X.; Yu, Y. G.; Yu, L.; Nagaraja, A.; Mason, T. O.; Zunger, A. Design and discovery of a novel half-Heusler transparent hole conductor made of all-metallic heavy elements. *Nat. Commun.* **2015**, *6*, 7308.

(5) Ceder, G.; Chiang, Y.-M.; Sadoway, D. R.; Aydinol, M. K.; Jang, Y.-I.; Huang, B. Identification of cathode materials for lithium batteries guided by first-principles calculations. *Nature* **1998**, *392*, 694−696.

(6) Ceder, G. Opportunities and challenges for first-principles materials design and applications to Li battery materials. *MRS Bull.* **2010**, *35*, 693−701.

(7) Ceder, G.; Hautier, G.; Jain, A.; Ong, S. P. Recharging lithium battery research with first-principles methods. *MRS Bull.* **2011**, *36*, 185−191.

(8) Hautier, G.; Jain, A.; Ong, S. P.; Kang, B.; Moore, C.; Doe, R.; Ceder, G. Phosphates as Lithium-Ion Battery Cathodes: An Evaluation Based on High-Throughput ab Initio Calculations. *Chem. Mater.* **2011**, *23*, 3495−3508.

(9) Mueller, T.; Hautier, G.; Jain, A.; Ceder, G. Evaluation of Tavorite-Structured Cathode Materials for Lithium-Ion Batteries Using High-Throughput Computing. *Chem. Mater.* **2011**, *23*, 3854−3862.

(10) Hautier, G.; Jain, A.; Chen, H.; Moore, C.; Ong, S. P.; Ceder, G. Novel mixed polyanions lithium-ion battery cathode materials predicted by high-throughput ab initio computations. *J. Mater. Chem.* **2011**, *21*, 17147−17153.

(11) Chen, H.; Hautier, G.; Jain, A.; Moore, C.; Kang, B.; Doe, R.; Wu, L.; Zhu, Y.; Tang, Y.; Ceder, G. Carbonophosphates: A New Family of Cathode Materials for Li-Ion Batteries Identified Computationally. *Chem. Mater.* **2012**, *24*, 2009−2016.

(12) Chen, H.; Hautier, G.; Ceder, G. Synthesis, Computed Stability, and Crystal Structure of a New Family of Inorganic Compounds: Carbonophosphates. *J. Am. Chem. Soc.* **2012**, *134*, 19619−19627.

(13) Huang, W.; Zhou, J.; Li, B.; Ma, J.; Tao, S.; Xia, D.; Chu, W.; Wu. Z. Detailed investigation of $Na_{2.24}FePO_4CO_3$ as a cathode material for Na-ion batteries. *Sci. Rep.* **2014**, *4*, 4188.

(14) Chen, H.; Hao, Q.; Zivkovic, O.; Hautier, G.; Du, L.; Tang, Y.; Hu, Y.; Ma, X.; Grey, C. P.; Ceder, G. Sidorenkite ($Na_3MnPO_4CO_3$): A New Intercalation Cathode Material for Na-Ion Batteries. *Chem. Mater.* **2013**, *25*, 2777−2786.

(15) Durif, A.; Tordjman, I.; Masse, R.; Guitel, J. –C. Structure cristalline du nitro-phosphate mercureux: $Hg_4PO_4NO_3,H_2O$. *J. solid. State Chem.* **1978**, *24*, 101−105.

(16) Ivashkevich, L.S.; Lyakhov, A.S.; Selevich, A.F.; Petrusevich, Yu.I. The crystal structure of $Er(HPO_4)(NO_3)\cdot 3H_2O$: ab initio determination from X-ray powder diffraction data. *Z. Kristallogr.* **2003**, *218*, 475−479.

(17) Wylie, E. M.; Dawes, C. M.; Burns, P. C. Synthesis, structure, and spectroscopic characterization of three uranyl phosphates with unique structural units. *J. solid State Chem.* **2012**, *196*, 482−488.

(18) Giannozzi, P.; Baroni, S.; Bonini, N.; Calandra, M.; Car, R.; Cavazzoni, C.; Ceresoli, D.; Chiarotti, G. L.; Cococcioni, M.; Dabo, I.; Dal Corso, A.; Fabris, S.; Fratesi, G.; de Gironcoli, S.; Gebauer, R.; Gerstmann, U.; Gougoussis, C.; Kokalj, A.; Lazzeri, M.; Martin-Samos, L.; Marzari, N.; Mauri, F.; Mazzarello, R.; Paolini, S.; Pasquarello, A.; Paulatto, L.; Sbraccia, C.; Scandolo, S.; Sclauzero, G.; Seitsonen, A. P.; Smogunov, A.; Umari, P.; Wentzcovitch, R. M. QUANTUM ESPRESSO: a modular and open-source software project for quantum simulations of materials. *J. Phys. Condens. Matter.* 2009, **21**, 395502.

(19) Perdew, J.; Burke, K.; Ernzerhof, M. Generalized Gradient Approximation Made Simple. *Phys. Rev. Lett.* **1996**, *77*, 3865−3868.

(20) Monkhorst, H. J.; Pack, J. D. Special points for Brillouin-zone integrations. *Phys. Rev. B* **1976**, *13*, 5188−5192.

(21) Favre-Nicolin, V.; Cerny, R. FOX, `free objects for crystallography': a modular approach to ab initio structure determination from powder diffraction. *J. Appl. Crystallogr.* **2002**, *35*, 734−743.

(22) Bruker AXS (2014) TOPAS V5: general profile and structure analysis software for powder diffraction data. Bruker AXS, Karlsruhe, Germany.

(23) Bruker- SMART. Bruker AXS Inc., Madison, Wisconsin, USA. **2002**.

(24) Bruker- SAINT and SADABS. Bruker AXS Inc., Madison, Wisconsin, USA, **2008**.

(25 Sheldrick, G. M. A short history of SHELX *Acta Cryst.* **2008**, *A64*, 112.

(26) Lagarec, K.; Rancourt, D. G. Extended Voigt-based analytic lineshape method for determining N-dimensional correlated hyperfine parameter distributions in Mössbauer spectroscopy. Nucl. Instrum. Meth. Phys. Res. B **1997**, 129, 266.

(27) Rodriguez-Carvajal, J.; Recent advances in magnetic structure determination by neutron powder diffraction. Physica B: Condensed Matter, **1993**, 192, 55–69.

(28) Gwon, H.; Kim, S.-U.; Park, Y.-U.; Hong, J.; Ceder, G.; Jeon, S.; Kang, K. Ion-Exchange Mechanism of Layered Transition-Metal Oxides: Case Study of $LiNi_{0.5}Mn_{0.5}O_2$. *Inorg. Chem.* **2014**, *53*, 8083–8087.

(29) Aryanpour, M.; Miara, L.; Ryu, Y.-G.; Staging and In-Plane Superstructures Formed in Layered $NaMO_2$ {M = Sc, Ti, V, Cr, Mn} during Na De-Intercalation: A Computational Study. *J. Electrochem. Soc.* **2015**, *162*, A511-A519.

(30) Pfannes, D.; Gonser, U. Goldanskii-Karyagin effect versus preferred orientations. *Appl. Phys.* **1973**, *1*, 93–102.

(31) Menil, F. Systematic trends of the 57Fe Mössbauer isomer shifts in (FeOn) and (FeFn) polyhedra. Evidence of a new correlation between the isomer shift and the inductive effect of the competing bond T-X (→ Fe) (where X is O or F and T any element with a formal positive charge) *J. Phys. Chem. Solids* **1985**, *46*, 763–789.

2. CONCLUSION

The transition metal polyanion chemistry is a fertile area of soli-state synthesis. This is mainly due to the vast possible number of combinations between the transition metals and polyanionic moieties. Unlike organic materials, there are not many firmly established rules for the synthesis of inorganic solid-state materials. Despite the fast growing first principle computational methods for predicting the stable phases at a fixed composition for a given set of empirical conditions, exploratory synthesis using chemical intuition and trial-and-error based methods are still the widely used synthetic strategies for finding new materials in this area. On the other hand, this provides an opportunity for solid-state chemists to investigate into the unexplored area by focusing on combinations where the products may have potential usage for a particular application, in this case solid-state electrodes for alkali-ion batteries. In most of the new materials discovered in this work, low melting fluxes were used as a medium to dissolve the precursors and/or reagents to grow crystals. Avoiding water as the solvent in hydrothermal syntheses, creates the condition required to move away from most thermodynamically stable phases and come close toward the meta-stable ones.

Moreover, avoiding water as the solvent eliminates the possibility of coordination of hydroxide ligand, which competes with other ligands for transition metal coordination. This in turn increases the chances of finding new phases by providing new compositional opportunities.

The diversity expected from polyanion chemistry is well reflected in the reactions containing iron and phosphorous acid, where it was found that the choice of the iron precursor's oxidation state (ferric, ferrous) and type (nitrate, chloride, oxide) will determine the fate of the product formed. Regarding the electrochemical properties of the phosphite containing phases, it is expected that due to the lower oxidation state of the phosphorous atom in the phosphite (+3) compared to the phosphate (+5), the increase in the Fe^{2+}/Fe^{3+} redox potential is weakened compared to the phosphate phases; however, it was experimentally found that due to structural reasons, the average cell voltages observed for

$Li_3Fe_2(HPO_3)_3Cl$ and $LiFe(HPO_3)_2$ is within those observed for some phosphate-based materials, surpassing some others, among them tavorite $LiFePO_4(OH)_{1-x}F_x$ can be mentioned.

Even though exploratory synthesis is believed to be the major tool for finding the new compositions, the rational design of new materials by appropriate utilization of existing information opens up another avenue for making new materials. This approach seeks new compositions from chemical and structural similarities between the already known materials and prospective ones. In this regard *ab initio* quantum mechanical modelling can be quite useful for comparison of the expected formation energies for certain structures with various compositions. Both of these approaches has been implemented in this work for the formation of $Li_{0.8}Fe(H_2O)_2B[P_2O_8]\bullet H_2O$ and $AFePO_4NO_3$ (*A*: NH_4/Li, K). These phases have been prepared based on previous knowledge from $AFe(H_2O)_2B[P_2O_8]\bullet H_2O$ (*A*: Na, K) and $AMPO_4CO_3$ (*A*: Li, Na; *M*: metal in +2 oxidation state).

This work has essentially focused on the synthesis of novel polyanionic compounds of iron which can reversibly intercalate Li^+ and Na^+ ions for Li-ion and Na-ion batteries. The conclusions drawn from each paper has been summarized in the following:

The crystal structure of tavorite $LiFePO_4OH$ has been reported for the first time from Single-Crystal XRD, complementing the available data from powder XRD and neutron diffraction information. Moreover, a new scalable synthetic method has been proposed for the production of tavorite, $LiFePO_4F$, based on low-cost eutectic salt melts. $LiFePO_4OH$ and $LiFePO_4F$ have been shown to exist as a solid-solution over the whole range, $LiFePO_4F_{1-x}(OH)_x$, ($0 \leq x \leq 1$). The Fe^{2+}/Fe^{3+} redox couple in iron tavorite is located between 2.5 to 2.9 V *vs* Li^+/Li (theoretical capacity 150 $mAh.g^{-1}$) and is strongly affected by the amount of fluoride anion coordinated to the iron center. Furthermore, electro-impedance measurements suggested that the mixed solid-solution phase, $LiFePO_4F_{1-x}(OH)_x$, exhibit the best high C-rate performance as a result of small particle size and Li—OH/F attractions intermediate between those of pure OH and F versions.

The new $Li_3Fe_2(HPO_3)_3Cl$ phase has been formed using the reaction between ferrous chloride, lithium hydroxide and phosphorous acid. This reaction shows the possibility of using phosphorous acid as a melt and reagent at the same time. Of the two theoretically removable Li^+ ions per formula unit (theoretical capacity 131.4 $mAh.g^{-1}$), only one could be reversibly de-intercalated in the safe potential window of the electrolyte. The insertion occurs at a potential of ca 3.1 V vs Li^+/Li and demonstrates the inductive effect of the chloride ligand. Moreover the studies of the cell performances demonstrate the high Li-ion kinetics, which is further studied through variable temperature AC-impedance measurements. Finally $Li_3Fe_2(HPO_3)_3Cl$ exhibits antiferromagnetic ordering of magnetic moments on Fe centers below 10 K with an unusual metamagnetic transition with an onset at a field strength of 3 T.

As a second phosphite containing phase we have demonstrated the synthesis and crystal structure of $LiFe(HPO_3)_2$ which has been obtained through a solvent-less reaction between iron oxide, lithium hydroxide and phosphorous acid. The crystal structure exhibits large diffusion channels in all 3 directions along the crystallographic axes, with a theoretical capacity of 120 $mAh.g^{-1}$ per formula unit. The iron center can be reduced by insertion of 0.3 Li^+ ions at an average voltage of 3.0 V. However, a deeper discharge with intercalation of 0.6 Li^+ ions requires a higher temperature of 40 °C, indicating the existence of thermally activated processes (electronic/ionic conduction). Quite interestingly the cells exhibit capacity gain on successive charge-discharge tests even after 1000 cycles (up to 200 cycles shown in the paper) underpinning their appropriateness for stationary applications where cost and cycle-life overrides the high energy density.

The new Li-containing $Li_{0.8}Fe(H_2O)_2B[P_2O_8]\bullet H_2O$ has been synthesized using phosphoric acid and boric acid under hydrothermal conditions. The compound crystallizes in the non-centrosymmetric space group, $P6_522$, and display a theoretical capacity of 87.5 $mAh.g^{-1}$. The crystal structure of the chemically delithiated phase, $Fe(H_2O)_2B[P_2O_8]\bullet H_2O$, has been solved by employing *ab initio* methods from synchrotron powder XRD which shows no phase transformation with respect to the lithiated phase. The lithiation and sodiation of the host has been

tested in Li-ion and Na-ion cells which exhibit reversible 0.8 alkali-ion (de)intercalation at an average voltage of 3.06 and 2.76 V, respectively. Moreover the differences in kinetics due to the Li^+ and Na^+ insertion has been studied using in-situ AC-impedance spectrometry, which demonstrated the sluggish nature of Na^+ insertion compared to the Li^+ ion counterpart.

Finally, $AFePO_4NO_3$ (A=NH_4/Li, K) has been obtained by a combination of DFT based computational methods and experimental synthesis. The results of the DFT prediction suggests that $FePO_4NO_3$ host may be stabilized only with NH_4^+ and K^+ ions, but not Li^+ or Na^+, per se. Accordingly $NH_4FePO_4NO_3$ and $KFePO_4NO_3$ has been obtained using nitrate-based fluxes. Moreover $NH_4FePO_4NO_3$ may be obtained as a solid solution with Li^+ ions by adding Li^+ during synthesis and by subsequent ion-exchange. The crystal structures of $(NH_4)_{1-x}Li_xFePO_4NO_3$ and $KFePO_4NO_3$ have been solved from synchrotron powder XRD and Single-Crystal XRD, respectively, and reveal the structural similarity of these phases to the previously discovered carbonophosphates, $AMPO_4CO_3$. The performance of Li-ion and Na-ion cells with the $(NH_4)_{1-x}Li_xFePO_4NO_3$ cathode has been evaluated, which in either case shows almost 80% of theoretical capacity (116 $mAh.g^{-1}$) achieved at an average voltage of 2.9 and 2.5 V, respectively. Despite the relatively low capacity and voltage of $(NH_4)_{1-x}Li_xFePO_4NO_3$ compared to the olivine $LiFePO_4$, the ease (beaker and oven) and fast (<2h) synthesis and widely available low-cost starting materials ($FePO_4 \bullet xH_2O$ and NH_4NO_3) and exceptionally good cycle life make this material as a candidate for large scale electrochemical energy storage applications.

APPENDIX A:
SUPPLEMENTARY INFORMATION

Phosphorous Acid Route Synthesis of Iron Tavorite Phases, $LiFePO_4(OH)_xF_{1-x}$ [$0 \leq x \leq 1$] and Comparative Study of Their Electrochemical Activities

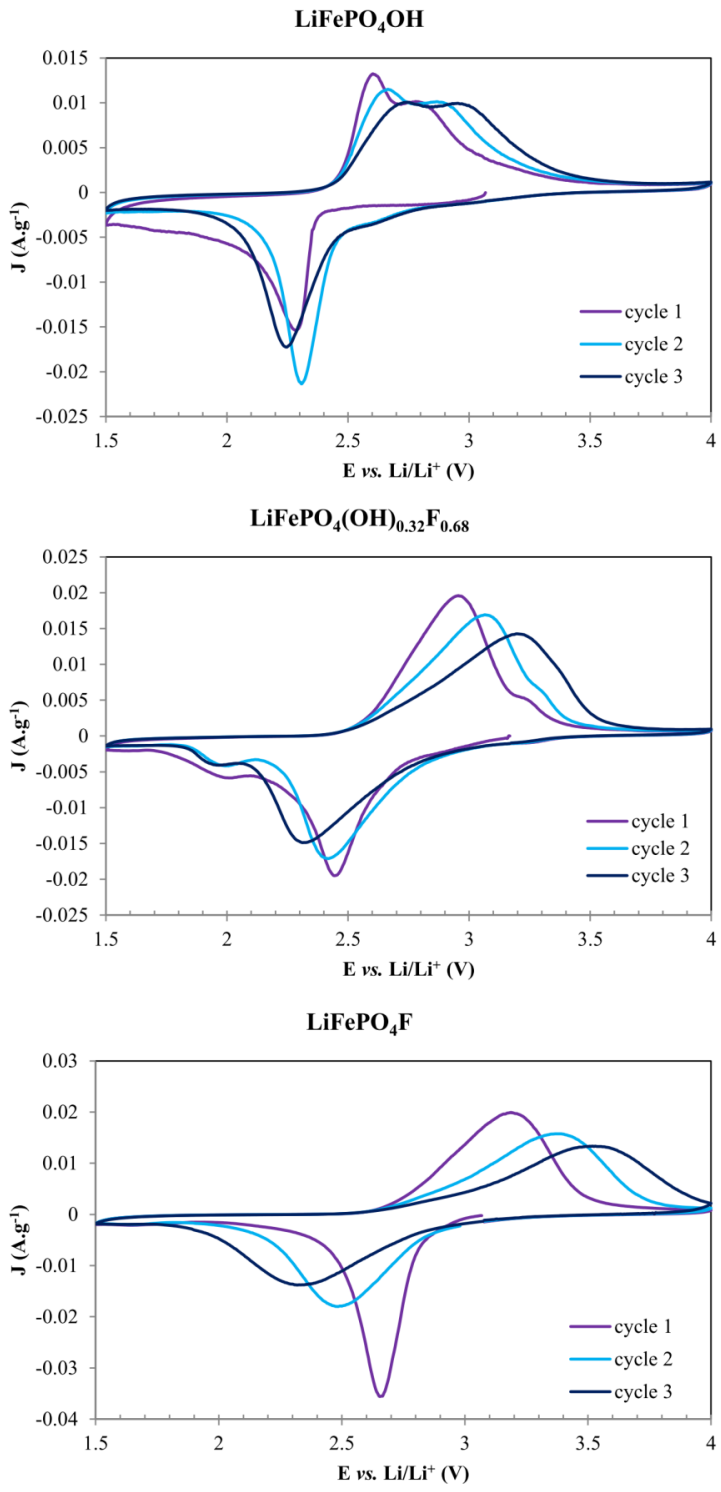

Figure S1. First 3 cycles of CV for the three iron tavorite phases.

APPENDIX B:
SUPPLEMENTARY INFORMATION

$Li_3Fe_2(HPO_3)_3Cl$: An Electroactive Iron Phosphite As a New Polyanionic Cathode Material for Li-ion Battery

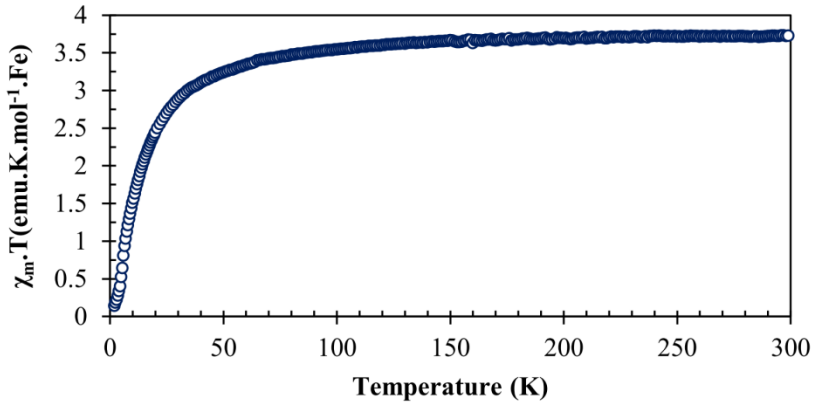

Figure S1. $\chi_m T$ versus T plot indicating the antiferromagnetic behavior of $Li_3Fe_2(HPO_3)_3Cl$ phase at low temperatures.

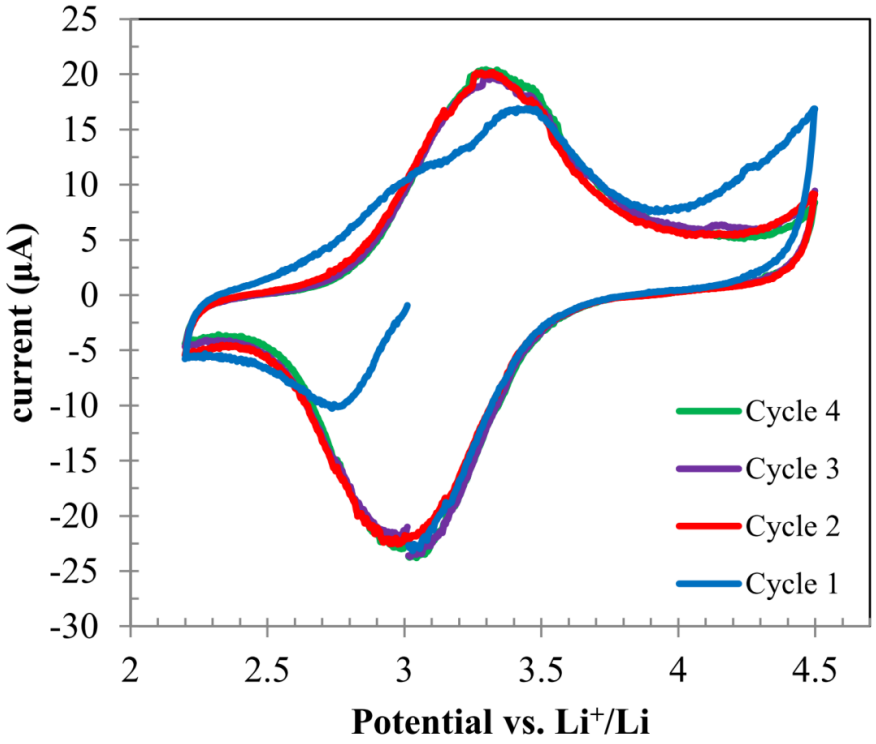

Figure S2. Cyclic voltammograms of $Li_3Fe_2(HPO_3)_3Cl$ cathode with scanning to the lower vertex potential initially.

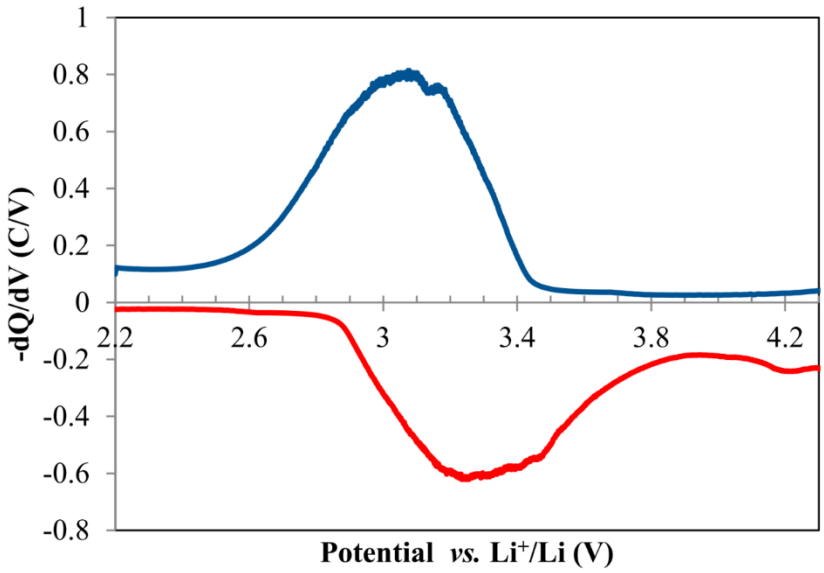

Figure S3. Voltage-charge derivative curve versus potential for discharge (blue) and charge (red) steps of $Li_3Fe_2(HPO_3)_3Cl$ cathode material.

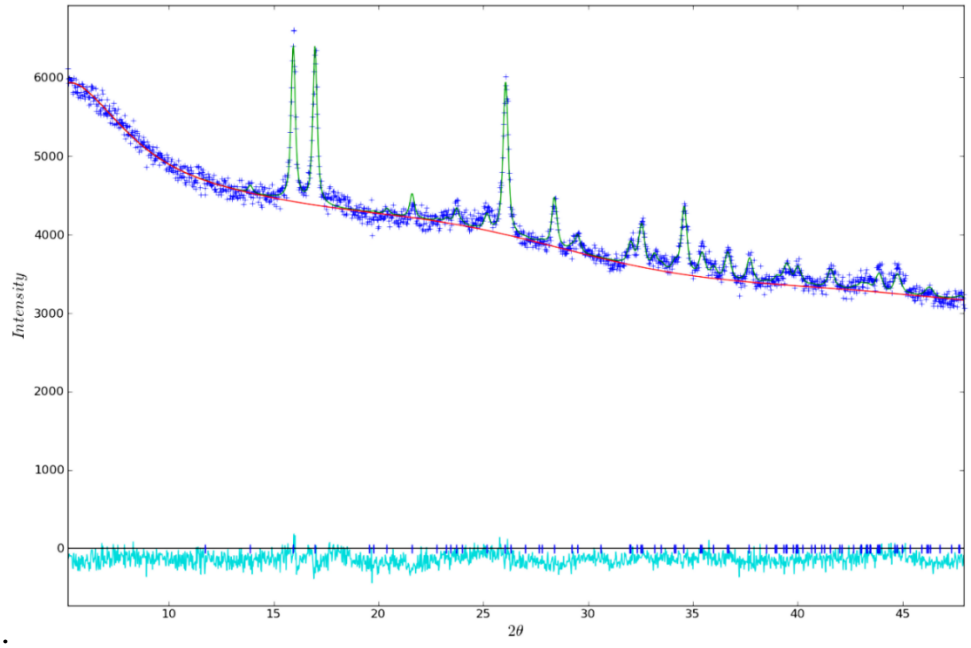

Figure S4. PXRD Rietveld refinement of $Li_3Fe_2(HPO_3)_3Cl$ phase after subjected to charge to 4.5 V *vs.* Li^+/Li.

Table S1. Impedance Fit Parameters for the equivalent circuit shown in Figure 12

Temperature (°C)	L1 (H)	R1 (Ω)	R2 (Ω)	CPE1-T (F)	CPE1-P	W1-R (Ω)	W1-τ (s)	W1-P
23	4.1×10^{-6}	11.8	341.5	5.35×10^{-5}	0.64	6039	204.4	0.70
29	8.8×10^{-6}	9.9	303.3	1.09×10^{-4}	0.55	5295	206.5	0.71
33	7.8×10^{-6}	8.2	259.5	7.44×10^{-5}	0.62	4707	206.3	0.70
36	7.1×10^{-6}	7.5	254.4	7.43×10^{-5}	0.62	4634	205.2	0.70
40	6.5×10^{-6}	6.3	236.1	8.64×10^{-5}	0.61	4234	202.8	0.70
45	4.9×10^{-6}	5.4	215.6	1.18×10^{-4}	0.59	3733	202.6	0.70
50	6.3×10^{-6}	4.7	206.5	1.43×10^{-4}	0.58	3337	198.2	0.70

$Z_{ws} = \frac{R_W \times tanh(j\omega\tau)^P}{(j\omega\tau)^P}$ where $\tau = {L^2}/{D}$ and L and D are effective diffusion length and diffusion coefficients, respectively.

APPENDIX C:
SUPPLEMENTARY INFORMATION

Phosphite as Polyanion-based Cathode for Li-ion Battery: Synthesis, Structure and Electrochemistry of $LiFe(HPO_3)_2$

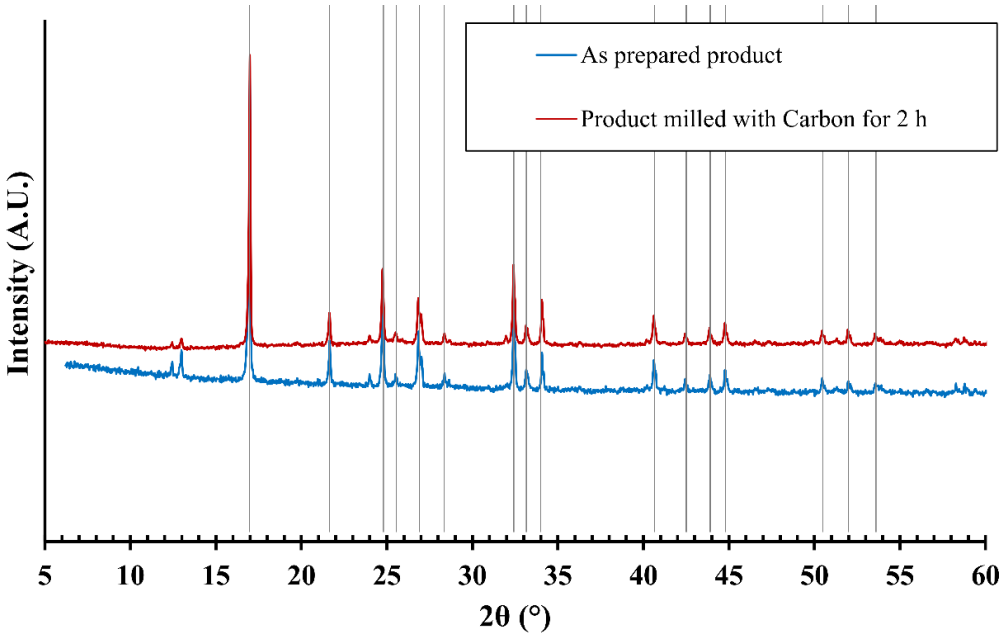

Figure S1. PXRD of the active material milled with carbon, showing the retention of crystal structure of $LiFe(HPO_3)_2$ during the cathode mix preparation.

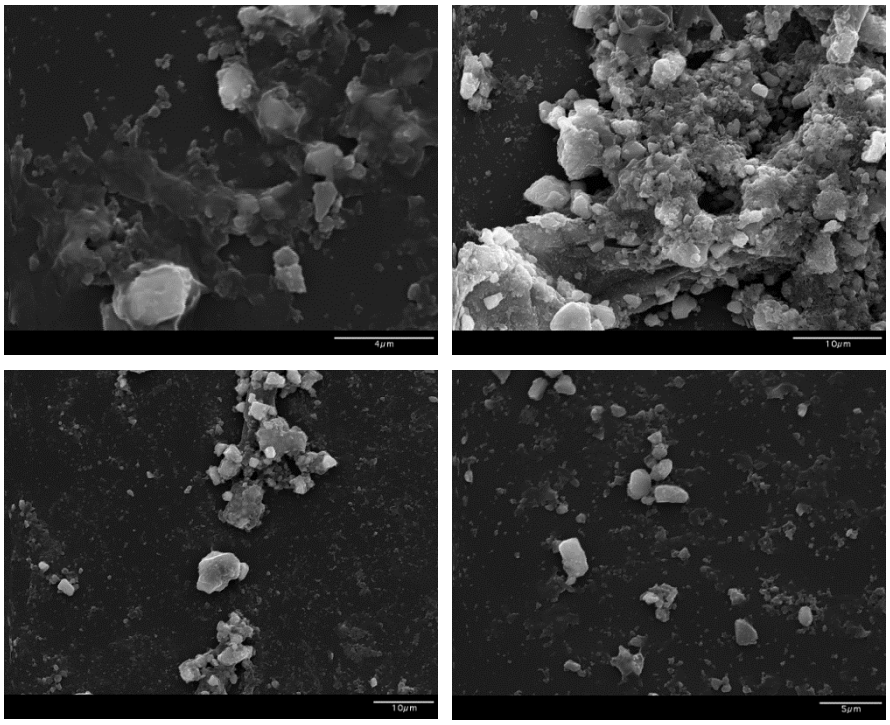

Figure S2. SEM micrographs of $LiFe(HPO_3)_2$ phase ball-milled with carbon for 2 hours prior to composite cathode preparation.

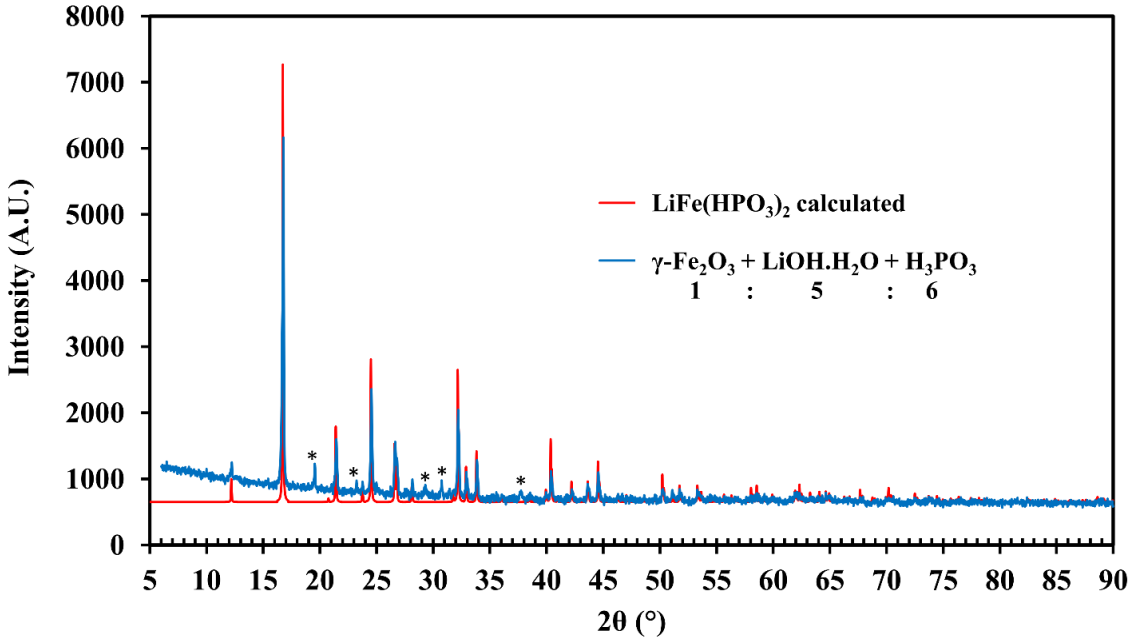

Figure S3. PXRD of the synthesis mixture with the unknown impurity phase(s) marked with star.

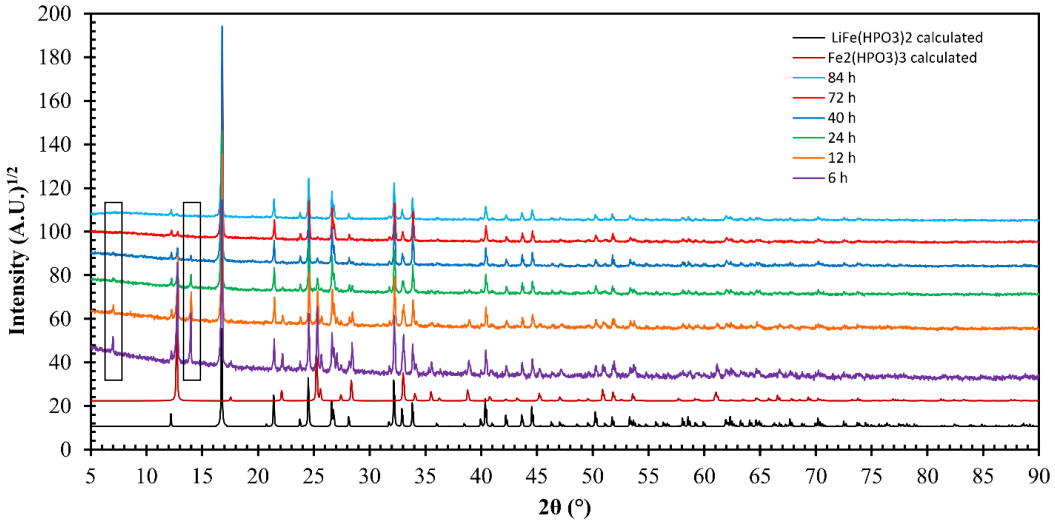

Figure S4. Time parameter optimization during the synthesis of $LiFe(HPO_3)_2$. Traces of another impurity peaks vanishes after72 hours (boxed area).

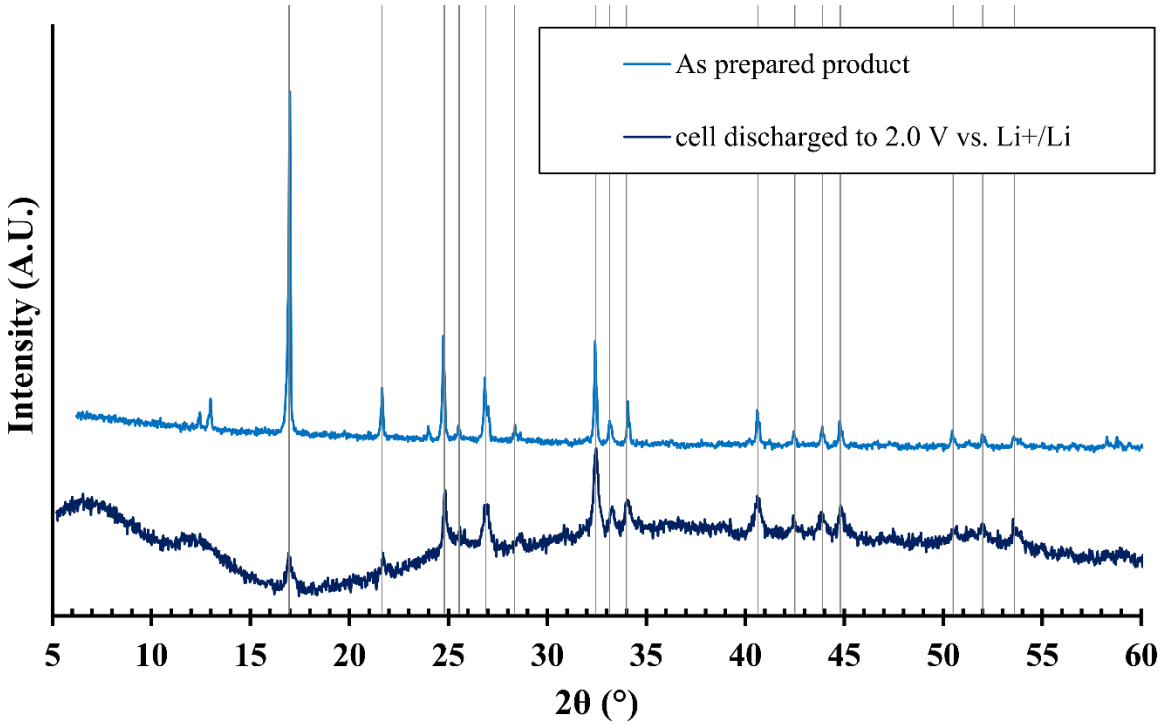

Figure S5. PXRD of the reduced cathode mix after breaking the button cells, when the cells were discharged. The retention of crystal structure of $LiFe(HPO_3)_2$ in evident in the PXRD pattern.

APPENDIX D:
SUPPLEMENTARY INFORMATION

Iron Borophosphate as Potential Cathode for Lithium and Sodium-ion Batteries

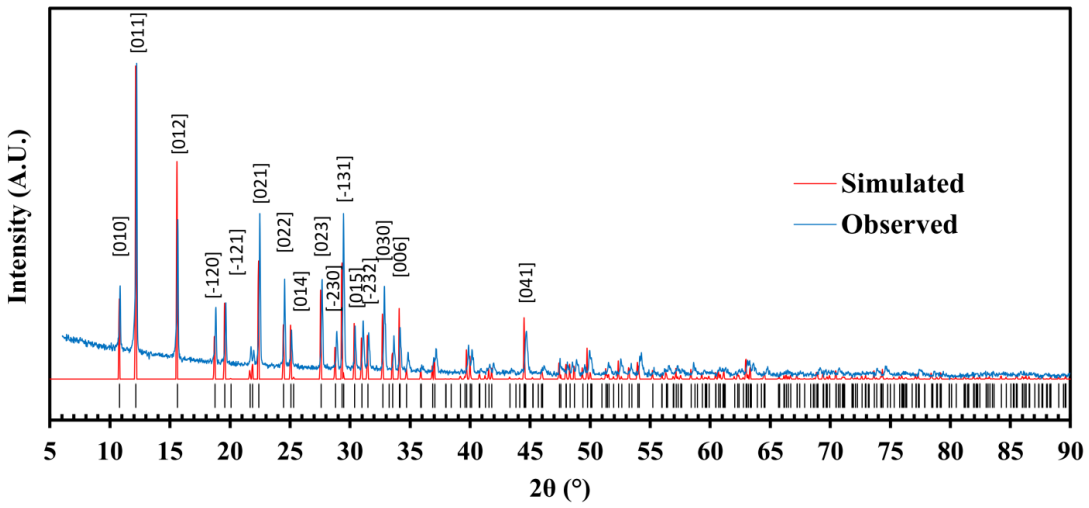

Figure S1. Acquired and calculated powder XRD patterns of $Li_{0.8}Fe(H_2O)_2[BP_2O_8]\cdot H_2O$.

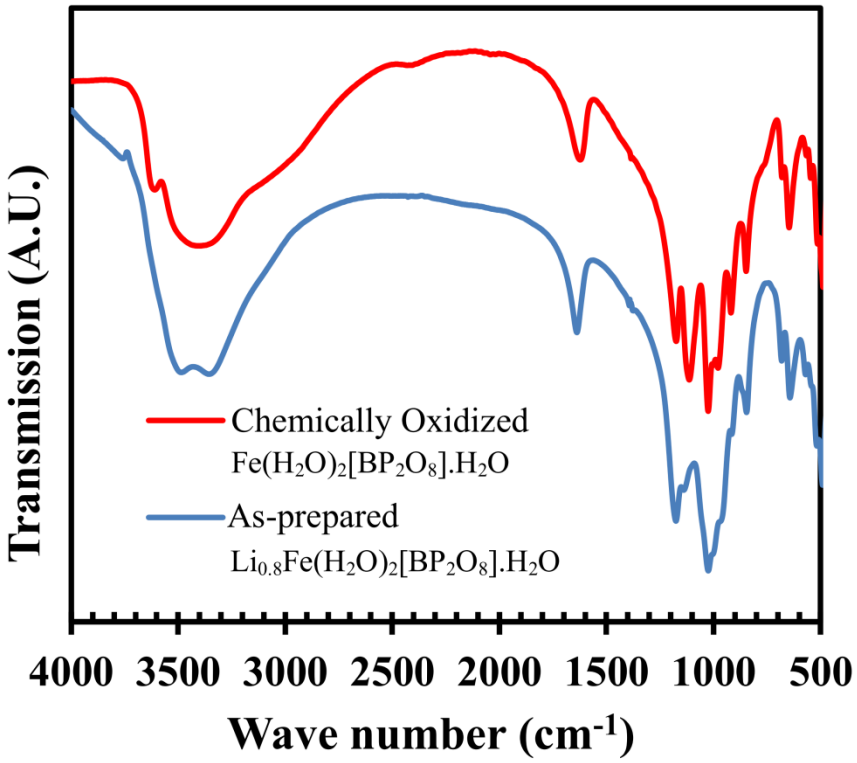

Figure S2. FT-IR spectra of $Li_{0.8}Fe(H_2O)_2[BP_2O_8]\cdot H_2O$ and its chemically oxidized phase.

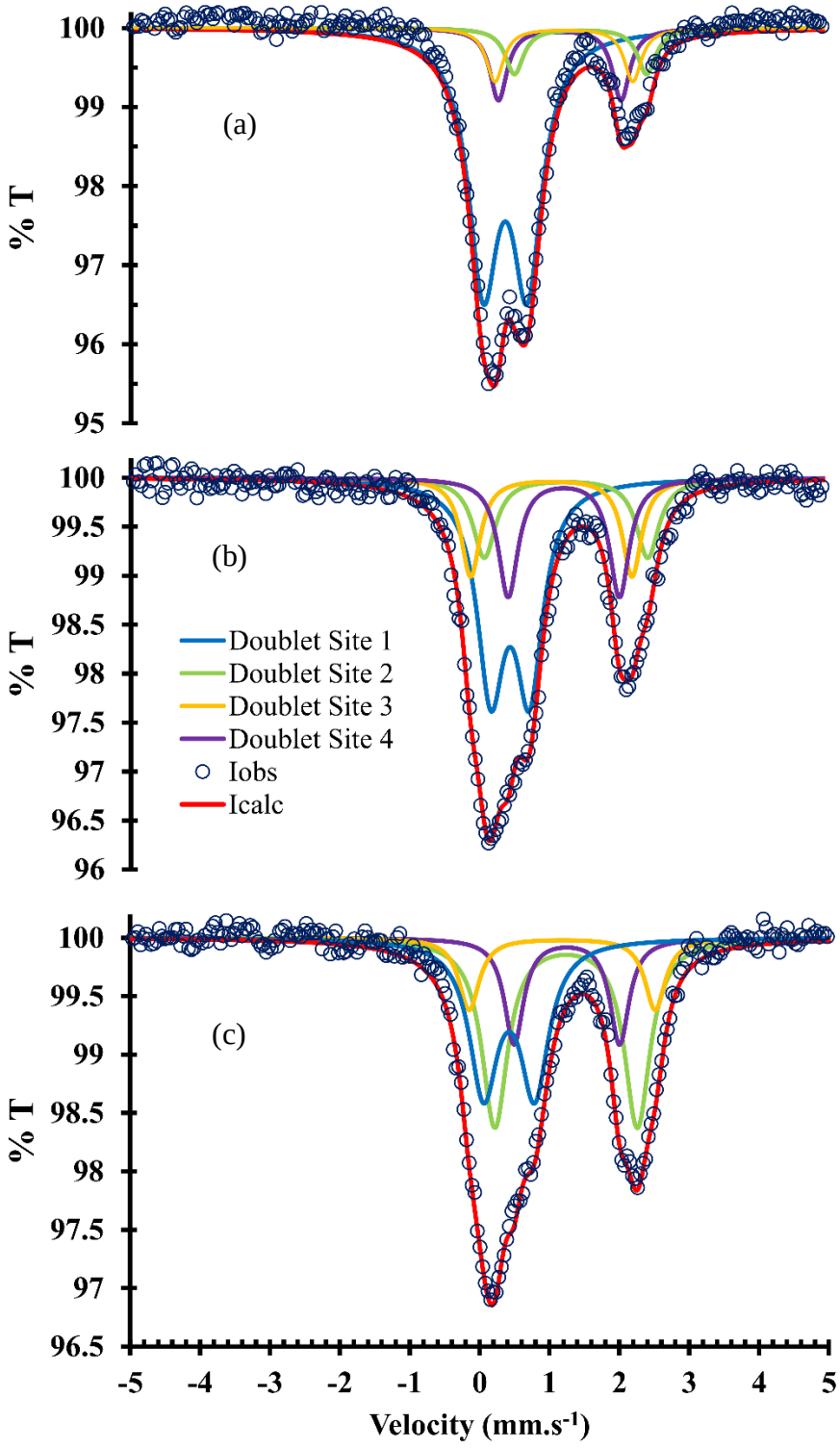

Figure S3. Mössbauer spectra of the $Li_xFe(H_2O)_2[BP_2O_8].H_2O$ cathode at various state-of-charge (SOC); (a) Charged to 4.0 V; (b) Discharged to 3.0 V; (c) Discharged to 2.0 V.

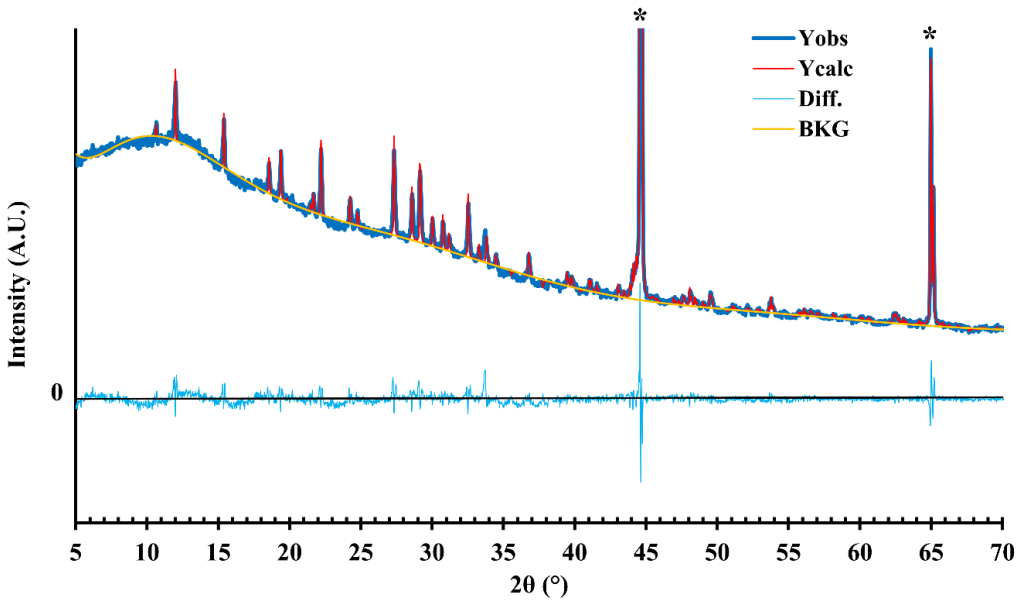

Figure S4. Pawley refinement on the unit cell parameters of the reduced (discharged) Na-ion cell cathode. The observed Al (200) and (220) reflections marked with stars (from the current collector) were used as an internal standard for 2θ axis calibration.

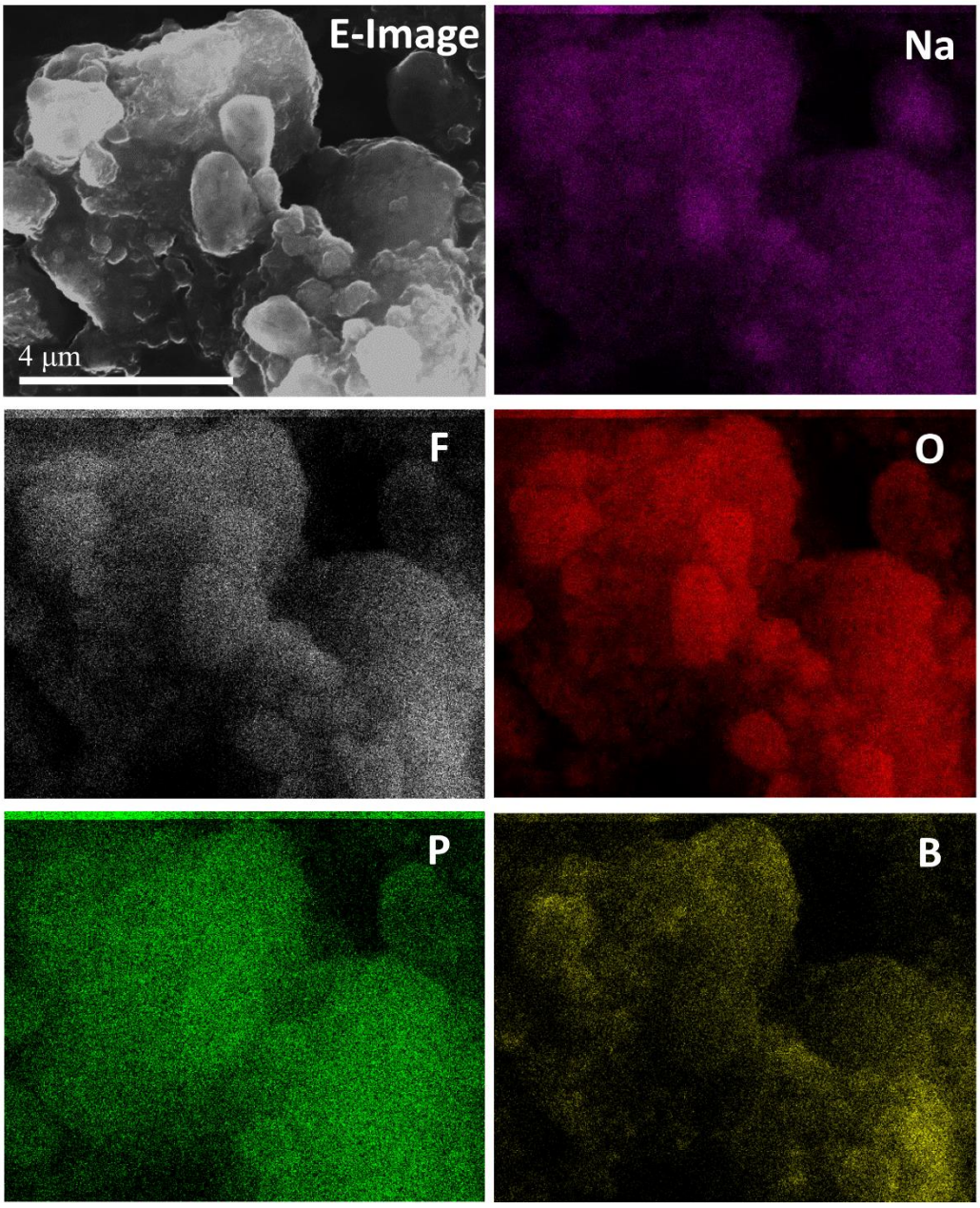

Figure S5. EDS elemental mapping of the sodium intercalated (discharged) active material particle on the cathode film retrieved from the Na-ion cell. Fluorine originates from PVDF binder.

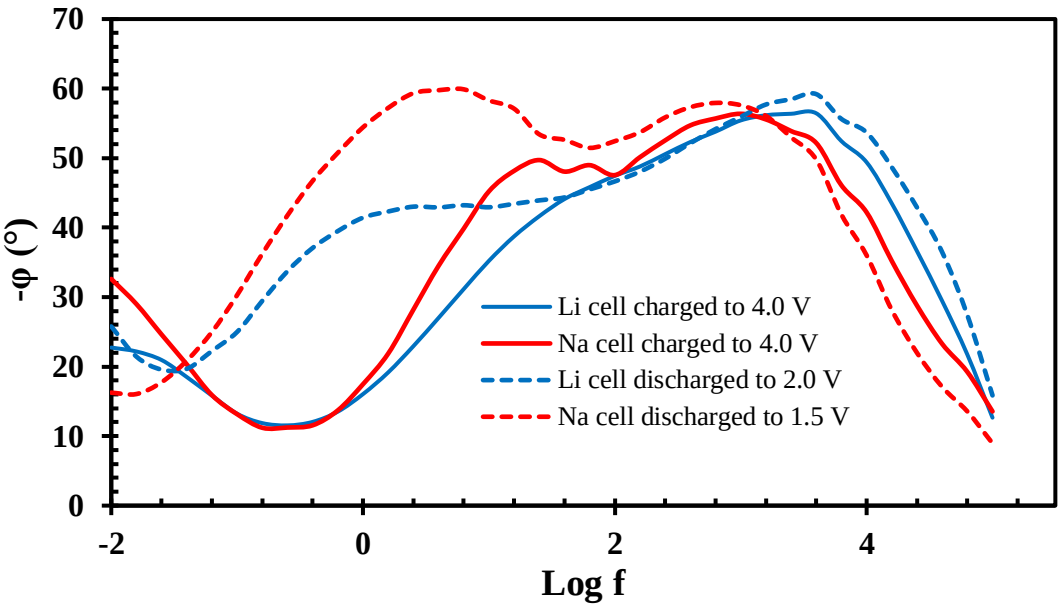

Figure S6. Phase Bode plot of the impedance curves acquired on Li- and Na-ion cells in charged and discharged states, respectively.

Table S1. Atomic coordinates and isotropic thermal parameter obtained via Rietveld refinement of $Fe(H_2O)_2[BP_2O_8]\cdot H_2O$ Powder XRD pattern

label	Wyckoff	Multiplicity	x	y	z	S.O.F.	Uiso. ($Å^2$)
Fe1	6b	6	0.553(6)	0.446(3)	0.083333	1	0.007(2)
P1	12c	12	0.171(3)	0.383(2)	0.080(6)	1	0.005(7)
B1	6b	6	0.848(4)	0.152(4)	0.083333	1	0.029(4)
O1	12c	12	0.174(1)	0.414(1)	0.179(1)	1	0.009(9)
O2	12c	12	0.026(4)	0.212(6)	0.062(8)	1	0.009(8)
O3	12c	12	0.141(7)	0.510(1)	0.036(9)	1	0.009(8)
O4	12c	12	0.327(6)	0.384(9)	0.053(2)	1	0.009(8)
O5	12c	12	0.486(4)	0.202(7)	0.051(6)	1	0.009(8)
O1W	6b	6	0.202(3)	0.101(1)	0.91666	1	0.17(4)

Table S2. The values for the Isomer Shift (IS) and Quadrupole Splitting (Q.S.) and site population of the iron sites obtained from Lorentzian fits of Mössbauer spectra of $Li_xFe(H_2O)_2[BP_2O_8].H_2O$ cathode at different potentials

Potential vs. Li^+/Li		I.S. ($mm.s^{-1}$)	Q.S. ($mm.s^{-1}$)	Site %
4.0 V	Doublet 1	0.4036	0.6241	68.8
	Doublet 2 (Average)	1.2955	1.8989	31.2
3.0 V	Doublet 1	0.3779	0.7211	47.7
	Doublet 2 (Average)	1.2860	1.9899	52.3
2.0 V	Doublet 1	0.3611	0.8592	34.0
	Doublet 2 (Average)	1.2655	1.9787	66.0

Table S3. Lattice parameters refinement of the reduced cathode retrieved from the discharged Na-ion cell

a	***b***	***c***	**Space group**	**Volume**
9.495(3)	9.495(3)	15.881(7)	$P6_522$	1240.1(1)

Table S4. Li- and Na-ion cell Impedance fit data at charged and discharged states

			High frequency			**Mid frequency**			**Low frequency**		
				CPE1[a]			CPE2			CPE3	
	L1 (H)	R1 (Ω)	R2 (Ω)	T ($s^P.\Omega^{-1}$)	P	R3 (Ω)	T ($s^P.\Omega^{-1}$)	P	R4 (Ω)	T ($s^P.\Omega^{-1}$)	P
Li-ion cell 4.0 V	$1.70x10^{-6}$	6.4	$1.12x10^{2}$	$1.92x10^{-5}$	0.82	$2.10x10^{3}$	$4.20x10^{-5}$	0.70	$6.00x10^{3}$	$2.30x10^{-3}$	0.71
Na-ion cell 4.0	$1.30x10^{-6}$	9.5	$3.28x100^{2}$	$2.28x10^{-5}$	0.74	$2.50x10^{3}$	$2.77x10^{-5}$	0.85	$2.13x10^{4}$	$2.06x10^{-3}$	0.75
Li-ion cell 2.0 V	$2.20x10^{-6}$	3.7	$2.80x100^{2}$	$2.70x10^{-5}$	0.77	$1.00x10^{4}$	$9.20x10^{-5}$	0.64	$2.80x10^{4}$	$6.90x10^{-3}$	0.95
Na-ion cell 1.5 V	$7.80x10^{-8}$	10.5	$1.44x100^{2}$	$1.97x10^{-5}$	0.85	$2.81x10^{4}$	$4.07x10^{-5}$	0.74	Not Obs.	Not Obs.	Not Obs.

[a] $Z_{CPE} = \frac{1}{T(i\omega)^P}$

Table S5. Ionic conductivity measurements on pressed pellet of $Li_{0.8}Fe(H_2O)_2[BP_2O_8]\cdot H_2O$

	Bulk			**grain boundary**			**blocking electrode**	
	R1 (Ω)	CPE1		R2 (Ω)	CPE2		CPE3	
T (K)		T ($s^P.\Omega^{-1}$)	P		T ($s^P.\Omega^{-1}$)	P	T ($s^P.\Omega^{-1}$)	P
303.95	7ta.$46x10^{6}$	$4.43x10^{-10}$	0.72	$2.51x10^{7}$	$8.83x10^{-9}$	0.66	$8.06x10^{-8}$	0.68
308.85	$5.95x10^{6}$	$5.89x10^{-10}$	0.70	$1.91x10^{7}$	$9.58x10^{-9}$	0.68	$1.42x10^{-7}$	0.73
313.65	$4.17x10^{6}$	$6.78x10^{-10}$	0.70	$1.62x10^{7}$	$1.10x10^{-8}$	0.67	$6.93x10^{-8}$	0.94
318.15	$3.29x10^{6}$	$8.80x10^{-10}$	0.69	$7.91x10^{6}$	$1.06x10^{-8}$	0.75	$1.70x10^{-8}$	0.70
323.65	$2.58x10^{6}$	$1.03x10^{-9}$	0.68	$5.91x10^{6}$	$1.22x10^{-8}$	0.74	$1.90x10^{-7}$	0.62
328.55	$1.94x10^{6}$	$1.30x10^{-9}$	0.67	$3.27x10^{6}$	$1.23x10^{-8}$	0.8	$2.16x10^{-7}$	0.51
333.75	$1.51x10^{6}$	$1.34x10^{-9}$	0.68	$2.37x10^{6}$	$1.48x10^{-8}$	0.78	$2.76x10^{-7}$	0.44
338.75	$1.25x10^{6}$	$1.60x10^{-9}$	0.67	$1.94x10^{6}$	$1.50x10^{-8}$	0.8	$3.26x10^{-7}$	0.43

APPENDIX E:
SUPPLEMENTARY INFORMATION

A Combined Theoretical and Experimental Approach to the Discovery of Mixed Polyanionic Phosphatonitrates, *A*$FePO_4NO_3$ (*A* = NH_4/Li, K)

Functional testing and computational method details:

The accuracy of the employed PBE functional and other parameters for calculating the energy states have been checked by calculating the sodiation potential of $Na_2FePO_4CO_3$ according to the following scheme, with the self-consistence energies reported:

$$Na_2FePO_4CO_3 \quad + \quad Na \rightarrow \quad Na_3FePO_4CO_3$$

E (Ry)/formula unit: -695.311645 -96.14465 -791.657529

Assuming $\Delta G \approx \Delta E$, one would get an average energy difference of 2.74 eV/formula unit for sodiation of bonshtedtite, which matches acceptably with the experimental average sodium cell voltage of 2.7 V [I]. Due to the high level of agreement between the calculated and observed energies no Hubbard-type +U correction found necessary with the above setup, as we found over-estimated energies with USPPs and DFT+U calculations.

For the self-consistent field (SCF) energy optimization runs for calculating the ground state energy of reactants and the proposed phosphatonitrate products the exact optimized parameters as above have been used. The crystal information and atomic coordinates for $FePO_4$ ($AlPO_4$ structure type), $LiNO_3$, β-KNO_3, $NaNO_3$ were taken as the closest stable phases in the reaction temperature employed. For NH_4NO_3 however, the crystal information of the 32.3—84.2 °C stable phase (phase (IV)) has been fed into the computational method as the high temperature NH_4NO_3 (phase I) exhibits a high degree of disorder and lacks some atomic coordinates due to the free rotation of NH_4 and to a lesser extent NO_3 moieties in the unit cell. Despite this the phase (IV) to phase (I) transformation enthalpy correction were applied to the calculated total energy, which is anyway negligible compared to the SCF value (+7.431 vs. -117.508 $kJ.mol^{-1}$). All the crystal information and atomic coordinates have been taken from Inorganic Crystal Structure Database (ICSD).

Experimental results

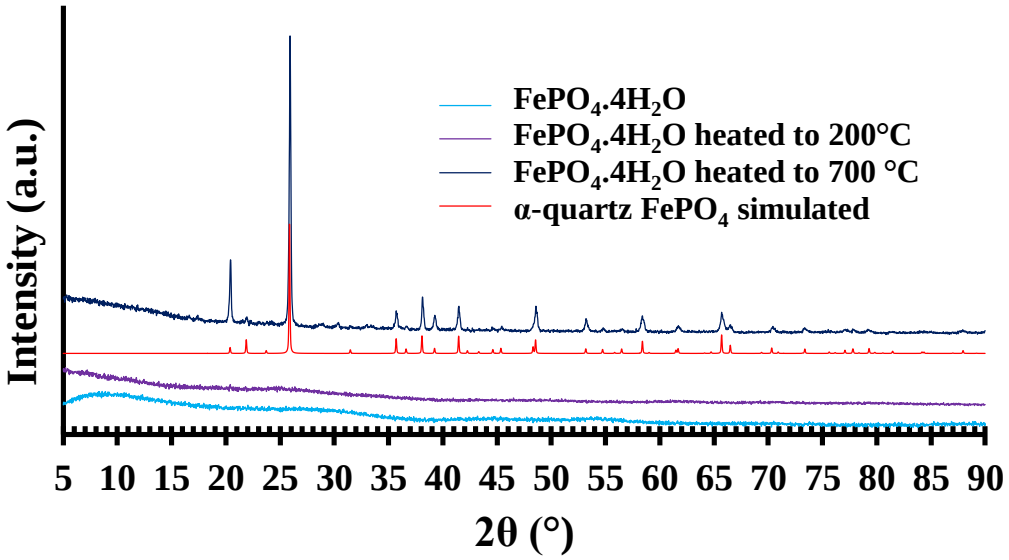

Figure S1. Powder XRD patterns exhibiting dehydration of $FePO_4.4H_2O$ to the trigonal ($AlPO_4$ structure type) $FePO_4$ as a function of temperature.

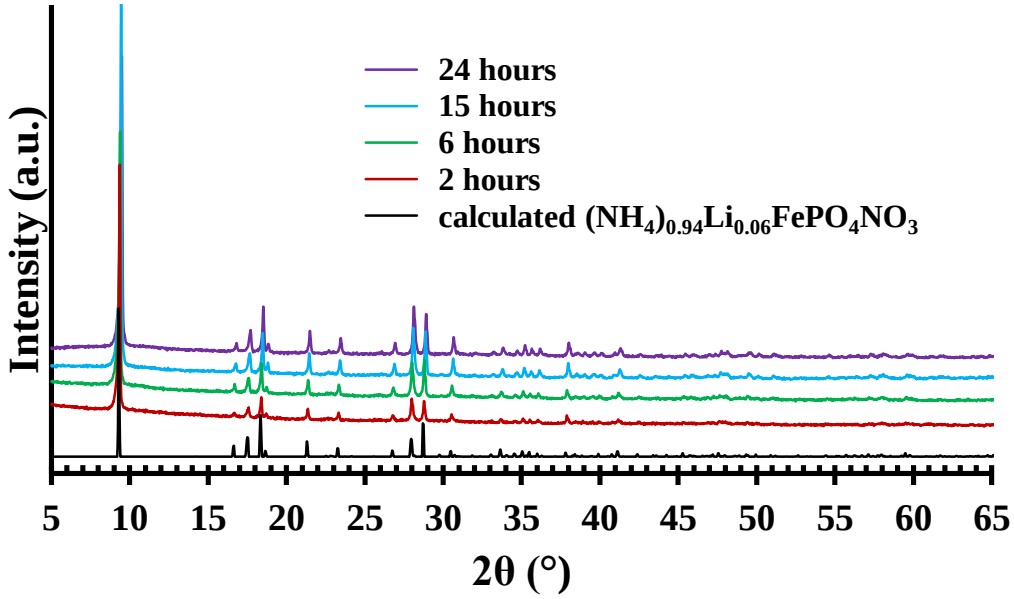

Figure S2. Time-evolution of $(NH_4)_{0.94}Li_{0.06}FePO_4NO_3$ synthesis as observed through ex-situ PXRD.

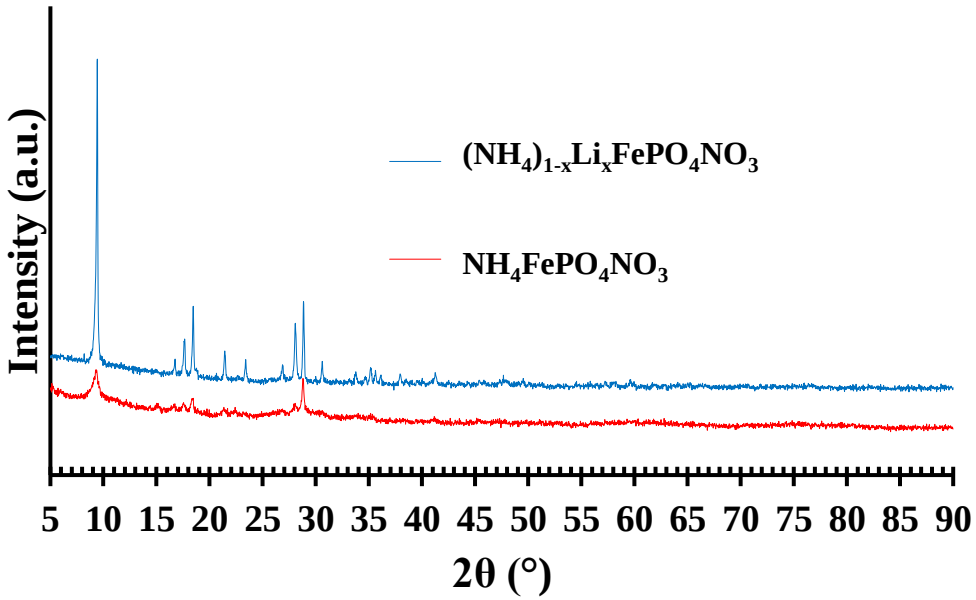

Figure S3. Demonstration of the lithium/ammonium site mixing on the crystallinity of phase.

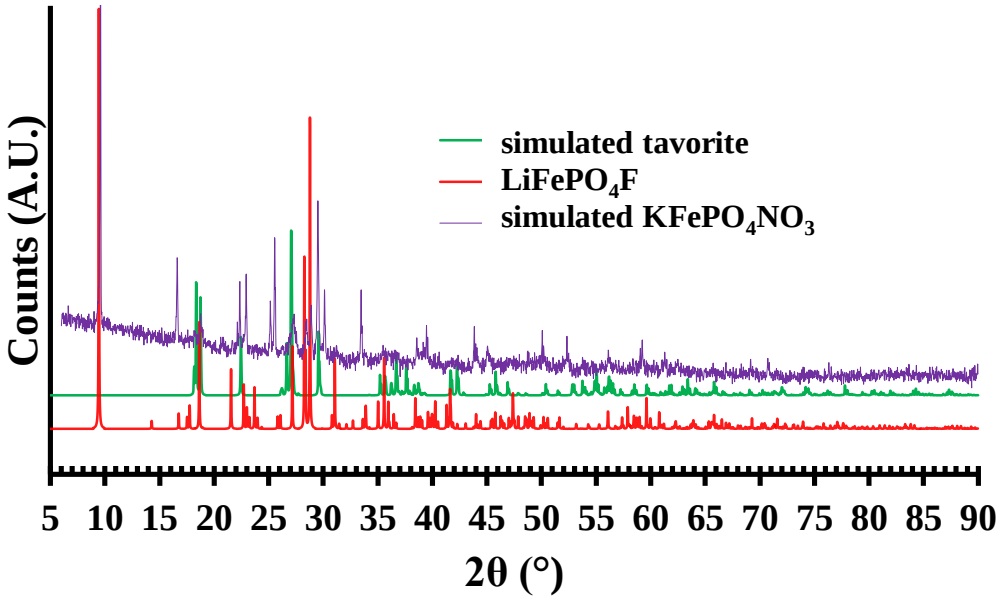

Figure S4. PXRD analysis of the $KFePO_4NO_3$ synthesis product.

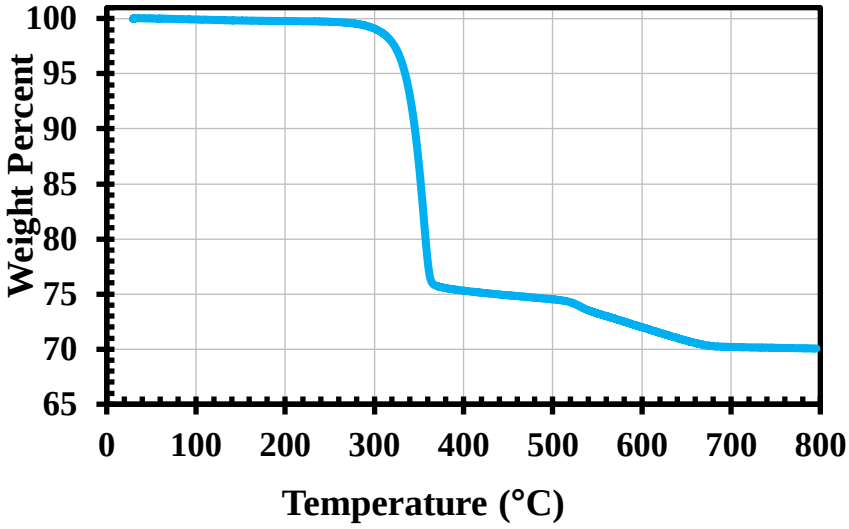

Figure S5. Thermo-gravimetric analysis of the as-synthesized $(NH_4)_{0.94}Li_{0.06}FePO_4NO_3$.

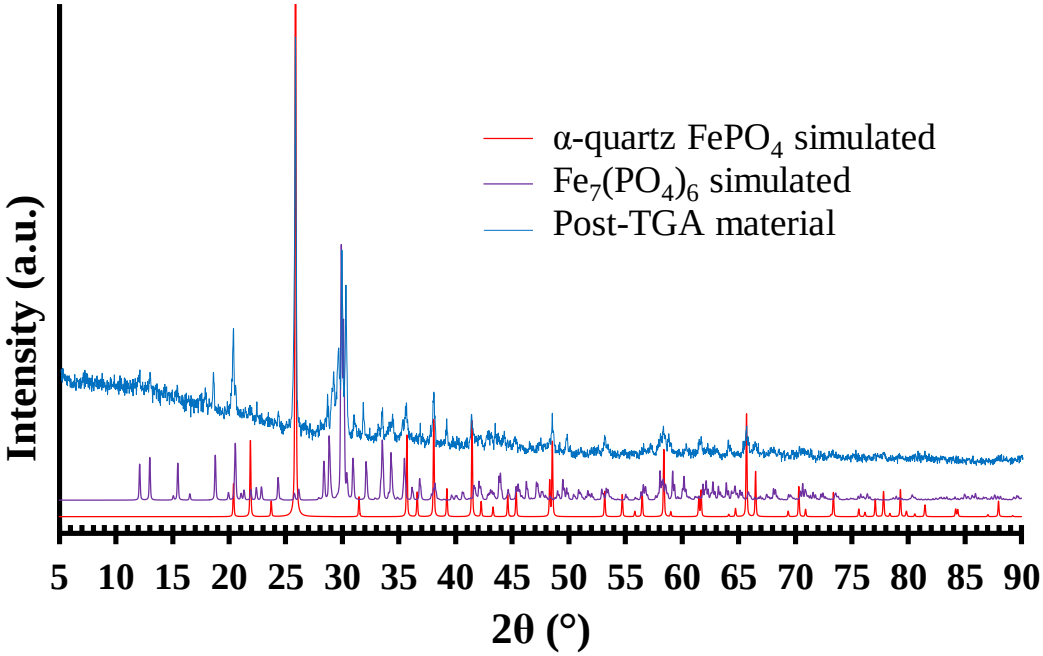

Figure S6. Post-TGA PXRD pattern of $(NH_4)_{0.94}Li_{0.06}FePO_4NO_3$ demonstrating decomposition of the phosphatonitrate phase to black $FePO_4$ and $Fe_7(PO_4)_6$.

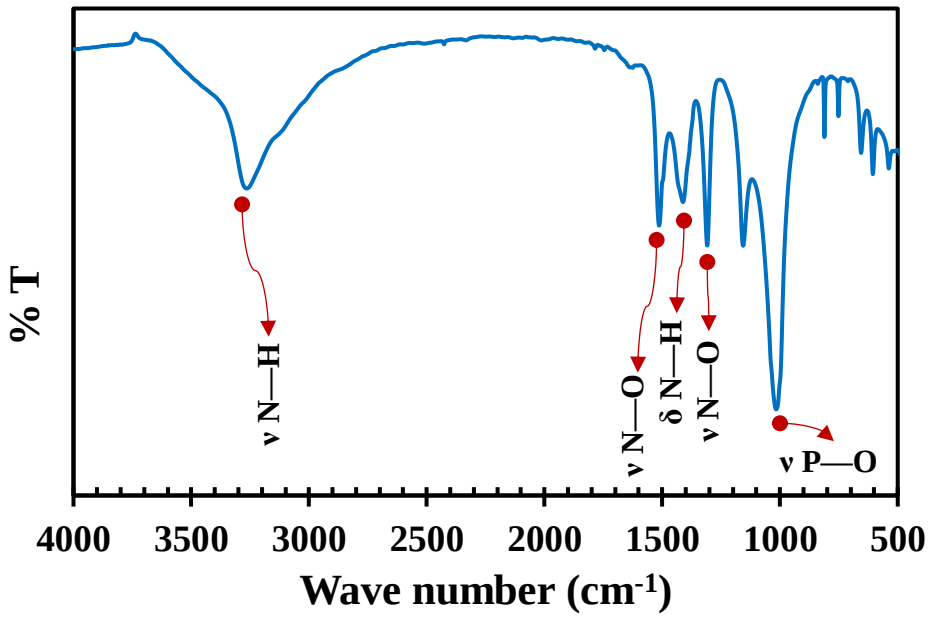

Figure S7. FT-IR spectrum of the as-synthesized $(NH_4)_{0.94}Li_{0.06}FePO_4NO_3$ phase.

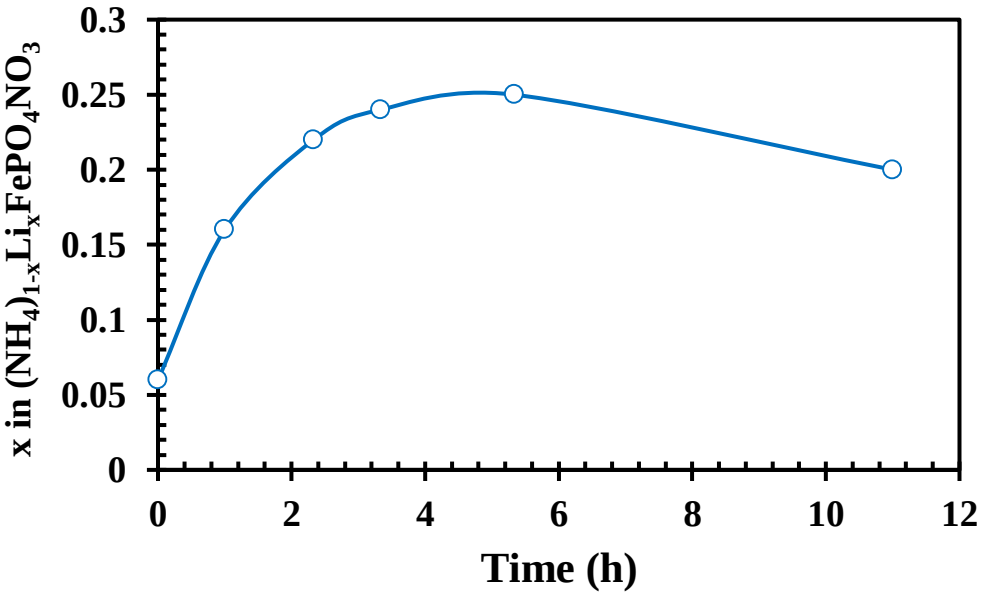

Figure S8. Atomic absorption spectrometric (AAS) measurement of Li content in $(NH_4)_{1-x}Li_xFePO_4NO_3$ as a function of Li^+/NH_4^+ ion-exchange time.

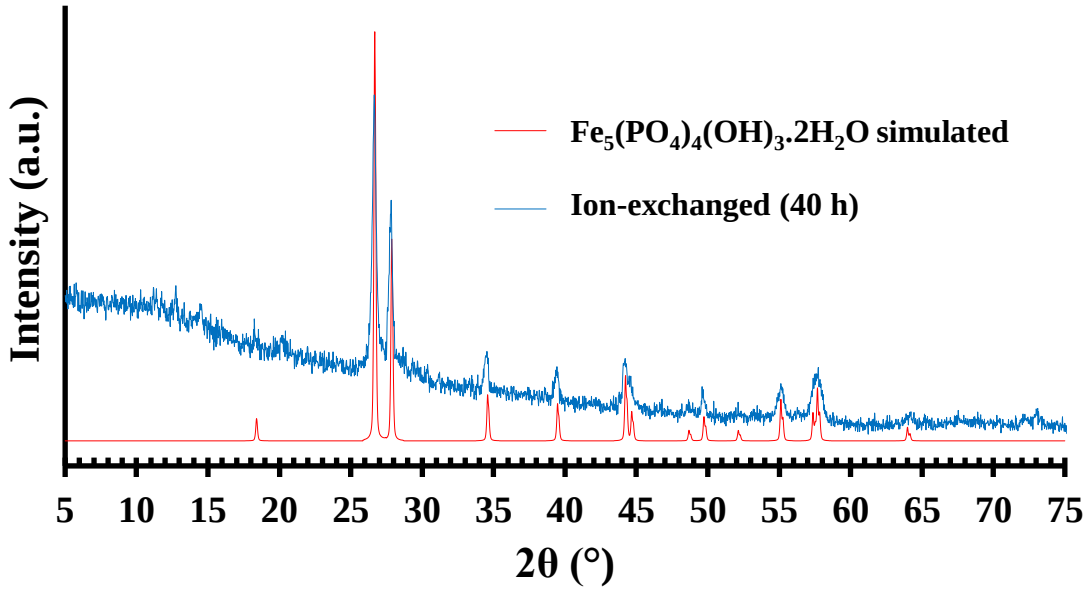

Figure S9. Powder XRD pattern of the $(NH_4)_{0.94}Li_{0.06}FePO_4NO_3/LiNO_3$ ion-exchange reaction after 40 h.

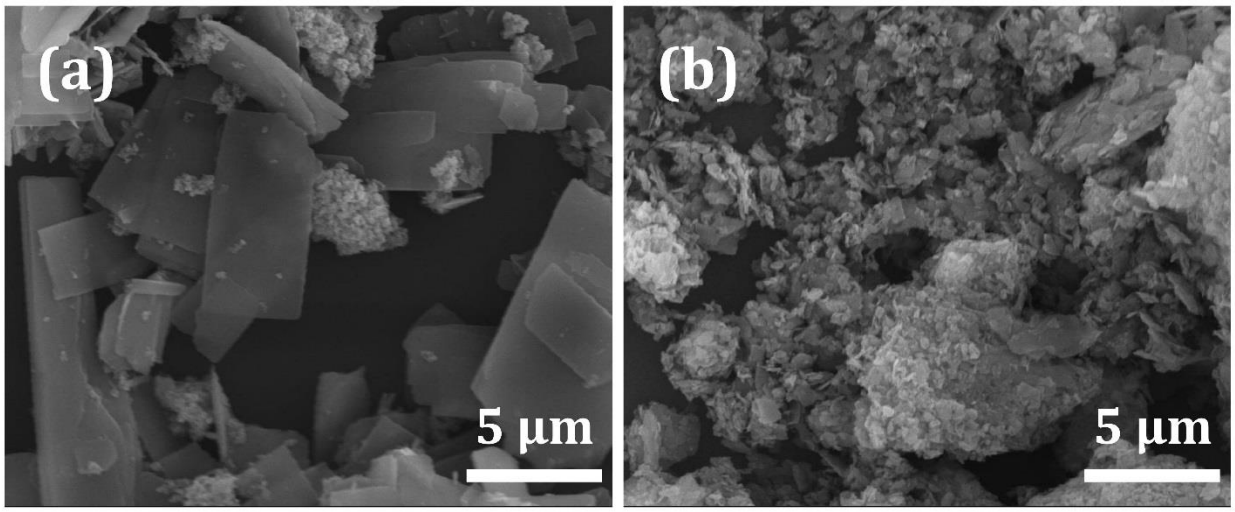

Figure S10. SEM micrographs of as-synthesized $(NH_4)_{1-x}Li_xFePO_4NO_3$ (a); and $NH_4FePO_4NO_3$ (b).

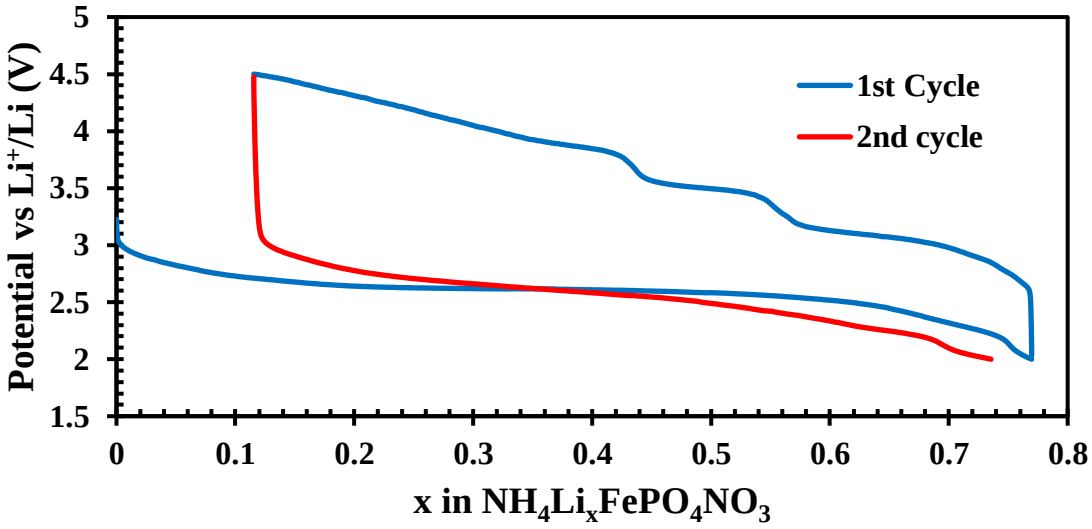

Figure S11. First and second galvanostatic discharge voltage profile of $NH_4FePO_4NO_3$ in Li-ion cell indicating an irreversible phase change following the first cycle lithiation.

References

[I] Huang, W.; Zhou, J.; Li, B.; Ma, J.; Tao, S.; Xia, D.; Chu, W.; Wu, Z. Scientific Reports, 2014, 4, 4188.

BIBLIOGRAPHY

[1] Larcher, D.; Tarascon, J-M. Towards greener and more sustainable batteries for electrical energy storage, Nature Chemistry 2015, *7*, 19-29.

[2] Tarascon, J.-M.; Armand, M. Issues and challenges facing rechargeable lithium batteries *Nature*, **2001**, *414*, 359-367.

[3] Goodenough, J. B., Electrochemical energy storage in a sustainable modern society. *Energy and Environmental Science* **2014,** *7* (1), 14-18.

[4] Whittingham, M. S. Chemistry of intercalation compounds: Metal guests in chalcogenide hosts, *Prog. Solid State Chem.* **1978**, *12*, 41 - 99.

[5] Goodenough J. B.; Park, K-S. The Li-Ion Rechargeable Battery: A Perspective, J. Am. Chem. Soc., **2013**, *135*, 1167–1176.

[6] Ohzuku, T.; Makimura, Y. Layered Lithium Insertion Material of LiCo1/3Ni1/3Mn1/3O2 for Lithium-Ion Batteries, *Chem. Lett.* **2003**, *30*, 642 – 643.

[7] Zhong, Q; Bonakdarpour, A.; Zhang M.; Gao, Y.; Dahn, J. R. Synthesis and Electrochemistry of LiNixMn2−xO4, *J. Electrochem. Soc.* **1997**, *144*, 205 - 213.

[8] Padhi, A. K.; Nanjundaswamy, K. S.; Goodenough, J. B., Phospho-olivines as positive-electrode materials for rechargeable lithium batteries. *Journal of the Electrochemical Society* **1997,** *144* (4), 1188-1194.

[9] Ellis, B. L.; Town, K.; Nazar, L. F., New composite materials for lithium-ion batteries. *Electrochimica Acta* **2012,** *84*, 145-154.

[10] Whittingham, M. S. Lithium Batteries and Cathode Materials, Chem. Rev. **2004**, *104*, 4271−4301.

[11] Arroyo-de Dompablo, M.E.; Armand, M.; Tarascon, J-M.; Amador, U. On-demand design of polyoxianionic cathode materials based on electronegativity correlations: An exploration of the Li2MSiO4 system (M = Fe, Mn, Co, Ni), *Electrochem. Commun.* **2006**, *8*, 1292–1298.

[12] Masquelier, C.; Padhi, A. K.; Nanjundaswamy, K. S.; Goodenough, J. B. New Cathode Materials for Rechargeable Lithium Batteries: The 3-D Framework Structures Li3Fe2(XO4)3(X=P, As), *J. Solid State Chem.* **1998**, *135*, 228 - 234.

[13] Gaubicher, J; Le Mercier, T.; Chabre, Y.; Angenault, J.; Quarton, M. Li/β-VOPO4: A New 4 V System for Lithium Batteries, *J. Electrochem. Soc.* **1999**, *146*, 4375 - 4379.

[14] Huang, H.; Yin, S.-C.; Kerr, T.; Nazar, L. F. Nanostructured Composites: A High Capacity, Fast Rate $Li_3V_2(PO_4)_3$/Carbon Cathode for Rechargeable Lithium Batteries, *Adv. Mater.* **2002**, *14*, 1525 - 1528.

[15] Wurm, C.; Morcrette, M.; Rousse, G.; Dupont, L.; Masquelier, C. Lithium Insertion/Extraction into/from $LiMX_2O_7$ Compositions (M = Fe, V; X = P, As) Prepared via a Solution Method, *Chem. Mater.* **2002**, *14*, 2701 - 2710.

[16] Barker, J.; Saidi, M. Y.; Swoyer, J. L. Electrochemical Insertion Properties of the Novel Lithium Vanadium Fluorophosphate, LiVPO4F, *J. Electrochem. Soc.* **2003**, *150*, A1394 – A1398.

[17] Abouimrane, A.; Armand, M.; Ravet, N. Carbon nano-painting: Application to non-phosphate oxyanions, e.g. Borates, Extended abstract. *203rd Meeting of the Electrochemical Society*, Paris, April 27-May 2, **2003**.

[18] Song, Y.; Zavalij, P. Y.; Chernova, N. A.; Whittingham, M. S. Synthesis, Crystal Structure, and Electrochemical and Magnetic Study of New Iron (III) Hydroxyl-Phosphates, Isostructural with Lipscombite, *Chem. Mater.* **2005**, *17*, 1139 - 1147.

[19] Nyten, A.; Abouimrane, A.; Armand, M.; Gustafsson, T.; Thomas, J. O. Electrochemical performance of Li_2FeSiO_4 as new Li-battery cathode material, *Electrochem. Comm.* **2005**, *7*, 156 - 160.

[20] Yin, S. –C.; Herle, S.; Higgins, A.; Taylor, N. J.; Makimura, Y.; Nazar, L. F. Dimensional Reduction: Synthesis and Structure of Layered $Li_5M(PO_4)_2F_2$ (M = V, Cr), *Chem. Mater.* **2006**, *18*, 1745 - 1752.

[21] Reddy, M. A.; Pralong, V.; Caignaert, V.; Varadaraju, U. V.; Rabeau, B. Monoclinic iron hydroxy sulphate: A new route to electrode materials, *Electrochem. Commun.* **2009**, *11*, 1807 - 1810.

[22] Recham, N.; Chotard, J-N.; Dupont, L.; Delacourt, C.; Walker, W.; Armand, M.; Tarascon, J-M. A 3.6 V lithium-based fluorosulfate insertion positive electrode for lithium-ion batteries, *Nat. Mater.* **2010**, *9*, 68 - 74.

[23] Tripathi, R.; Ramesh, T. N.; Ellis, B. L.; Nazar, L. F. Scalable synthesis of tavorite LiFeSO4F and $NaFeSO_4F$ cathode materials, *Angew. Chem. Int. Ed.* **2010**, *49*, 8738 - 8742.

[24] Ati, M.; Melot, B. C.; Chotard, J. N.; Rousse, G.; Reynaud, M.; Tarascon, J. M. Synthesis and electrochemical properties of pure LiFeSO4F in the triplite structure, *Electrochem. Commun.* **2011**, *13*, 1280−1283.

[25] Barpanda, P.; Ati, M.; Melot, B. C.; Rousse, G.; Chotard, J. N.; Doublet, M. L.; Sougrati, M. T.; Corr, S. A.; Jumas, J. C.; Tarascon, J. M. A 3.90 V iron-based fluorosulphate material for lithium-ion batteries crystallizing in the triplite structure, Nat. Mater. **2011**, *10*, 772−779.

[26] Subban, C. V.; Ati, M.; Rousse, G.; Abakumov, A. M.; Van Tendeloo, G.; Janot, R.; Tarascon, J.-M. Preparation, Structure, and Electrochemistry of Layered Polyanionic Hydroxysulfates: LiMSO4OH (M = Fe, Co, Mn) Electrodes for Li-Ion Batteries, J. Am. Chem. Soc. **2013**, *135*, 3653−3661.

[27] Marx, N.; Croguennec, L.; Carlier, D.; Bourgeois, L.; Kubiak, P.; Le Cras, F.; Delmas, C. Structural and Electrochemical Study of a New Crystalline Hydrated Iron(III) Phosphate $FePO_4 \cdot H_2O$ Obtained from $LiFePO_4(OH)$ by Ion Exchange, *Chem. Mater.* **2010**, *22*, 1854 - 1861.

[28] Marx, N.; Croguennec, L.; Carlier, D.; Wattiaux, A.; Le Cras, F.; Suard, E.; Delmas, C. The structure of tavorite $LiFePO_4(OH)$ from diffraction and GGA + *U* studies and its preliminary electrochemical characterization, *Dalton Trans.* **2010**, *39*, 5108 - 5116.

[29] Recham, N.; Chotard, J-N.; Jumas,J-C.; Laffont, L.; Armand, M.; Tarascon, J-M. Ionothermal synthesis of Li-based fluorophosphates electrodes, *Chem. Mater.* **2010**, *22*, 1142 - 1148.

[30] Ramesh, T. N.; Lee, K. T.; Ellis, B. L.; Nazar, L. F. Tavorite lithium iron fluorophosphate cathode materials: Phase transition and electrochemistry of $LiFePO_4F$-Li_2FePO_4F, *Electrochem. Solid-State Lett.* **2010**, *13*, A43 – A47.

[31] Nishimura, S. –I.; Nakamura, M.; Natsui, R.; Yamada, A. New Lithium Iron Pyrophosphate as 3.5 V Class Cathode Material for Lithium Ion Battery, *J. Am. Chem. Soc.* **2010**, *132*, 13596 – 13597.

[32] Kim, S. – W.; Seo, D. – H.; Kim, H.; Park, K. – Y.; Kang, K. A comparative study on Na_2MnPO_4F and Li_2MnPO_4F for rechargeable battery cathodes, *Phys. Chem. Chem. Phys.* **2012**, *14*, 3299 – 3303.

[33] Khasanova, N. R.; Gavrilov, A. N.; Antipov, E. V.; Bramnik, K. G.; Hibst, H. Structural transformation of Li2CoPO4F upon Li-deintercalation, Journal of Power Sources **2011**, *196*, 355 – 360.

[34] Kuang, Q.; Xu, J.; Zhao, Y.; Chen, X.; Chen, L. Layered monodiphosphate $Li_9V_3(P_2O_7)_3(PO_4)_2$: A novel cathode material for lithium-ion batteries, *Electrochimica Acta*, **2011**, *56*, 2201 – 2205.

[35] Hailong Chen, H.; Hautier, G.; Jain, A.; Moore, C.; Kang, B.; Doe, R.; Wu, L.; Zhu, Y.; Tang, Y.; Ceder, G. Carbonophosphates: A New Family of Cathode Materials for Li-Ion Batteries Identified Computationally *Chem. Mater.* **2012**, *24*, 2009 – 2016.

[36] Reynaud, M.; Ati, M.; Melot, B. C.; Sougrati, M. T.; Rousse, G.; Chotard, J. N.; Tarascon, J. M. $Li_2Fe(SO_4)_2$ as a 3.83 V positive electrode material *Electrochem. Commun.* **2012**, *21*, 77 − 80.

[37] Gonga, Z.; Yang, Y. Recent advances in the research of polyanion-type cathode materials for Li-ion batteries, Energy Environ. Sci., **2011**, *4*, 3223–324.

VITA

Hooman Yaghoobnejad Asl was born in Tehran, Iran on September 1984. He received his B.S. in pure chemistry from the University of Isfahan, Isfahan, Iran in Sep. 2006 and the M.Sc. in analytical chemistry from University of Isfahan in Feb. 2009 with a 1st Class Rank. The subject of M.Sc. research was separation of transition metals ions using weak ion-exchangers based on zirconium phosphonates.

On December 2016 he received his Ph.D. in chemistry from the Missouri University of Science and Technology, Missouri, USA.

During his work as a Ph.D. fellow, He received a number of awards, among them the Dissertation Completion Fellowship from the Graduate Office of Missouri University of Science and Technology, and the Graduate Research Award from the chemistry department at the same institution may be mentioned.

Hooman's Ph.D. research was focused on exploratory synthesis of new polyanionic based transition metal compounds, crystallography and structure solution of inorganic materials and electrochemical energy storage in secondary Li-ion and Na-ion batteries and first principle study of solid-state materials based on quantum mechanical techniques.

He has published 7 papers as the first author and a number of co-authorships in peer-reviewed and high impact scientific journals, a number of which presented in different sections of this dissertation. He is also a member of the American Chemical Society since 2014.